HAL
open science

Synchrotron Nano-scale X-ray studies of Materials in CO2 environment

Elvia Anabela Chavez Panduro

To cite this version:

Elvia Anabela Chavez Panduro. Synchrotron Nano-scale X-ray studies of Materials in CO2 environment. Other [q-bio.OT]. Le Mans Université, 2014. English. NNT : 2014LEMA1010 . tel-01215985

HAL Id: tel-01215985

https://theses.hal.science/tel-01215985

Submitted on 15 Oct 2015

HAL is a multi-disciplinary open access archive for the deposit and dissemination of scientific research documents, whether they are published or not. The documents may come from teaching and research institutions in France or abroad, or from public or private research centers.

L'archive ouverte pluridisciplinaire **HAL**, est destinée au dépôt et à la diffusion de documents scientifiques de niveau recherche, publiés ou non, émanant des établissements d'enseignement et de recherche français ou étrangers, des laboratoires publics ou privés.

Académie de Nantes
ECOLE DOCTORALE DE L'UNIVERSITÉ DU MAINE
Le Mans, France

THÈSE DE DOCTORAT
Spécialité : physique des matériaux

préparée au sein de **l'Université du Maine et l'Installation Européenne de Rayonnement Synchrotron (ESRF)**

Synchrotron Nano-scale X-ray studies of Materials in CO_2 environment

Elvia A. CHAVEZ PANDURO

Thèse soutenue le 26 septembre 2014 devant le jury composé de :

Jean DAILLANT, Directeur général du synchrotron SOLEIL, Président

Michel GOLDMANN, Professeur à l'université de Paris V, Rapporteur

Franck ARTZNER, Directeur de recherche à l'université de Rennes, Rapporteur

Pascal ANDREAZZA, Maitre de conférences à l'université d'Orléans, Examinateur

Alain GIBAUD Professeur à l'université du Maine, Directeur de thèse

Oleg KONOVALOV, Ingenieur de recherche à l'ESRF. Codirecteur de thèse

Acknowledgments

I would like to express my deep and sincere gratitude to my supervisor, Professor Alain Gibaud; his wide knowledge and her logical way of thinking have been of great value for me. His understanding, encouraging and personal guidance have provided a good basis for the present work. I am deeply grateful to my co-supervisor, Oleg Konovalov, scientist in charge of the Beamline ID10 at the ESRF, for sharing his technical expertise during the long experimental runs carried out at beamline ID10.

Beside my advisors, I would like to thank all the members of the lecture commitee : Jean Daillant, Michel Goldmann, Franck Artzner, Pascal Andreaza for their constructive discussion and comments on this manuscript.

I would like to thank to Theyencheri Narayanan and Michael Sztucki for giving me the oportunity to work at ID02 Beamline, Yuriy Chushkin for giving me the oportunity to perform CXDI experiment, Thomas Beuvier for his help and his constructive discussions, Karim Lhoste, for all the technical help for the experiments with the pressure cell.

I wish to express my warm and sincere thanks to other members of Université du Maine, ID10 and ID02 staff: M. Chebil, J. Bal, F. Amiard, Anne Cecile, G. Ripault, B. Ruta, F. Zontone, G. Li Destri, A. Payès, A. Gasperini, M. Fernandez, G. Lotze, J. Gorini for their contribution with technical skill, innovative ideas and their cooperation and assistance.

Finally, I would like to thank everybody who was important to my PhD journey, as well as my apology that I could not mention everyone personally.

Dedicated to my loving mother, Zonia,

for always believing in and encouraging me.

Contents

Preliminary **13**

1. Introduction 15

1.1. Advantage of the Synchrotron for studying materials under CO_2 environment.... 15

1.2. Supercritical carbon dioxide 16

1.2.1. Background 16

1.2.2. Applications 18

1.2.3. Polymer thin film in CO_2 19

1.3. Dissertation Outline 20

2. Theoretical and Experimental Overview 25

2.1. Synchrotron Radiation 25

2.1.1. Properties 28

2.1.2. Specificity of the ID10 beam line 31

2.1.3. Specificity of the ID02 beamline 33

2.2. X-ray interaction with matter 35

2.3. X-ray reflectivity (XRR) 39

2.3.1. General principles 39

2.3.2. Ideal surface: Fresnel Reflectivity 40

2.3.3. Reflectivity from a layered material 42

2.3.4. Analysis of the curves 47

2.4. Small angle X-ray Scattering (SAXS) 51

2.4.1. General principles 52

2.4.2. Structural parameters 56

2.5. Grazing-Incidence Small Angle X-ray scattering (GISAXS) 60

2.5.1. Geometry of GISAXS 60

2.5.2. The scattered intensity 61

2.5.3. Form factors of particles 63

2.5.4. Correlated Particles on a substrate 66

2.5.5. Distorted Wave Born Approximation 69
2.6. Coherent X-ray Diffraction Imaging (CXDI) 73
2.6.1. Phase Problem 74
2.6.2. Phase Retrieval Method 75
2.6.3. Details of the experimental setup 76
3. Analysis of porous powder of $CaCO_3$ prepared via sc-CO_2 using Small Angle X-ray Scattering 81
3.1. Introduction 82
3.2. Experimental part 85
3.2.1. $CaCO_3$ synthesis 85
3.2.2. Methods 87
3.3. Morphologic study of $CaCO_3$ particles by SAXS 87
3.3.1. The GUINIER-POROD model 87
3.3.2. Results and Discussions 89
3.4. Application of SAXS in evaluation of porosity and surface area of $CaCO_3$ 90
3.4.1. Determination of the Porosity 91
3.4.2. Determination of the specific area 95
3.4.3. Results and Discussions 96
3.5. Study of $CaCO_3$ particles by Coherent Diffraction Imaging 99
3.5.1. Introduction 99
3.5.2. Sample preparation and details of reconstruction 100
3.5.3. Results and Discussions 101
3.6. Conclusion 102
4. Study of Polystyrene Ultra thin films exposed to supercritical CO_2 107
4.1. Generalities about Polystyrene 108
4.1.1. Molecule 108
4.1.2. Glass Transition and Free volume 109
4.1.3. Stability of thin films and the dewetting process 111
4.2. Preparation of Polystyrene Ultra thin film and Stability 119
4.2.1. Polystyrene Film Preparation 120
4.2.2. Observation of the Dewetting of the system PS/Si (treated HF) 121
4.3. X-ray Characterization at ambient conditions 127
4.3.1. Homogeneous Polystyrene Thin Film using XRR 127
4.3.2. Polystyrene Islands using GISAXS 128
4.4. Exposure of PS thin films and islands to CO_2 134
4.4.1. Introduction 134

4.4.2. Experimental Procedure 135
4.4.3. Polystyrene Thin film 136
4.4.4. Polystyrene Islands 139
4.4.5. Spreading or stability of islands with CO_2 143
5. Analysis of Silica Mesoporous thin film 153
5.1. Preparation of mesoporous thin films 154
5.1.1. Inorganic matrix: Sol-gel process 155
5.1.2. Surfactants 156
5.1.3. EISA mechanism 159
5.2. Preparation and Characterization of mesoporous thin films 160
5.2.1. Using CTAB as a surfactant: 161
5.2.2. Using FSN as a surfactant : 164
5.3. Using GISAXS analysis to probe pore deformation in mesoporous silica films 169
5.3.1. Introduction 169
5.3.2. Results and Discusions 171
5.4. Surfactant extraction analysis 176
5.4.1. Mesoporous silica template by CTAB having a 3D structure 177
5.4.2. Mesoporous silica templated by CTAB having a 2D structure 182
5.5. Fluorinated surfactant (FSN) removal from mesoporous film using Sc-CO_2 183
GENERAL CONCLUSIONS AND PERSPECTIVES **193**
APPENDICES **197**
A. CO_2 Pressure cell 199
B. Influence of CO_2 pressure on the data analysis 203

Acronym List

Sc-CO_2: supercritical carbon dioxide
sc-state: supercritical state
n: refractive index
ε: complex dielectric constant
$\varepsilon_{0:}$ dielectric constant in the vacuum
λ: wavelength
α_{inc}: incident beam
α_{sca}: scattered beam
ρ_e: electron density
h: Planck's constant
K: Boltzmann's constant
γ: Surface tension
HF: Hydrofluoric acid
PMMA: Poly(methyl methacrylate)
PS: Polystyrene
FSN or FSN-100: Fluororinated surfactant ($C_8F_{17}C_2H_4(OCH_2CH_2)_9OH$)
TMOS: Tetramethyl ortosilicate
TEOS: Tetraethyl ortosilicate
CTE: Coefficient of thermal expansion
GISAXS: Grazing Incidence Small Angle X-ray scattering
SAXS: Small Angle X-ray scattering
XRR: X-ray reflectivity
FWHM: Full width at half maximum
CMC: Critical Micelle Concentration
EISA : Evaporation-Induced Self-Assembly
Rg: Radius of gyration
D_f: Fractal dimension

Preliminary

The work that is presented in this manuscript is the result of a series of experiments that were performed both at the Université du Maine (IMMM Le Mans) and at the ID10 and ID02 beam lines of the ESRF (Grenoble) where I have equally spent half of my time. No wonder that this manuscript will contain the description of this third generation synchrotron facility and of specific experiments that were carried out at these beam lines.

The project I have been working on for three years was mostly oriented on the study by means of x-ray scattering probes of nanomaterials that were exposed to supercritical CO_2. As a result another part of this work will be also dedicated to describing the properties of this supercritical fluid and how it interacts with materials such as polymers for instance.

As the specificity of nanomaterials is to present a typical size of a few nanometers to several hundreds of nanometers, the x-ray probes that were extensively used in this work were small Angle X-ray scattering (SAXS), Grazing Angle Small Angle X-ray Scattering (GISAXS) and X-ray Reflectivity (XRR). For sake of clarity and as a result of some software development, the manuscript also contains some information about the formalisms used to analyze the scattering data.

CHAPTER 1

1. Introduction

1.1. Advantage of the Synchrotron for studying materials under CO_2 environment

The majority of the work under CO_2 presented in this thesis work has been performed at the European Synchrotron Radiation Facilities (ESRF–Grenoble) where I had the opportunity to perform in-situ experiments on the interaction of CO_2 under different pressures on different materials.

Such experiences are almost impossible to perform on a standard laboratory instrument due to the weakness of the brilliance and to the low energy of the sources available in Le Mans (Copper sources working at 8keV). It must be noted that to perform X-ray scattering experiments on this films exposed to CO_2 under pressure necessitates the use of a specific cell through which x-rays must come in and exit without being too much absorbed. The cell which is quite large (100 cm^3) must sustain a pressure of at least 200 bar. These stringent constraints rule out the use of a conventional source for running such experiments and necessitate the use of 3rd generation synchrotron facilities or at least a rotating anode working at the Molybdenum K-edge.

The use of radiation generated by a synchrotron overcome these limitations encountered with conventional sources since the energy is tunable and the brilliance is 8 to 10 orders of magnitude bigger than the one of a conventional source. One of the most important advantages of synchrotron radiation over a laboratory X-ray source is indeed its brilliance. A synchrotron source like the ESRF has a brilliance that is more than a billion times higher than a laboratory source (see Figure 1.1.1a). Brilliance is a term that describes both the

brightness and the angular spread of the beam. High brilliance is of particular importance to perform in-situ experiments and real-time monitoring.

The other advantage is to have high energy beams to penetrate deeper into matter. The high energy X-rays are required to minimise the absorption of the beam going through the diamond windows of the pressure cell (1 mm) and 35 mm of CO_2 in gas, liquid or sc- state. At 22keV, the X-ray pass through the diamond window with a 89% transmission (see Figure 1.1.1b).

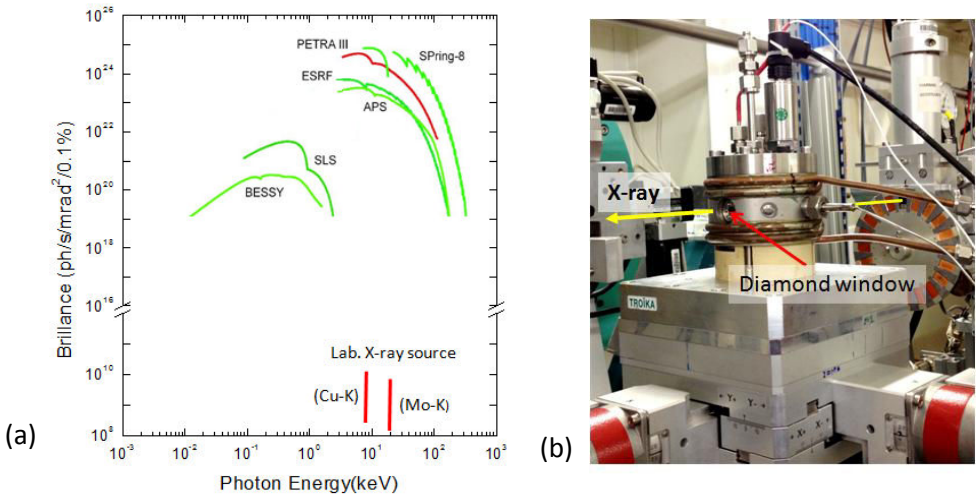

Figure 1.1.1 a) Source Brilliance versus energy for various facilities in the world including the Cu-K and Mo-K line brilliance. b) Pressure cell for in-situ X-ray scattering studies under CO_2. The X-ray pass through the diamond window with a 89% transmission at 22keV.

1.2. Supercritical carbon dioxide

1.2.1. Background

The use of supercritical fluids (SCF) such as carbon dioxide has recently emerged as an efficient environmentally friendly alternative to toxic organic solvents in polymer chemistry [Bruno1991, Kazarian2000, DeSimone2002, Cooper&DeSimone1996]. One of the main reasons is that it has intrinsic environmental compensations: it is nontoxic, nonflammable, and can be easily separated and recycled. In addition to environmental benefits, CO_2 offers other advantages in materials processing due to its low surface tension and its ability to swell, plasticize, and selectively dissolve compounds. The specific

properties of CO_2 have been used favorably in the modification of polymeric films through extractions and impregnations[Kiran1991, Smith1987] plasticization[Kikic2003], foaming [DeSimone1996], coatings[Smith1987], developing [Quadir1997], drying, and stripping of photoresist films in lithography[Bruno1991, DeSimone1992, Magee1991] or nonsolvent for the production of porous materials, aerogels and particles [Tsioptsias2008].

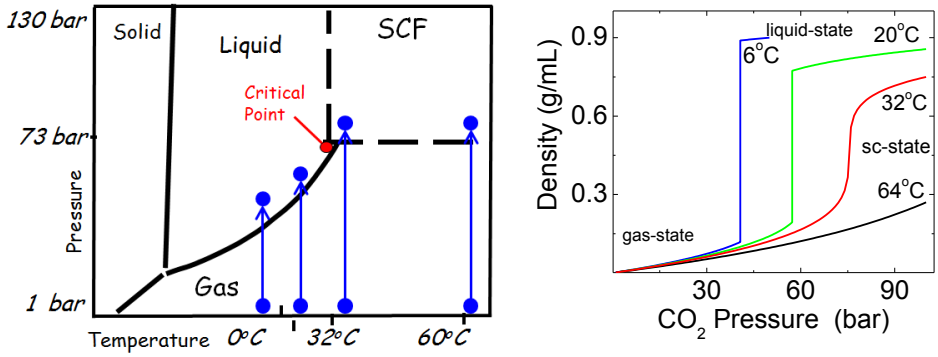

Figure 1.1.2 a) CO_2 phase diagram b) Density versus CO_2 pressure at various isotherms.

Above its critical temperature (T_C) and critical pressure (P_C) [Bruno1991], CO_2 does not behave as a typical gas or liquid but exhibits hybrid properties typical of these two states. With their low viscosity SCF are highly compressible and it is possible to tune the density, viscosity and dielectric constant of a SCF isothermally, simply by raising or lowering the pressure (see Figure 1.1.2). From a practical standpoint, CO_2 has rather modest supercritical parameters (T_C= 31°C, P_C=73.8 bar) and supercritical conditions are therefore quite easily obtained. A visual representation of the transition to the supercritical state for carbon dioxide is shown in Figure 1.1.3.

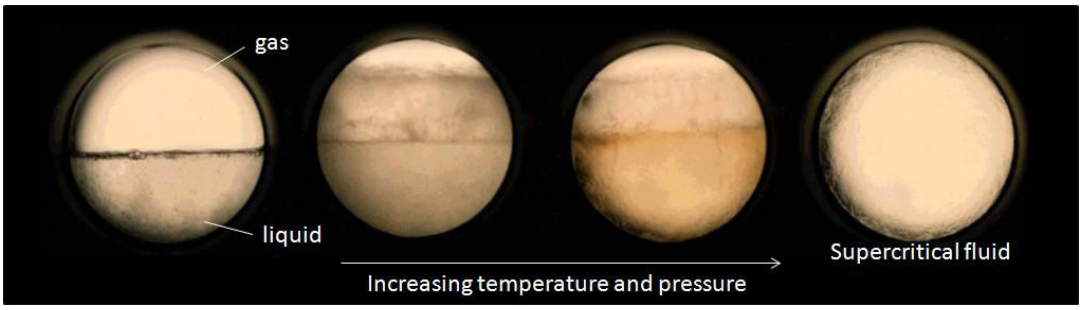

Figure 1.1.3 A visual representation of Carbon Dioxide in the two phase region (Left Picture) reaching a supercritical state (Right Picture) with increasing temperature and pressure [Rayner2001].

1.2.2. Applications

The most widespread use of supercritical carbon dioxide is in Supercritical Fluid Extraction (SFE). Some common examples include the decaffeination of coffee and tea, the processing of hops, tobacco extraction, creation of spice extracts, and the extraction of fats and oils. Nearly all industrial uses of supercritical carbon dioxide are carried out via SFE [Sinvonen1999].

Supercritical Fluid Chromatography (SFC) using carbon dioxide has recently gained popularity. Similar to traditional liquid chromatographic separation, SFC replaces liquid solvents with supercritical carbon dioxide. Although it's mainly used as an analytical technique, it has been demonstrated on an industrial scale by the fractionation of essential oils and fats [Sinvonen1999].

Many chemists have also been turning to supercritical carbon dioxide as a reaction medium. Supercritical carbon dioxide's unique solvent capabilities have proven useful in the pharmaceutical industry where traditional reaction processes may not be suitable for delicate pharmaceutical compounds such as lipophilic materials. The relative safety and effectiveness of supercritical carbon dioxide has led to its natural incorporation into the field of 'Green Chemistry' [Sheldon2005].

Another emerging application is in supercritical particle formation. Recent research has indicated that supercritical carbon dioxide can be used to form micro or nano-sized homogenous particles. This would be a boon for improving inhalable medications, such as insulin. The two most promising methods are the Rapid Expansion of Supercritical Solutions (RESS) technique for non-polar molecules and the Supercritical Antisolvent Crystallization technique for polar molecules [Sinvonen1999].

Many companies specializing in coating are beginning to study supercritical carbon dioxide application techniques. These coatings range from metal primers to biomedical devices to glass coatings. There has even been interest in using supercritical carbon dioxide to remove existing coatings. The flexibility of supercritical carbon dioxide has allowed for its application in a variety of situations [Hay2002].

1.2.3. Polymer thin film in CO_2

One of the most promising applications of supercritical carbon dioxide has been in polymer processing. Carbon dioxide has some unique effects on polymer matrices. In most polymers it acts as a plasticizer, lowering the polymers glass transition temperature and viscosity. This is useful in several polymer processing techniques such as extrusion mixing or foaming. Supercritical carbon dioxide has also demonstrated an ability to increase mass transport of large molecules into the polymer matrix, a useful property for the pharmaceutical industry. Carbon dioxide has also been used as a suitable substitute for traditional foaming agents such as Chlorofluorocarbons because of its ability to increase polymer molecular mobility while retaining the polymer's physical durability [Tomasko2003].

To gain more control over the polymer behaviour in CO_2, it is also important to examine the interactions between both. It is well known that CO_2 has no dipole moment and extremely weak van der Waals forces. Consequently, CO_2 possesses a low cohesive energy density and most hydrocarbon polymers only have limited solubility in supercritical CO_2. The so called "CO_2 philic" polymers are either polysiloxanes or fluorocarbons, both of which have low cohesive energy density and thus small surface energy, just like CO_2. However, Sarbu et al. recently designed CO_2 soluble hydrocarbon copolymers by optimizing the balance between the enthalpy and entropy contribution to the solubility of polymers in CO_2 [Sarbu2000].

Generally speaking, the solubility of CO_2 in polymers increases with increasing CO_2 pressure while decreases with increasing CO_2 temperature. Polymers-CO_2 interactions also influence the solubility of CO_2 in polymers. For example, specific intermolecular interactions were found between CO_2 and the carbonyl group in poly(methyl methacrylate) (PMMA) [Kazarian1996]. Hence the solubility of PMMA in CO_2 is almost twice as much as polystyrene under the same conditions [Wissinger1987].

With regard to thin films, experimental works have explored many aspects on the physical properties of various polymer films under pressurized CO_2 environment [Sirard2001, Pham2004, Koga2002, Meli2004]. Pham et al. show the existence of a glass transition pressure "Pg" induced by sc-CO_2. They also show that the referred 'Pg' at which the transition occurs decreases with decreasing film thickness in PMMA and PS thin films

[Phan2003]. Meli et al. showed that PS thin films formed on SiO_2/Si are metastable in a CO_2 environment. In addition, they found that the contact angle formed for PS droplets on SiO2/Si in CO_2 are higher than for PS droplets in air. This result is a clear indication that the wetting is less favourable under CO_2 exposure [Meli2004]. In addition, the structure of end-grafted polymer brush in CO_2 has also been investigated by neutron reflectivity [Koga2004]. However, the effects of CO_2-polymer, CO_2-substrate and polymer-substrate interactions on the structure and physical properties of polymer thin films in CO_2 are still unclear. One of the most fundamental and best studied properties of polymer thin film is swelling. Many studies have pointed out that the swelling and adsorption of CO_2 into polymer thin films are higher than that of the bulk values, and increase substantially as the films thickness decreases [Sirard2002, Koga2002, Koga2003]. In addition, several studies have consistently found that the swelling isotherms of polymer thin films in CO_2 have an anomalous peak in the regime where the compressibility of CO_2 is at maximum [Sirard2002, Koga2002].

1.3. Dissertation Outline

The main objective of this dissertation is the study of the effects of supercritical CO_2 (sc-CO_2) on materials. My research is mainly focused on the study of the interaction of sc-CO_2 with polymers such as Polystyrene and fluorinated molecules as well as the study of the effects of CO_2 in the formation process of $CaCO_3$ particles. As this Ph.D. was carried out in part at the ESRF, it is obvious that a large part of the dissertation is devoted to the interaction of synchrotron radiation with materials exposed to sc-CO_2. The main body of this dissertation is divided into five chapters.

In Chapter 2 are described the characterization methods used throughout this thesis. Some of these techniques are used for powder materials such as SAXS (Small Angle X-ray Scattering) and CXDI (Coherent X-ray Diffraction) and others are used for thin films as XRR (X-ray Reflectivity) and GISAXS (Grazing Incidence Small Angle X-ray Scattering). In the particular case of the GISAXS technique, detailed information is presented to explain how the experimental results reported in Chapters 4 and 5 were analysed.

In Chapter 3, the results of Small Angle and Ultra Small Angle X-ray Scattering and Coherent X-ray Diffraction Imaging on porous $CaCO_3$ micro particles of pulverulent vaterite made by a conventional chemical route and by supercritical CO_2 are presented.

The scattering curves are analyzed in the framework of the Guinier-Porod model which gives the radii of gyration of the scattering objects and their fractal dimension. In addition, we determine the porosity and the specific surface area by using the Porod invariant which is modified to take in account the effective thickness of the pellet. The results of this analysis are compared to the ones obtained by nitrogen adsorption.

Chapter 4 is mainly devoted to the study of polystyrene ultra thin films exposed to CO_2 under pressure. The first part of this chapter is devoted to a discussion concerning the possible dewetting of a PS film at the surface of silicon. In the remaining part, we study the influence of CO_2 pressure on homogeneous films and islands focusing mainly on the swelling of PS and on the effect of pressure on the islands stability.

Chapter 5 describes the study of mesoporous silica thin films by x-ray scattering. We first focus on the preparation of these silica films using two types of surfactants to template and structure the silica backbone. One of them is the well-know cethyl trimetyl ammonium bromide CTAB while the second one is a fluorinated one the so-called FSN. It is very important to understand that once a silica thin film has been templated by a surfactant and is highly organized, the removal of the surfactant is a critical issue. This is addressed in section 5.3 in which we report in-situ x-ray measurements. For CTAB templated thin films, the surfactant was removed by simple annealing while for FSN, we used an alternative method to extract the surfactant, based on the use of supercritical carbon dioxide. Finally we show in this chapter that GISAXS patterns of thin films with ordered internal 3D mesoscale structures can be quantitatively modelled, using the Distorted Wave Born Approximation (DWBA). We go beyond what has previously been achieved in this field by addressing how the anisotropy of the scattering objects can be assessed from a complete fit to the data contained in the GISAXS patterns.

Bibliography

[BeckTan1198] Beck Tan, N. C.; Wu, W. L.; Wallace, W. E.; Davis, G. T. J. Poly. Sci. B: Polym. Phys. (1998) 36, 155.

[Bruno&Ely1991] Bruno, T. J.; Ely, J. F. Supercritical Fluid Technology: Reviews in Modern Theory and Applications: CRC Press: Boston, MA, 1991.

[Carbonell2006] Carbonell, R. G.; Carla, V.; Hussain, Y.; Doghieri, F. Eighth Conference on Supercritical Fluids and Their Applications, Ischia, Italy, 28-31 May, 2006.

[Cooper&DeSimone1996] Cooper, A. I.; DeSimone, J. M. Curr. Opin. Solid State Mater. Sci.(1996) 1, 761−766.

[DeSimone1992] DeSimone, J. M.; Guan, Z.; Eisbernd, C. S. Science (1992) 257, 945−947.

[DeSimone1996] Canelas, D. A.; Betts, D. E.; DeSimone, J. M. Macromolecules (1996) 29, 2818 −2821.

[DeSimone2002] DeSimone, J. M. Science (2002) 297, 799−803.

[Hay2002] Hay, J.N.; Khan, A. Materials Science (2002) 37. 4743-4752.

[Kazarian1996] Kazarian, S. G.; Vincent, M. F.; Bright, F.; Liotta, C. L.; Eckert, C. A. J. Am.Chem. Soc. (1996) 118, 1729.

[Kazarian2000] Kazarian, S. G. Polym. Sci. Ser. C. (2000) 42, 78.

[Kikic2003] Kikic, I.; Vecchione, F.; Alessi, P.; Cortesi, A.; Eva, F.; Elvassore, N. Ind. Eng. Chem. Res. (2003) 42, 3022−3029.

[Kiran1991] Kiran, E.; Brennecke, J. F. Supercritical Fluid Engineering Science; American Chemical Society: Washington D.C., 1991.

[Koga2003] Koga, T.; Seo, Y. S.; Shin, K.; Zhang, Y.; Rafailovich, M. H.; Sokolov, J. C.;Chu, B.; Satija, S. K. Macromolecules (2003) 36, 5236.

[Koga2002] Koga, T.; Seo, Y. S.; Zhang, Y.; Shin, K.; Kusano, K.; Nishikawa, K.;Rafailovich, M. H.; Sokolov, J. C.; Chu, B.; Peiffer, D.; Occhiogrosso, R.; Satija, S. K. Phys. Rev. Lett. (2002) 89, 125506.

[Koga2004] T. Koga, Y. Ji, Y. S. Seo, C. Gordon, F. Qu, M. H. Rafailovich, J. C. Sokolov, S. K. Satija. Journal of Polymer Science: Part B: Polymer Physics (2004) Vol. 42, 3282–3289.

[Koga2005] Koga, T.; Jerome, J. L.; Seo, Y. S.; Rafailovich, M. H.; Sokolov, J. C.; Satija, S. K. Langmuir (2005) 21, 6157.

[Magee1991] Magee, J. W. Supercritical Fluid Technology, Bruno, T. J.; Ely, J.F., Eds.; CRC Press: Boston, MA, (1991) pp 325−334.

[Meli2004] Meli, L.; Pham, J. Q.; Johnston, K. P.; Green, P. F. Phys. Rev. E (2004) 69,051601.

[Quadir1997] Quadir, M. A.; Kipp, B. E.; Gilbert, R. G.; DeSimone, J. M.Macromolecules (1997) 30, 6015−6023.

[Pham2003] Pham, J. Q.; Sirard, S. M.; Johnston, K. P.; Green, P. F. Phys. Rev. Lett. (2003) 91,175503 **[Pham2004]** Pham, J. Q.; Johnston, K. P.; Green, P. F. J. Phys. Chem. B (2004) 108, 3457.

[Rayner2001] Rayner, C.M; More about supercritical carbon dioxide. Leeds Cleaner Synthesis Group. 2001. http://www.chem.leeds.ac.uk/People/CMR/criticalpics.html

[Sarbu2000] Sarbu, T.; Styranec, T.; Beckman, E. J. Nature (2000) 405, 165.

[Sheldon2005] Sheldon, R.A. Green Chemistry. (2005) 7, 267-278.

[Sirard2001] Sirard, S. M.; Green, P. F.; Johnston, K. P. J. Phys. Chem. B (2001) 105, 766.

[Sirard2002] Sirard, S. M.; Ziegler, K. J.; Sanchez, I. C.; Green, P. F.; Johnston, K. P. Macromolecules (2002) 35, 1928.

[Sirard2003] Sirard, S. M.; Gupta, R. R.; Russell, T. P.; Watkins, J. J.; Green, P. F.; Johnston,K. P. Macromolecules (2003) 36, 3365.

[Sinvonen1999] Sihvonen, M.; Jarvenpaa, E.; Hietaniemi, V.; Huopalahti, R. Trends in Food Science and Technology (1999) 10, 217-222.

[Smith1987] Smith, J. M.; VanNess, H. C. Introduction to Chemical Engineering Thermodynamics, 4th ed.; MacGraw Hill, Inc.: New York, 1987.

[Tsioptsias2008] Tsioptsias, C.; Stefopoulos, A.; Kokkinomalis, I.; Papadopoulou, L.; Panayiotou, C. Green Chem. (2008) 10, 965−971.

[Tomasko2003] Tomasko, D.L.; Li, H.; Liu, D.; Han, X.; Wingert, M.J.; Lee, L.J.; Koelling, K.W. Industrial and Engineering Chemistry Research. (2003) 42, 6431-6456.

[Vogt2004] Vogt, B. D.; Soles, C. L.; Jones, R. L.; Wang, C. Y.; Lin, E. K.; Wu, W. L.; Satija, S. K. Langmuir (2004) 20, 5285.

[Wissinger1987] Wissinger, R. G.; Paulaitis, M. E. J. Poly. Sci. B: Polym. Phys. (1987) 25, 2497.

CHAPTER 2

2. Theoretical and Experimental Overview

2.1. Synchrotron Radiation

X-rays are electromagnetic radiations having a wavelength in a range which goes from 0.1 to more than 10 Å (i.e. energy ranging from 1.24 to 124keV). The wavelength is therefore of the same order as the interatomic distance in condensed matter which makes x-ray radiation a key radiation for studying crystallized materials. The energy (E) of x-ray photons is defined by:

$$\boldsymbol{E} = \boldsymbol{h}\upsilon = \frac{\boldsymbol{hc}}{\lambda} \qquad [2.1.1]$$

where h is the Planck constant, ν the radiation frequency, $c=3x10^{8}$ ms^{-1} is the velocity of light in a vacuum and λ the wavelength. In practice, X-rays can be nowadays produced by two methods that use either - X-ray tubes or Synchrotron accelerators.

In conventional X-ray sources, thermal electron emission is achieved by heating a tungsten filament (cathode). A high voltage (30-150kV) is then used to accelerate them inside an evacuated tube. Their impact on a cooled-metallic target (anode) produces X-rays by either *Bremstrablung* and X-ray fluorescence. The first effect is related to the loss of kinetic energy by the electrons when they hit the metallic anode. This gives rise to radiations having an energy that cannot overpass the one corresponding to the accelerating voltage. The second effect corresponds to the production of monochromatic ($\Delta E/E=10^{-4}$) fluorescence lines characteristic of the anode material (as for instance, 8keV for Copper Kα line). However, current X-ray sources exhibit some limitations among which the size of the filament, the limited power and the divergence of the beam that all reduce the brilliance of the source.

Since a bit more than four decades, highly brilliant x-ray sources have been implemented at synchrotron radiation facilities all over the world. Synchrotron radiation is produced when a beam of relativistic electrons are deviated in a magnetic field. Electrons are initially emitted by an electron gun and pre accelerated using a linear accelerator (LINAC). Afterwards they are transferred to a circular accelerator (BOOSTER) until they achieve energy of several GeV (e.g. 6GeV at the ESRF). Then they are injected into the storage ring, which is a gigantic vacuum chamber of several hundred meters (i.e. 844m at the ESRF) of circumference composed of straight (insertion-devices) and curved (bending magnet)sections (Fig 2.1.1)

Inside the ring, electrons turn at an almost constant energy during several hours. Their trajectory is defined by the magnetic fields that they pass through. Three types of devices can be distinguished by the geometry and each of them influences the beam properties in a different way. The Bending Magnet (BM) causes a circular deflection of the incident straight path of the electrons. Each time a bunch of electrons passes through a BM it is accelerated and it adopts a circular motion. During this phase, electrons are accelerated and emit a large and medium intensity x-ray spectrum with a broad continuum of x-ray energies (Fig 2.1.2a). In contrast to BM, undulators are constituted by a series of magnets of alternated polarity that force the electrons to follow a wavy-path with a small deviation angle. All along this trajectory, the emitted electric fields can interfere. These nterferences produce very intense and parallel X-rays at some specific wavelengths

(Figure 2.1.2b). The synchrotron x-ray beam is always tangent to the trajectory of the electrons in the magnetic field, and can be delivered to the experimental stations (beamlines) which are located around the ring.

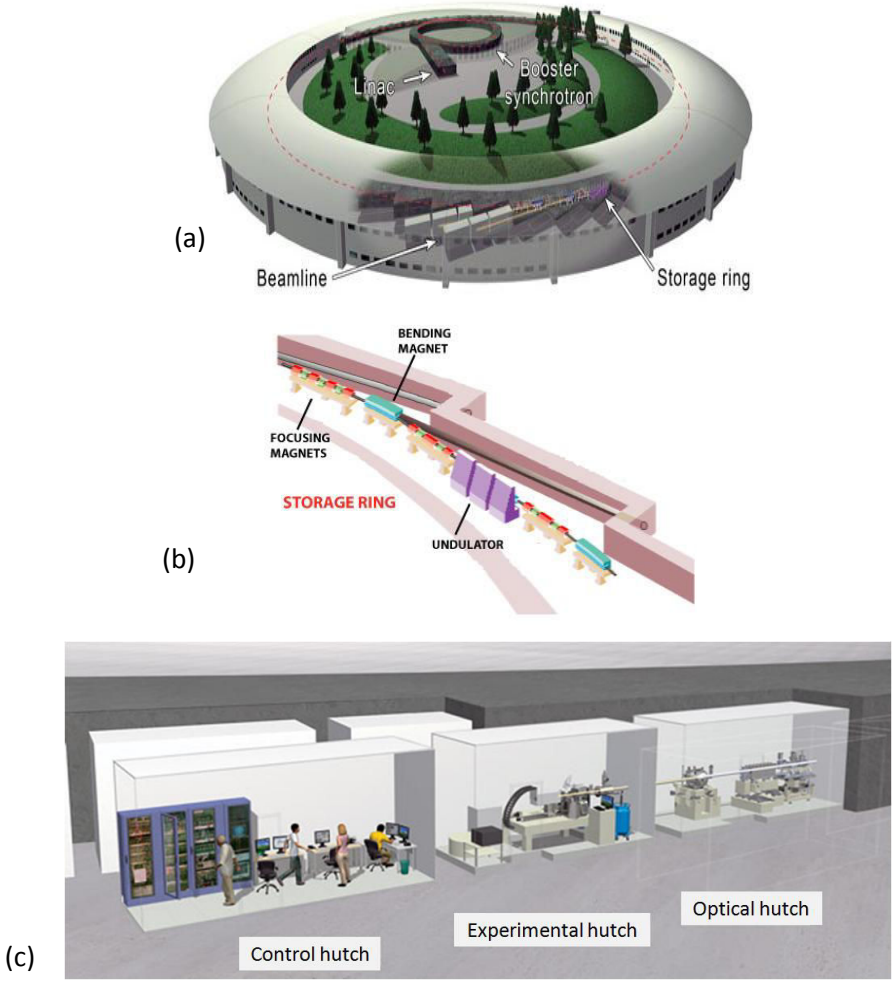

Figure 2.1.1 Scheme of a synchrotron showing (a) the linear and circular pre-accelerators (b) insertion devices and bending magnets inside the storage ring, (c) a typical beam line. *(Courtesy of the ESRF*)

Each beam line uses specific optics to shape and tune the beam in such a way that it fills the requirements of a determined technique. A beamline is usually composed of three hutches (Fig. 2.1.1.c): (1) the optical hutch located next to the storage ring containing the optical instruments needed for beam-shaping (i.e. monochromators for selecting a given wavelength, mirrors to focus down the beam size); (2) the experimental hutch hosting the sample and the experimental set-up (sample environment, detectors, motors, cameras,

etc) and (3) an additional room allowing researchers to control their experimental and collect the data.

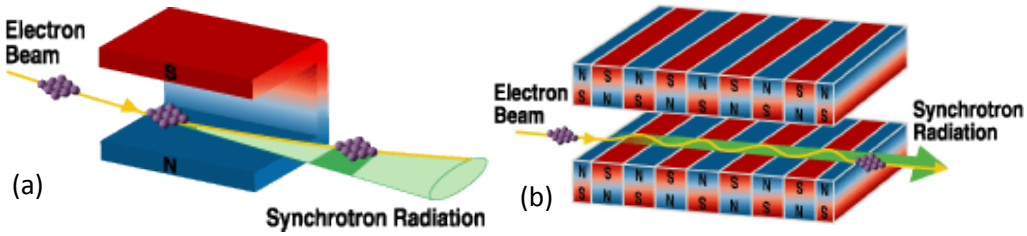

Figure 2.1.2 Synchrotron radiation produced at (bending magnet) and (b) undulators.

Nowadays light sources of this kind are becoming widespread and easily accessible. Among the most important third generation synchrotron sources, one can cite the Advanced Photon Source (APS) in USA, Spring-8 in Japan, Soleil in France, Petra in Germany, Elettra in Italy and the European Synchrotron Radiation Facility (ESRF) in Grenoble.

2.1.1. Properties

The synchrotron radiation offers several advantages for the development of scattering/diffraction, spectroscopy, imaging and tomography techniques due to its intrinsic properties e.g. high brilliance, tunable energy, high collimation, spatial coherence, polarized and pulsed beams.

a) *High Brilliance*: The source brilliance is defined as a number of photons per second (flux) emitted per unit area and per unit solid angle in a given bandwidth. It is expressed in (photons/s/mm^2/mrad^2/0.1%bw). What makes the synchrotron sources highly brilliant is the very weak angular divergence that arises from the high collimation of the synchrotron beam. This is a natural phenomenon caused by relativistic effects and by the horizontal movement of the electrons which precludes any vertical divergence of the beam. The narrow bandwidth of radiation and also a high flux and small geometrical divergence results in exceptional brilliance ($1x10^{21}$ photons/s/mm^2/mrad^2/0.1%bw for ESRF since 2011). **High brilliance is of particular importance to perform in-situ experiments and real-time monitoring.**

b) *Monocromaticity:* The very high flux allows to select an homogeneous and monochromatic beam by using single-crystal or channel cut monochromators and by modulating the gap of undulators. Bending magnets provide a broad continuum of X-rays energies (white beam) whereas undulators produce very intense and parallel X- rays concentrated in narrow energy bands in the spectrum. A single or double mirror is used for the higher harmonics suppression.

c) *Focused Beam*: Due to the high collimation of the beam and the progress in X-ray optics, micro and nano focused beams (cross sections ranging between 100µm-100nm) can be achieved and used to measure the weakly scattering sample with high sensitivity and precision.

d) *Coherent beam:* The high degree of coherence of the beam allows performing **the coherence diffraction imaging** techniques. Coherent properties of the X-rays beam is characterised with the two type of coherence: transverse and longitudinal coherences defined as [Als-Nielsen&McMorrow2010]:

- The longitudinal coherence length (also called temporal coherence length) is the distance over which two waves from the same source point with slightly different wavelengths that will be completely out of phase.

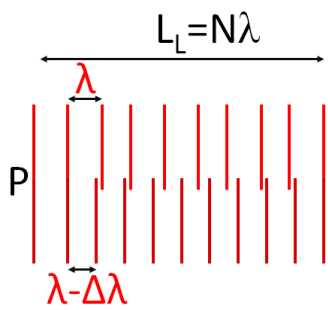

Figure 2.1.3 Longitudinal coherence length.

Two waves of slightly different wavelength λ and λ-Δλ are emitted from the same point in space simultaneously. As shown in Fig. 2.1.3. , the two waves are back in phase when Nλ=(N-1)(λ-Δλ). This defines the coherence length L_L which can be easily expressed as

$$L_L = N\lambda = \frac{\lambda^2}{\Delta\lambda} \qquad [2.1.2]$$

- The transverse coherence length (also called spatial coherence length) is the lateral distance along a wavefront over which there is a complete dephasing between two waves, of the same wavelength, which originate from two separate points in space.

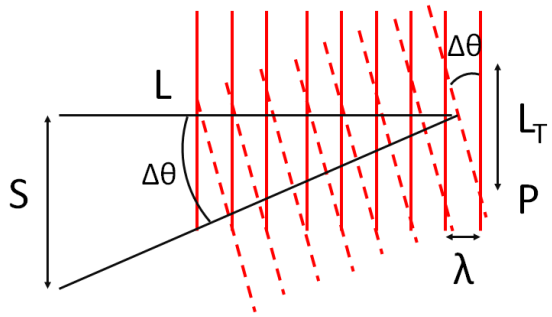

Figure 2.1.4 Transverse coherence length.

The path length difference between the two waves is given by SxΔθ. When this path length is equal to λ the two waves coming from two points distant of S in the source are in phase. This distance S defines the lateral coherence length and is given by

$$Sx\Delta\theta = \lambda \qquad S = L_T = \frac{\lambda}{\Delta\theta} = \frac{\lambda L}{S} \qquad [2.1.3]$$

where L is the observation point-source distance and S is the source size.

e) Sample Environment: Samples can be mounted in a special sample environment to vary external parameters (temperature, pressure, etc). **During my thesis work, a pressure cell for carbon dioxide has been used to perform GISAXS and XRR measurement.**

f) *High Energies*: The high energy X-rays are required to minimise the absorption of the beam going through the 35 mm of CO_2 in gas, liquid or sc- state specially **design sample cell** and through 1mm of diamond windows required to resist high pressure and to be X-rays transparent.

2.1.2. Specificity of the ID10 beam line

This section is dedicated to the description of the beamline ID10 of the European Synchrotron Radiation Facility (ESRF) where GISAXS and XRR measurement has been performed using the cell pressure.

The beam line is composed of two experimental hutches: one (ID10-LSIS) devoted to structural studies on soft condensed matter surfaces and interfaces using grazing-incidence diffraction (GID), X-ray reflectivity (XRR), grazing-incidence small-angle scattering (GISAXS) and Grazing Incidence X-Ray Fluorescence (GIXRF) and another (ID10-CS) fully dedicated for experiments with coherent X-rays to study slow dynamics in soft and hard condensed matter with X-ray Photon Correlation Spectroscopy (XPCS) and to lens-less imaging applications with Coherent Diffraction Imaging (CXDI). The X-ray source of ID10 is composed of three independent undulator segments in series. Two segments are stationary and host a U27 (27mm period) and a U35 (35mm period) standard ESRF undulator, respectively. The third segment is modular (revolver-type) and either a U27 or a U35 may be inserted rapidly and used depending on energy requirements. All undulators are operating ex vacuum with a minimum gap of ~11 mm. This undulator configuration allows optimizing the flux over a broad range of energies. When combining 2×U27+U35 with the 1st harmonic of U27 and the 3rd harmonic of U35 tuned to 8keV the measured peak brilliance exceeds 10^{20}photons/s/mm^2/mrad^2/0.1%bw at 100mA. The source size (FWHM) is 19µm x 945µm. ID10-LSIS is operating over a broad energy range between 7keV and 30keV.The peak performance is achieved when the two U27 segments are used, i.e. between 7-11keV with the first harmonic and 21-30keV with the third harmonic. ID10-CS operates in the range 7-10keV, the range where the ID10 section delivers the highest brilliance. The standard working energy is 8 keV where the focusing capabilities are optimized, and the coherent flux on the sample exceeds $1x10^{11}$ph/s/100µm^2 with all three undulators tuned and phased.

The optics to focus the beam at ID10 is composed of Beryllium lenses installed in a machine named *transfocator.* This system allows us to focus the beam on the detector position or at the sample position with a few micrometers size spot in a large energy range by selecting the appropriate number of lenses.

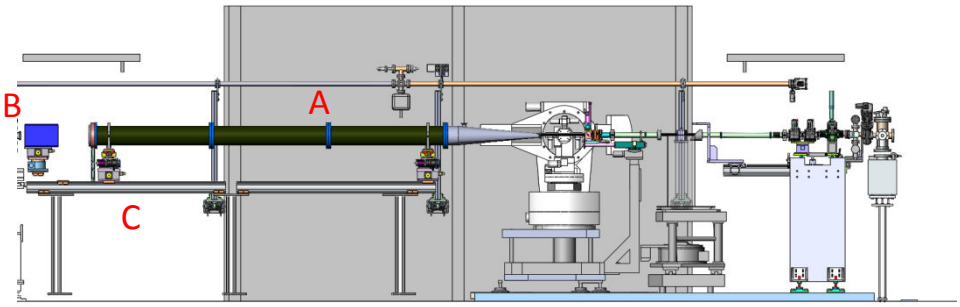

Figure 2.1.5 The high resolution GISAXS setup: A – variable length evacuated flightpath; B – two dimensional detector on the translation stage; C – optical rail. *(Courtesy of the ESRF*)

The ID10-LSIS has a large hutch, which allows us positioning the detector at 4m from the sample and perform GISAXS studies **on my samples of Polystyrene Island supported on silicon.** The permanent GISAXS setup comprises the optical rail (Fig.2.1.5 C), mounted on three pillars downstream the diffractometer, the 2D MAXIPIX detector with its holder (Fig.2.1.5 B) and the evacuated flightpath (Fig.2.1.5A).

The principle of the setup was tested for the first time during my experiments using high energy (22keV) to minimize the absorption in air in absence of the long evacuated flight path. The measured GISAXS image clearly shows the island-island correlation peak (Fig. 2.1.6).

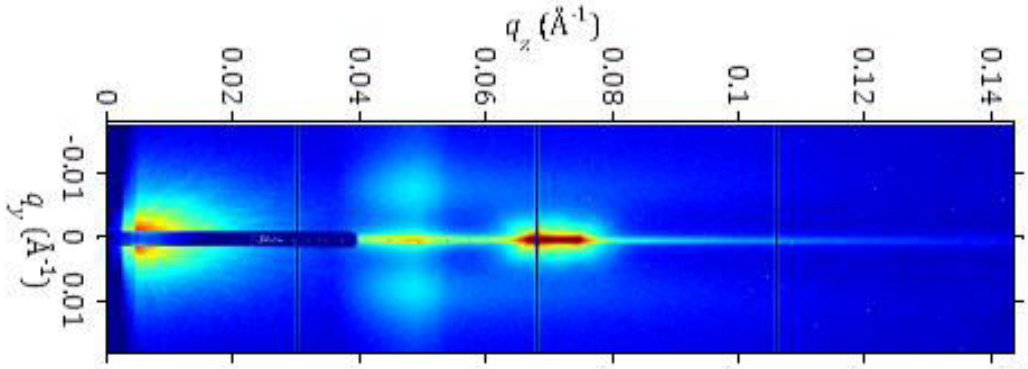

Figure.2.1.6 First experimental test with the high resolution GISAXS setup. Experimental conditions: energy - 22keV; grazing angle – 0.18 deg; sample-detector distance - 4m; detector – Maxipix 5 x 1. Sample: polystyrene islands on a silicon wafer in CO_2 atmosphere; islands height is 5nm and island-island correlation length is 100nm.

Another key component that makes it possible to collect GISAXS patterns with a high resolution is the detector. During my thesis work I had the opportunity to use the MAXIPIX detector which has a pixel size of 55µm and working area 14x70 mm^2. This detector was developed at CERN and built at the ESRF.

2.1.3. Specificity of the ID02 beamline

Following the details about the ID02 beamline are given. This beamline was recently upgraded and is available for the users since july. It is important to note that all the SAXS and USAXS measurements were performed in the ID02 beamline before the upgrade mentioned.

The beamline ID02 is primarily a combined (ultra) small-angle and wide-angle scattering instrument. The high brilliance of an undulator source is exploited to probe the microstructure and non-equilibrium dynamics of soft matter and related systems from a few Angstroms to micron scale, and down to millisecond time range. The figure 2.1.7 schematically depicts the beamline ID02 with two end-stations for SAXS/WAXS and Bonse-Hart USAXS. Typically, photon flux of the order of $4x10^{13}$ photons/sec at 100mA is obtained at the sample position when two U21 undulators are closed to their optimum gaps for 12.4keV. The standard beam size is 200 µm x 400 µm (vertical and horizontal, respectively) with divergence of 20 µrad x 40 µrad.

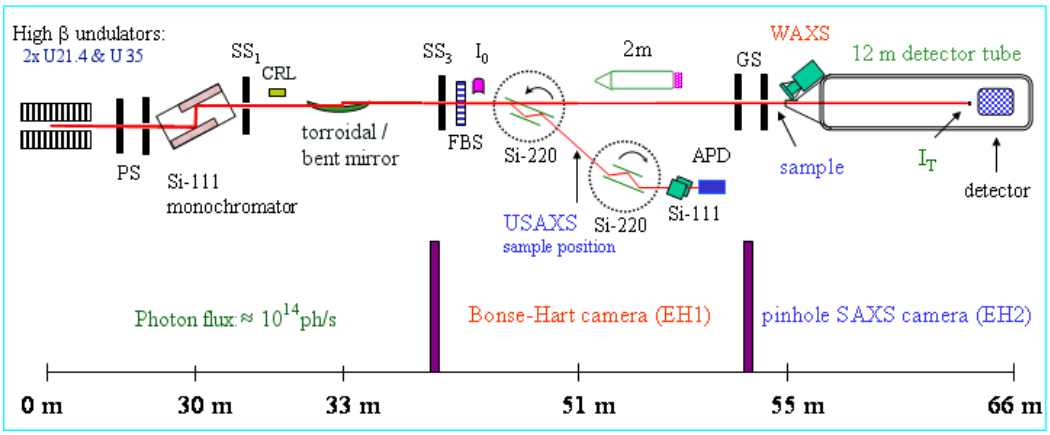

Figure 2.1.7 Schematic layout of the existing beamline displaying SAXS/ WAXS and Bonse-Hart USAXS stations *(Courtesy of the ESRF)*.

The SAXS detector is mounted on a wagon inside the 12 m detector tube. The sample-to-detector distance can be varied from 1 m to 10 m covering a wide scattering wave vector q-range, $6x10^{-3}$ nm^{-1} < q < 6 nm^{-1}, where $q=(4\pi/\lambda)\sin(\theta/2)$, with λ the wave length (~0.1 nm) and θ the scattering angle. The q resolution limited by the beam divergence (~25 µrad) and size (~100 µm) is about $3x10^{-3}nm^{-1}$. However, the smallest q reachable at 10m detector distance is also limited by the detector point spread function and the parasitic scattering to about $6x10^{-3}nm^{-1}$. In normal operation, q is further curtailed to about $0.008nm^{-1}$ due to the parasitic background and limited dynamic range of the detector.

The USAXS setup use a Bonse-Hart crystal analyser configuration. This technique was used to complement the SAXS measurement on the study of $CaCO_3$ particles (see Figure 2.1.8a). The resolution that can be achieved with this configuration is (0.001 nm^{-1}) which allows to extent the q range in the scattering measurement. In Figure 2.1.8b shown the typical space and time scales accessible with SAXS, WAXS and USAXS techniques.

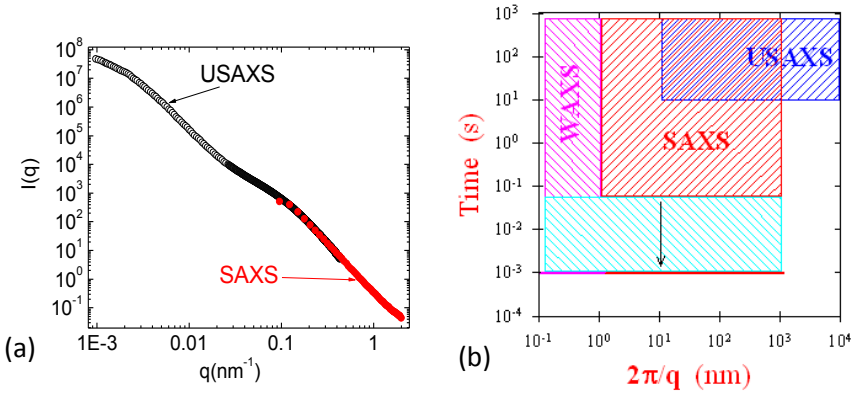

Figure 2.1.8 a) SAXS and USAXS measurement, sample-detector distance for SAXS was 2m at 12.4keV. b) Full range of space and time scales accessible by SAXS/WAXS and USAXS techniques. (*Courtesy of the ESRF*)

The upgrade of this beamline comprises a novel focusing scheme chosen to preserve the brilliance of the source, a new detector vacuum tube of 30m length and a suit of detectors tuned for different applications. All three techniques, SAXS, WAXS and USAXS, are combined to a single instrument with sample-to-detector distance variable from 0.6 m to 30 m.

2.2. X-ray interaction with matter

This section deals with the presentation of the fundamental aspects of x-ray interactions with matter which are important to explain the principles of X-ray reflectivity, GISAXS and SAXS. A more detailed and exhaustive treatment of those techniques can be found in several books as [Gibaud2009, Als-Nielsen&McMorrow2010].

When an x-ray beam interacts with a sample, basically three processes may be observed The incident beam may be either **refracted/reflected**, or **scattered** or **absorbed**. These three processes are illustrated in the Figure 2.2.1.

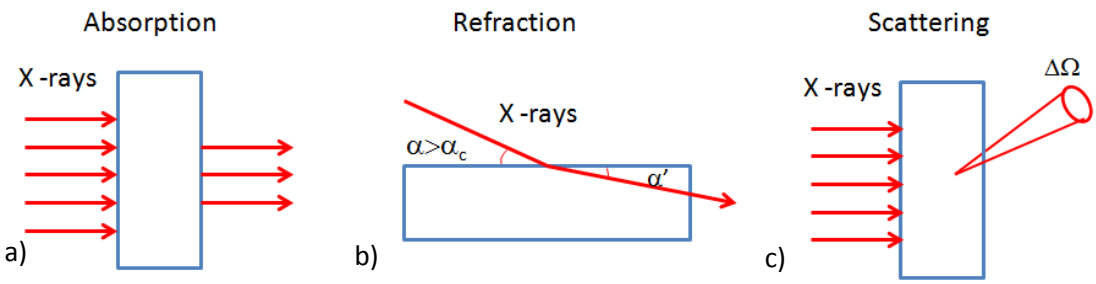

Figure 2.2.1 The x-ray beam interacts with a sample in three different ways: a) absorption, refraction, or scattering.

- **Absorption**

In practice, the absorption is characterized by the linear absorption coefficient μ. It is straightforward to show that the transmitted intensity I(z) at a depth z from the surface of material at the normal incidence is given by the well known Beer-Lambert's law

$$I(z) = I_0 \exp(-\mu z) \qquad [2.2.1]$$

When an x-ray photon is absorbed by an atom, its energy is transferred to some electrons which might be either expelled from the atom leaving it ionized or absorbed so as to increase their energy by changing their levels. The process is known as photoelectric absorption. When the energy exceeds the threshold for expelling an electron from a certain shell, another channel of absorption is opened up and the cross section exhibits a discontinuous jump at the threshold energy. These discontinuities are called absorption edges.

Near a threshold energy, the cross section has actually more structure than just a discontinus jump. The detailed energy dependence is called EXAFS (Extended X-ray Absorption Fine Structure). The electron wave is scattered by the electron clouds of neighboring atoms and interference phenomena (oscillations) occurs versus the X-ray energy. The EXAFS spectrum is interpreted either by comparing with theoretical models or with the spectra from known complexes.

- **Refraction**

When the x-ray beam impinges at a surface, it slightly changes its direction by refraction (Fig. 2.2.1b). This phenomenon, very well known for visible light, is for instance responsible for the deviation of light when it passed through a prism. X-ray beams can also be refracted. However the refractive index of a material for X-rays does not differ very much from unity so that refraction is barely visible. The refractive index can be expressed as [Born&Wolf1980]

$$n = 1 - \delta - i\beta \qquad [2.2.2]$$

where δ and β account for the scattering and absorption of the material, respectively. The values of δ and β (which are positive) depend on the electron density, ρ_e, and linear absorption coefficient, μ, of the material through the following relations

$$\delta = \frac{r_e}{2\pi}\lambda^2 \sum_k \frac{Z_k + f'_k}{V_m} = \frac{r_e}{2\pi}\lambda^2 \rho_e \qquad [2.2.3]$$

$$\beta = \frac{r_e}{2\pi}\lambda^2 \sum_k \frac{f''_k}{V_m} = \frac{\lambda}{4\pi}\mu \qquad [2.2.4]$$

where r_e = 2.813 .10^{-5} Å is the classical radius of the electron, V_m is the volume of the unit cell, Z_k is the number of electrons of the atom k in the unit cell, f' and f'' are the real and imaginary parts of the atomic scattering factor for the specific energy of the incident radiation λ. Note that these relations stand for crystalline materials only but can be also expressed for liquids or amorphous materials if their density is known.

In view of the fact that δ is positive, the refractive index of a material is always smaller than unity. Passing from vacuum (n = 1) to the reflecting material (n < 1), it is possible to totally reflect the beam if the grazing angle α (which is the angle between the surface of the sample and the incident beam) is small enough (below few milli-radians). This is known as the **total external reflection of X-rays**. For this to occur, the incident angle must be smaller than the critical angle α_c defined by the Snell's law as:

$$\cos\alpha_c = \boldsymbol{n} = 1 - \delta - \boldsymbol{i}\beta \qquad [2.2.5]$$

Since 1>>δ>> 0 the expression for critical angle can be approximated as [Als-Nielsen&McMorrow2010]

$$\alpha_c^2 = 2\delta = \frac{\boldsymbol{r}_e \lambda^2}{\pi}\rho_e \qquad [2.2.6]$$

• **Scattering**

The scattering process is illustrated in Fig. 2.2.1c in which an X-ray beam of intensity I_0 photons per second is incident on a sample, and where the sample is large enough that it intercepts the entire beam. Our objective is to calculate the number of X-ray photons, I_{SC}, scattered per second into a detector that subtends a solid angle ΔΩ. If there are N particles in the sample per unit area seen along the beam direction, then I_{SC} will be proportional to N and to I_0. It will of course also be proportional to ΔΩ. Most importantly it will depend on how efficiently the particles in the sample scatter the radiation, this is given by the differential cross-section, (dσ/dΩ), so that we may write

$$\boldsymbol{I}_{sc} = \boldsymbol{I}_0 \boldsymbol{N}\Delta\Omega\left(\frac{\boldsymbol{d}\sigma}{\boldsymbol{d}\Omega}\right) \qquad [2.2.7]$$

Thus the differential cross –section per scattering particle will be defined by:

$$\left(\frac{\boldsymbol{d}\sigma}{\boldsymbol{d}\Omega}\right) = \frac{\text{No. of X-ray photons scattered per second into } \Delta\Omega}{\boldsymbol{I}_0 \boldsymbol{N}\Delta\Omega} \qquad [2.2.8]$$

The differential cross section for an electron is given by Pr_0^2, where r_0 is the classical electron radius and P is the polarisation factor. This factor depends on the X-ray source: P=1, for synchrotron: vertical scattering plane, $P=\cos^2\psi$ for synchrotron: horizontal scattering plane and $P=1/2(1+\cos^2\psi)$ for unpolarized source, where $\sin\psi=\hat{\varepsilon}.\hat{\varepsilon}'$ and $\hat{\varepsilon}$ is polarization of the incident field and $\hat{\varepsilon}'$ is polarization of the radiated field.

If an atom with Z electrons is considered then it is compulsory to take in account the phase difference between the waves due to their different geometric paths through the electron cloud. This gives rise to the well known atomic form factor f(q). Finally for a crystal, the scattering cross-section can lead to the diffraction phenomena.

The techniques that have been used to complete this thesis are Small Angle X-ray Scattering (SAXS), XRR, GISAXS and Coherent X-ray Diffraction Imaging (CXDI). For thin films, the sensibility to the surface is enhanced using grazing incidence geometry rather than the transmission one. By selecting an incident angle on the sample surface close or even below angle of the total external reflection of x-rays (see eq. 2.2.6), the penetration depth is considerably decreased down to a few nanometers thus enhancing the surface or subsurface signal compared to the one of the volume. At grazing incidence, two experimental geometries are commonly found :

- the coplanar geometry (in the incidence plane) for which specular X-ray reflectivity (XRR) and off-specular diffuse scattering are utilized.
- the non coplanar geometry which is the field of Grazing Incidence Small Angle X-ray Scattering (GISAXS).

2.3. X-ray reflectivity (XRR)

The XRR measurement technique described in this section is used to analyse the X-ray reflection intensity as a function of the grazing angle to determine parameters of a thin-film including the thickness, density, and roughness. This section provides a quick overview of the principles of X-ray reflectivity and the analysis methods [Gibaud2009].

2.3.1. General principles

The basic idea behind XRR is to reflect a beam of x-rays from a flat enough surface and to collect the reflected intensity of x-rays in the specular direction, i.e. in a condition where the reflected angle and incident angles are equal.

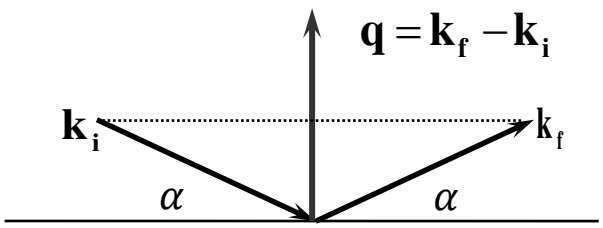

Figure 2.3.1 Schematic of the X-ray reflectivity method and wave-vector transfer. In specular reflection the wave vector is normal to the surface.

The absolute reflectivity is defined as a ratio of the reflected beam intensity I(α) to the intensity of the direct beam I_0.

$$\boldsymbol{R}(\alpha) = \frac{\boldsymbol{I}(\alpha)}{\boldsymbol{I}_0} \qquad [2.3.1]$$

It is often expressed in terms of the modulus of the wave vector transfer. Recall that this vector, which by definition characterizes the change in wave vector after reflection on the sample, is given by

$$\vec{q} = \vec{k}_{sc} - \vec{k}_{in} \qquad [2.3.2]$$

As the incident angle is equal to the reflected angle, it follows that the wave vector transfer q is normal to the sample surface and is directed along q_z (see Figure 2.3.1). The modulus of the wave-vector transfer 'q' is therefore

$$\boldsymbol{q}_z = 2\boldsymbol{k}_z = \frac{4\pi \sin(\alpha)}{\lambda} \qquad [2.3.3]$$

2.3.2. Ideal surface: Fresnel Reflectivity

The intensity of the reflected specular signal from an ideal flat surface can be calculated by considering the usual boundary conditions for electromagnetic waves [Gibaud2009]. The result is known as the Fresnel relationships that defines the reflection and transmission coefficients of the beam that is reflected at the interface separating the two media j and j+1

$$\boldsymbol{r}_{j,j+1} = \frac{\boldsymbol{k}_{j,z} - \boldsymbol{k}_{j+1,z}}{\boldsymbol{k}_{j,z} + \boldsymbol{k}_{j+1,z}} \quad \boldsymbol{t}_{j,j+1} = \frac{2\boldsymbol{k}_{j,z}}{\boldsymbol{k}_{j,z} + \boldsymbol{k}_{j+1,z}} \qquad [2.3.4]$$

with $\boldsymbol{k}_{j,z}$ which represents the z component of the wave vector k_j in medium j. From these expressions, it follows that the reflectivity of an electromagnetic wave is primarily determined by the knowledge of the component along z of the wave vector in each medium. We will apply this result to the case of the reflectivity of a silicon surface by a monochromatic beam of X-rays (see Figure 2.3.2).

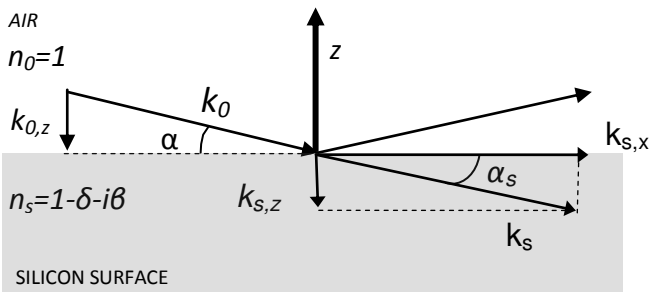

Figure 2.3.2 Schematic of the components of the wave vector involved in the calculation of the reflectivity of a silicon surface.

Replacing medium j by air and medium j+1 by the silicon yields

$$\boldsymbol{r}_{0,S} = \frac{\boldsymbol{k}_{0,z} - \boldsymbol{k}_{S,z}}{\boldsymbol{k}_{0,z} + \boldsymbol{k}_{S,z}} = \frac{-\boldsymbol{k}_0 \sin\alpha + \boldsymbol{n}\boldsymbol{k}_0 \sin\alpha_S}{-\boldsymbol{k}_0 \sin\alpha - \boldsymbol{n}\boldsymbol{k}_0 \sin\alpha_S} = \frac{\sin\alpha - \boldsymbol{n}\sqrt{1-\cos^2\alpha_s}}{\sin\alpha + \boldsymbol{n}\sqrt{1-\cos^2\alpha_s}} \qquad [2.3.5]$$

in which $k_S = nk_0$. According to Snell-Descartes 's law $(\boldsymbol{k}_0 \cos\alpha = \boldsymbol{n}\boldsymbol{k}_0 \cos\alpha_S)$, it follows that the reflection and transmission coefficients are

$$r_{0,s} = \frac{\sin\alpha - \sqrt{n^2 - \cos^2\alpha}}{\sin\alpha + \sqrt{n^2 - \cos^2\alpha}} \qquad t_{0,s} = \frac{2\sin\alpha}{\sin\alpha + \sqrt{n^2 - \cos^2\alpha}} \qquad [2.3.6]$$

At small angle of incidence and with n close to 1, the reflectivity and transmitted intensity are given by

$$R(\alpha) = \left| \frac{\alpha - \sqrt{\alpha^2 - 2\delta - 2i\beta}}{\alpha + \sqrt{\alpha^2 - 2\delta - 2i\beta}} \right|^2 \qquad T(\alpha) = \left| \frac{2\alpha}{\alpha + \sqrt{\alpha^2 - 2\delta - 2i\beta}} \right|^2 \qquad [2.3.7]$$

This expression shows that the reflectivity exhibits two asymptotic regimes:

- Below the critical angle, $R = 1$
- Above the critical angle, R is given by

$$R_F = \frac{\alpha_c^4}{16\alpha^4} = \frac{(4\pi\rho_{bulk})^2}{q_z^4} \qquad [2.3.8]$$

Moreover we can also show that the penetration depth is given by

$$\frac{1}{\Lambda(\alpha)} = -2k_0 \,\mathrm{Im}(\sqrt{\alpha^2 - 2\delta - 2i\beta}) \qquad [2.3.9]$$

This equation is used to determine how much of the incident beam penetrates into the material in the perpendicular direction to the sample surface. We clearly see in this expression that if there is no absorption the penetration depth is infinite whereas if the amount is significant, the penetration depth decreases. The penetration depth is thus strongly depending on the absorption coefficient β and on the incident angle α.

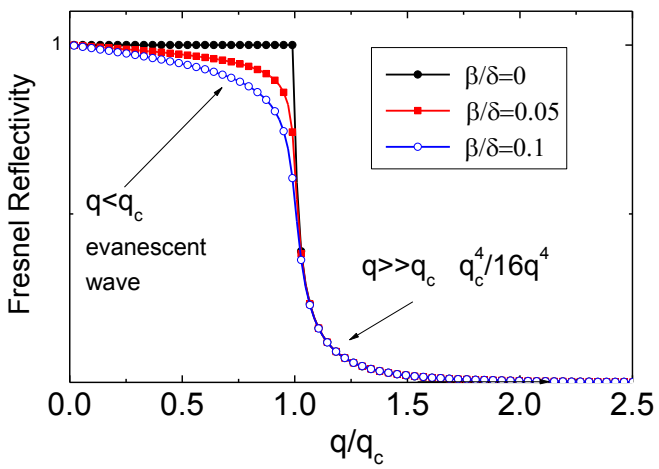

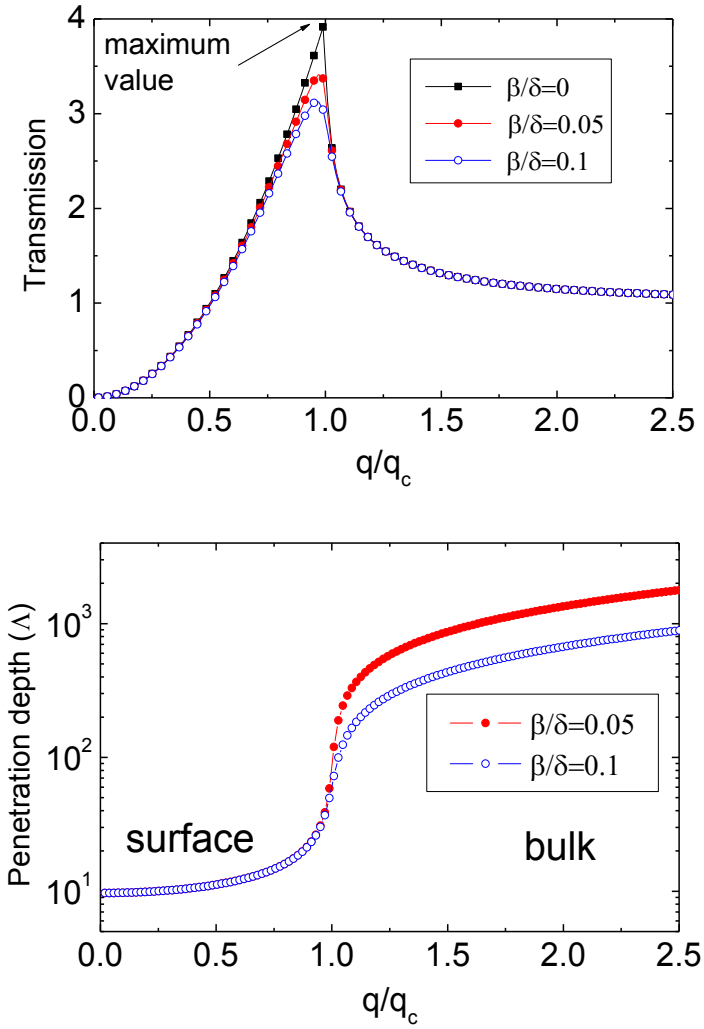

Figure 2.3.3 The reflectivity R, the transmission T and the penetration depth Λ versus q/q_c. In each case, a family of curves is given corresponding to different values of to the ratio β / δ. When q<<1 there is total reflection and the reflected wave propagates along the surface with a minimal penetration depth of $1/q_c$. Due to the small penetration depth, this wave is called an evanescent wave. When q>>1 the reflectivity falls off as $R(q)=1/(q)^4$ and there is almost complete transmission.

2.3.3. Reflectivity from a layered material

2.3.3.1. Dynamical Theory (Matrix Formalism)

When the wave propagates in heterogeneous medium presenting regions of different electron densities, it is not possible to directly use the Fresnel relationship. The calculation is performed by applying the boundary conditions of the electric and magnetic fields at each interface [Gibaud1999, Parrat1954, and Born1980]. The fact that multiple reflections are taken into account in the calculation leads to the ***dynamical theory*** of

reflection and the result is either presented as a product of matrices or by the famous recursive Parrat's formula.

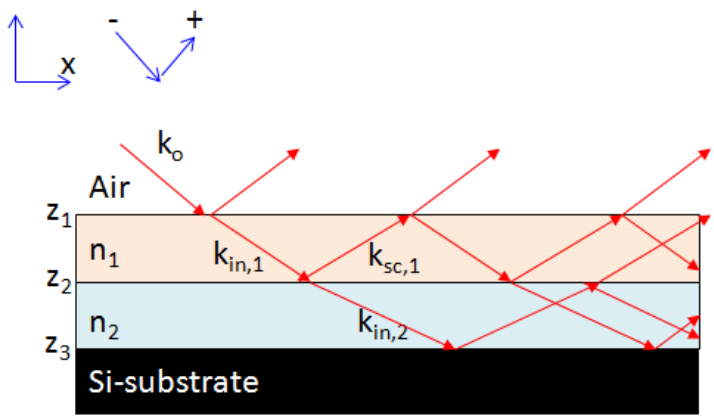

Figure 2.3.4 Schematic of the reflectivity method described by a dynamical theory. (Note that the first air–material interface begins at altitude z_1.)

The reflection matrix (Abel matrix [Born&Wolf1980]) between two slabs j and j+1 and the translation matrix for a slab of altitude h is given by:

$$\boldsymbol{R}_{j,j+1} = \begin{bmatrix} \boldsymbol{p}_{j,j+1} & \boldsymbol{m}_{j,j+1} \\ \boldsymbol{m}_{j,j+1} & \boldsymbol{p}_{j,j+1} \end{bmatrix} \text{ and } \boldsymbol{T}_j = \begin{bmatrix} \boldsymbol{e}^{-i\boldsymbol{k}_{z,1}\boldsymbol{h}} & 0 \\ 0 & \boldsymbol{e}^{i\boldsymbol{k}_{z,1}\boldsymbol{h}} \end{bmatrix} \quad [2.3.10]$$

Where h

$$p_{j,j+1} = \frac{k_{z,j} + k_{z,j+1}}{2k_{z,j}}, \quad m_{j,j+1} = \frac{k_{z,j} - k_{z,j+1}}{2k_{z,j}} \quad [2.3.11]$$

Here, $R_{j,j+1}$ is the matrix which transforms the amplitudes of the electric fields from medium j to medium j+1 and T_j is the translation matrix which represents the variation of their amplitude with the altitude h. The product of all these matrices is a 2x2 matrix called the transfer matrix M.

$$M = R_{0.,1} T_1 R_{1,2} \ldots\ldots R_{sub-1,sub} = \begin{bmatrix} M_{11} & M_{12} \\ M_{21} & M_{22} \end{bmatrix} \quad [2.3.12]$$

Thus, from this matrix, the coefficients of reflection and transmission in amplitude of the electric field at the surface of a material are given by:

$$r = \frac{M_{12}}{M_{22}} \text{ and } t = \frac{1}{M_{22}} \quad [2.3.13]$$

In all this expressions $k_{z,j}$ is the normal component of the wave vector in medium j and that is equal to

$$\boldsymbol{k}_{z,j} = -\boldsymbol{k}_j \sin\alpha_j = -\sqrt{\boldsymbol{k}_j^2 - \boldsymbol{k}_{x,j}^2} \quad [2.3.14]$$

$k_{x,j}$ is conserved and it is equal to kcosα. As the result of this, the z component of k_0 in medium j is

$$\boldsymbol{k}_{z,j} = -\sqrt{\boldsymbol{k}_0^2 \boldsymbol{n}_j^2 - \boldsymbol{k}_0^2 \cos^2 \alpha} \qquad [2.3.15]$$

Where k_0 is the wave vector in air. In the limit of small angle and substituting the expression of the refractive index for x-rays, this becomes

$$\boldsymbol{k}_{z,j} = -\boldsymbol{k}_0 \sqrt{\alpha^2 - 2\delta_j - 2\boldsymbol{i}\beta_j} = \boldsymbol{k}_0 \sqrt{\alpha^2 - \alpha_c^2} \quad \text{and} \quad \boldsymbol{q}_{z,j} = \sqrt{\boldsymbol{q}_z^2 - \boldsymbol{q}_c^2} \qquad [2.3.16]$$

A similar expressions can be obtained for $k_{z,j+1}$ so that the coefficients $p_{j,j+1}$ and $m_{j,j+1}$ are entirely determinate by the incident angle and by the value of δ and β in each layer.

For example for a single layer on a substrate, the transfer matrix is given by

$$\boldsymbol{R}_{0,1}\boldsymbol{T}_1\boldsymbol{R}_{1,2} = \begin{bmatrix} \boldsymbol{p}_{0,1} & \boldsymbol{m}_{0,1} \\ \boldsymbol{m}_{0,1} & \boldsymbol{p}_{0,1} \end{bmatrix} \begin{bmatrix} \boldsymbol{e}^{-i\boldsymbol{k}_{z,1}\boldsymbol{h}} & 0 \\ 0 & \boldsymbol{e}^{i\boldsymbol{k}_{z,1}\boldsymbol{h}} \end{bmatrix} \begin{bmatrix} \boldsymbol{p}_{1,2} & \boldsymbol{m}_{1,2} \\ \boldsymbol{m}_{1,2} & \boldsymbol{p}_{1,2} \end{bmatrix} \qquad [2.3.17]$$

Then considering that the reflection coefficients is $r=M_{11}/M_{22}$ and introducing the reflection coefficients $\boldsymbol{r}_{j,j+1} = \boldsymbol{m}_{j,j+1} / \boldsymbol{p}_{j,j+1}$ at the interface j,j+1 we get:

$$\boldsymbol{r}^{LAYER} = \frac{\boldsymbol{r}_{0,1} + \boldsymbol{r}_{1,2}\boldsymbol{e}^{-2i\boldsymbol{k}_{z,1}\boldsymbol{h}}}{1 + \boldsymbol{r}_{0,1}\boldsymbol{r}_{1,2}\boldsymbol{e}^{-2i\boldsymbol{k}_{z,1}\boldsymbol{h}}} \qquad [2.3.18]$$

It is worth noting that the denominator of this expression differs from unity by a term which corresponds to multiple reflections in the material as evidenced by the product of the two reflection coefficients $\boldsymbol{r}_{0,1}\boldsymbol{r}_{1,2}$.

2.3.3.2. Kinematical Theory

The full dynamical theory described above is exact but does not clearly show the physics of scattering because numerical calculations are necessary. Sometimes, one can be more interested in an approximated analytical expression. That is why the use of the kinematical theory which simplifies the expression of the reflected intensity taking in accounts the three Born approximations [Born1980, Hamley1994, Gibaud2009].

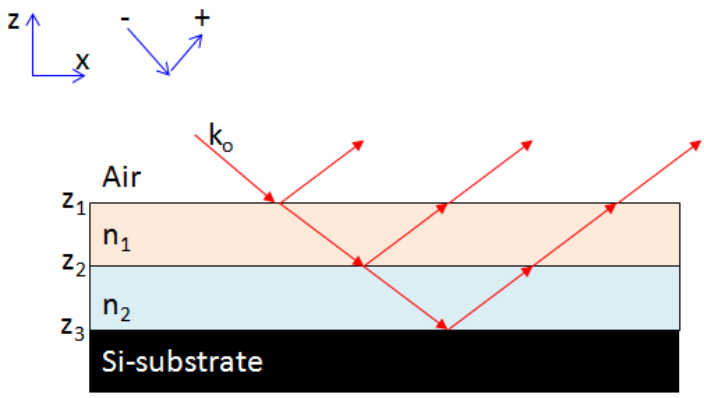

Figure 2.3.5 Schematic of the reflectivity method described by a kinematical theory.

- The <u>first approximation</u> consist in neglecting the effect of the multiple reflections, this means that reflected intensity will be only from the electrons that interact with the incident beam. Under this approximation, the reflection coefficient r for a stratified medium composed of N layers is

$$r = r_{0,1} + r_{1,2} e^{i q_{z,1} d_1} + r_{2,3} e^{i(q_{z,1} d_1 + q_{z,2} d_2)} + ... + r_{j,j+1} e^{i \sum_{k=0}^{j} q_{z,k} d_k} \qquad [2.3.19]$$

- A <u>second approximation</u> consist in neglecting the refraction and the absorption in the layers in the phase factor

$$r = \sum_{j=0}^{n} r_{j,j+1} e^{i q_z \sum_{m=0}^{j} d_m} \qquad [2.3.20]$$

- The <u>final approximation</u> consist in consider that $q_{z,j}$ will not change from a layer to the other layer:

$$r_{j,j+1} = \frac{q_{z,j}^2 - q_{z,j+1}^2}{(q_{z,j} + q_{z,j+1})^2} = \frac{q_{c,j+1}^2 - q_{c,j}^2}{4 q_z^2} = \frac{4\pi r_e (\rho_{j+1} - \rho_j)}{q_z^2} \qquad [2.3.21]$$

With $q_{c,j} = \sqrt{16\pi r_e \rho_j}$ in which r_e stands for the classical radius of the electron.

These approximations lead to the following expression for the reflection coefficient.

$$\boldsymbol{r} = 4\pi \boldsymbol{r}_e \sum_{j=0}^{n} \frac{(\rho_{j+1} - \rho_j)}{\boldsymbol{q}_z^2} \boldsymbol{e}^{\boldsymbol{iq}_z \sum_{m=0}^{j} \boldsymbol{d}_m} \qquad [2.3.22]$$

If the origin of the z axis is chosen to be at the upper surface (medium 0 at the depth Z_1=0), then the sum over d_m in the phase factor can be replaced by the depth Z_{j+1} of the interface j,j+1 and the equation becomes

$$r = 4\pi r_e \sum_{j=0}^{n} \frac{(\rho_{j+1} - \rho_j)}{q_z^2} e^{iq_z Z_{j+1}} \qquad [2.3.23]$$

Finally, the kinematic theory make it possible to write the reflectivity of the materials composed by n layers for angles far from the total reflection as:

$$R(q_z) = 4\pi r_e \left| \sum_{j=0}^{n} \frac{(\rho_{j+1} - \rho_j)}{q_z^2} e^{iq_z Z_{j+1}} \right|^2 \qquad [2.3.24]$$

Master Formula

If we consider that the material is made of an infinitive number of thin layers, the sum then can be transformed into an integral over z, and the reflection coefficient r has the form

$$\boldsymbol{r} = \frac{4\pi \boldsymbol{r}_e}{\boldsymbol{q}_z^2} \int_{-\infty}^{+\infty} \frac{\boldsymbol{d}\rho(z)}{\boldsymbol{dz}} \boldsymbol{e}^{\boldsymbol{iq}_z z} \boldsymbol{dz} \qquad [2.3.25]$$

The introduction of the Fresnel reflectivity of the substrate R_F (Eq. 2.3.8), in the above expression shows that in the kinematical theory the reflectivity can be written as

$$R(q_z) = R_F(q_z).\left|\Phi(q_z)\right|^2 \qquad [2.3.26]$$

Where, $\Phi(q_z)$ is the surface form factor, and it is defined as the Fourier transform of the derivative of the in plane average of the electron density along the surface normal:

$$\Phi(\boldsymbol{q}_z) = \frac{1}{\rho_{\boldsymbol{bulk}}} \int_{-\infty}^{+\infty} \frac{\boldsymbol{d}\rho(z)}{\boldsymbol{dz}} \boldsymbol{e}^{\boldsymbol{iq}_z z} \boldsymbol{dz} \qquad [2.3.27]$$

The above expression of $R(q_z)$ is not rigorous but can be easily handled in analytical calculations (ρ_{bulk} is the electron density of the substrate bulk).

2.3.4. Analysis of the curves

As seen above, the quantitative analysis of X-ray reflectivity curves may be obtained through curve fitting calculations based on the matrix formalism. However, this procedure requires a prior knowledge of the system; this information can be obtained by performing a preliminary qualitative study of curves. In this section is described in detail the information that can be obtained on a layered material layer by using a simple qualitative analysis of the experimental curves.

We illustrate as an example the cases of two systems that we have studied in this thesis:

- the determination of the electron density obtained from the XRR measurements of a film of polystyrene deposited on a silicon substrate.
- the XRR characteristics of a thin film of mesoporous silica deposited on a silicon substrate.

2.3.4.1. Electron density of a PS film

For qualitative discussion, it is adequate to consider an absorption close to (β=0) but it should be noted that β cannot be ignored in the simulation of XRR. For incident angles below the critical angle ($\alpha<\alpha_c$) of PS, total reflection occurs. By applying Snell's law and small angle approximations, the critical angle can be expressed as:

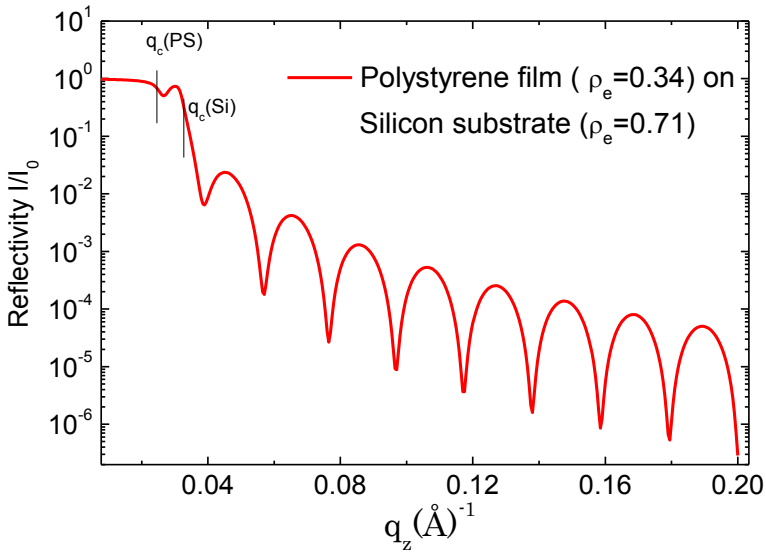

Figure 2.3.6 X-ray reflectivity curves of Polystyrene on a silicon substrate.

$$1-\delta=\cos(\alpha_c)\approx 1-\frac{\alpha_c^2}{2}$$

$$\alpha_c\approx\sqrt{2\delta}=\sqrt{\frac{r_e\lambda^2\rho_e}{\pi}} \qquad [2.3.28]$$

$$\Rightarrow \rho_e=\frac{\pi}{\lambda^2 r_e}\alpha_c^2=\frac{q_c^2}{16\pi r_e}$$

Thus, the electron density of the layer can be obtained from the critical wave-vector transfer q_c. A typical measurement is shown in Fig.2.3.6 where q_c is determined from the first dip in the plateau of total external reflection. Note that an abrupt change in XRR is found at $q_z=q_{c(Si)}$. Note that this method is only valid for film having a thickness t>20nm otherwise the dip is barely visible.

2.3.4.2. Film Thickness

For incident angles greater than α_c(layer) ($\alpha > \alpha_c$) the x-ray beam penetrates inside the film. Reflection therefore occurs at the top and the bottom surfaces of the film. The interferences between the rays reflected from the top and the bottom of the film surfaces give rise to interference fringes; the so-called Kiessig fringes (see Fig.2.3.7).

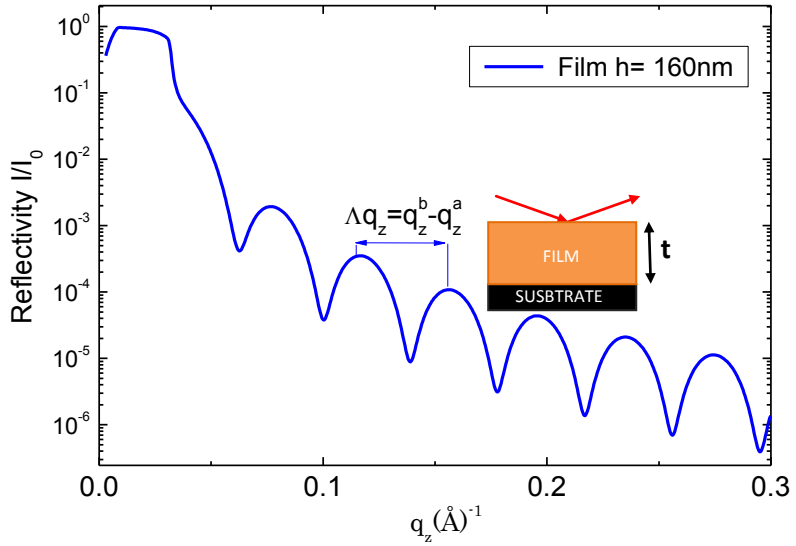

Figure2.3.7 Reflectivity of Polystyrene film deposited on silicon substrate with 160nm of thickness.

The difference between the consecutive maxima of these fringes is inversely proportional to the thickness of the layer "t":

$$t = \frac{2\pi}{q_z^b - q_z^a} \quad \text{using the kinematical theory}$$

$$t = \frac{2\pi}{\sqrt{\left(q_z^b\right)^2 - q_{c,j}^2} - \sqrt{\left(q_z^a\right)^2 - q_{c,j}^2}} \quad \text{using the dynamical theory} \qquad [2.3.29]$$

Where $q_{c,j}$ is the critical wave vector transfer in the medium j.

2.3.4.3. Periodicity for a N-bi layer

Mesoporous silica thin films can be simulated by a composition of N-bilayers made of a layer 1 (average electron density ρ_1, thickness: t_1) and a layer 2 (ρ_2, t_2), where $\Lambda=(t_1+t_2)$ is the lattice spacing parameter and 't=N Λ' is roughly the total thickness of the film (see figure 2.3.8). The reflectivity of this kind of materials can be approached for sake of simplicity in the kinematical approximation although a correct calculation necessitates the use of the dynamical theory . This model can be qualitatively described by a density function $\rho(z)$:

$$\rho(z)=\begin{array}{c}(\rho_2-\rho_{air})e^{iq_zZ_0}\\ +(\rho_1-\rho_2)e^{iq_zt_2}(1+e^{iq_z\Lambda}+e^{iq_z2\Lambda}+\ldots+e^{iq_z'(N-1)\Lambda})\\ +(\rho_2-\rho_1)e^{iq_z(t_2+t_1)}(1+e^{iq_z\Lambda}+e^{iq_z2\Lambda}+\ldots+e^{iq_z'(N-1)\Lambda})\\ +(\rho_S-\rho_1)e^{iq_z(N\Lambda+t_2)}\end{array} \qquad [2.3.30]$$

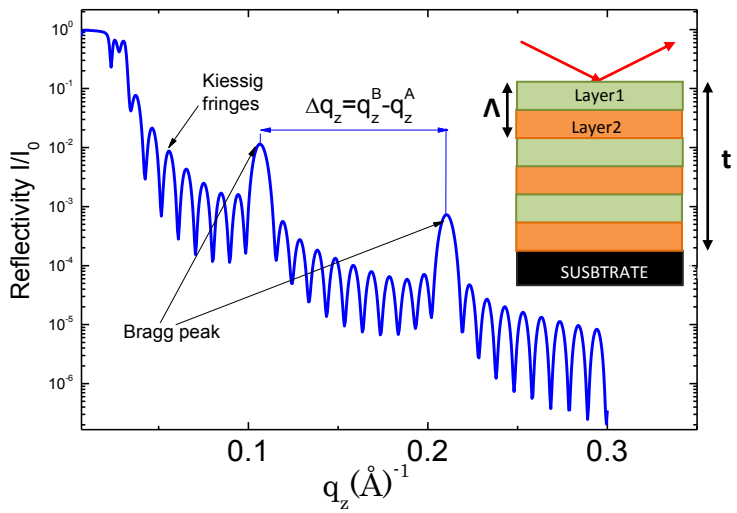

Figure 2.3.8 Example of a reflectivity curve showing the Kiessig fringes and Bragg peak.

By considering N sufficiently large to neglect the phenomena of interfaces with the air and the substrate, one neglects the first and the last term of the expression. After some mathematical rewritings, one obtains the following expression of reflectivity:

$$R(q_z)=\left(\frac{4\pi r_e}{q_z^2}\right)^2(\rho_2-\rho_1)^2t_1\,\mathrm{sinc}^2\left(\frac{q_zt_1}{2}\right)\frac{\sin^2\left(\frac{Nq_z\Lambda}{2}\right)}{\sin^2\left(\frac{q_z\Lambda}{2}\right)} \qquad [2.3.31]$$

This last expression, valid for the q_z>>q_c is rich in information:

- The term $\left(\frac{4\pi r_e}{q_z^2}\right)^2$ shows that one obtains as the case of the Fresnel reflectivity the decrease in $1/q_z^4$ for q_z>>q_c.
- The reflectivity is modulated by a sinus cardinal function $\frac{\sin^2\left(\frac{Nq_z\Lambda}{2}\right)}{\sin^2\left(\frac{q_z\Lambda}{2}\right)}$. This function represented by this expression have a main and secondary maxima :

The main maximum, called Bragg peak has a period:

$$\Lambda = \frac{2\pi}{q_z^B - q_z^A} \quad \text{using the kinematical theory}$$

$$\Lambda = \frac{2\pi}{\sqrt{\left(q_z^B\right)^2 - q_{c,j}^2} - \sqrt{\left(q_z^A\right)^2 - q_{c,j}^2}} \quad \text{using the dynamical theory} \qquad [2.3.32]$$

The secondary maxima are less intense and are related to the Kiessig fringes of period

$$t = N\Lambda = \frac{2\pi}{q_z^b - q_z^a} \quad \text{using the kinematical theory}$$

$$t = \frac{2\pi}{\sqrt{\left(q_z^b\right)^2 - q_{c,j}^2} - \sqrt{\left(q_z^a\right)^2 - q_{c,j}^2}} \quad \text{using the dynamical theory} \qquad [2.3.33]$$

Where $q_{c,j}$ is the critical wave vector transfer in the medium j.

2.4. Small angle X-ray Scattering (SAXS)

SAXS contrary to XRR is a technique used in transmission through the volume of the sample. The objective of this technique is to measure the scattered signal by large objects (from a few angstroms to micron scale) contained in the sample which requires working at small angle.

A schematic description of scattering principle is shown in Fig. 2.4.1. X-rays from the source are collimated into a fine beam, often by slits, and strike the samples. A small fraction of this beam is scattered in other directions, e. g. an angle 2θ with the direction of the incoming beam. D is a detector, used to record the scattering intensity (the square of the scattering amplitude) and its dependence on the scattering angle. During an experiment of SAXS, it is recommended, in order to obtain absolute intensity, to measure the intensity of the direct beam as well as the transmission “T” and the thickness of the sample “e”. From the practical point of view, one has

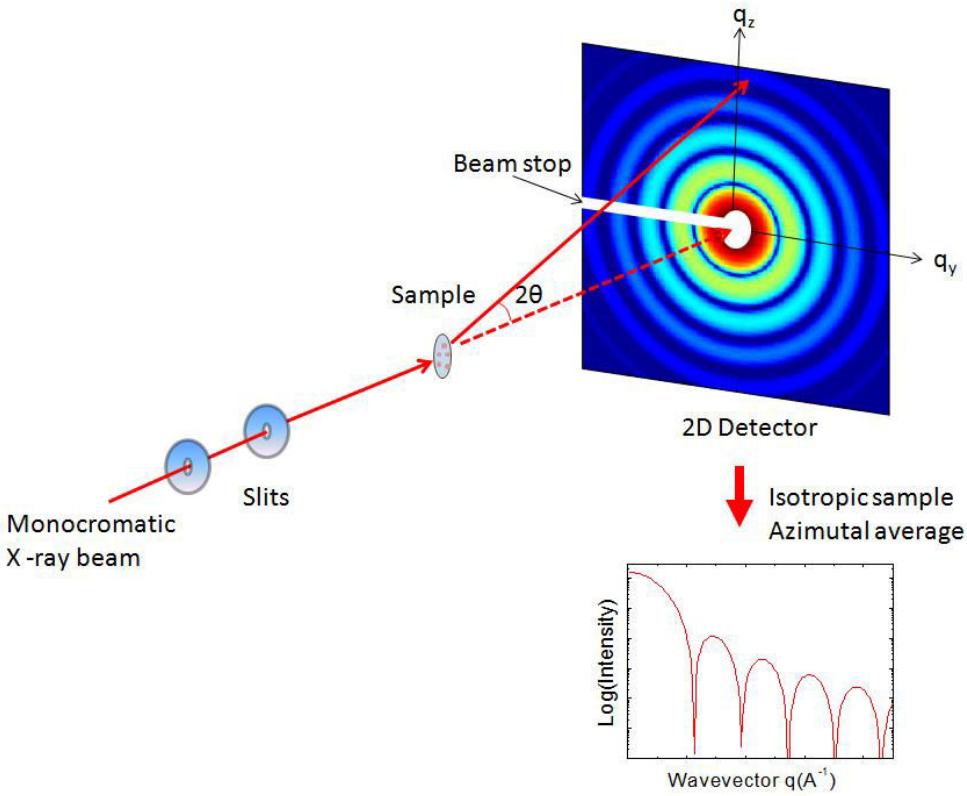

Fig. 2.4.1 Schematic layout of a small-angle X-ray scattering measurement. A monochromatic X-ray beam is collimated using a set of slits and then impinges on the sample. The scattered beam is detected on a two-dimensional detector. For isotropic sample, the scattering can be azimuthally averaged to produce a plot of scattered intensity versus wavevector transfer.

$$I(q) = \frac{N(q)}{N_0}\frac{1}{Te\Delta\Omega} \qquad [2.4.1]$$

where N(q) is the number of photons collected per second in the detector , N_0 is the number of photons in the direct beam, e is the thickness of the sample, $\Delta\Omega$ is the size of a pixel seen from the sample, T is the transmission coefficient. Then the intensity I(q) is expressed in absolute units (cm^{-1}).

2.4.1. General principles

General scattering theory [Guinier1955,Glatter1982,Svergun1994] tells us that the amplitude measured at the scattering vector q of wave elastically scattered from an atom located at r is proportional to e^{iqr}, where $q=k_{in}-k_{sc}$ and k_{in} ,k_{sc} are the wavevector of

outgoing and incoming wave, respectively. If the scattering angle is 2θ and the wavelength λ then,

$$\boldsymbol{q} = |\boldsymbol{q}| = \frac{4\pi}{\lambda}\sin\theta \qquad [2.4.2]$$

The total amplitude at q position is the sum of the waves scattered by all the atoms in the sample.

$$\boldsymbol{A}(\boldsymbol{q}) = \boldsymbol{A}_e \int_V \rho(\boldsymbol{r})\boldsymbol{e}^{-i\boldsymbol{q}\boldsymbol{r}}\boldsymbol{dr} \qquad [2.4.3]$$

Where A_e denotes the scattering amplitude of one electron and ρ(r) is the electron density distribution of the scatterers. The scattering intensity of one particle I(q) is the absolute square given by the product of the amplitude by its complex conjugate.

$$\begin{aligned}\boldsymbol{I}(\boldsymbol{q}) = |\boldsymbol{A}(\boldsymbol{q})|^2 &= \boldsymbol{A}(\boldsymbol{q})\boldsymbol{A}(\boldsymbol{q})^* = \\ &= \mathrm{I_e}\int_V \mathrm{dr_1}\int_V \mathrm{dr_2}\,\rho(\boldsymbol{r}_1)\rho(\boldsymbol{r}_2)\boldsymbol{e}^{-i\boldsymbol{q}(\boldsymbol{r}_1-\boldsymbol{r}_2)}\end{aligned} \qquad [2.4.4]$$

The electron scattering intensity I_e has been given by the Thomson cross section. As the electron scattering intensity I_e applies to all formulae to follow, it will be omitted for brevity, i.e., the SAXS scattering intensity is expressed in units of the scattering intensity of a single electron (e.u., electron units).

So far we discussed the scattering process of a particle in fixed orientation in vacuum. At this point we will make two assumptions concerning the sample that will simplify the formalism:

i) The particles are statistically isotropic and no long-range order exists, i.e., there is no correlation between particles at great spatial distances.

ii) The sample is made of two media (denoted 1 and 2) separated by a sharp interface; each one is characterized by a constant electron density ρ_i and volume fraction ϕ_i so that the average density of the sample is $\rho = \rho_1\phi_1 + \rho_2\phi_2$ with $\phi_1 + \phi_2 = 1$. In doing so we somewhat limit the generality of the system. However this description is adequate for our cases and the scattered intensity can be calculated easily.

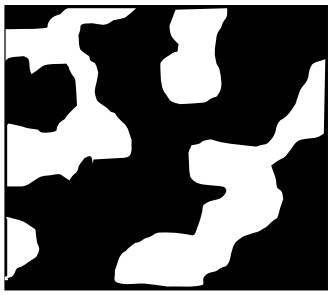

Figure 2.4.2 Two-dimensional representation of a sample containing two media separated by sharp interface.

In this case the average over all orientations leads to the fundamental formula of Debye,

$$\left\langle \boldsymbol{e}^{-i\boldsymbol{qr}} \right\rangle_{\Omega} = \frac{\sin(\boldsymbol{qr})}{\boldsymbol{qr}} \qquad [2.4.5]$$

Thus, equation [2.4.4] reduces to the form

$$\boldsymbol{I}(\boldsymbol{q}) = 4\pi \int_0^{\infty} \gamma(\mathrm{r}) \frac{\sin(\mathrm{qr})}{\mathrm{qr}} \boldsymbol{r}^2 \boldsymbol{dr} \qquad [2.4.6]$$

Equation [2.4.6] is the most general formula for the scattering pattern of any systems, which obey the above two restrictions. γ(r) is the so-called *correlation function* [Debye&Bueche1949], or characteristic function . It can be obtained by the inverse Fourier transform with

$$\gamma(\boldsymbol{r}) = \frac{1}{2\pi^2} \int_0^{\infty} \boldsymbol{I}(\mathrm{q}) \frac{\sin(\mathrm{qr})}{\mathrm{qr}} \boldsymbol{q}^2 \boldsymbol{dq} \qquad [2.4.7]$$

The invariant

To get a more physical insight in the meaning of the correlation function let us to imagine that we draw, at random a line of length r on the two dimensional image of our sample (Fig. 2.4.2) and we count how many times both ends are in medium 1, or in medium 2, or one end in each medium and we define the associated probabilities as P_{11}, P_{22} and P_{12} respectively. If the two media are distributed in a completely random way, then

$$\boldsymbol{P}_{11} = \phi_1^2, \qquad \boldsymbol{P}_{22} = \phi_2^2, \qquad \boldsymbol{P}_{12} = \boldsymbol{P}_{21} = \phi_1\phi_2 \qquad [2.4.8]$$

If there is a correlation in the distribution of the two media, there will be some deviation to those probabilities that can be described by a function $\gamma_0(\boldsymbol{r})$ such that:

$$\boldsymbol{P}_{11}(\boldsymbol{r}) = \phi_1^2 + \gamma_0(\boldsymbol{r})\phi_1\phi_2$$

$$\boldsymbol{P}_{22}(\boldsymbol{r}) = \phi_2^2 + \gamma_0(\boldsymbol{r})\phi_1\phi_2 \qquad [2.4.9]$$

$$\boldsymbol{P}_{12}(\boldsymbol{r}) = \boldsymbol{P}_{21}(\boldsymbol{r}) = \phi_1\phi_2(1-\gamma_0(\boldsymbol{r}))$$

If $\gamma_0(\boldsymbol{r}) = 0$, then point separated by r are not correlated ; if it is >0, then they are more likely to be in the same region than if is random; if it is <0 they are more likely to be in different media; If $\gamma_0(\boldsymbol{r}) = 1$, both points are in the same region. For r=0, this is evidently the case and thus, $\gamma_0(0) = 1$. Using these definitions, equations [2.4.4] becomes,

$$\gamma(\boldsymbol{r}) = \phi_1\phi_2(\rho_1 - \rho_2)^2\gamma_0(\boldsymbol{r}) \qquad [2.4.10]$$

independently of the topology or the geometry of the sample.

Setting r=0 in [Eq. 2.4.7] and [Eq. 2.4.10], one has a relation between the parameters defining the sample and the scattered intensity as:

$$\boldsymbol{Q} = \int_0^\infty \boldsymbol{q}^2\boldsymbol{I}(\mathrm{q})\boldsymbol{q}\boldsymbol{d}\boldsymbol{q} = 2\pi^2\phi_1\phi_2(\rho_1 - \rho_2)^2 \qquad [2.4.11]$$

The quantity Q is called the invariant because it is independent of the details of the structure: a sample containing isolated spheres of 1 in 2 will show a very different scattering profile from that of a random bicontinuous arrangement of 1 and 2, but both will have the same invariant, provided that ρ_1, ρ_2, and ϕ_1, ϕ_2 are the same.

Equation [2.4.11] is important because it relates directly the sample composition to the measurement of the scattered intensity. For instance if ρ_1- ρ_2= $\Delta\rho$ is known, the invariant gives an evaluation of the total scattering in the sample which can in turn be compared to the amount of material that should have phase-separated.

We have to notice that a precise determination of Q requires data in an adequate q-range, i.e. where all the scattering that characterizes the structure of the sample takes place. In addition this needs to carry out measurements in absolute units I(q) in [cm^{-1}].

The Porod's limit

Suppose now that we look at the correlations over distances r that are much smaller that some typical length in the sample (size, distance), which we call D, i.e. r<<D. If we draw a

line as we did previously, most of these will have both ends in the same phase an only those line crossing an interface will be weighted by a non-zero Δρ and will participate to the scattered intensity at large q's ($q>>D^{-1}$). Hence data in that region will only contain information about the characteristics of the interface.

An exact calculation shows that the surface area per unit volume Σ=S/V is related to the scattered intensity by

$$\sum = \frac{1}{2\pi(\Delta\rho)^2 V} \lim_{q\to\infty} q^4 I(q) \qquad [2.4.12]$$

Or, using the invariant to eliminate scale constants,

$$\sum = \frac{\pi\phi_1\phi_2}{Q} \lim_{q\to\infty} q^4 I(q) \qquad [2.4.13]$$

2.4.2. Structural parameters

Valuable information can be gained from determination of the invariant and Porod's limit but these are independent of the geometry of the two media in the sample and hence, are of no use to describe the structure. However, some structural parameters can be extracted from the intensity profile.

2.4.2.1. The form factor of isolated particle

The simplest case to analyse is a dilute solution of molecules, or more generally particles, allowing inter-particle correlations to be neglected, and where it is assumed that the particles are identical. If the scattering length density of each particle is uniform and represented by ρ_1, and that of the solvent is ρ_2, then the intensity scattered normalized by a single particle is

$$I(q) = (\rho_1 - \rho_2)^2 \left| \int_{Vp} e^{iqr} d^3 r \right|^2 \qquad [2.4.14]$$

Where Vp is the volume of the particle. By introducing the single particle form factor,

$$P(q) = \frac{1}{V_P} \int_{Vp} e^{iqr} d^3 r \qquad [2.4.15]$$

This becomes

$$I(q) = (\Delta\rho)^2 V_P^2 \left| P(q) \right|^2 \qquad [2.4.16]$$

With $\Delta\rho = \rho_1 - \rho_2$

The form factor depends on the morphology – size and shape – of the particle through the integral over its volume, V_P. Unfortunately, it can only be evaluated analytically in few cases. When this is not possible, the appropriate integrals have to be evaluated numerically. Probably the easiest case to consider is a sphere of radius R, for which the form factor can be readily calculated as

$$P(q) = \frac{1}{V_P} \int_0^R \int_0^{2\pi} \int_0^{\pi} e^{iqr\cos\theta} r^2 \sin\theta \, d\theta \, d\phi \, dr = \frac{1}{V_P} \int_0^R 4\pi \frac{\sin qr}{qr} r^2 dr \qquad [2.4.17]$$

$$P(q) = 3\left[\frac{\sin qR - qR\cos qR}{(qR)^3} \right] \qquad [2.4.18]$$

In the Figure 2.4.4, we illustrate the variation of $|P(q)|^2$ with particle size by plotting it for two different choices of sphere radius.

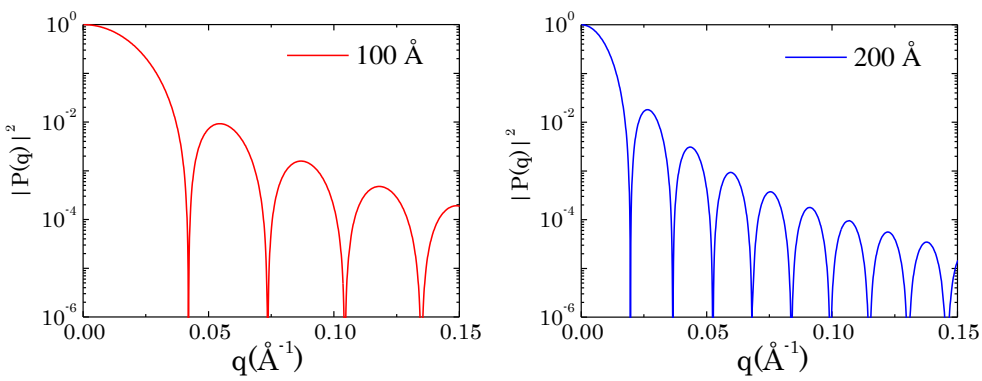

Figure 2.4.4 Calculated small-angle scattering from a sphere with 100Å and 200 Å of radius (Eq. 2.4.18).

2.4.2.2. Guinier analysis

At low q region, i.e., for qr << 1 the Debye factor sin(qr)/(qr) ≅ 1 - (qr)2/3! + …, eq. [2.4.6] reduces to [Guinier1939]

$$\boldsymbol{I}(\boldsymbol{q}) = 4\pi\int_0^\infty \gamma(\mathrm{r})\left(1 - \frac{(\mathrm{qr})^2}{6} + \ldots\right)\boldsymbol{r}^2\boldsymbol{dr} \cong \mathrm{I}_0(0)\left(1 - \frac{\mathrm{q}^2\mathrm{R}_\mathrm{g}^2}{3}\right) \qquad [2.4.19]$$

Where R_g is the radius of gyration given by

$$\boldsymbol{R}_g^2 = \frac{\int \rho(\boldsymbol{s})\boldsymbol{s}^2\boldsymbol{ds}}{\int \rho(\boldsymbol{s})\boldsymbol{ds}} \qquad [2.4.20]$$

With defining s as the vector taken from the center of gravity of ρ(r).

For homogeneous particles, the radius of gyration is only related to the geometrical parameters of simple triaxal bodies [Mittelbach1964], e.g., $\boldsymbol{R}_g = \sqrt{3/5}\boldsymbol{R}$ for spheres with radius R.

Because $e^{-x} \cong 1-x$, for qr << 1 eq. [2.4.19] can be also expressed as

$$\boldsymbol{I}(\boldsymbol{q}) = \boldsymbol{I}_0(0)\exp\left(-\frac{\boldsymbol{q}^2\boldsymbol{R}_g^2}{3}\right) \qquad [2.4.21]$$

This is so-called Guinier's law , which is a most useful relation in SAXS analysis since it allows to obtaining Rg and $I_0(0)$ from the scattering data in the region of smallest angles without any prior assumption on the shape and internal structure of the particle .

2.4.2.3. Fractals

Porous material or rough materials are considered to be fractal objects. Here we exploit the technique of SAXS to characterize these fractal objects.

Basically, all fractals show a power-law dependence of scattered intensity, I, on the momentum transfer q

$$\boldsymbol{I}(\boldsymbol{q}) \propto \boldsymbol{q}^{-x} \qquad [2.4.22]$$

We call x the 'Porod exponent' and refer to the scattering curve. Interpretation of the exponent, x depends on the origin of the scattering [Schaffer1984]. For so-called mass fractals (i.e. polymer-like structures) the exponent is simply D_f, the fractal dimension which relates the size R of the objects to the mass,

$$\boldsymbol{M} \propto \boldsymbol{R}^{D_f} \qquad [2.4.23]$$

For scattering from 3-dimensional objects with fractal surface $x=6-D_f$, where D_f is the fractal dimension of the surface ($2 \leq D_f \leq 3$). D_f =2 represents a classical smooth surface [Bale-Schmidt1984].

In summary, let us note that at intermediate q-values the decay of the scattered intensity, proportional to q^{-x}, is related to the dimensionality of the structure: linear structure x=-1, platelets x=-2, dense structure with smooth surfaces x=-4; and intermediate exponent between 1 and 3 is obtained with mass fractals where surface fractals exponents are between 3 and 4.

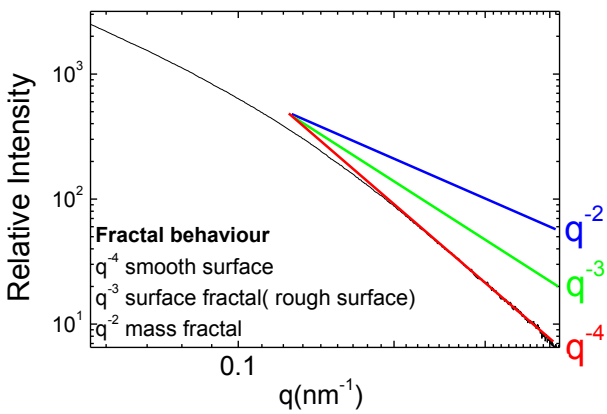

Figure 2.4.5 SAXS pattern showing the slope for different fractal behavior.

2.4.2.4. Inter-particle interactions

We now consider briefly how to extend the theory that has been developed so far to describe the small-angle scattering from a concentrated system of particles. Inter-particle correlations may be accounted for by introducing a structure factor S(q). Equation (2.4.16) then has to be amended to read

$$\boldsymbol{I}(\boldsymbol{q}) = (\Delta\rho)^2 \boldsymbol{V}_{\boldsymbol{P}}^2 \left|\boldsymbol{P}(\boldsymbol{q})\right|^2 \left|\boldsymbol{S}(\boldsymbol{q})\right|^2 \qquad [2.4.24]$$

Thus starting from the dilute limit, increasing the particle concentration will progressively lead to additional peaks in the intensity as a function of q.

2.5. Grazing-Incidence Small Angle X-ray scattering (GISAXS)

The GISAXS technique is derived from classical small-angle scattering but applied to nano sized objects at surfaces or embedded in a host matrix. The principle of GISAXS is sketched in Fig. 2.5.1. It consists in sending a monochromatic beam of X-rays on the sample surface under grazing incidence. Any kind of roughness on the surface or any kind of electronic contrast variation in the subsurface region leads to beam scattering in an off-specular direction [Lazzari2009, Daillant1992, and Muller-Buschbaum2003]. In particular, this is the case for PS islands on a substrate and for mesorporous thin films.

2.5.1. Geometry of GISAXS

A typical GISAXS experiment is illustrated in Figure 2.5.1; it consists in measuring the diffuse scattering around the specular beam at fixed incident angle α_i that is frequently chosen to be between the critical angle of the film and of the substrate. The scattering angles (α_{sc} ,ψ) are related to the wavevector transfer $q=k_{sc}-k_{in}$ through:

$$\begin{aligned} q_x &= k_0[\cos(\alpha_{sc})\cos(\psi) + \cos(\alpha_{in})] \\ q_y &= k_0[\cos(\alpha_{sc})\sin(\psi)] \\ q_z &= k_0[\sin(\alpha_{sc}) + \sin(\alpha_{in})] \end{aligned} \qquad [2.5.1]$$

Here, α_{sc} and ψ are defined as the out-of–plane and in-plane scattering angles, respectively. The pattern captured by the area detector is given in the q_y-q_z plane, where q_y is the scattering vector component parallel to the sample surface and perpendicular to the scattering plane and q_z is the component perpendicular to the sample surface.

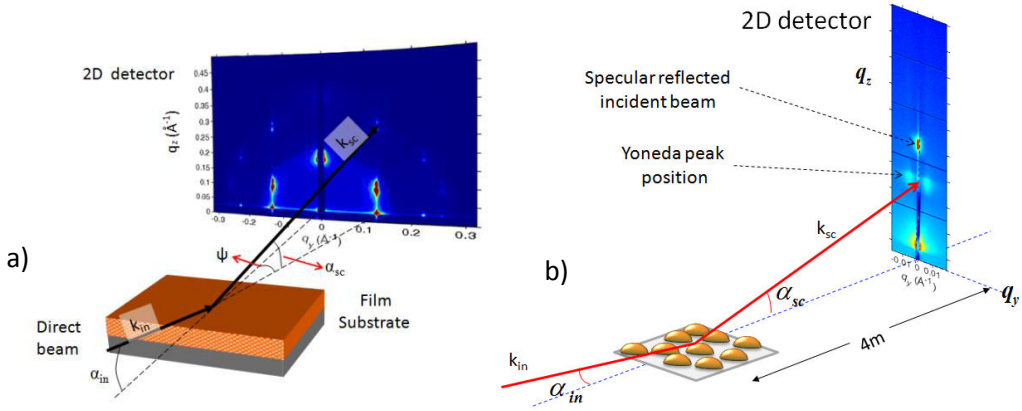

Figure 2.5.1 Principle of a GISAXS experiment. An X-ray beam of wavevector k_{in} impinges on the sample surface under a grazing incidence α_{in} and is reflected and transmited by the smooth surface but also scattered along k_{sc} in the direction (ψ,α_{sc}) by the surface roughness or density heterogeneities. The specular reflection which is located at $\psi = 0$ is hidden by a beam stop to avoid the damage on the detector due to the specularly reflected beam. a) Scheme representative for mesoporous silica thin film and for b)Island on a substrate.

2.5.2. The scattered intensity

The goal of this section is to show how to compute the scattered intensity I(q) defined by

$$I(q) = I_0 \int \frac{d\sigma}{d\Omega} d\Omega \qquad [2.5.2]$$

where I_0 is the incident intensity and ($d\sigma/d\Omega$) is the total differential cross section defined as follow

$$\left(\frac{d\sigma}{d\Omega}\right)_{total} = \frac{k_0 r_e^2}{16\pi^2} (\Delta\rho_e)^2 N \left(\frac{d\sigma}{d\Omega}\right)_{particle} \qquad [2.5.3]$$

k_0 is the modulus of the incident beam, N is the number of scatterers, r_e is the classical radius of the electron and $\Delta\rho_e$ is the electron density contrast of the system.

On a perfectly flat surface, all the intensity is concentrated in the specular rod. In fact, the off-specular scattering appears whenever any type of surface roughness, scattering entity or contrast variation is present at the surface. In the actual case, the roughness is restricted to small particles on a surface or to a plane of particle embedded in a host

matrix with well defined geometrical shapes. Each particle is characterized by its position on the substrate R^i and its shape function $f^i(r)$ equal to one inside the object and zero outside. The scattering density (electronic density) is given by:

$$\rho_e(\boldsymbol{r}) = \rho_0 \sum_i \boldsymbol{f}^i(\boldsymbol{r}) \otimes \delta(\boldsymbol{r} - \boldsymbol{R}^i) \qquad [2.5.4]$$

where $\otimes$ is the notation for the convolution product and ρ_0 is the mean electronic density. In the framework of the kinematic approximation, the differential cross section per particle is proportional to the modulus square of the Fourier transform of the electronic density. Thus, the differential cross section per a particle and par unit area in an off-specular direction is given by

$$\left(\frac{d\sigma}{d\Omega}(\boldsymbol{q})\right)_{particle} = \left|\boldsymbol{P}(\boldsymbol{q})\boldsymbol{S}(\boldsymbol{q})\right|^2 = \left|\boldsymbol{A}(\boldsymbol{q})\right|^2 \qquad [2.5.5]$$

where P(q) is the form factor of the object and the S(q) represent the interference term which takes in account the position of objects.

During the course of this thesis, 2 systems have been studied using GISAXS:

- polystyrene islands
- mesoporous silica thin films.

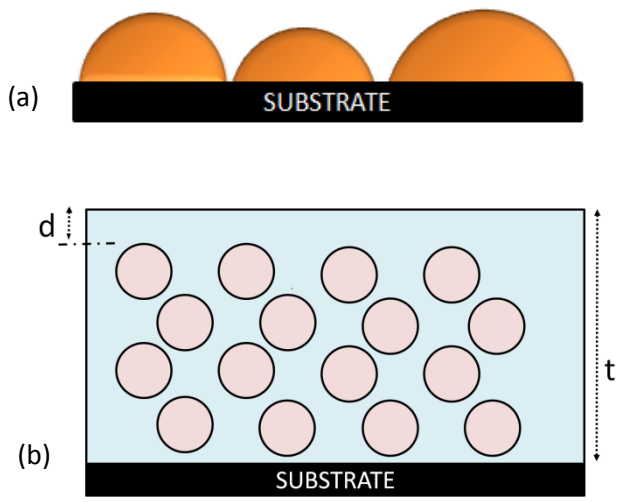

Figure 2.5.2 (a) Islands supported on a substrate (e.g. Polystyrene Island) (b) Particles encapsulated in an overlayer on a substrate (e.g. Mesoporous silica film)

Both systems will be studied in details in the following sections where we show how to make the calculations of the scattered intensity in the DWBA approximation. For sake of simplicity, we first consider the calculation in the Born approximation and then we provide the way to introduce the corrections to apply for the DWBA formalism.

2.5.3. Form factors of particles

The **form factor** P(q) is only the Fourier transform of the shape of a particle. Various "standard" shapes have been expressed analytically and tabulated in the literature [Lazzari2002].

For a spherical particle of homogeneous density, **the form factor** with origin taken at the center of the particle is given by

$$\boldsymbol{p}(\boldsymbol{q}) = 4\pi \boldsymbol{R}^3 \frac{\sin(\boldsymbol{qR}) - \boldsymbol{qr}\cos(\boldsymbol{qR})}{(\boldsymbol{qR})^3} \qquad [2.5.6]$$

For a spheroid, it becomes

$$\begin{aligned} \boldsymbol{p}(\boldsymbol{q}) &= \int_0^{\boldsymbol{H}/2} 4\pi \boldsymbol{R}_z^2 \frac{\boldsymbol{J}_1(\boldsymbol{q}_{//}\boldsymbol{R}_z)}{\boldsymbol{q}_{//}\boldsymbol{R}_z} \cos(\boldsymbol{q}_z z) \boldsymbol{dz} \\ \boldsymbol{q}_{//} &= (\boldsymbol{q}_x^2 + \boldsymbol{q}_y^2)^{1/2} \\ \boldsymbol{R}_z &= \boldsymbol{R}(1 - 4\boldsymbol{z}^2/\boldsymbol{H}^2) \end{aligned} \qquad [2.5.7]$$

For a cylinder and hemisphere the form factor with origin taken at the bottom of the particle is given by:

For a cylinder:

$$\begin{aligned} \boldsymbol{p}(\boldsymbol{q}, \boldsymbol{R}, \boldsymbol{H}) &= 2\pi \boldsymbol{R}^2 \boldsymbol{H} \frac{\boldsymbol{J}_1(\boldsymbol{q}_{//}\boldsymbol{R})}{\boldsymbol{q}_{//}\boldsymbol{R}} \sin_c(\boldsymbol{q}_z \boldsymbol{R}/2) \exp[-\boldsymbol{i}\boldsymbol{q}_z \boldsymbol{H}/2] \\ \mathrm{q}_{//} &= (\boldsymbol{q}_x^2 + \boldsymbol{q}_y^2)^{1/2} \end{aligned} \qquad [2.5.8]$$

For hemisphere:

$$p(q,R,H) = 2\pi \int_0^H R_z^2 \frac{J_1(q_{//}R_z)}{q_{//}R_z} \exp(iq_z z)dz$$

$$R_z = R(1-(z/H)^2)^{1/2} \qquad [2.5.9]$$

In the case of Polystyrene island (see Chapter 4), it is quite important to understand that the islands are extremely thin (4nm thick) but quite large in size. In a first approximation one can describe the islands by polydisperse shallow cylinders while in a second step it is possible to consider that they are more like hemispheroids.

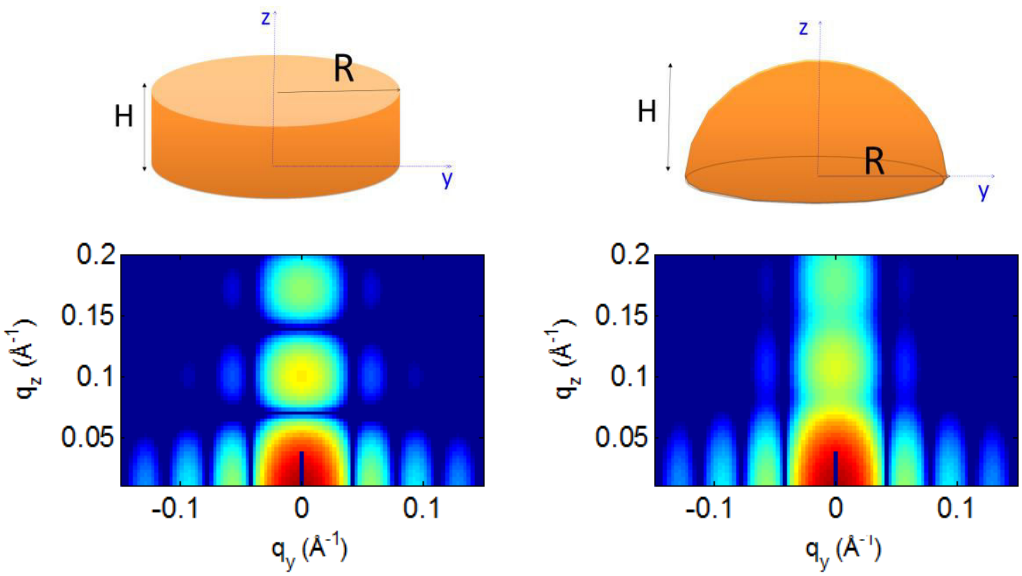

Figure 2.5.3 Top part: a) Cylinder and b) Hemisphere particle. Bottom part: Corresponding 2D patterns showing the modulus square of the form factor (H=R=9 nm for both cases)

For mesoporous silica (see Chapter 5), the micelles or pore could be modelled by a sphere or spheroid. As shown in (Fig. 2.5.4), the modulus of the form factor for a sphere is isotropic in *q* and exhibits minima circular in shape, in agreement with the Curie principle of symmetry, stipulating that the scattering must have the same symmetry as the scattering object. The intensity of the minima is very low if the polydispersity of the pores is small. For a spheroid, which is here taken to be a sphere compressed in the *z* direction, the principle of Curie implies that the minima are no more located on circles but rather on ellipses as shown in the (Fig. 2.5.4).

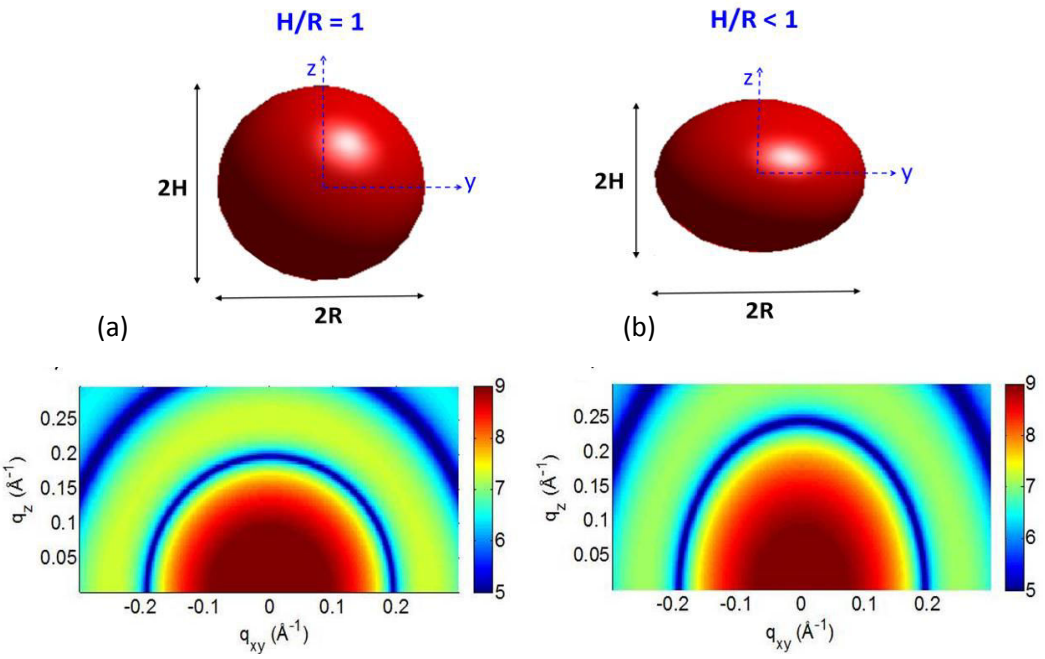

Figure 2.5.4 Top part: a) Spherical and b) Spheroidal pore or micelle. Bottom part: Corresponding 2D patterns showing the modulus square of the form factor.

Structure Factor

In the particular case of mesoporous materials, the structure factor can be expressed as the sum of the form factors of the individual objects $p^j(q)$ weighted by a phase shift which depends on the location of these objects in the unit cell. This basically defines in an analytical way the electron density in the unit cell (see Fig. 2.5.5).

$$P(q) = \sum_j p^j(q) e^{-iqr_j} \qquad (2.5.10)$$

Here, r_j defines the position of the j-th object in the unit cell. In the 3D hexagonal unit cell, there are two micelles per unit cell located are r_1 and r_2 so that the structure factor of the system can be expressed as follows:

$$\boldsymbol{P(q) = p(q)e^{-i\vec{q}\vec{r}_1} + p(q)e^{-i\vec{q}\vec{r}_2}}$$

$$\boldsymbol{P(q) = p(q)(e^{-i\vec{q}\vec{r}_1} + e^{-i\vec{q}\vec{r}_2})} \qquad (2.5.11)$$

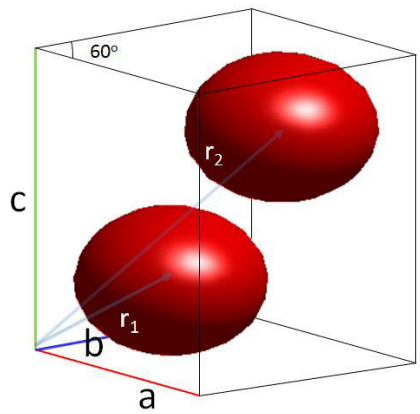

Figure 2.5.5 Hexagonal unit cell with slightly compressed, i.e. spheroidal, pores *R*=2.3 nm and *H*=1.85 nm.

Polydispersity

The factor $\boldsymbol{P(q,R,H)}$ is the form factor of a monodisperse particle. For polydisperse particle, the form factor needs to be weighted with a log-normal distribution defined as $f(x) = \exp(-(\log(x) - \log(x_{av}))^2)$.

Assuming that the average radius of the islands is R_{av} and the average thickness is H_{av}, the average form factor is given by

$$\boldsymbol{P(q_{//},q_z,R_{av},H_{av})} = \sum_m \sum_k \boldsymbol{f(H_m)f(R_k)P(q_{//},q_z,R_k,H_m)} \qquad [2.5.12]$$

2.5.4. Correlated Particles on a substrate

2.5.4.1. The case of island on a substrate

The interference term S(Q) is given by the pair correlation function which defines the lateral organization of the islands a short-range. The function developed by Hosemann and Bagui [Hoseman&Bagui1952] for 'paracrystalline' systems in which the relevant parameters are the nearest- neighbour distance D and the r.m.s. (root mean square) deviation σ of the distribution (Hosemann and Bagui) is given by

$$|S(q_{//})|^2 = \frac{1-g^2(q_{//})}{1-2g(q_{//})\cos(q_{//}D)+g^2(q_{//})} \qquad [2.5.13]$$

where $g(q_{//})$ is the Fourier transform of the Gaussian distribution of the first neighbour $g(q_{//}) = \exp(-q_{//}^2\sigma^2)$ and $q_{//} = \sqrt{q_x^2 + q_y^2}$.

The interference function is showed in Figure 2.5.6 for various disorder parameter σ/D. The broadening of the peak with increasing the ratio σ/D shows the transition from an ordered lattice to a disordered lattice.

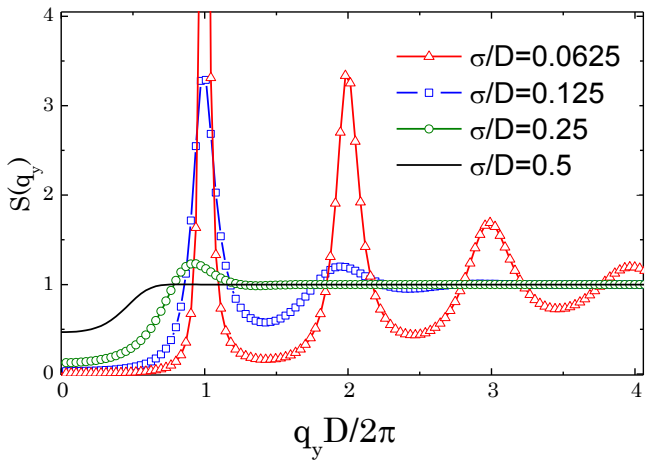

Figure 2.5.6 Interference function using the function developed by Hosemann for various disorder parameter σ/D, where D= 1500 Å.

2.5.4.2. The case of mesoporous silica thin film

The **interference term S(q)** is generally defined by the formula,

$$S(q) = \sum_{Rn} e^{-iq.Rn} \qquad (2.5.14)$$

where for a three dimensional system $R_n = n\vec{a} + m\vec{b} + l\vec{c}$ is a lattice vector, n,m,l are integer numbers and a,b, c represent the lattice parameters.

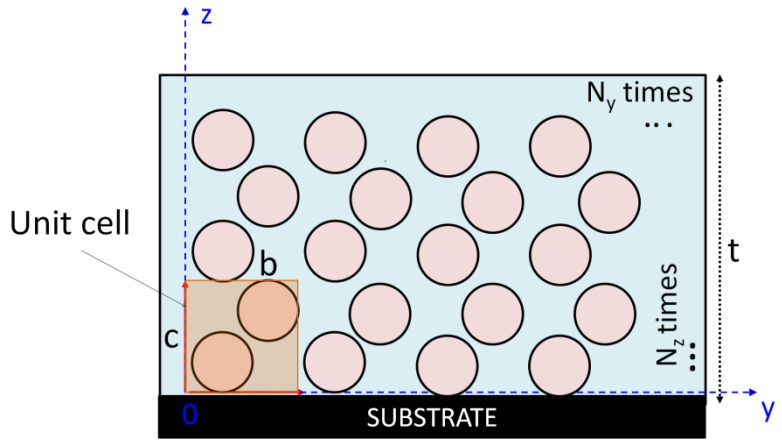

Figure 2.5.7 Schematic representation of mesoporous thin film where $\vec{d}$ is the depth of the first scattering object and 'a' and 'c' represents the unit cell vectors and t is the thickness of the film.

In the case of a mesoporous thin film as described in Fig. 2.5.7, the perpendicular direction (z-axis) is restricted to a finite size determined by the thickness of the film. In this direction it is considered as a finite lattice defined by Nz unit cells. Thus the expression of the interference term given in Eq. 2.5.14 can be expressed as,

$$S(q_z) = \frac{1 - e^{N_z q_z c}}{1 - e^{q_z c}} \qquad (2.5.15)$$

For $q_{x,y}$ terms, the in-plane coherent length ξ of the scattering domains is sufficiently large for replacing the sum by a Gaussian or a pseudo-Voigt function as follows:

$$S(q_{x,y}) = e^{-\xi^2 (q_{x,y} - q_{hkl}^{x,y})^2} \qquad (2.5.16)$$

where the vector q_{hkl} for the case of a close-packed hexagonal is expressed as followed :

$$q_{hkl}^{x,y} = \sqrt{\frac{16\pi^2 (h^2 + k^2 + l^2)}{3a^2}}, \quad q_{hkl}^{z} = \frac{2\pi l}{c} \qquad (2.5.17)$$

Then, putting together the terms (Eq. 5.4.75) and (Eq. 5.4.76), the structure factor can be written as:

$$S(q) = e^{-\xi^2 (q_{x,y} - q_{hkl}^{x,y})^2} \frac{1 - e^{N_z q_z c}}{1 - e^{q_z c}} \qquad (2.5.18)$$

In Figure 2.5.8, the structure factor profile along the z direction is represented. This profile is characterized for a series of peaks of high intensity located at the Bragg positions.

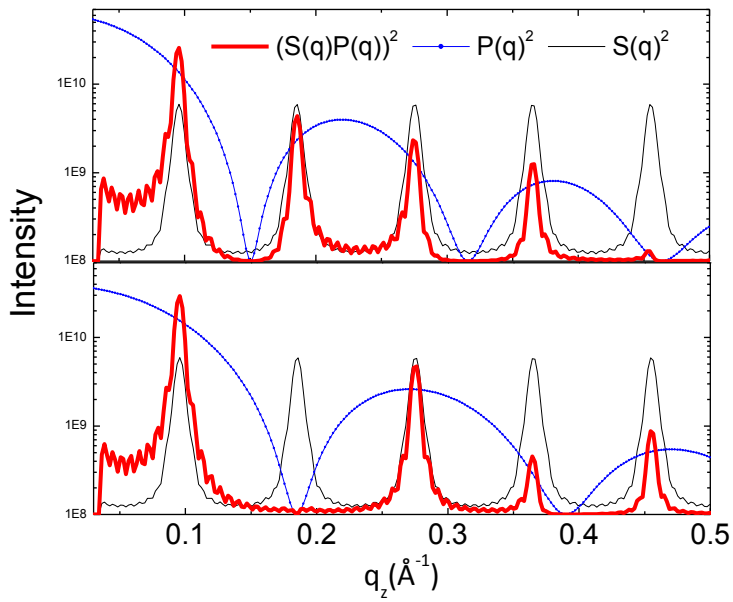

Figure 2.5.8 Intensity profile in the q_z direction, at a value of q_y=0.14 Å^{-1}. The Structure factor is modulated by the form factor of a sphere with two different radius. For this scheme, the Born Approximation was used.

In the same figure is also shown, the result of the product of the form factor P(q) with the structure factor S(q) for two situations. It is observed that the form factor modulates the intensity of Bragg peaks, making them more or less intense. Thus, from this figure, it is observed that the extinction of some allowed reflections in the structure are caused by the minimum of the form factor of the scattering objects.

2.5.5. Distorted Wave Born Approximation

The passage from the Born (BA) to the **Distorted Wave Born Approximation** (DWBA) is made by taking in account the *refraction* correction in the q_z direction together with the fact that radiation *reflected* at the *substrate interface* will contribute to the total scattering [Lazzari2002,Rauscher1995].

2.5.5.1. The case of island on a substrate

Figure 2.5.9 illustrates the physical picture of the full calculation for the scattering cross section in the DWBA, which is given by following 4 terms

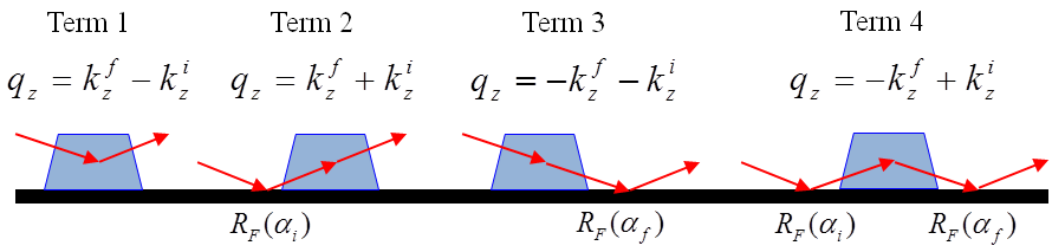

Figure 2.5.9 The four terms scattering for a supported island

The four terms involved are associated to different scattering events, which involve or not a reflection of either the incident beam or the scattered beam collected on the detector. These waves interfere coherently, giving rise $\boldsymbol{A}(\boldsymbol{q}_{//},\pm\boldsymbol{k}_z^f,\pm\boldsymbol{k})$, in which the classical factor A(q) comes into play but with respect to each specific wavevector transfer. Each term is weighted by the corresponding Fresnel reflection coefficient , either in incidence or in reflection.

$$\begin{aligned}\boldsymbol{A}(\boldsymbol{q}_{\parallel},\boldsymbol{k}_z^i,\boldsymbol{k}_z^f) = \boldsymbol{P}(\boldsymbol{q}_{\parallel},\boldsymbol{k}_z^i,\boldsymbol{k}_z^f)\boldsymbol{S}(\boldsymbol{q}_{\parallel},\boldsymbol{k}_z^i,\boldsymbol{k}_z^f) = {} & \boldsymbol{A}(\boldsymbol{q}_{//},\boldsymbol{k}_{z,0}^f - \boldsymbol{k}_{z,0}^i) \\ & + \boldsymbol{r}_{0,1}^f \boldsymbol{A}(\boldsymbol{q}_{//},\boldsymbol{k}_{z,0}^f + \boldsymbol{k}_{z,0}^i) \\ & + \boldsymbol{r}_{0,1}^i \boldsymbol{A}(\boldsymbol{q}_{//},-\boldsymbol{k}_{z,0}^f - \boldsymbol{k}_{z,0}^i) \\ & + \boldsymbol{r}_{0,1}^i \boldsymbol{r}_{0,1}^f \boldsymbol{A}(\boldsymbol{q}_{//},-\boldsymbol{k}_{z,0}^f + \boldsymbol{k}_{z,0}^i)\end{aligned} \qquad [2.5.19]$$

where the reflection coefficient $r_{0,1}$ at the interface 0,1 is given by,

$$\boldsymbol{r}_{0,1} = \frac{\boldsymbol{k}_{z,0} - \boldsymbol{k}_{z,1}}{\boldsymbol{k}_{z,0} + \boldsymbol{k}_{z,1}} \qquad [2.5.20]$$

and $\boldsymbol{k}_{z,1}^i = \boldsymbol{k}_0(\alpha_i^{\,2} - \alpha_c^2 - 2\boldsymbol{i}\mu)^{1/2}$ and $\boldsymbol{k}_{z,1}^f = \boldsymbol{k}_0(\alpha_f^2 - \alpha_c^2 - 2\boldsymbol{i}\mu)^{1/2}$.

A typical example using the DWBA is given in Fig. 2.5.10c for a cylindrical island. At $\alpha_f=\alpha_C$ an enhancement of intensity, known as the Yoneda peak, is found whose shape is driven by α_i and the index of refraction of the substrate. In the DWBA the interference fringes of the Born form factor are smeared out by the coherent interference between the four scattering events (see Fig. 2.5.10a and Fig. 2.5.10b).

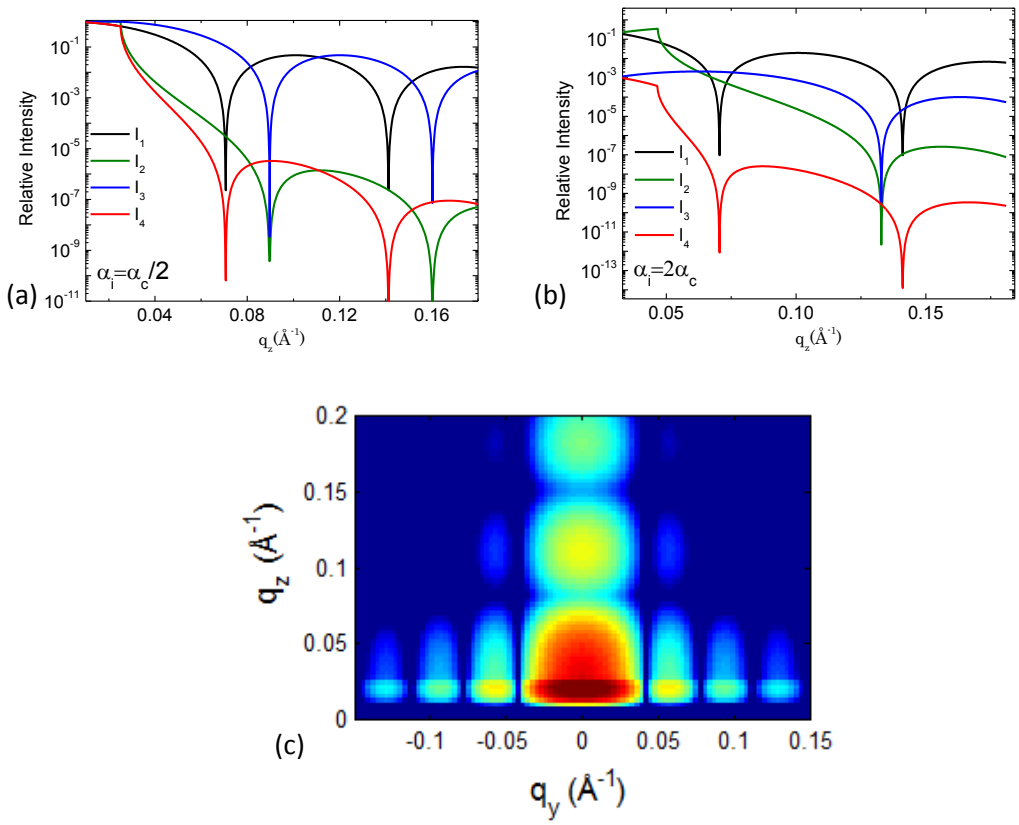

Figure 2.5.10 The modulus squared of the various component involved in the cylinder DWBA form factor shown in the eq 2.5.19. The line (black, green, blue, red) correspond respectively, to the four events of Fig. 2.5.9 from left to right. When (a) $\alpha_i=\alpha_c/2$ (b) $\alpha_i=2\alpha_c$. (c) Form factor of a cylindrical island including all the four term of scattering with an incidence angle $\alpha_i=\alpha_c$ and considering that S(q)=1, R=H=9nm .

If the substrate is covered with a continuous layer of thickness 't' as we show in Figure 2.5.11,

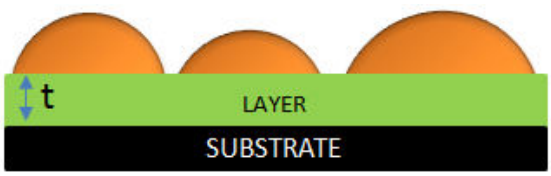

Figure 2.5.11 Island supported on a layer on a substrate

the reflection coefficient in the Eq. 2.2.66 becomes:

$$\boldsymbol{R} = \frac{\boldsymbol{r}_{0,1} + \boldsymbol{r}_{1,2}\exp(2\boldsymbol{i}\boldsymbol{k}_z\boldsymbol{t})}{1 + \boldsymbol{r}_{0,1}\boldsymbol{r}_{1,2}\exp(2\boldsymbol{i}\boldsymbol{k}_z\boldsymbol{t})} \quad \text{where } \boldsymbol{r}_{i,j} = \frac{\boldsymbol{k}_{z,i} - \boldsymbol{k}_{z,j}}{\boldsymbol{k}_{z,i} - \boldsymbol{k}_{z,j}} \qquad [2.5.21]$$

$r_{0,1}$ and $r_{1,2}$ are the Fresnel coefficients of the air-layer and layer substrate interface. Thus the $\boldsymbol{A}(\boldsymbol{q}_{//},\pm\boldsymbol{k}_z^f,\pm\boldsymbol{k})$ is modulated by the Kiessig fringes of this overlayer.

2.5.5.2. The case of mesoporous silica thin film

A physical picture for the possible diffusion processes are shown in the Fig. 2.5.12:

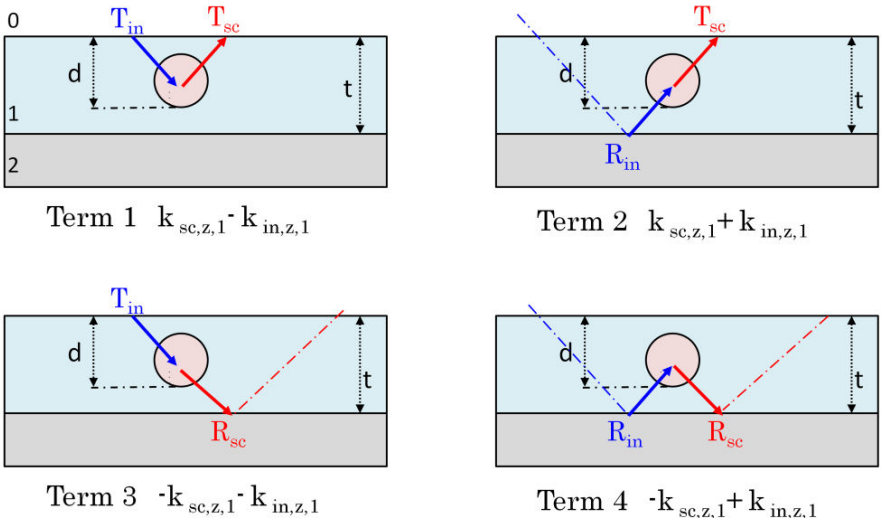

Figure 2.5.12 The four terms in the scattering for a particle encapsulated in the layer on substrate. The first term correspond to the Born Approximation (BA).

Each term corresponds to a specific wave vector q_z inside the film and to different modified amplitudes, as described in the literature by Rauscher et al. [Rauscher1995] and by Lazzari [Lazzari2002]. These process involve transmission and reflection phenomena at each interfaces and the scattered amplitude becomes

$$\begin{aligned}\boldsymbol{A}(\boldsymbol{q}_{\parallel},\boldsymbol{k}_z^i,\boldsymbol{k}_z^f) = (&\boldsymbol{T}_i\boldsymbol{T}_f \cdot \boldsymbol{A}(\boldsymbol{q}_{\parallel},\mathrm{k}_{sc,z,1}-\mathrm{k}_{in,z,1}) \\ &+\boldsymbol{T}_f\boldsymbol{R}_i.\boldsymbol{A}(\boldsymbol{q}_{\parallel},\mathrm{k}_{sc,z,1}+\mathrm{k}_{in,z,1}) \\ &+\boldsymbol{T}_i\boldsymbol{R}_f \cdot \boldsymbol{A}(\boldsymbol{q}_{\parallel},-\mathrm{k}_{sc,z,1}-\mathrm{k}_{in,z,1}) \\ &+\boldsymbol{R}_i\boldsymbol{R}_f \cdot \boldsymbol{A}(\boldsymbol{q}_{\parallel},-\mathrm{k}_{sc,z,1}+\mathrm{k}_{in,z,1}))\end{aligned} \qquad [2.5.22]$$

Ri and Ti are the reflection and transmission coefficients in the layer 1 given by

$$R_i = \frac{t_{0,1}^{in} r_{1,2}^{in} e^{2ik_{in,z,1}t}}{1 + r_{0,1}^{in} r_{1,2}^{in} e^{2ik_{in,z,1}t}}, \quad T_{i\cdot} = \frac{t_{0,1}^{in}}{1 + r_{0,1}^{in} r_{1,2}^{in} e^{2ik_{in,z,1}t}}$$

$$R_f = \frac{t_{0,1}^{sca} r_{1,2}^{sca} e^{2ik_{sca,z,1}t}}{1 + r_{0,1}^{sca} r_{1,2}^{sca} e^{2ik_{sca,z,1}t}}, \quad T_f = \frac{t_{0,1}^{sca}}{1 + r_{0,1}^{sca} r_{1,2}^{sca} e^{2ik_{sca,z,1}t}} \qquad [2.5.23]$$

in which t is the thickness of the film, with $k_{in,z,1}$ and $k_{sc,z,1}$ are the z-axis component of the incident and scattered wave vector in medium 1, $k_{in,z,1} = -k_0\sqrt{\alpha^2 - \alpha_{c,1}^2 - 2i\beta_1}$, $k_{sc,z,1} = -k_0\sqrt{\beta^2 - \alpha_{c,1}^2 - 2i\beta_1}$ in which $\alpha_{c,1}$ is the critical angle of the film and β_1 the absorption in the film. The coefficients $r_{i,j}$ and $t_{i,j}$ are the Fresnel coefficients at the interface between two media *i* and *j* and are defined by

$$r_{i,j}^{in} = \frac{k_{in,z,i} - k_{in,z,j}}{k_{in,z,i} - k_{in,z,j}}, \quad t_{i,j}^{in} = \frac{2k_{in,z,i}}{k_{in,z,i} - k_{in,z,j}} \qquad [2.5.24]$$

Similar relationships hold for the scattered values.

2.6. Coherent X-ray Diffraction Imaging (CXDI)

CXDI is a new technique promising for high resolution lens-less imaging of non-crystalline and biological microscopic specimens. In CXDI, a fully coherent beam of x-rays is impinging on a single particle whose dimension is typically of the order of the µm. If the incident plane wave encounters some heterogeneities inside the particle like voids, grains or even a rough surface, a speckle pattern is measured in the far-field region. The speckle pattern arises from the interferences between all the scattering heterogeneities. It is characterized by a large number of small spots with no apparent periodicity. The speckle is thus the signature of a non uniform object and it is therefore particularly tempting to unravel its structure. This is a difficult task as in all scattering processes, the phase which is a key parameter to locate the position of the heterogeneities inside a scattering object is lost. The only information that remains in the scattering pattern is the modulus square of the scattered amplitude. However, it has been shown that when the diffraction pattern is sampled twice finer than the Nyquist frequency, the phase can be recovered using an

iterative phase retrieval algorithm. Once the phase is known, a real space image of the object is readily obtained by inverse Fourier transform.

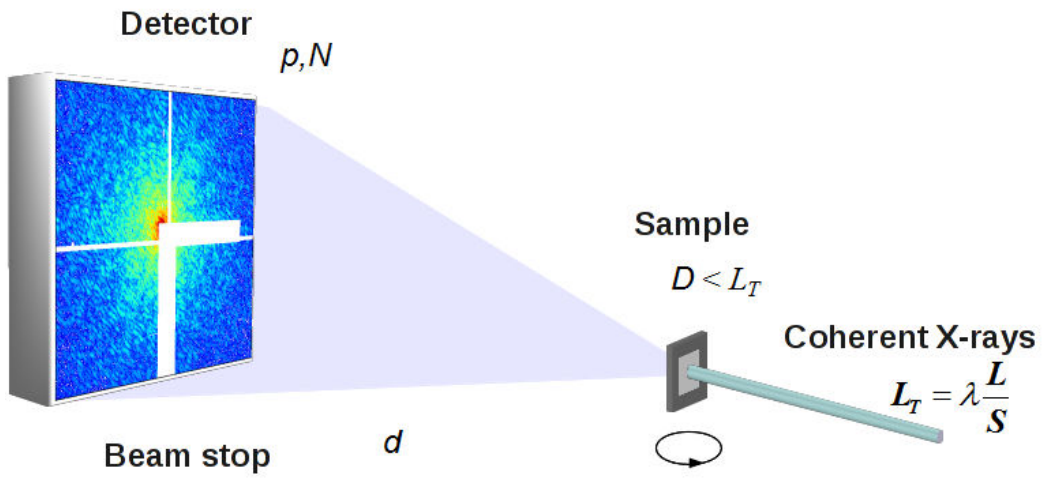

Figure 2.6.1 A object is illuminated by a coherent X-ray beam and the diffracted intensity, I(Q), is recorded on a position sensitive area detector placed in the far-field, where d is the sample-to-detector distance, λ the wavelength of the radiation, p the detector pixel size and N is the number of pixels in the detector, S is the source size and L is the distance from the undulator to the sample.

2.6.1. Phase Problem

There are two relevant parameters for diffracted waves: amplitude and phase. In optical microscopy using lenses there is no phase problem, as phase information is retained when waves are refracted. When a diffraction pattern is collected, the data is described in terms of absolute counts of photons or electrons, a measurement which describes amplitudes but loses phase information. This results in an ill-posed inverse problem as any phase could be assigned to the amplitudes prior to an inverse Fourier transform to real space.

The unknown phase can only be uniquely found when the measured amplitude is sampled more finely than the Nyquist frecuency [Sayre1952, 1980]. According to Bates, in order to solve the phase problem the diffraction pattern must be oversampled at least by a factor of two in each dimension [Bates1982]. However, Miao et al. showed that the solution can be obtained if the total number of pixels is twice the number of unknown pixels [Miao1998]. This implies that a two-dimensional speckle pattern must be oversampled by at least a factor of $\sigma=2^{1/2}$ in each dimension. Miao et al. emphasized that higher oversampling is required during the experiment to obtain reliable image reconstruction [Miao2003]. This is because the measured intensity in each pixel is the intensity

integrated over the solid angle defined by the detector pixel size. The measured intensity at low oversampling ratios can deviate substantially from the exact sampled data [Song 2007].

A representative example about the importance of the phase value in the image reconstruction process is shown in Figure 2.6.2. In this figure, it is possible to observe the problem linked to the phase loss which makes impossible the image reconstruction from a diffraction pattern (see Figure 2.6.2a). When a good phase is associated to the amplitude information is possible to reconstruct the diffracted object (see Figure 2.6.2 b).

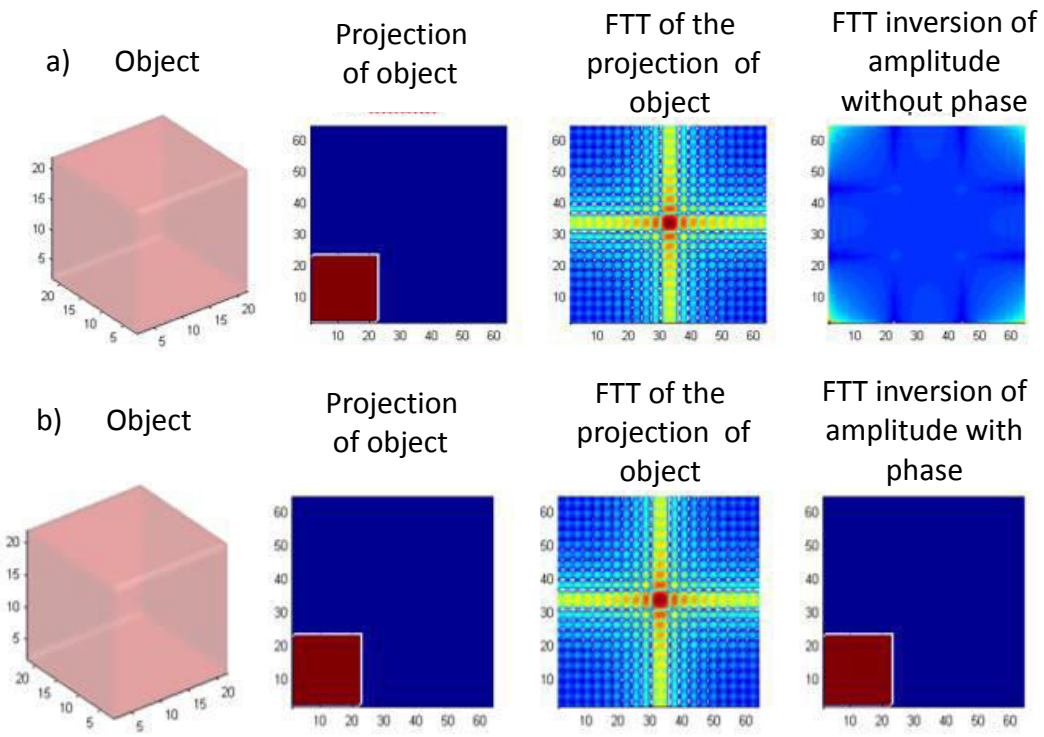

Figure 2.6.2 The importance of the phase on the reconstruction of the image

2.6.2. Phase Retrieval Method

In a typical reconstruction [Vartanyants2005] the first step is to generate random phases φ(q) and to combine them with the amplitude information A(q) from the reciprocal space pattern. Then a Fourier transform is applied back and forth to move between real space and reciprocal space with the modulus squared of the diffracted wave field set equal to the measured diffraction intensities at each cycle. By applying various constraints in real and reciprocal space the pattern evolves into an image after enough iterations of the

hybrid input output (HIO) process. To ensure reproducibility the process is typically repeated with new sets of random phases with each run having typically hundreds to thousands of cycles [Vartanyants2005]. The schematic operation of the error-reduction, iterative algorithm used to retrieve the phases from an oversampled diffraction pattern is shown in Fig.2.6.3. The constraints imposed in real and reciprocal space typically depend on the experimental setup and the sample to be imaged.

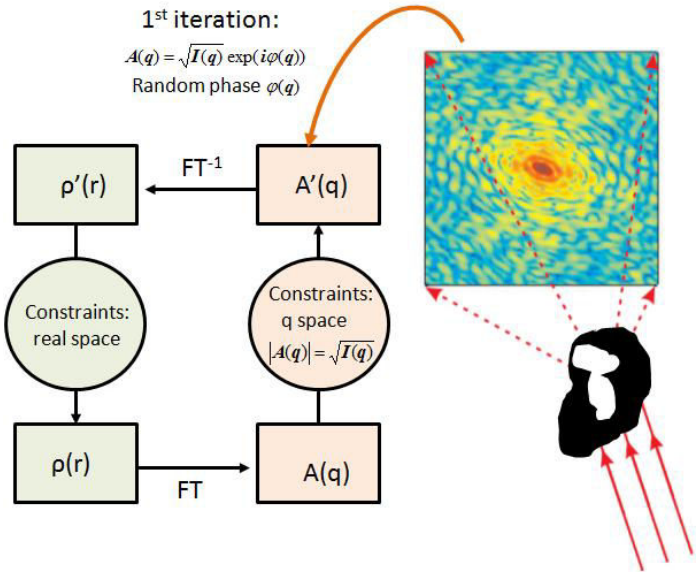

Figure 2.6.3 Schematic of the iterative, phase retrieval algorithm used to reconstruct real space images from coherent X-ray diffraction images.

2.6.3. Details of the experimental setup

To perform a CXDI experiment one requires a source of coherent illumination on the sample and a detector of sufficient resolution and spatial extent to collect the data required.

The coherent X-ray illumination is obtained by the combination of monochromator, mirrors, pinhole, and guard slits. After the silicon (111) monochromator and the higher-harmonics-rejecting mirrors, 8 keV X-rays were spatially filtered by a 10µm square pinhole to illuminate the samples coherently. The unwanted Airy pattern from the pinhole was blocked by secondary (guard) slits. The final diffraction data were collected on a MAXIPIX detector with direct illumination and a pixel size of 55µm, situated 4m downstream of the sample. The experimental setup is shown schematically in figure 2.6.4.

The appropriate source of x-rays for a coherent diffraction experiment is a synchrotron due to the high flux and brightness of the x-rays produced. This experiment was performed at ID10 at ESRF. This beamline delivers a coherent flux of $5x10^{10}$ph/s/100mA. To conduct CXDI measurements there is a high precision goniometer based on an air-bearing rotation. The goniometer is equipped with the on-axis optical microscope which has a 7-fold zoom to facilitate the sample positioning and alignment. The samples on Si_3N_4 thin membranes are mounted on a high precision stage with 50 nm resolution in x, y and z directions. The stage can be rotated around vertical axis (in the horizontal plane) by 360 degrees.

For the reconstruction, the detector imposes technical and geometric constraints on achieving both high oversampling "σ" in reciprocal space and high spatial resolution "r" in real space. The linear oversampling ratio $\sigma = d\lambda/pS$ is a function of the sample-to-detector distance d, the wavelength of the radiation λ, the detector pixel size p and the sample size S. Since σS is the field of view in real space, the number of detector pixels N_{pix} will set the maximum achievable resolution in real space $r = d\lambda/pN_{pix}$ is therefore the key parameter that determines the ultimate geometric resolution in CXDI once the condition for oversampling ($\sigma<2^{1/2}$) is met.

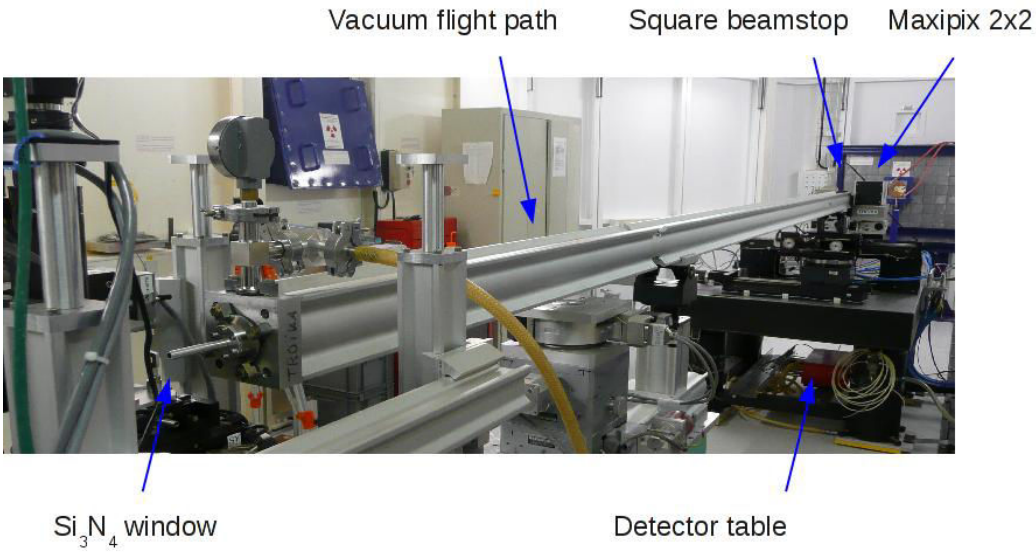

Figure 2.6.4 Flight path and detector table. The sample to detector distance can be tuned up to 7m at ID10 (ESRF).

Bibliography

[Als-Nielsen&McMorrow2010] Als-Nielsen, J.; McMorrow, D. Elements of Modern X-Ray Physics. John Wiley & Sons, New York, 2nd edition, 2010.

[Bale-Schmidt 1984] Bale, H.D.; Schmidt, P.W. Phys. Rev. Lett. (1994)53, 596-599.

[Bates1982] Bates, R. H. T. Optik, (1982) 61, 247–262.

[Born&Wolf1980] Born, M.; Wolf, E. Principles of Optics, Oxford: Pergamon Press, 1980.

[Daillant1992] Daillant, J.; Belorgey O., J. Chem. Phys. (1992) 97, 5824-5835.

[Gibaud2009] Gibaud, A. Specular Reflectivity from Smooth and Rough Surfaces, X Ray and Neutron Reflectivity: Principle and Applications, Edited by Daillant, J. and Gibaud, A. (Springer, Paris 2009), pp 133-182.

[Debye&Bueche1949] Debye, P.; Bueche, A. M., J. Appl. Phys. (1949) 20, 518.

[Glatter1982] Glatter, O; and Krattky, O., Small Angle x-ray scattering, Academic Press London, 1982.

[Guinier1955] Guinier A.; Fournet, G., Small Angle sacttering of x-rays Wiley , 1955.

[Hamley1994] Hamley, I. W; Pedersen, J. S., J. Appl. Crystallogr. (1994) 27, 29.

[Hoseman&Bagui1952] Hosemann, R.; Baghi, S. N., Acta Crystallogr. (1952) 5, 612.

[Lazzari2002] Lazzari, R. J. Appl. Crystallogr. (2002) 35, 406-421.

[Lazzari2009] Lazzari, R. Grazing Incidence Small-Angle X-Ray Scattering from Nanostructures, X Ray and Neutron Reflectivity: Principle and Applications, Edited by Daillant, J. and Gibaud, A. (Springer, Paris 2009), pp 283-344.

[Miao1998] Miao, J.; Sayre, D. ; Chapman, H. N. J. Opt. Soc. Am. A (1998) 15,1662–1669.

[Miao2003] Miao, J.; Ishikawa, T.; Anderson, E. H. Phys. Rev. B (2003) 67,174104.

[Mulller-Buschbaum2003] Muller-Buschbaum, P. Analytical and Bioanalytical Chemistry (2003) 376(1):310.

[Parrat1954] Parrat, L.G., Phys. Rev. (1954) 95, 359.

[Rauscher1995] Rauscher M.; Salditt T.; and Spohn H. Phys. Rev. B (1995) 52(23), 16855-16863.

[Roentgen1896] W. C. Roentgen. Nature (1896) 53:274-276.

[Sayre1952] Sayre, D. Acta Cryst. (1952) 5: 843.

[Sayre1980] Sayre, D. Imaging Processes and Coherence in Physics. Lecture Notes in Physics, Vol. 112, edited by M. Schlenker, M. Fink, J.-P. Goedgebuer, C. Malgrange, J.-C. Vienot & R. H. Wade, pp. 229–235. Heidelberg: Springer, 1980.

[Song2007] Song, C.; Ramunno-Johnson, D.; Nishino, Y.; Kohmura, Y.; Ishikawa, T.; Chen, C. C.; Lee, T. K.; Miao, J. Phys. Rev. B (2007) 75, 012102.

[Svergun1994] Svergun, D.I., Acta Cryst A (1994) 50, 391-402.

[Vartanyants2005] Vartanyants, I.A.; Robinson, I.K.; Onken, J.D.; Pfeifer, M.A.; Williams, G.J.; Pfeiffer, F.; Metzger, H.; Zhong, Z. ; G. Bauer, Phys. Rev. B (2005) 71: 245302.

CHAPTER 3

3. Analysis of porous powder of $CaCO_3$ prepared via sc-CO_2 using Small Angle X-ray Scattering

In this chapter, the results of Small Angle and Ultra Small Angle X-ray Scattering on porous $CaCO_3$ microparticles of pulverulent vaterite made by a conventional chemical route and by supercritical CO_2 are presented. The scattering curves are analyzed in the framework of the Guinier-Porod model which gives the radii of gyration of the scattering objects and their fractal dimension. In addition, we determine the porosity and the specific surface area by using the Porod invariant which is modified to take in account the effective thickness of the pellet. The results of this analysis are compared to the ones obtained by nitrogen adsorption.

In addition, we also show the first results of Coherent Diffraction Imaging (CDI) experiments performed at the ID10A beam line on single particles of vaterite.

Material in this chapter appears in the paper 'Analysis of porous powder of $CaCO_3$ prepared via sc-CO_2 using Small Angle X-ray Scattering' E. A. Chavez Panduro, T. Beuvier, M. Fernandez Martinez, L. Hassani, B. Calvignac, F. Boury, A. Gibaud, Journal of Applied Crystallography 01/2012; 45.

3.1. Introduction

Small-angle x-ray scattering (SAXS) is nowadays one of the very few techniques that can provide statistical information about the morphology, porosity and specific surface area of materials at the nanometer scale. Among the most studied materials by this technique for which there is an abundant literature on the topics one finds coal powders [Gibaud.1996, Radlinski2004, Schmidt1982, Kalliat1981]. For extracting all the information, it is important to measure the scattered intensity in absolute units which in turn necessitates to correct the measured intensity from the transmission coefficient and from the thickness of the material. This is one of the major problem to solve when one wants to analyze the data obtained from powders since i) the transmitted beam intensity decays exponentially with the thickness of the sample and ii) the real thickness can be difficult to ascertain when one is dealing with powdered samples. The analysis of the data strongly depends on how the experiment has been performed and how much effort the analyst wants to put into the model. For many years, many researchers were satisfied with standard analysis through linear plots such as Guinier or Porod plots [Guinier&Fournet1955, Glatter&Kratky1982]. Nonlinear least-squares fits in which the electron density was refined, were then introduced to analyze the data [Feigin&Svergun1987].

Guinier and Porod plots are the basic starting points for reaching immediate information about the particle size (radius of gyration) and about scattering inhomogeneities through the Porod exponent, i.e. the slope of the scattering curve in a log-log representation. A Porod exponent of 4, points to particles with smooth surfaces while an exponent of 3, points to very rough surfaces. An exponent 3 can also point to scattering from 'collapsed' polymer chains (in a bad solvent) and exponent of 5/3 points to scattering from 'fully swollen' chains (in a good solvent). An exponent of 2 can represent scattering either from Gaussian polymer chains or from a two-dimensional structure (such as lamellae or platelets).

Although this is quite basic, there are still some improvements on the way to analyze the data through this type of modelling. In particular, Beaucage wrote in 1994 [Beaucage1994] a paper in which he was showing how to combine the two approaches into a unified version. This approach is widely used nowadays but it was found that sometimes it yields unrealistic values for the Porod exponent. This is why

[Hammouda2010], proposed to correct the Beaucage approach by imposing the continuity of the scattering between the Guinier and the Porod behaviours. His model labelled as the Guinier-Porod model contains a constraint which is necessary to solve the problems encountered in the Porod regime found in the unified Beaucage model.

For going beyond this type of model, it is necessary to make very careful measurements of the scattered intensity, of the transmitted intensity and of the thickness of the sample. In such conditions, it is possible to obtain the porosity and the specific surface of powdered materials. The full description of the modelling was described in a very professional way in the paper by [Spalla2003]

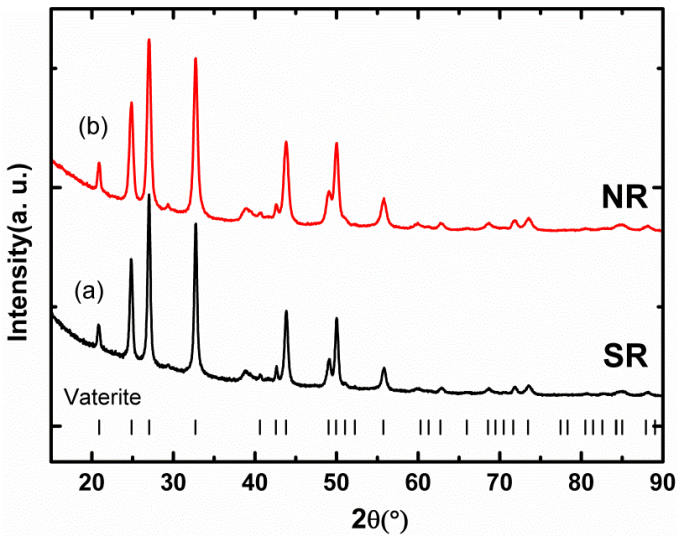

Figure 3.1.1 X-ray diffractogram of particles a) using the high-pressure supercritical route (SR) and b) using the normal route (NR). Bragg reflexions of vaterite (ICSD 15879) are indicated by vertical markers.

In this chapter, our aim is to analyze the SAXS data of meso and macro porous spheres of $CaCO_3$ having the vaterite structure as shown in Figure 3.1.1. Indeed, vaterite exhibits a porous structure which is suitable for protein encapsulation and drugs delivery [Wei2008; Peng2010]. This fact is supported by a number of scientific reports addressing loading of CaCO3 with functional nanoparticles [Zhao2010], various bioactive molecules including low-molecular weight drugs [Peng2010, Ikoma2007,Lucas-Girot2005], DNA [Fujiwara2008, Zhao2012], Si-RNA [He*2009*] and a wide range of proteins [Temmerma2011, Xiong2012].

Currently, the group of F. Boury (INSERM - Angers) is investigating on direct encapsulation of a model protein, lyzozyme, into $CaCO_3$ microparticules using sc-CO_2 process. They compared two different approaches for direct encapsulation. In the first approach, lysozyme was entrapped during the growth of $CaCO_3$ particles in supercritical (SR) CO_2, and in aqueous medium in the second one (called normal route (NR)). It is therefore important for potential application to understand the morphology of such host matrix and to see how the synthesis affects the porosity. The samples are powdered samples of vaterite which are analyzed at small and ultra small angles at the ID02 beam line of ESRF. They exhibit beautiful scattering patterns arising from the hierarchical architectures observed in the microspheres of vaterite shown in the Scanning Electron Microscopy Figure 3.1.2. The inner structure of the $CaCO_3$ microparticles can be unravelled after grinding the particles in a mortar [Beuvier2010] or by cutting them by a focused ion beam (FIB) [Suzuki2006]. In order to access the internal structure of particles, powder was pressed at 240 MPa and the pellet was cut in small pieces. The slide containing many broken particles was subsequently analysed by SEM. The size distributions were determined by measuring the diameter of about 200 particles. As shown in Figures 3.1.2a and 3.2b, the microspheres made by the normal route (NR) have an average diameter of 2.3±1.0 µm. They are composed of agglomerated nanograins. Figures 3.1.2c, 3.1.2d and 3.1.2e show the morphology of the broken particles. Radial fibrous units are observed with an important macroporosity at the cores of the particles. There is no sign of any hollow core in such particles.

On the contrary, particles made by the supercritical route (SR) have a higher diameter (4.9±1.0 µm) (Figure 3.1.2f). The surface and the inner part of the particles look more compact than the ones of particles made by NR (Figures 3.1.2g and 3.1.2h). This should likely affect the porosity. Moreover particles made by SR have a hollow core with an average diameter of 0.7 µm (Figure 3.1.2h). Bigger particles display a larger core (Figure 3.1.2i).

As the distribution and sizes of the macro- and meso-pores in the $CaCO_3$ particles may differ from one particle to one another, it is very difficult to analytically model the SAXS data. Therefore, we have used in this analysis both [Hammouda2010] and [Spalla2003]'s approaches to extract real space information contained in the scattering curves. In the SAXS analysis, we first apply the Guinier-Porod model and then we use the Porod

invariant to extract the porosity and specific surface area according to the approach of [Spalla2003]

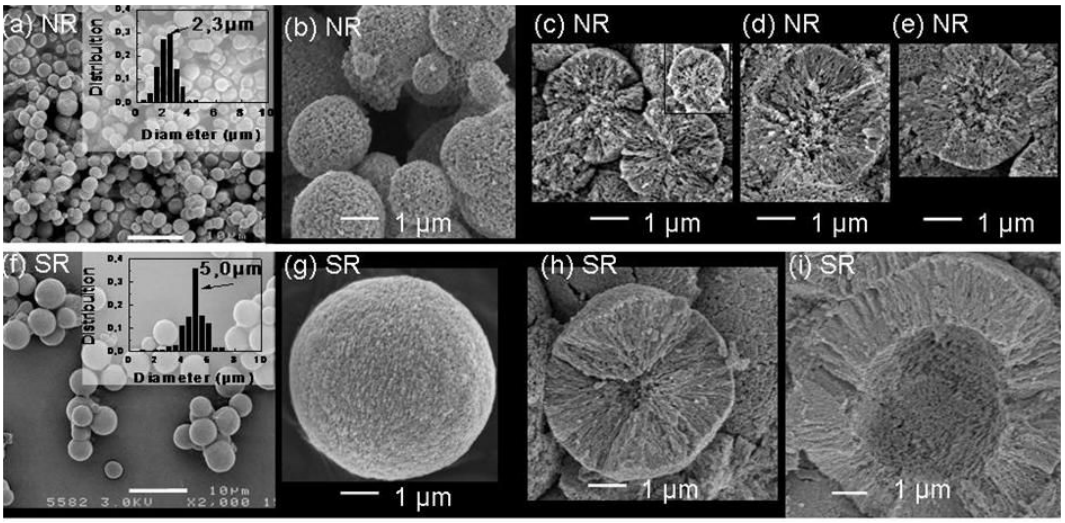

Figure 3.1.2 SEM image of $CaCO_3$ microparticles showing the presence of a porous core having a diameter of the order of 700nm surrounded by a porous shell which contains grains of crystalline vaterite and mesopores (SEM image extracted from (Beuvier *et al.,* 2011)) .

The experimental steps in data acquisition and treatment via the Guinier-Porod model are described in the first part of this chapter. This is done for two samples obtained by different synthesis routes. In the second part, we explain how the porosity and the specific surface can be measured and a comparison with BET measurements is provided.

3.2. Experimental part

3.2.1. $CaCO_3$ synthesis

$CaCO_3$ powders were made by two different routes called supercritical route (SR) and normal route (NR). First, a solution containing 0.62 M NaCl (VWR international, Fontenay-sous-bois, France) and 0.62 M glycine (Sigma-Aldrich, Saint-Quentin-Fallavier, France) buffer at pH 10 was prepared. This solution is called "buffer solution". Then, calcium hydroxide $Ca(OH)_2$ (Sigma-Aldrich) is added (0.8% w/v for SR and 1.6%w/v for NR) to this buffer solution before adjustment of the pH to 10 and filtration (0.45 mm). Lastly, hyaluronic acid obtained from Streptococcus equi. (Sigma-Aldrich, Mw: 1630 kDa) is added (0.1% w/v) to behave as a template molecule directing the polymorphism of $CaCO_3$ particles.

In the normal route (NR), the calcic solution was mixed in equal quantity with the buffer solution containing 1.6%w/v of Na_2CO_3. The suspension was stirred during 5 min at 400 RPM and at ambient temperature. Suspension of $CaCO_3$ microparticles is collected and centrifuged at 2400 g for 10 min. Lastly, microparticles are washed with 50 mL of ultrapure water (Millipore, Molsheim, France), centrifuged and lyophilised (Model Lyovax GT2, Steris, Mentor, USA) to obtain a dry powder of $CaCO_3$.

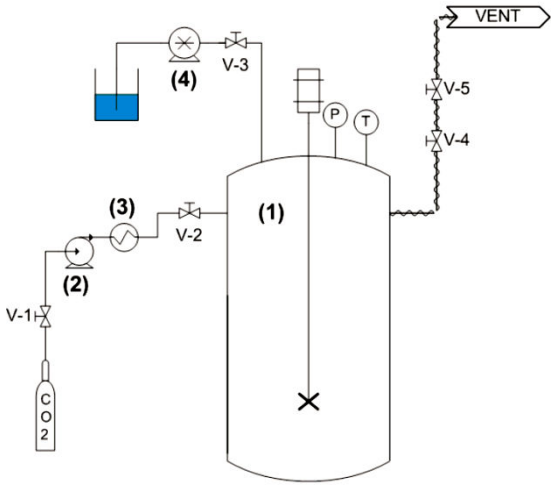

Figure 3.2.1 Scheme of the experimental setup [Beuvier2011] for the preparation of $CaCO_3$ particles in supercritical carbon dioxide.

In the supercritical route (SR) [Beuvier2011], the stainless autoclave (1) with a capacity of 500 mL (Separex, Champigneulles, France) is heated at 40.0°C and pressurized with CO_2 at 200 bars. Liquid CO_2 is pumped by a high pressure membrane pump (Milton Roy Europe, Pont Saint Pierre, France) (2) and preheated by a heat exchanger (Separex, Champigneulles, France) (3) before feeding the autoclave equipped with a stirring mechanical device (Topindustrie, Vaux le Penil, France). The axis of the magnetic stirrer is equipped with an anchor stirrer and the stirring speed is 1200 rpm. Once, the equilibrium is reached (temperature and pressure constant), 25 mL of aqueous solution previously prepared are injected by means of an HPLC pump (Model 307, Gilson, Villiers le bel, France) (4). Injection flow is fixed to 10 mL min^{-1}. Once addition is achieved, the final pressure is 240 bars and stirring is maintained at 1200 rpm for 5 min. Thereafter, stirring is stopped and the autoclave depressurized at a rate of 40–50 bar min^{-1}. The particles are collected in the same way as for NR.

In both cases, powder is placed in a cell closed by 2 kapton windows with a thickness of 50 µm separated by 1.5 mm. The powder is therefore not compressed in the cell.

3.2.2. Methods

SAXS and ultra-small-angle X-rays (USAXS) measurements were performed at the High Brilliance beamline (ID02) at the ESRF. For the SAXS experiments, a highly collimated monochromatic x-ray beam of wavelength λ=0.995 Å passed through the pellet and the scattered intensity was recorded by an image intensified charge coupled device (CCD) based x-ray detector (FReLoN) housed in an evacuated flight tube. The measurements were performed to detector distance of 2 m and typical acquisition time ranged from 0.1 to 0.3 s. The measured two-dimensional SAXS patterns were normalized to an absolute scale, azimuthally averaged, and background subtracted to obtain the scattered intensity I(q) as a function of scattering vector, $q=(4\pi/\lambda)\sin(\theta/2)$, where θ is the scattering angle. USAXS experiments were carried out in a Bonse-Hart (BH) configuration, which involves a multiple bounce crossed-analyzer. The set-up provides a useful q range of $10^{-3}<q<1$ nm^{-1} at 12.4 keV. The instrumental background is significantly reduced using specially fabricated analyzer crystals which allowed us to measure scattered intensities down to $q\geq0.001$ nm^{-1}. The two sets of experiments, SAXS and USAXS, were overlapped in order to obtain a complete scattering curve, from q = 0.001 to q = 1 nm^{-1}.

3.3. Morphologic study of $CaCO_3$ particles by SAXS

3.3.1. The GUINIER-POROD model

The elementary analysis of the data consisting in determining the radii of gyration and fractal dimension of the scattering objects was carried out using the Guinier-Porod model proposed by [Hammouda2010]. A more elaborated analysis in which the porosity and the specific surface area were determined, was then performed using the approach developed by [Spalla2003]. Let us first consider the Guinier-Porod Model.

It is well known since the pioneering work of A. Guinier [Guinier&Fournet1955] that at very small angles of incidence and provided that the condition $qR_g << 1$ is fulfilled, SAXS data decrease exponentially as $e^{-q^2R_g^2/3}$. This behaviour is generally limited to very small angles of incidence. The range of validity fundamentally depends on the radius of gyration of the scattering particle. Beyond the Guinier'regime, i.e. for $qR_g >>1$ (Porod'regime), a

steep decay of the scattered intensity is generally observed. This decay is found to behave as a power law of the type q^{-Df} in which D_f is the fractal dimension associated with the scattering objects. Beaucage proposed 20 years ago to combine these two limiting regimes into a unified equation. As pointed out in the introduction this way of analyzing the data is generally quite efficient but it has the drawback to yield overestimated values of the fractal dimension. This is why [Hammouda2010] an improvement of the model by imposing to the Guinier's regime to be continuous with the Porod's one. [Hammouda2010] used a model valid for only one type of radius of gyration. In the present work, as we observed in our scattering data at least two different characteristic particle sizes, it was necessary to implement the Guinier-Porod model proposed by [Hammouda2010] for this specific case. The scattered intensity is thus described by the following equations

$$\begin{aligned} I_{11} &= G_1 e^{-q^2 R_{g1}^2/3} \quad \text{for} \quad q < q_1 \\ I_{12} &= D_1/q^{D_{f1}}\, e^{-q^2 R_{g2}^2/3} \text{ for } q > q_1 \\ I_{21} &= G_2 e^{-q^2 R_{g2}^2/3} \text{ for } q < q_2 \\ I_{22} &= D_2/q^{D_{f2}} \text{ for } q > q_2 \end{aligned} \qquad [3.3.1]$$

where the Guinier and Porod terms are constrained by continuity at the positions

$$q_i = \frac{1}{R_{gi}}\sqrt{\frac{3D_{fi}}{2}} \text{ with } D_i = G_i e^{\frac{D_{fi}}{2}} \left(\frac{3D_{fi}}{2}\right)^{Dfi/2} R_{gi}^{-D_f i} \qquad [3.3.2]$$

for which i=1 or 2 according to which domain one considers.

A typical scattering curve following such a model is presented in Figure 3.3.1. It shows that the scattered intensity exhibits two plateaus of constant intensity followed by two steep decays the slope of which depends on the fractal dimension of the scattering objects. Each plateau is limited in the upward q range by a curvature of the scattering curve located at a q position defined by $\boldsymbol{q} = (\sqrt{3\boldsymbol{D}_{fi}/2})/\boldsymbol{R}_g$ where R_g is the radius of gyration of the scattering object. The linear decay observed in log-log plots which is following the curvature provides information about the fractal dimension of the scattering object. In Figure 3.3.1, the exponent was considered to be equal to 4 assuming smooth interfaces between the pores and the solid phase.

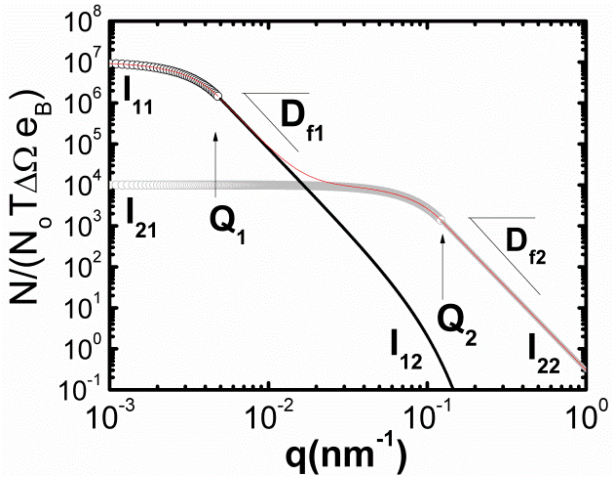

Figure 3.3.1 Typical SAXS curve calculated according to the Guinier Porod Model proposed by [Hammouda2010] for the specific case of two components. $N/(N_0T\Delta\Omega e_B)$ (cm^{-1}) versus q, where each component is characterized by a plateau followed by a steep decay having a q^{-Df} dependence.

3.3.2. Results and Discussions

As shown in Figure 3.3.2, one can clearly see that the scattering curve for both samples NR and SR are in perfect agreement with the model described in the previous section. The two samples which differ by the synthesis route exhibit very similar scattering curves showing that the porous structure of the two samples is somewhat similar. The differences are in the value of the radii of gyration of the two domains and in the fractal dimension of the scattering objects. After adjustment, we observe that the $CaCO_3$ particles are composed of objects with fractal dimension of the scattering objects close to $D_f = 4$. $D_f = 4$ indicates that the object has a smooth interface. $3 < D_f < 4$ indicates that the object has a rough surface. The size and the fractal dimension of objects are determined from a fit to the data according to Eq. 3.3.1. The fitted parameters are the radii of gyration and the fractal dimensions for each domain. By supposing that the pores have a spherical shape, the real radius of pores (R) can be deduced from the radii of gyration (R_g) by this relation (Feigin & Svergun, 1987): $\boldsymbol{R} = \sqrt{5/3}\boldsymbol{R}_g$ .We can conclude from the results that:

a) the first domain ($q < 0.02$ nm^{-1}) defines the macropores of the pellet located inside and outside the microspheres. These macropores are big objects of diameter 720 nm with $D_f = 4$ for SC and 764 nm for NR with $D_f = 3.85$. These fractal dimensions are close to 4 which is consistent with the fact that macropores have a smooth surface.

b) the second domain ($q > 0.02 nm^{-1}$) characterizes the presence of mesopores inside the microspheres. These mesopores are small objects of diameter 36 nm with a fractal dimension $D_f = 3.45$ for SR. For sample NR the diameter is bigger (72 nm) and the fractal dimension is $D_f = 3.73$. The fractal dimensions are inferior to 4 which highlights that mesopores have a rough surface.(see Table 3.3.1)

It is important to notice that it was possible to access this information only because SAXS and USAXS experiments were carried out. Indeed it is impossible to probe a radius of gyration of 280 nm by conventional SAXS experiments.

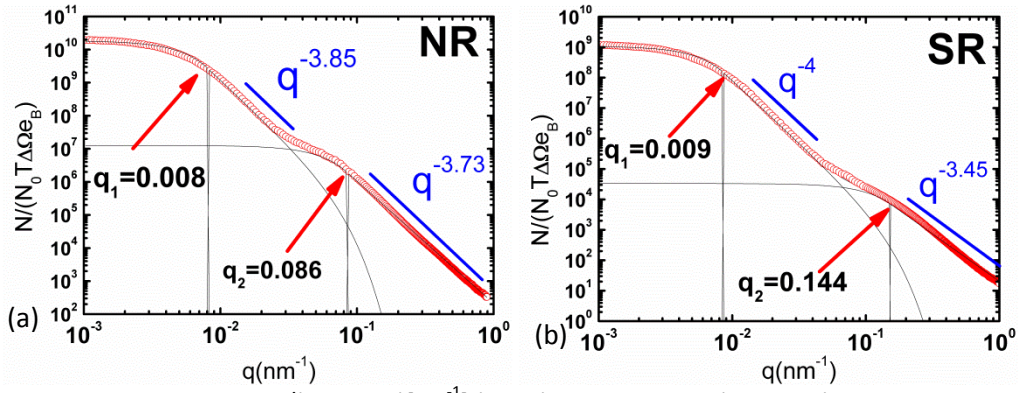

Figure 3.3.2 Experimental $N/(N_0T\Delta\Omega e_B)[cm^{-1}]$ (circle) and calculated (solid line) SAXS curve with Guinier- model of $CaCO_3$ particles synthesised by the a) normal chemical route and by b) the supercritical route.

Sample	**Guinier Radius (R_{g1})[nm]**	**Fractal dimension (D_{f1})**	**Guinier Radius (R_{g2})[nm]**	**Fractal dimension (D_{f2})**
Normal Route	**764**	**3.85**	**72**	**3.73**
Supercritical Route	**720**	**4**	**36**	**3.45**

Table 3.3.1 Guinier Radius and Fractal Dimension calculated using the Guinier-Porod model.

3.4. Application of SAXS in evaluation of porosity and surface area of $CaCO_3$

In this type of sample, it is easy to understand that several types of hierachical porosities exist. The first one is the macroporosity of the core (intragrain) together with the porosity existing between the grains of powder (intergrain). The second one is the mesoporosity

observed inside a macroparticle of vaterite (intragrain). Such porosities can be accessed by SAXS. As seen in Figure 3.3.2, SAXS curves exhibit a typical shape that can be divided into two parts. The first part of the scattering curve (at small q) is due to the macropores inside and outside the microspheres while the second one is related to the contrast of electron density between the mesopores contained in the inner structure of the microspheres. We now address how we have defined the porosity and how it can be accessed by the analysis of SAXS curves.

3.4.1. Determination of the Porosity

In a first step, the total volume of the pellet (V_{Pellet}) is considered as the sum of the volumes occupied by the different phases: the macropores, the mesopores and the solid phase of vaterite,

$$\boldsymbol{V}_{Pellet} = \boldsymbol{V}_{Macro} + \boldsymbol{V}_{Meso} + \boldsymbol{V}_{solid} \qquad [3.4.1]$$

The total porosity of pellet (Φ_P) is thus given,

$$\Phi_P = \frac{\boldsymbol{V}_{Macro} + \boldsymbol{V}_{Meso}}{\boldsymbol{V}_{Pellet}} \qquad [3.4.2]$$

Thus the system can therefore be considered as consisting of two phases: a solid phase constituted of crystalline vaterite and a porous phase composed of mesopores (located inside the shell of the particles) and macropores either found in the core of the particles or between the particles.

For a system made of two phases, it can be shown that Porod's invariant, Q, is directly related to the porosity. , the value of Q is calculated using the scattered intensity measured in absolute units [cm^{-1}].

$$\boldsymbol{Q} = \int_0^\infty \boldsymbol{I}_{ABS}(\boldsymbol{q})\boldsymbol{q}^2 d\boldsymbol{q} = 2\pi^2 \Phi_P (1-\Phi_P) \boldsymbol{r}_e^2 (\Delta\rho)^2 \qquad [3.4.3]$$

where $\boldsymbol{I}_{ABS}(\boldsymbol{q}) = \boldsymbol{N} / (\boldsymbol{N}_0 \boldsymbol{T} \boldsymbol{e}_p \Delta\Omega)$ is the absolute intensity, N is the number of photons collected per seconds in the detector, N_0 the number of photons in the direct beam , e_p is

the thickness of the pellet, ΔΩ is the size of a pixel seen from the sample, T is the transmission coefficient. Φ_P is the total porosity of the pellet and (1- Φ_P) is therefore the volume fraction of solid inside the pellet (Figure 3.5.1a).

Since the invariant is calculated from q=0 to ∞, it is important to understand that the total porosity Φ_P is not accessible. As measurements are limited to the range q=0.001nm^{-1} to q=1nm^{-1}, equation 3..4.3 gives access only to pores that are in a range inverse to the accessible q range. For the analysis, powder is therefore arranged in a double layer conformation (see, Figure 3.5.1a and 3.5.1b): one layer contains the material and the pores visible to x-rays (named 'layer visible to x-rays') of thickness 'e_V' and volume 'V_V' and the other with a thickness '$e_P - e_V$' contains only the non visible pores to x-rays.

Thus, we can express the porosity of the 'layer visible to x-rays' as

$$\varphi^v = \frac{V_{\mathrm{Macro(s<2\mu m)}} + V_{Meso}}{V_V} \qquad [3.4.4]$$

As a result the total porosity is given by

$$1 - \Phi_P = \frac{V_V}{V_{Pellet}}(1 - \varphi^v) \qquad [3.4.5]$$

In the expression of the invariant, the scattering which is not taken in account is the one in the range q< 0.001nm^{-1} which corresponds to the non visible porosity. It follows that the intensity of the 'layer visible to x-rays' is equal to

$$\frac{I_{\mathrm{V}}}{I_{ABS}} = \frac{e_P}{e_V} = \frac{1-\varphi^v}{1-\Phi_P} \qquad [3.4.6]$$

Equation (3.4.3) is directly applicable to the 'layer visible to x-rays' by replacing the limits of integration by the accessible limits of the experiment and the porosity by the visible porosity φ^v. This yields a specific invariant denoted Q_V and defined as:

$$Q_V = \int_{0.001nm^{-1}}^{1nm^{-1}} I_{\mathrm{V}}(q) q^2 dq = 2\pi^2 \varphi^v \left(1-\varphi^v\right) r_e^2 \left(\Delta\rho\right)^2 \qquad [3.4.7]$$

where $I_{\mathrm{V}}(q) = N/(N_0 T e_V \Delta\Omega)$

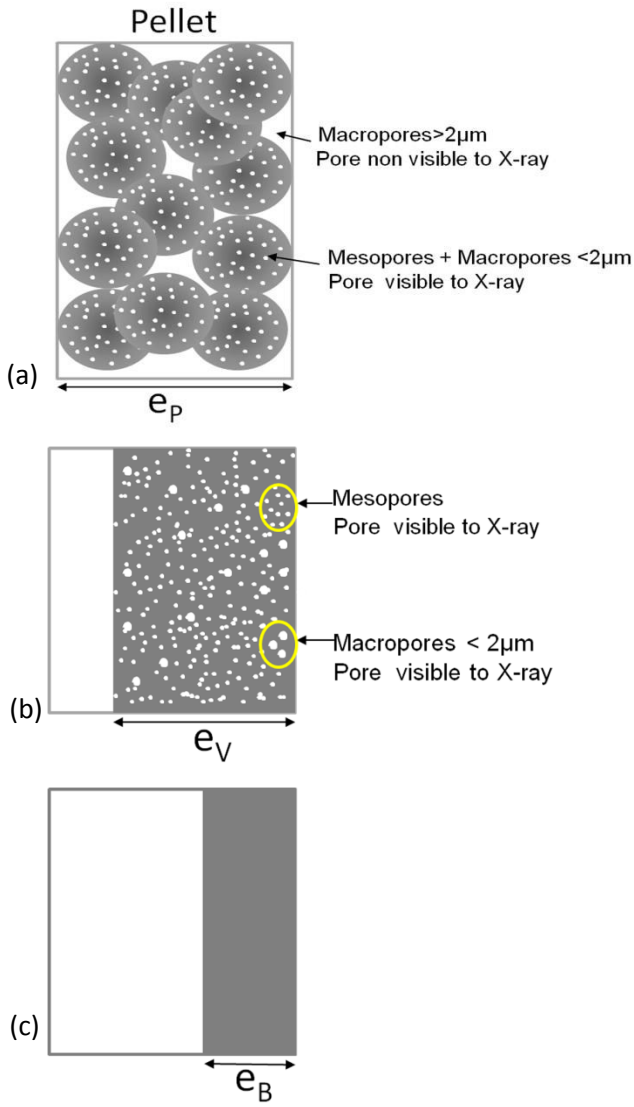

Figure 3.5.1 (a) Representative picture of the pellet 'granular layer' with a thickness 'e_P' (b) visible layer to X-rays with a thickness 'e_V' and (c) solid inside the pellet with an effective thickness 'e_B' obtained from the transmission coefficient T.

As shown by Spalla *et al.,* (2003) the major problem in a pulverulent material is that e_P and e_V are not known. Nevertheless, an effective thickness e_B can be obtained from the transmission coefficient T (see Figure 3.5.1c),

$$e_B = -\frac{\ln T}{\mu_{solid}} \qquad [3.4.8]$$

if the absorption of the solid is known. Considering that the pellet has a cylindrical shape with a thickness e_P, it is possible to connect the two thicknesses, e_P and e_B , from the following relation,

$$(1-\Phi_P) = \frac{e_B}{e_P} \qquad [3.4.9]$$

Following the work by (Spalla *et al.,* 2003) and the Eq. 3.4.6 and 3.4.9 we define the intensity of the 'visible layer to the X-rays' in terms of the effective thickness (e_B) and porosity (φ^v) as follows:

$$I_V(q) = \frac{N}{N_0 T \Delta\Omega e_B}(1-\varphi^v) \qquad [3.4.10]$$

Then replacing Eq. 3.4.10 in Eq. 3.4.7, we obtain an expression in terms of measurable and know parameters,

$$\int_{0.001nm^{-1}}^{1nm^{-1}} \frac{N}{N_0 T \Delta\Omega e_B}(1-\varphi^v) q^2 dq = 2\pi^2 \varphi^v \left(1-\varphi^v\right) r_e^2 (\Delta\rho)^2 \qquad [3.4.11]$$

so that the porosity can be derived as

$$\varphi^v = \frac{1}{2\pi r_e^2 (\Delta\rho)^2} \int_{0.001nm^{-1}}^{1nm^{-1}} \frac{N}{N_0 T \Delta\Omega e_B} q^2 dq = \frac{1}{2\pi r_e^2 (\Delta\rho)^2} Q_B \qquad [3.4.12]$$

The new invariant Q_B shown in Eq. 3.4.12 allows direct calculation of the visible porosity to x-rays 'φ^v' of the pellet. Figure 3.5.2a shows how the quantity $Nq^2 / N_0 T \Delta\Omega e_B$ evolves as a function of q. It can be seen in such a plot that the two types of porosities give rise to two broad humps separated by a minimum. The calculation of the area between each hump and the q axis provides information about the macroporosity (<2µm) and the mesoporosity with the possibility to discriminate between each component.

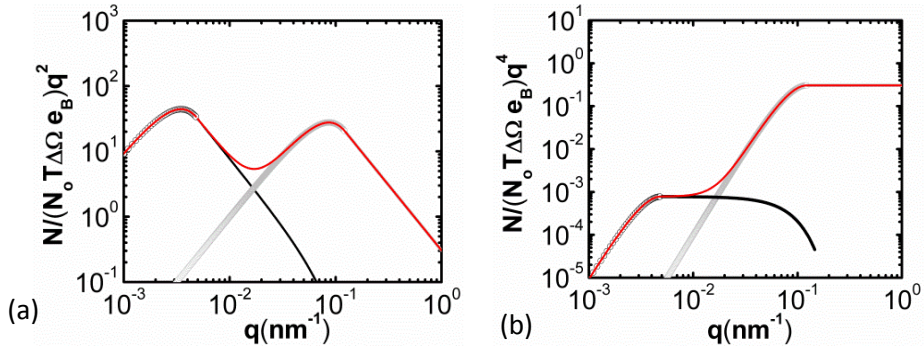

Figure 3.5.2 (a) $N/(N_0T\Delta\Omega e_B)q^2$ (cm^{-3}) versus q. (b) Porod representation $N/(N_0T\Delta\Omega e_B)q^4$ (cm^{-5}) versus q.

3.4.2. Determination of the specific area

We now address how one can calculate the specific area associated with the macro and mesopores found in the porous particles of vaterite. For this it is important to notice that the specific area can be calculated from the limit of the scattered intensity at high q values. For both components, the specific area can be written as

$$S_{Macropores} = \frac{1}{(1-\Phi_P)} \frac{[I_{ABS} q^4]_{[1]}}{2\pi\Delta\rho_e^{\,2} r_e^2} = \frac{1}{2\pi\Delta\rho_e^{\,2} r_e^2} \left[\frac{N}{N_O T \Delta\Omega e_B} q^4 \right]_{[1]} \qquad [3.4.13]$$

$$S_{Mesopores} + S_{Macropores} = \frac{1}{(1-\Phi_P)} \frac{[I_{ABS} q^4]_{[2]}}{2\pi\Delta\rho_e^{\,2} r_e^2} = \frac{1}{2\pi\Delta\rho_e^{\,2} r_e^2} \left[\frac{N}{N_O T \Delta\Omega e_B} q^4 \right]_{[2]} \qquad [3.4.14]$$

It is clear that if the scattered intensity decays as a power law with a fractal exponent equal to 4, the plot of Iq^4 versus q will produce a straight line parallel to the q axis at high values of q. Such behaviour is shown in Figure 3.5.2b where one can see that two lines run parallel to the q axis. The lowest one is due to the surface area of the macropores (such as for instance the hollow core) while the upper one is related to both the macropores and mesopores. As the macropores contribution is known it is possible to separate the contributions of the macroscospic and mesoscopic objects.

In addition one can also foresee that the straight line parallel to the q axis will deviate from this behaviour if the fractal dimension of the object differs from 4. For objects having smaller values of D_f than 4, this plot will produce lines at high q having a positive slope.

3.4.3. Results and Discussions

The effective thickness e_B of the sample was calculated using Eq. 3.4.8 with the transmission coefficients (T) at 12.4 keV shown in Table 3.5.1. Taking Eq. 3.4.8 and 3.4.9 with $\overline{e_P}$ = 1.5 mm (see experimental section), the estimated total porosity is 90 and 95% for NR and SR respectively (these values are important due to fact that pellet are not pressed). The electron density of vaterite was calculated from the hexagonal structure of vaterite and was found to be equal to 810 e^-/nm^3. The mass density of vaterite was taken to be 2.66 g/cm^3 as expected from its crystalline structure which was checked by complementary wide angle x-ray scattering measurements. With all these information it was possible to calculate (1) the invariant $Q_B = \int N/(N_0 T \Delta\Omega e_B) q^2 dq$ using the TRAPZ function in Matlab which is a built in function for numerical integration and (2) the porosity. The interval of integration in q space was chosen to range from 10^{-3} nm^{-1} to $1nm^1$. Since the integration is truncated to experimental boundaries, the determination of Q_B is underestimated. At low q, a correction can be applied by assuming that the intensity is constant. At high q, the correction can be estimated by assuming that the Porod behaviour $I(q) \approx q^{-Df}$ is still valid. With such assumptions, we can estimate that Q_B is reduced by about 1% at low-q, while at high-q the underestimation is about 20% of the value corresponding to the mesopores. The results of porosity are shown in Table 3.5.1.

The porosities calculated by the Porod invariant are φ^v = 42% for SR and φ^v = 46% for the NR. It can be seen on the plots shown in Figures 3.5.3a and 3.5.3b that the two curves are quite similar in the low q region while they significantly differ at large q values. The discrimination between macro and mesoporosities is possible from the fits to the data. Each component can be calculated by replacing in Q_B the scattered intensity by $I_1(q)$ and $I_2(q)$. The results for the meso and macro porosities are shown in Table 3.5.1. It can be seen that the mesoporosity is much smaller for the supercritical route (φ^v_{Meso} =12%) than for the normal route (φ^v_{meso}=22%). Note that if we take into account the correction of Q_B at high q , the mesoporosity would be for the normal route φ^v_{meso}≈26% and for the supercritical route φ^v_{Meso} ≈14%. On the other hand, the macroporosities are similar for both samples with a somewhat higher value for the SR route $\varphi^v_{macro,SR}$=30% > $\varphi^v_{macro,NR}$ =24%. This could be the consequence of the presence of the hollow core inside the samples prepared by the SR route or of the free space between the microspheres.

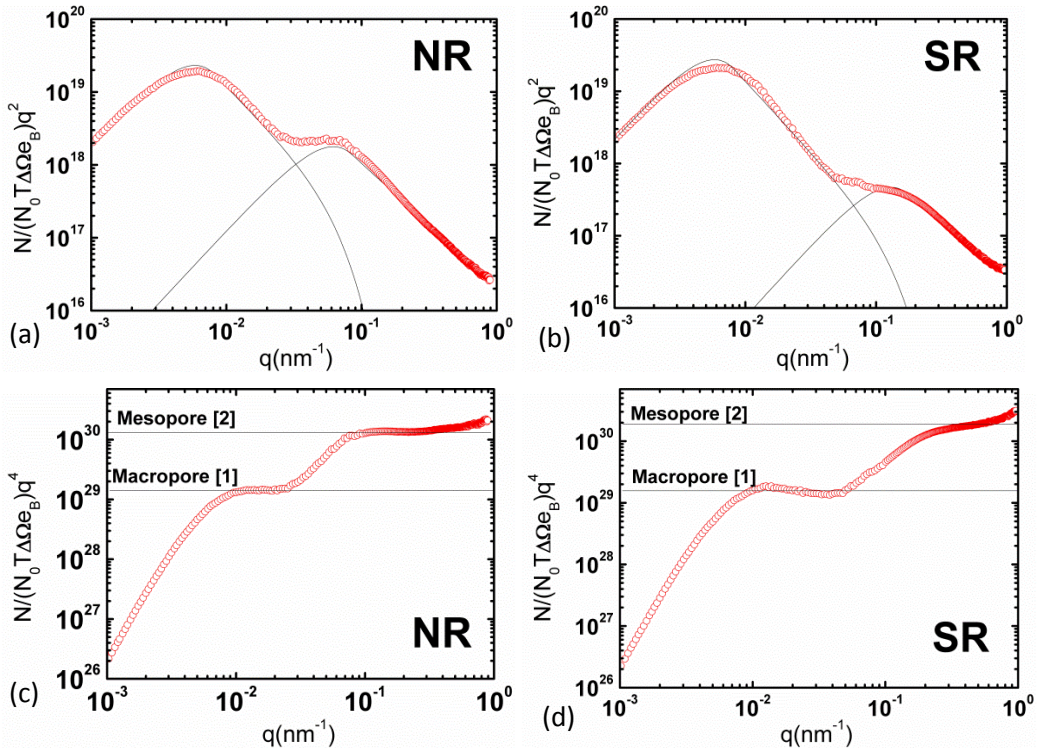

Figure 3.5.3 $N/(N_0T\Delta\Omega e_B)q^2[cm^{-3}]$ vs q for the calculation of the invariant are shown in panels (a and b). Porod representation $N/(N_0T\Delta\Omega e_B)q^4[cm^{-5}]$ vs q of the intensity of $CaCO_3$ particles by the normal chemical route (a and b) and by the supercritical route (c and d))

Sample	T	φ^v (%)	φ^v_{MACRO} (%)	φ^v_{MESO} (%)	S_{MACRO} [m^2/g]	S_{MESO} [m^2/g]
Normal Route	**0.42**	**46**	**24**	**22**	**1.65**	**16**
Supercritical Route	**0.64**	**42**	**30**	**12**	**1.83**	**21**

Table 3.5.1 Calculation of the porosity and surface area of $CaCO_3$ particles from SAXS-USAXS curves (q = 0.001 to 1 nm^{-1}) using the Porod invariant and Porod plots**.**

Figures 3.5.3c and 3.5.3d show the plot of Iq^4 versus q. As explain in the theoretical section, the two straight lines parallel to the q axis correspond to the specific surface area arising from the macropores (First plateau) and the mesopores (Second plateau). The results for the specific surface area 'S' are shown in Table 3.5.1. These values are calculated from Eq. 3.4.13 and 3.4.14. The surface area of macropores is small and quite similar for the two samples (S_{Macro} = 1.65m^2/g for NR, S_{Macro} = 1.83m^2/g for SR). The slightly higher value for SR may originate from the hollow core. The surface area of mesopores is

much more important (S_{Meso} = 16m^2/g for NR and S_{Meso} = 21m^2/g for SR) with a higher value for SR mainly because of its smaller radius of gyration (R_g=14 nm for SR and R_g=28nm for NR) and rougher surface (D_f = 3.45 for SR and 3.73 for NR).

To compare these results, powder were analyzed by N_2 absorption-desorption at 77K. BJH and BET methods were used to extract the mesoporosity and the specific surface area respectively (Figure 3.5.4). This technique was already used on $CaCO_3$ vaterite. Several BET values were reported (S_{BET} = 2m²/g [Fujiwara2010], S_{BET}=8.8m²/g [Volodkin2004], S_{BET}=15.3 m²/g [Yu2006] S_{BET} = 77m²/g [Peng2010], S_{BET}=90m²/g [Cai2008]). However, only few BJH porosity are reported. For example, [Yu2006] obtained a mesoporosity of 16% on small hollow microspheres. Note that the analysis is restricted to pore diameters ranging between 2 nm and 200 nm which in this case allow access only to mesoporosity. The results for SR and NR are shown in Table 3.5.2. BET surface areas are 14 m²/g for NR (against 16 m^2/g by SAXS analysis) and 16m²/g for SR (against 21 m²/g by SAXS analysis). The BJH porosity obtained in desorption are 19% for NR (against 22% by SAXS) and 10% for SR (against 12% by SAXS). The agreement between these values is also quite fair and confirms that SAXS-USAXS is a convenient technique for both the surface area and the mesoporosity determination.

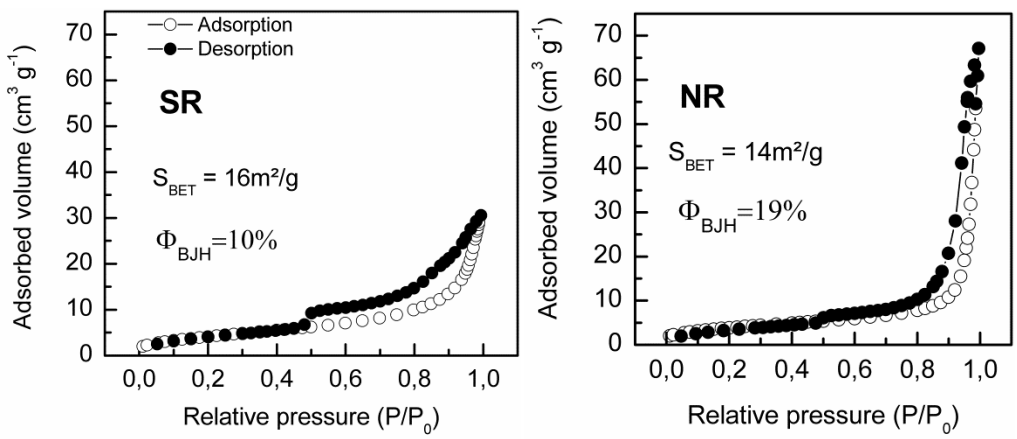

Figure 3.5.4 Nitrogen adsorption-desorption isotherms of the $CaCO_3$ a) SR, b) NR.

Sample	S_{MESO} [m^2/g] (X-rays)	S [m^2/g] (BET)	$\varphi^v_{MESOPORE}$(%) (X-rays)	φ (%) (BJH)
Normal Route	16	14	22	19
Supercritical Route	21	16	12	10

Table 3.5.2 Comparison of porosity and surface area obtained by two methods: (BJH in desorption, BET) and SAXS-USAXS (q = 0.001 to 1 nm^{-1}).

Our results shows that x-ray scattering measured by USAXS provide additional information about macroporosity which is not accessible by BJH. The large value of the macroporosity (24% for NR and 30% for SR) is interesting for drug encapsulation. However, we need to discriminate the proportion of macropores inside and the one outside the microspheres. Complementary investigations are presently carried out on $CaCO_3$ pellets in order to see the evolution of the porosities with the pressure.

3.5. Study of $CaCO_3$ particles by Coherent Diffraction Imaging

3.5.1. Introduction

The aim of this section is to study by coherent scattering hollow spheres of vaterite to evidence the inner structure of these beads and their porosity. As shown in the previous section, the hollow core is about 0.7 µm in diameter on the average and the shell is also porous with pores which are the mesoscopic scale in size (see Table 3.3.1). Such beads are of great interest as a host matrix for proteins [Hassani2013]. Hassani et al. shown using fluorescence spectroscopy that proteins can be imbedded in such porous mineral structures [Hassani2013]. For that reason, one of our objectives was to image coherently such beads with and without the proteins to verify if the proteins can be located inside the hollow core of the particle. We present the results obtained for $CaCO_3$ particles (without proteins) synthetized using the supercritical route and the normal route. However, particles with proteins are > 6 µm in diameter (above the limit size) which make difficult to obtain a good resolution in the speckles and be able to reconstruct the real image.

3.5.2. Sample preparation and details of reconstruction

Particles were deposited on a 100 nm-thick Si_3N_4 membrane. The membrane on which the spherical particles were deposited after immersion in ethanol was then mounted on the diffractometer of the CDI ID10 beam line for sequential imaging via the rotation of the membrane. To get a full image of an object in 3D, a series of patterns were collected at different tilts every 1-2° over ±80°. These 2D patterns were them assembled into a 3D diffraction pattern on which the iterative phase retrieval algorithm was applied using 3D Fast Fourier transform.

For this experiment, we selected a 2µm-sized particle. The CXDI experiment was performed on the ID10-CS Beamline at ESRF. 7 keV radiation was selected (λ=1.76Å). The scattering pattern was recorded on a MAXIPIX 2x2 detector with 516 x 516 pixels and a pixel size of 55µm, placed 5 m downstream from the sample position. Diffraction images from $CaCO_3$ particle made by normal (Fig.3.5.1a) and supercritical route (Fig.3.5.1b) was recorded for 60 seconds.

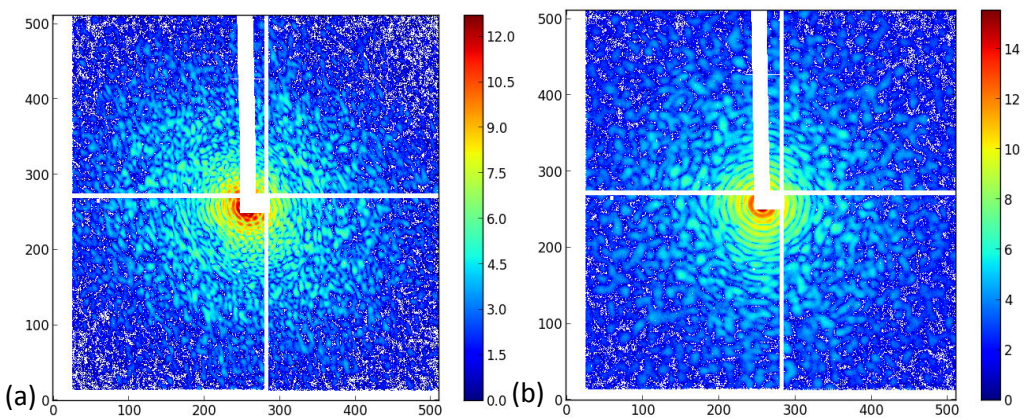

Figure3.5.1 Diffraction pattern of a) $CaCO_3$ particle made by Normal route (NR) and b) Supercritical route (SR).

When performing a FFT of a scattering pattern, one must keep in mind that the FFT has the same dimension as the initial pattern. So if for clarity we work in one dimension with N_{pix}=516 pixels in the scattering pattern, there will be also N_{pix}=516 pixels in the real space image obtained by FFT. If we assume that 'p' is the pixel size on the detector and that the detector is located at a distance'd' from the sample, the resolution in q space in the scattering pattern will be given as

$$\Delta \boldsymbol{q} = \frac{4\pi\Delta\theta}{\lambda} = \frac{2\pi \boldsymbol{p}}{\lambda \boldsymbol{d}} \qquad [3.4.15]$$

The maximum value that can be reached in q space is thus given by

$$\boldsymbol{q}_{\max} = \frac{2\pi \boldsymbol{N}_{pix} \boldsymbol{p}}{\lambda \boldsymbol{d}} \qquad [3.4.16]$$

As a result the resolution in real space image is defined by r= $d\lambda/pN_{pix}$ where 'd' is the sample-to-detector distance, λ the wavelength of the radiation, p the detector pixel size and N_{pix} is the number of pixels in the detector. This gives us a resolution of about 30 nm with a maximum value in direct space given by dλ/p =15µm.

3.5.3. Results and Discussions

We show in Figure 3.5.2 the results obtained after Fourier inversion of the scattering data and phase retrieval via an algorithm provided by Y. Chushkin. The Fourier inversion of the data with the correct phase provides directly the 3D image of the particle. The data are contained in a 3D matrix of points in which each point of the particle is defined by its coordinates (x,y,z) and some intensity proportional to the density of the particle at this point. Using a Matlab program it is then possible to plot in 3D the image of the inner and outer parts of the particle. In some cases we were even able to locate the position of the particle on the membrane and to perform SEM measurements on the same particle studied by CDI. This is of great interest when one wants to test the validity of the data inversion. Note that with the accessible q range of measurements by CDI and with the pixel size we had, we were able to get a reconstructed image with a resolution of 30nm in CDI which is less than the SEM resolution. Nevertheless the great advantage of CDI is that it is possible to see the inner part of the particle.

A better resolution could be easily achieved in the CDI image if a larger detector was available. Indeed the resolution is inversely proportional to the number of pixels in the detector and to the distance between the sample and the detector. To increase the resolution one should act on these two parameters or alternatively reduce the pixel size of the detector.

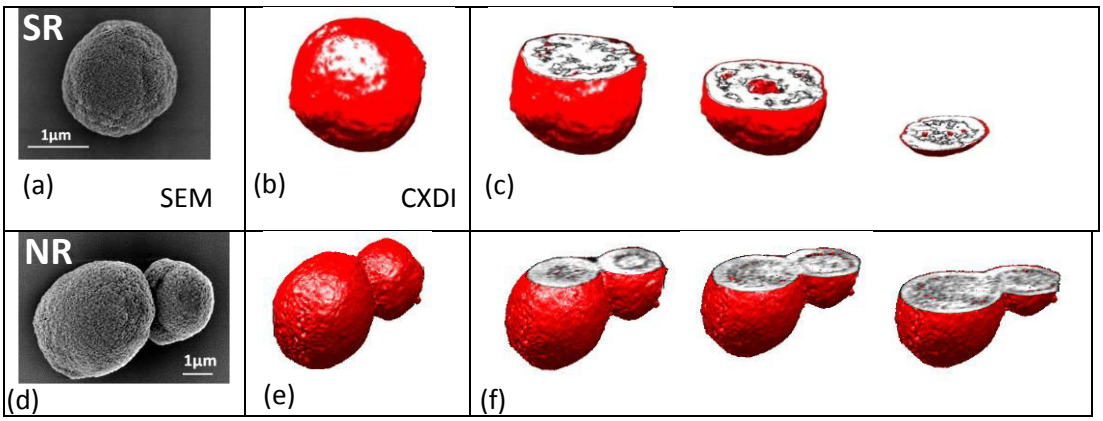

Figure 3.5.2 a) SEM image b) reconstructed 3D image and c) Cross-section of $CaCO_3$ particle made by supercritical route (diameter = 1.9µm) d) ,e) and f) $CaCO_3$ particles made by normal route (diameter=3.2µm).

Figure 3.5.2 shows the comparison of the SEM picture of the sample used with the reconstructed image. The agreement between both images is striking. The internal structure of the particle can be observed in the cross section of the reconstructed image (see Figure 3.5.2 c) and f)) where high and low density region confirm the porosity of the particles.

As shown in Figures 3.5.2c) and f), the particle made by the supercritical route (SR) and by the normal route have an average diameter of 2µm. These figures show that particles have an important mesoporosity, in addition we can observe that particles made by supercritical route have a hollow core, while particles made by the NR do not have this hollow core. We have to notice that $CaCO_3$ particles (SR) analysed by USAXS and SAXS were bigger than particles analysed by CXDI. This proves that regardless of the particle size of $CaCO_3$ powders made by SR these particles possess a hollow core, which is important for applications in drug delivery.

3.6. Conclusion

We have shown in this chapter that microspheres of vaterite exhibit hierarchical porosity made of macropores and mesopores. The quantitative determination of the pore size and of the pore smoothness was achieved by implementing the Guinier Porod model recently proposed by [Hammouda2010] for two types of pores. The radii of gyration of the two components and their fractal dimension were obtained. It was found that macropores

have fractal dimension close to 4 indicating smooth surfaces whereas mesopores located inside the microspheres have smaller fractal dimension which highlights a rough surface. In both cases radii of gyration are of the order of 280 nm for the macropores and about 20 times smaller for the mesopores. The porosity and the surface area was furthermore determined following the approach of [Spalla2003] for powders by calculating a Porod invariant based on the effective thickness of the pulverulent pellet. The specific surface and the mesoporosity are much closed to the results extracted from the N_2 adsorption-desorption analysis. This analysis was recently complemented by CDI experiments at the ID10A beam line of the ESRF. We were able to reconstruct in 3D the complete shape of these particles and to evidence their inner geometry by 3D tomography.

Bibliography

[Beaucage1994] Beaucage, G.; Schaefer, D. W.. J. of Non-Cryst. Solids, (1994) 172-174,797-805.

[Beaucage2007] Sztucki, M.; Narayanan, T.; Beaucage, G., Journal of Applied Physics, (2007) 101, 114304.

[Beuvier2011] Beuvier, T.; Calvignac, B.; Delcroix, J.R.; Tram, M. K.; Kodjikian, S.; Delorme, N. **;** Bardeau, J.F.; Gibaud A. ; Boury F. J. Mater. Chem. (2011) 21, 9757-9761.

[Cho2008] Cai, A.; Xu, X.; Pan, H.; Tao, J.; Liu, R.; Tang, R.; Cho, K. J. Phys. Chem. (2008) 112, 11324–11330.

[Feigin&Svergun1987] Feigin L. A; Svergun D. I. Structure Analysis by Small-Angle X-Ray and Neutron Scattering, edited by George W. Taylor Plenun Press. New York and London, 1987.

[Fujiwara2008] Fujiwara, M.; Shiokawa, K.; Morigaki, K.; Zhu, Y.; Nakahara, Y., Chem. Eng. J., (2008) 137, 14–22.

[Fujiwara2010] Fujiwara, M.; Shiokawa, K.; Araki, M.; Ashitaka, N.; Morigaki, K.; Kubota, T.; Nakahara Y. Crystal Growth Design (2010) 10 (9), 4030-4037.

[Gibaud1996] Gibaud, A.; Xue J.S.; Dahn, J. R. Carbon, (1996) 34, 499.

[Glatter&Kratiky1982] Glatter,O.; Kratiky, O. Small Angle x-ray scattering, Academic Press London, 1982.

[Guinier&Fournet1955] Guinier, A. ; Fournet, G. Small Angle sacttering of x-rays, Wiley, 1955.

[Kalliat1981] Kalliat, M.; Kwak, C. Y.; Schmidt P. W. in "New Approaches in Coal Chemisty" (B. D. Blaustein; B. C. Bockrath,; S. Friedman, Eds.), (1981). Am.Chem. Soc. Symp. Ser. 169, p.3. Am. Chem. Soc., Washington, DC.

[Hammouda2010] Hammouda, B. J. Appl. Cryst. (2010) 43, 716-719.

[Hassani2013] Hassani, L.; Hindré, F.; Beuvier, T.; Calvignac, B.; Lautram, N.; Gibaud, A.; Boury, F., J. Mater. Chem. B, (2013) 1, 4011.

[He2009] He, X. W.; Liu, T.; Xiao, Y.; Feng, Y. L.; Cheng, D. J.; Tingting, G.; Zhang, L.; Zhang, Y.; Chen, Y. X., Cancer Biother.Radiopharm. (2009) 24, 249–259.

[Ikoma2007] Ikoma, T.; Tonegawa, T., Watanaba, H.; Chen, G.; Tanaka J.; Mizushima, Y.; J. Nanosci. Nanotechnol., (2007) 7, 822–827.

[Lucas-Girot2005] Lucas-Girot, A.; Verdier, M.C.; Tribut, O.; Sangleboeuf, J. C.; Allain; H.; Oudadesse, H., J. Biomed. Mater. Res., Part B, (2005) 73, 164–170.

[Peng2010] Peng, C.; Zhao, Q.; Gao, C. Colloids Surf. A, (2010) 353, 132– 139.

[Radlinski2004] Radlinski, A.P.; Mastalerz, M.; Hinde, A.L.; Hainbuchner, M.; Rauch, H.; Baron, M.; Lin, J.S.; Fan, L. ; Thiyagarajan, P., International Journal of Coal Geology. (2004) 59, 245– 271.

[Schmidt1982] Schmidt, P.W. J. Appl. Cryst. (1982), 15, 567–569.

[Spalla2003] Spalla, O.; Lyonnard, S.; Testard, F. J. Appl. Cryst. (2003) 36, 338-347.

[Temmerman2011] De Temmerman, M.L. ; Demeester, J. ; De Vos, F. ; De Smedt S. C., Biomacromolecules (2011) 12, 1283–1289.

[Volodkin2004] Volodkin, D.; Larionova, N. I.; Sukhorukov, G. B.; Biomacromolecules, (2004) 5, 1962-1972.

[Wie 2008] Wei, W.; Ma, G.H.; Hu, G.; Yu, D.; Mcleish, T.; Su, Z.G.; Shen, Z.Y. J. Am. Chem. Soc. (2008) 130, 15808–15810.

[Yu2006] Yu, J.; Guo, H.; Davis, S. A.; Mann, S. Adv. Funct. Mater. (2006) 16, 2035–2041.

[Zhao2010] Zhao, Y.; Lu, Y.; Hu, Y.; Li, J.P.; Dong, L.; Lin, L.N.; Yu, S.H.; Small, (2010) 6, 2436–2442.

[Zhao2012] Zhao, D.; Zhuo, R.X.; Cheng, S.X. Mol. BioSyst. (2012) 8, 753–759.

CHAPTER 4

4. Study of Polystyrene Ultra thin films exposed to supercritical CO_2

This chapter is mainly devoted to the study of polystyrene ultra thin films exposed to CO_2 under pressure. Before discussing the effect of pressure, it is important to highlight that PS may dewet the HF-treated surface of a silicon substrate depending on the thickness of the film which is initially formed. For very thin films, one can observe that films dewet the surface yielding the formation of islands with a given shape and a certain degree of correlation. After some generalities about polystyrene which is the polymer used in this study, the first part of this chapter will be devoted to a discussion concerning the reasons for which a thin film may dewet the surface of silicon in the framework of the effective interfacial potential. In the remaining part, we study the influence of CO_2 pressure on homogeneous films and islands focusing mainly on the swelling of PS and on the effect of pressure on the islands stability.

4.1. Generalities about Polystyrene

4.1.1. Molecule

Polystyrene is an inexpensive, hard plastic and one of the most common polymers in our everyday life. Polystyrene is a vinyl polymer. Structurally, it has a long hydrocarbon chain, with phenyl groups attached to one carbon atom. Polystyrene is produced by free radical vinyl polymerization from styrene.

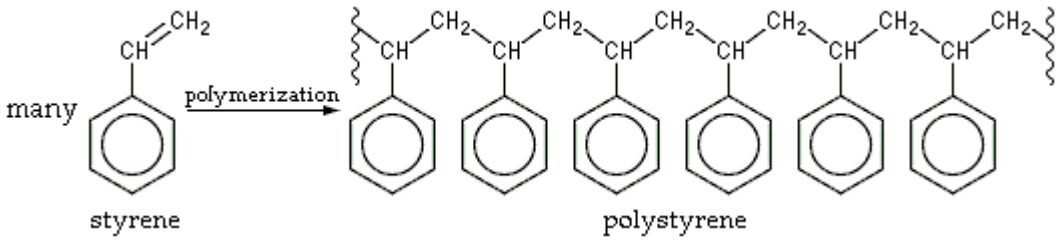

Figure 4.1.1 Schematic representation of an isotactic polystyrene.

Polystyrene exits under three different forms:

- the isotactic form, where the phenyl groups are on the same side of polymer chain, this form of polystyrene is not produced commercially (see Figure 4.1.1).
- the syndiotactic form, where the phenyl groups are positioned on alternating sides of the polymer chain. It is highly crystalline and melts at 270°C.
- the 'normal' or atactic form in which there is no order with regard to the side of the chain on which the phenyl groups are attached. This last form is amorphous and is the most commercialized one.

Polystyrene used in this study is atactic and was provided by "Polymer Source Inc". Its molar mass and polydispersity index 'PDI' are presented in Table 4.1.1:

M_w(g/mol)	136500
M_n(g/mol)	130000
PDI=M_w/M_n	1.05

Table: 4.1.1 Molar masse and polysdispersity index of the polystyrene used.

M_w is the weight average molar mass while M_n is the number average molar mass. One of the key parameters that is important in this study is the radius of gyration of the polymer. This quantity gives an estimation of the size of the polymer folded chains formed by the

polymer. It is defined by the root mean square distance from the centre of mass to any points in the polymer coil. For atactic polystyrene, the unperturbed radius of gyration is given by R_G=0.0272 $M_W^{1/2}$ where M_W is expressed in g/mol and R_G in nm. With the polystyrene used in this study, we obtain $R_G \approx$ 10.04nm [Israelachvili2011].

4.1.2. Glass Transition and Free volume

In polymers, the ***glass transition*** describes the change from a glassy state to a rubbery state. This change is defined by the glass transition temperature T_g. Despite a huge amount of studies devoted to the characterization of the physical properties through the glass transition of polymers samples both in bulk and in thin films, a detailed understanding of the glass transition in thin films is still a matter of continuous debate and research. For a discussion of the relevant issues, the reader can refer to the papers of [Donth2001, Angell2000].

Of particular interest to describe the glass transition and in a more general point of view to explain the evolution of physical properties with temperature are the concepts of *chain mobility* and *free volume* [Cohen1959].

When a polymer is in the liquid or rubbery state, the amount of free volume increases with temperature as a result of easier molecular motion. When temperature is decreased, the free volume contracts and eventually reaches a critical value where there is insufficient free space to allow large scale segmental motion to take place. The temperature for which this critical volume is reached is the glass transition temperature. Below Tg the free volume remains essentially constant as the temperature decreases further, since the chains are immobilized and frozen in position [Cohen1959, Dinelli2000].

The free volume of polymers is generally defined by $V_f = V - V_{occ}$ where V is the total and V_{occ} the occupied volume. The occupied volume corresponds to the van der Waals volume. This volume is dictated by the size of the atoms and their covalent bonds and is also independent of the conformation of the polymer. The free volume is defined as the difference between the specific and occupied volumes. It can be defined as the small amount of unfilled volume. Recent investigations using positron annihilation reveals that the diameter of these holes is approximately 0.5 nm [Ata2009]. The free volume is associated with inter chains and end chains free volumes. The later is represented in the diagram below).

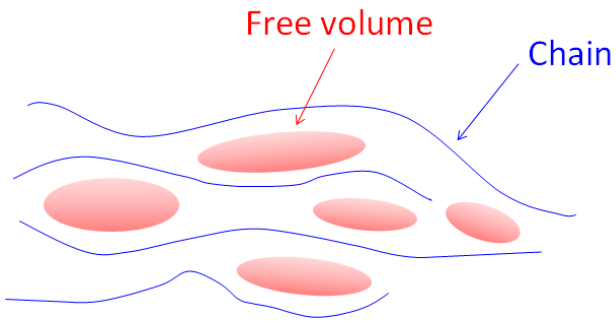

Figure 4.1.2 Representation of the free volume

According to the work of [Dublek2004] on a bulk atactic polystyrene with a molar mass of 175kg/mol, the free volume fraction can be estimated to be equal to 7.3% at ambient temperature and increases with temperature to reach ~9% at 100°C corresponding to the glass temperature (Figure 4.1.3). Let us precise that the value of the free volume in the glassy state also depends on the history of the polymer and notably on the physical aging during which V_f decreases progressively [Struik1977].

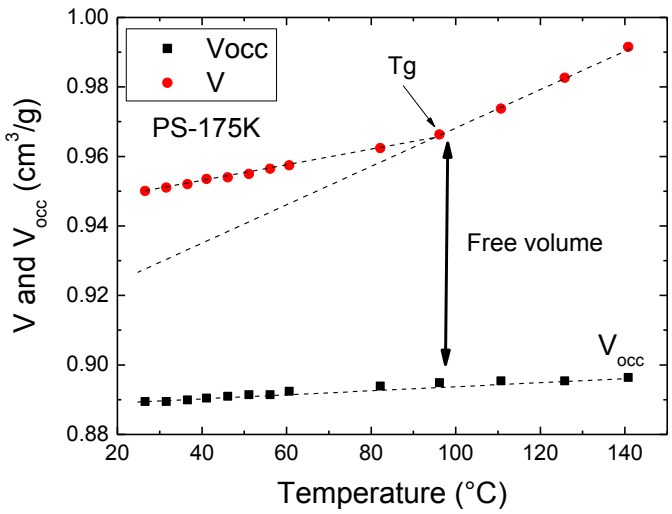

Figure 4.1.3 The specific volume 'V' (circles) and occupied volume Vocc (square) of Polystyrene as a function of the temperature. The free volume is defined as the difference between the specific and occupied volume and in the glassy state, includes the unrelaxed volume, which is defined as a gap between the specified volume and the hypothetical volume of the polymer completely relaxed.

We now consider in the next section the stability of thin films at ambient conditions with the idea to get a better understanding whether PS films may dewet or not on silicon substrates.

4.1.3. Stability of thin films and the dewetting process

4.1.3.1. Spreading coefficient

The *dewetting* process is one of the most remarquable phenomena that can occur at a solid–liquid or liquid–liquid interface. In general, dewetting describes the rupture of a thin liquid film on a substrate and the subsequent formation of droplets. A very simple example of this phenomenon is the formation of drops at the surface of leafs after raining. The opposite process is called *spreading*. Dewetting and spreading are fundamental processes in the daily life with numerous applications for instance in painting, hydrophobic coatings, oil recovery [Bertrand2002], efficient deposition of pesticides on plant leaves [Bergeron2000], but also in the drainage of water from highways [Shahidzadeh2003] and the cooling of industrial reactors. On a smaller scale, wetting solutions have been proposed to solve technological problems in microfluidics and nanoprinting, inkjet printing etc. [Tabeling2004]. As underlined by Bonn et al. wetting phenomena are a playground where chemistry, physics and engineering intersect [Bonn2009]. From a macroscopic point of view, the spontaneous spreading or dewetting for a drop placed on a solid substrate is governed by the so-called *spreading coefficient* ***S***. This parameter is defined as the difference between the energy of the dry substrate and the energy of the same substrate wetted by the liquid.

$$S = E_{DRY} - E_{WET} \qquad [4.1.3]$$

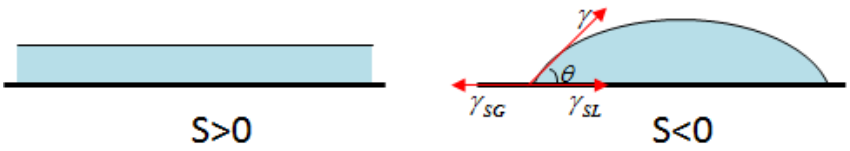

Figure 4.1.4 Two situations of spreading coefficients: S>0, total wetting situation, the liquid spreads spontaneously on the substrate and form a film. S<0 the liquid does not spread spontaneously, the triple line form an angle with the substrate.

Considering *E* as the energy per unit area we can write :

$$\boldsymbol{S} = \gamma_{SG} - \gamma_{SL} - \gamma \qquad [4.1.4]$$

with γ_{SG}, γ_{SL} and γ the solid-gas, solid-liquid and liquid-gas interfacial tensions, respectively. E_{DRY} corresponds to γ_{SG}. E_{WET} corresponds to γ_{SL} + γ. The parameter S is used to evaluate qualitatively the behavior of the liquid on the substrate.

If S is negative, the situation where the solid is covered by a liquid film is not favorable. The equilibrium shape of a drop that is smaller than the capillary length is a spherical cap, characterized by its equilibrium contact angle θ (see Fig. 4.1.4), defined by the Young-Dupré's equation. If S is positive, the liquid spreads and tends to cover the maximum surface area.

γ_{SG} (mJ/m^2) (Si with native oxide)	36.5	Zhao1993
γ_{SG} (mJ/m^2) (Si treated with HF)	44.7	Zhao1993
γ (mJ/m^2) (PS)	38.7 36	Wu1982 Lee1968

Table 4.1.2 List of interfacial tensions.

4.1.3.2. Stability and excess free energy of a thin film

The stability of a polymer thin film with respect to dewetting is related to its thickness. As expected from the definition of the spreading coefficient, thick film (h> 100nm) are stable when S is positive. However, for thinner film (h< 100 nm), excess intermolecular interaction free energy can be dominant and spontaneous dewetting can occur even though the spreading coefficient S is positive.

The stability of a system depending on a single parameter such as the thickness h can be apprehended by using the conceptual model of free energy. The free energy of a system based on its potential energy is the key physical quantity that describes the stability of a system. In many areas of physics, this concept is of fundamental importance because it allows to predicting the stability of a system independently of the time variable as for instance in astronomy for the observation of periodic comets or in condensed matter physics to understand the behavior of phase transitions via the order parameter. One of the major problems to address with thin films is to properly determine the free energy of

the system. This is not a simple question and many authors have tried to explain how to describe it without being able to give its exact analytical expression. The work of F. Brochard-Wyart et al. is of great interest to understand in a conceptual way how a thin film behaves when it is cast on a substrate [Brochard-Wyart1990]. For this reason we are going to first present some of the key points introduced in this paper keeping in mind that other models have also been proposed by other authors [Mukherjee2011, Seeman2001].

In the model of Brochard-Wyart , the free energy G(h) is written as a function of the film thickness as :

$$\boldsymbol{G}(\boldsymbol{h}) = \gamma_{SL} + \gamma + \Delta\boldsymbol{G}(\boldsymbol{h}) \qquad [4.1.5]$$

In this expression ΔG is the excess free energy that is determined by the difference between the cohesive interactions holding the liquid together, and the adhesive interactions between the liquid and the solid. Thus, the excess free energy has to be given by a combination of short-range (repulsive) and long-range (attractive) interactions.

In the model of Brochard-Wyart et al. the short range interactions are related to spreading coefficient S through , $\Delta G(h \rightarrow 0)=S$ and the long range interactions are given by the van der Waals interaction , $\Delta G(h)= -A/12\pi h^2$, where A is the Hamaker constant (Note that the sign of A is not defined like this in the original paper). From these relations, we can observe that ΔG(h) is governed by two parameters: the sign of the Hamaker constant A and the sign of S. It is worth noting that the true expression of ΔG(h) cannot be this one since when $h \rightarrow 0$, the Van der Waals interaction is not physically defined and must be corrected by a repulsive term that precludes the penetration of molecules.

Since for a thin film on a substrate, A and S may have any sign, four different cases are to be distinguished. For instance when S >0 and A>0 which is the model mostly used in our calculations, a final equilibrium state is a wetting film of thickness h_{eq} and a residual droplet over the wetting film. (see Fig. 4.1.5 c) and d)). This kind of situation is very interesting since it is contrary to the common belief that the formation of droplets is only valid for S<0. Hence for thin films (h<100nm) the sign of the Hamaker constant has also to be specified to evaluate the stability of the system.

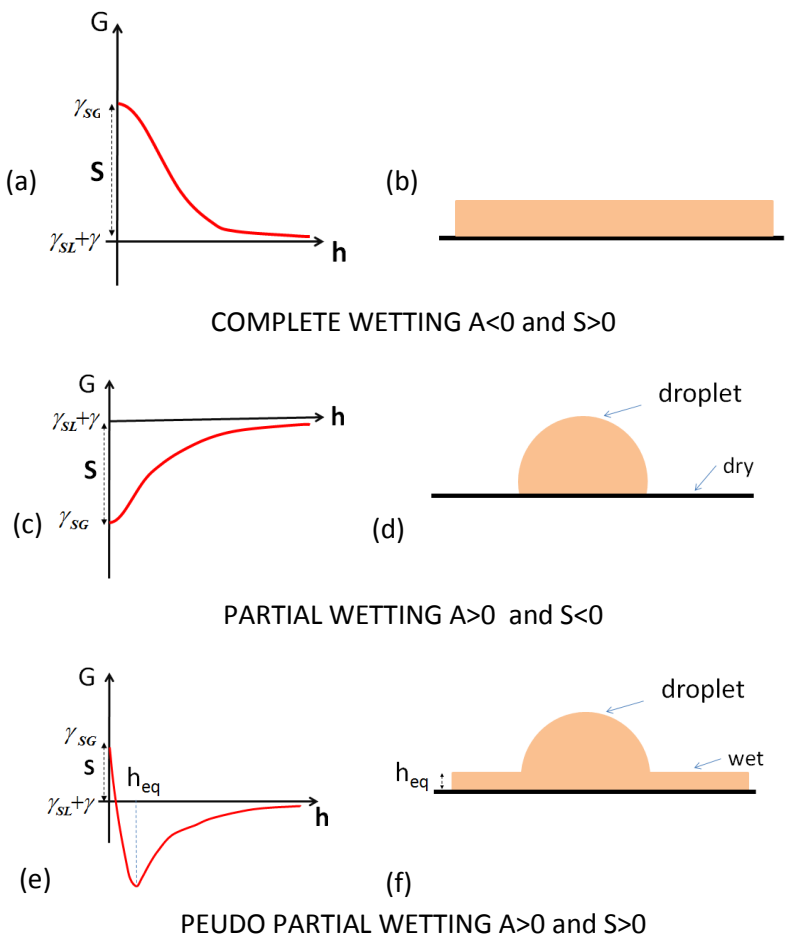

Figure 4.1.5 a), c) and e) Free energy corresponding to A<0, S>0 , A>0, S<0 and A>0, S>0 and its associated b),d) and f) final equilibrium state of a film showing a droplet and a wetting layer of thickness h_{eq}.

The main drawback of Brochard Wyart et al.'s model is that it does not provide the full analytical expression for the potential. To circumvent such a drawback a few authors have proposed to include in the potential a repulsive term that is generally not very well justified. For instance, Seemann et al. proposes an analytic expression for the free energy in which the , van der Walls potential as usually defined by [Semann2001] :

$$\Phi_{VDW}(\boldsymbol{h}) = -\frac{\boldsymbol{A}}{12\pi \boldsymbol{h}^2} \qquad [4.1.6]$$

is modified by a repulsive term that characterizes short-range interactions of strength c as:

$$\Phi(\boldsymbol{h}) = \frac{\boldsymbol{c}}{\boldsymbol{h}^8} + \Phi_{VDW}(\boldsymbol{h}) \qquad [4.1.7]$$

This expression is called the effective intermolecular potential Φ(h) and is frequently used in the literature to explain the different behaviours encountered in the dewetting process. Other non justified expressions are found as [Zhao1993, Mukherjee2011].

In all these equations, A is the effective Hamaker constant that is related to the Hamaker constant for binary interactions of the system components (see Fig. 4.1.6).

$$\begin{aligned} A_{132} &= A_{33} + A_{12} - A_{13} - A_{23} \\ &= (\sqrt{A_{22}} - \sqrt{A_{33}})(\sqrt{A_{11}} - \sqrt{A_{33}}) \end{aligned} \qquad [4.1.8]$$

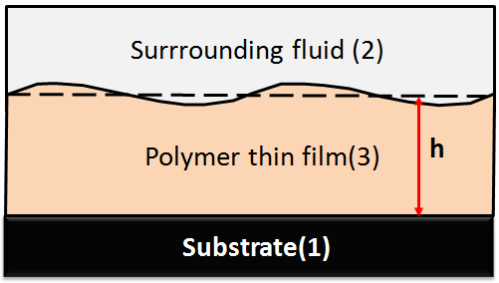

Figure 4.1.6 Schematic presentation of the film (3) of thickness "h" on a substrate (1) in a surrounding fluid (2).

Since the surrounding fluid is usually vacuum or air, A_{22}=0. As a result

$$A_{132} = (\sqrt{A_{33}})(\sqrt{A_{33}} - \sqrt{A_{11}}) \qquad [4.1.9]$$

It is worth noting that the Hamaker constant of each material is always positive (i.e attractive), however the effective Hamaker constant A_{132} of three materials could be positive or negative due to different attractive interactions that may exist between the fluid and the film or the film and the substrate.

For the specific situation involving PS on SiO_2/Si substrates, the form of the van der Waals contribution to the effective intermolecular potential is modified to include the additional interface created by the silicon oxide layer of thickness h:

$$\Phi(h) = \frac{c}{h^8} + -\frac{A_{SiO_2/PS/Air}}{12\pi h^2} + \frac{A_{SiO_2/PS/Air} - A_{Si/PS/Air}}{12\pi(h+d)^2} \qquad [4.1.10]$$

where ***d*** is the silicon oxide thickness, $\mathbf{A_{SiO2/PS/Ai}}$ is the Hamaker constant of the SiO_2/PS/Air and $\mathbf{A_{Si/PS/Air}}$ is the Hamaker constant of the Si/PS/Air.

Seemann et al. assesses the stability of the film by the second derivative of the potential $\Phi''(h)$. If $\Phi''(h)<0$ the film will dewet spontaneously, but if $\Phi''(h)>0$, the film will be stable. As an illustration, qualitative variations of $\Phi(h)$ and $\Phi''(h)$ are shown in Figure 4.1.7 using a realistic set of parameters. Figure 4.1.7a shows a scenario where $\Phi(h)> 0$. In this case, the film is stable. In Figure 4.1.7b there is a global minimum $\Phi(h)$ at $h=h_{eq}$. Here the system can gain energy by changing its thickness to $h_0=h_{eq}$. If the initial thickness is larger than h_{eq}, the film will dewet and the film will be unstable. Finally, in Figure 4.1.7c the film is unstable for $\Phi''(h)<0$ and stable for $\Phi''(h)>0$.

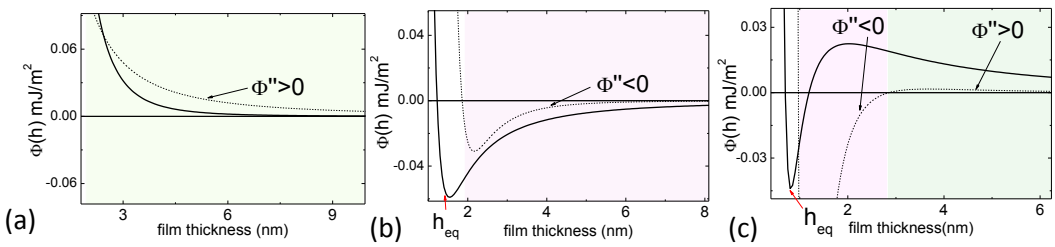

Figure 4.1.7 Sketches of the effective interface potential ϕ(h) (solid line) and ϕ''(h) (dashed line) for (a) a stable (b)an unstable and (c)a metastable system. The parameters used for the simulations of these curves are: for (a) system Si/PS/Air, $A_{Si/PS/Air}$ =–5.9×10^{-20}J, (b) system Si/SiO_2/PS/Air (h_{SiO2}=190nm) $A_{Si/PS/Air}$ = –5.9×10^{-20}J, $A_{SiO2/PS/Air}$ = 2.2x10^{-20}J , c= 6.3x10^{-76}Jm^6, for (c) system Si/SiO_2/PS/Air (h_{SiO2}=1nm), $A_{Si/PS/Air}$ = -5.9×10^{-20}J, $A_{SiO2/PS/Air}$ = 2.2x10^{-20}J , c=0.09x10^{-76}Jm^6

The position of the minimum defines the equilibrium film thickness h_{eq} due to the fact that a stable residual film of this thickness remains after dewetting, also called the wetting layer or residual layer. This has been experimentally verified by X-ray scattering measurements for short-chained polystyrene films (h_{eq} = 1.3 nm for a molecular weight Mw =2.05 kg mol^{-1}, termed 'PS(2k)') on a Si wafer with a 191 nm SiO_2 layer [Seemann2001].

4.1.3.3. Theoretical and Experimental expressions of the Hamaker constant

The non retarded Hamaker constant A_{123} for medium 2 between medium 1 and 3 is given from Lifshitz theory [Israelachvili2011] by

$$\begin{aligned} A_{123} &= A_{\nu=0} + A_{\nu>0} \\ &\approx \frac{3}{4}kT\left(\frac{\varepsilon_1-\varepsilon_3}{\varepsilon_1+\varepsilon_3}\right)\left(\frac{\varepsilon_2-\varepsilon_3}{\varepsilon_2+\varepsilon_3}\right) \\ &+ \frac{3h\upsilon_e}{8\sqrt{2}}\frac{(n_1^2-n_3^2)(n_2^2-n_3^2)}{(n_1^2+n_3^2)^{1/2}(n_2^2+n_3^2)^{1/2}[(n_1^2+n_3^2)^{1/2}+(n_2^2+n_3^2)^{1/2}]} \end{aligned} \qquad [4.1.11]$$

where ε_i is the dielectric constant of medium i in the zero frequency limit, n_i the index of refraction in the visible frequency, υ_e the electronic absorption frequency, *h* is the Planck constant, K is the Boltzmann constant and T is the temperature . A typical value for υ_e is $\approx 3\times10^{15}$ Hz. In the symmetrical case where medium 3 and 1 are the same, eq. 4.1.11 reduces to

$$A_{121} \approx \frac{3}{4}kT\left(\frac{\varepsilon_1-\varepsilon_2}{\varepsilon_1+\varepsilon_2}\right)^2 + \frac{3h\upsilon_e}{8\sqrt{2}}\frac{(n_1^2-n_2^2)^2}{\left(n_1^2+n_2^2\right)^{3/2}} \qquad [4.1.12]$$

$A_{PS/PS}$ x10^{-20} (J)	6.15 - 6.60 6.5 ~10.7	Hough1980 Calculated using eq. [4.1.12]* PS thin film [Li2007]**
$A_{Si/Si}$ x10^{-20} (J)	22.1 - 25.6 18	Visser1972 Calculated using eq. [4.1.12]***
$A_{SiO2/SiO2}$ x10^{-20} (J)	6.4 - 6.6 6.3	Hough1980, Bergstrom1997 Calculated using eq. [4.1.12]****
$A_{Si/PS/Air}$ (J)	-6.2 x 10^{-20} -5.9x10^{-20} -13 x 10^{-20}	Calculated using eq. [4.1.9] and $A_{Si/Si}$=25.6 x10^{-20}(J) and $A_{PS/PS}$=6.3 x10^{-20}(J) Calculated using eq. [4.1.9] and $A_{Si/Si}$=25.6 x10^{-20}(J) and $A_{PS/PS}$=10.7 x10^{-20}(J) for thin film Seemann 2001 (exp.)
$A_{SiO2/PS/Air}$ (J)	2.2 x 10^{-20}	Seeman2001 (exp.)

* ε =2.55, n=1.557, υ_e=2.3x10^{-15} s^{-1} for Polystyrene bulk
* *ε =3.5, n=1.75, υ_e=2.3x10^{-15} s^{-1} for Polystyrene thin film [Ata2012]
*** ε =11.6, n=3.44, υ_e=0.80x10^{-15} s^{-1} for Silicon[Israelachvili2011]
**** ε =3.8, n=1.448, υ_e=3.2x10^{-15} s^{-1} for SiO_2 [Israelachvili2011]

Table 4.1.3 List of Hamaker constant calculated and reported in the literature.

The first term in the eq. 4.1.12 gives the zero frequency contribution to the Van der Waals interaction. The second term is the contribution from the dispersion energy. It is only an approximation containing the first term of an infinite series. Since $h\upsilon_e >> kT$, the dispersive part usually dominates unless the refractive index of two involved materials e are similar. The zero-frequency contribution therefore only accounts for few percents of the total magnitude of the Hamaker constant since it cannot excess the value of $3/4k_BT = 10^{-21}$J.

The next table gives the Hamaker constants of PS, SiO_2, Si, Si/PS/Air, SiO_2/PS/Air calculated using the eq. [4.1.9] and [4.1.12]. Experimentally determined values are also included**.**

4.1.3.4. Dewetting Mechanism

In the following is discussed the two most important mechanisms occurring in the dewetting process of thin polymer films on a solid substrate. These two are called the spinodal dewetting and the nucleation of holes [Xie1998, Seemann2000].

- <u>Spinodal Dewetting</u>

Spinodal dewetting is an intrinsic mechanism leading to the rupture of a film. It involves an amplification of the capillary waves induced by thermal fluctuations, due to VdW instability. This dewetting generally occurs for very thin films (<10nm). For this mechanism, the term "spinodal dewetting" has been coined in analogy to the phase separation involved in a composition and decomposition process. In this process, the height fluctuations in dewetting correspond to the composition fluctuations in phase separation. The spatial-temporal fluctuation of the film thickness was given by [Xie1998]:

$$\boldsymbol{Z}(\boldsymbol{x},\boldsymbol{t}) = \boldsymbol{h}_0 + \delta\boldsymbol{h}\exp\left(\frac{\boldsymbol{i}2\pi\boldsymbol{x}}{\lambda}\right) \ , \ \delta h = \delta h_0 \exp(Rt) \qquad [4.1.13]$$

where h_0 is the film thickness, δh is the amplitude fluctuation and R is the growth rate. The x-coordinate is taken to be parallel to the surface and λ denote the characteristic wave length. Eventually the roughening leads to rupturing of the initially smooth and

continuous films, at the point where the undulations grow sufficiently to expose the underlying substrate.

Figure 4.1.8 Schematic figure illustrating a liquid film of initial height h_o that undergoes a surface height fluctuations due to capillary waves. These fluctuations in the film thickness are amplified and lead to spontaneous dewetting of the liquid (spinodal dewetting).

- Nucleation Dewetting

Another way for a film to break up is the nucleation and growth of holes. The nucleation mechanism considers the dewetting phenomena induced either by defects (contamination, etc) in polymer film, by defects on the solid surface or by thermal fluctuations of the polymer surface. The presence of particles or impurities can lower the energy barrier leading to film thinning and holes appearing in the film at the sites of particles (which are normally randomly distributed) [Jacobs1998].

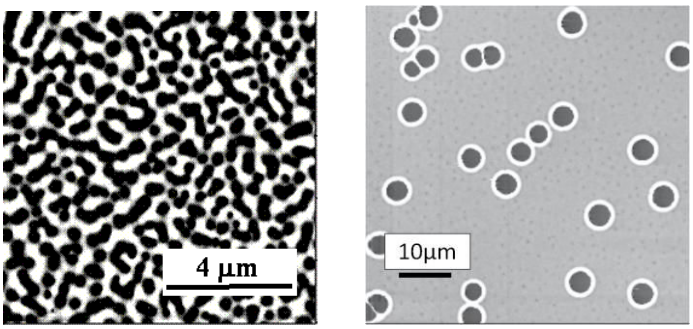

Spinoidal dewetting **Nucleation of holes**

Figure 4.1.9 Two major rupture mechanisms of thin film are: Spinoidal dewetting and the nucleation of holes. Pictures taken from [Tsui2003]

4.2. Preparation of Polystyrene Ultra thin film and Stability

In this section, the procedure used to prepare PS thin films is described. In addition the stability of polystyrene thin films at ambient conditions is studied by AFM and GISAXS.

4.2.1. Polystyrene Film Preparation

4.2.1.1. Solution PS/toluene

The polystyrene used in this study was 'PS' (purchased from Polymer Source Mw=136K with a radius of gyration Rg=10nm and Tg =373K). The surface tension of the PS is 36 mJ/m^2 [Lee1968]. Polystyrene was dissolved in toluene with an 'x g/L' concentration.

4.2.1.2. Substrate Preparation

Silicon <100> p-type wafers were used in this work as the substrate. In order to remove all organic contaminants, it was necessary to carry out a pretreatment of the surface by an aggressive cleaning step. The sample was immersed for 30 min in a solution containing 2/3 of sulfuric acid and 1/3 of hydrogen peroxide at 80°C 'Piranha solution'.

In order to remove the native oxide, the substrate (previously rinsed with de-ionized water and dried) was then immersed for 5 min in a HF solution of 5% by volume. Finally the sample was rinsed and dried.

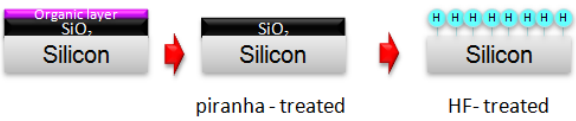

Figure 4.2.1 Silicon substrate after being preteated with a solution of piranha and HF.

Films were then made by the classical spin-coating technique.

4.2.1.3. Spin coating

An adequate amount of polymer solution was deposited onto the flat surface of the substrate which was hold in place by a vacuum chuck. Subsequently, it was rotated to a set frequency v (typically 2000 rpm). Due to centrifugal forces, the liquid spreads across the surface. The volatile solvent evaporates leaving behind a film.

The sample was then heated up to 160°C under3 vacuum for 24h to remove any residual solvent and any residual stress produced by the spin coating.

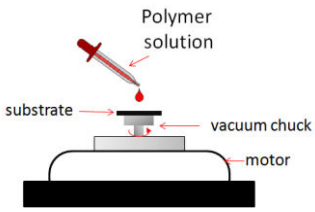

Figure 4.2.2 Representation of the spin-coating technique for the deposition of a flat polymer.

4.2.2. Observation of the Dewetting of the system PS/Si (treated HF)

In order to directly observe the morphology formed by PS films, the surfaces were first studied by atomic force microscopy (AFM). Several pictures were taken in the tapping mode with a force of approximately 40nN. No damage was observed after several scans with a magnification of 2x2 μm^2. The results for PS film with a concentration of 0.4g/L just after being spun on silicon treated with HF are shown in the Figure 4.2.3.

In this image we observe the formation of an ultra thin film of Polystyrene with an average thickness of 2.5 nm (thickness determined from the AFM profile). We also observe the apparition of small holes and islands inside each hole. As proposed by several authors, in film prepared by spin coating, the polymer chain may be not fully equilibrated, generating residual stress that can oblige the film to wet the surface.

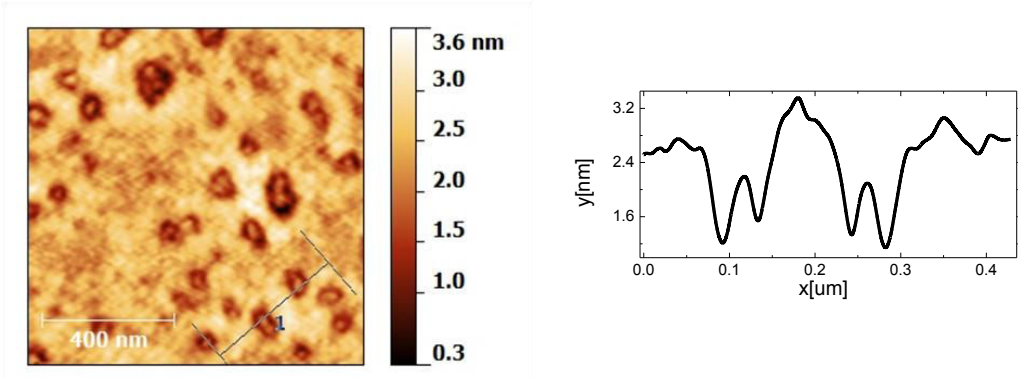

Figure 4.2.3 Before thermal treatment (a) AFM image and b) AFM profile of a thin film of Polystyrene with a concentration of 0.4g/L just after being spun on silicon.

After the thermal treatment this residual stress disappears and finally it is possible to have a film with an equilibrium thickness defined by the free energy of the system.

In order to analyse the stability of the system, we first focus on the spreading coefficients given in eq. 4.1.4. At 21°C, with γ_{SG}=44.7.mJ/m^2 for the Si treated with HF [Zhao1993] and γ=36 mJ/m^2 for polystyrene [Lee1968]. With these values, it is found that the macroscopic spreading coefficients S is positive. We should therefore expect a wetting of the silicon surface. This is clearly consistent with the observed results for polystyrene films at high concentration c > 2.0 g/L in toluene (see Fig 4.2.4).

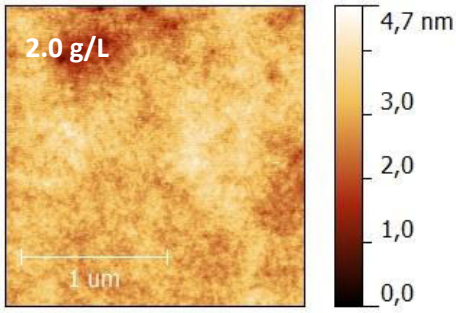

Figure 4.2.4 AFM image of a thin film of Polystyrene prepared by spin-coating from a solution with a concentration of 2.0 g/L , after the thermal treatment.

For small concentrations the effective intermolecular potential given by Seemann [Seemann2001] needs to be taken in account. If only the effective intermolecular potential is considered, the stability of the Si(HF)/PS/air (1/3/2) system is governed by the sign of the Hamaker constant of the system (A_{132}) , which could be computed from the Hamaker constants of each materials. When inserting the values from table 4.1.3 into eq. 4.1.9, a negative value for A_{132} (about -5.9×10^{-20} J) is obtained. Replacing this Hamaker constant in equation 4.1.7, we obtain the following curve which suggests that the Polystyrene film is stable on HF treated silicon.

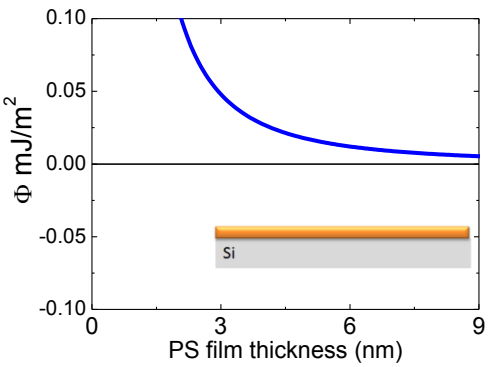

Figure 4.2.5 Reconstructed effective interface potential Φ (h) for polystyrene film on silicon wafer treated with HF using the equation 4.1.7 with $A_{Si/PS/Air} = -5.9\times 10^{-20}$ J

However, despite this evidence, we present results showing that PS films of 4nm can dewet the surface of HF treated silicon, in contrast to theoretical expectations based on the negativity of A_{132}. The observed dewetting behaviour resembles spinodal dewetting when the concentration of PS in toluene is less than 1g/L (Figure 4.2.6).

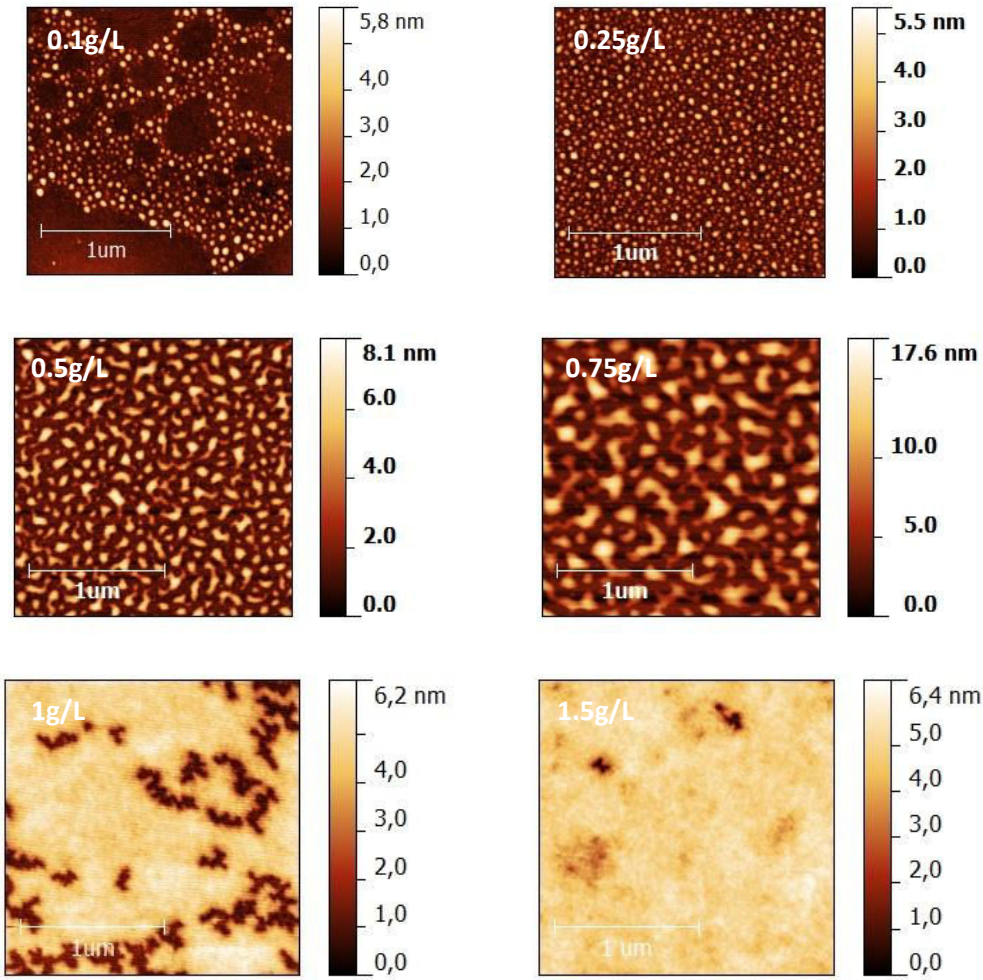

Figure 4.2.6 AFM images of PS films on silicon treated HF. Scale bars indicate 1µm. After the thermal treatment.

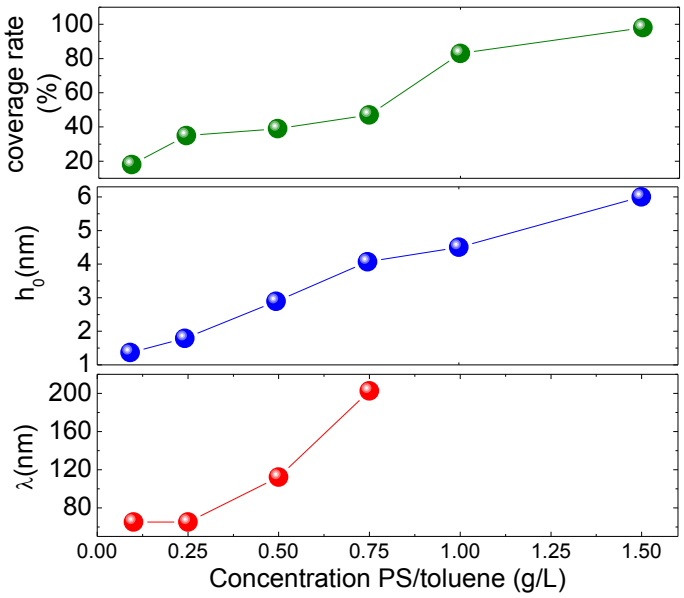

Figure 4.2.7 a) Coverage rate obtained from the AFM image for various concentrations PS/toluene. b) Average thickness h_0 (After the thermal treatment) calculated from the AFM height profile **c)** Wavelength calculated from Fourier transform from AFM images.

The discrepancy between the observed results and the theoretical prediction suggests that either additional forces or a different model have to be considered to probe the stability of the film :

- A first assumption is the possible existence of a silica layer covering the surface. It has been reported in the literature that after a HF treatment, the silicon surface is not stable [Li2002, Graf1990]. This is due to the quick oxidation of the surface of silicon in contact with air. This fact suggests the formation of a very thin film of silica over the surface before the polymer deposition. The thickness reported in the literature is ranging from 0.6 up 0.8 nm of silica in the interval of 10min of exposure in air.

  In this case the effective intermolecular potential is given by equation [eq. 4.1.10] in which the values from table 4.1.3 are introduced. The potential $\Phi(h)$ and its second derivative $\Phi''(h)$ are plotted in the Figure 4.2.8 for PS film thicknesses up to 6 nm . $\Phi''(h)<0$ takes place at h_c=2.1nm. Hence, according to eq. 4.1.10, PS film thinner than h' should dewet spontaneously. This result does not correspond exactly to the observation made by AFM, where islands were formed for thicknesses less than h_c=4.5 nm.

-

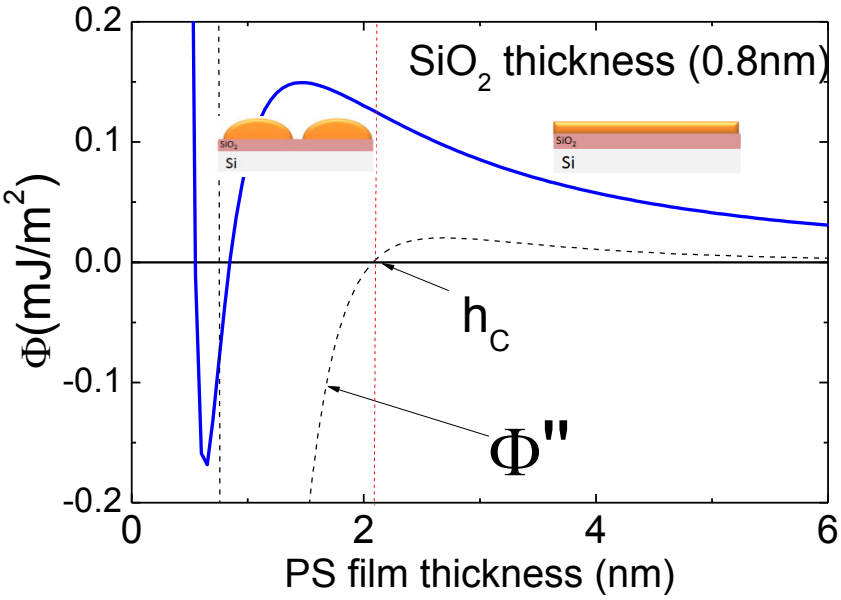

Figure 4.2.8 Reconstructed effective interface potential Φ(h) for polystyrene film on silicon wafer with oxide layer thicknesses of only 0.8nm using the equation 4.1.10 with $A_{Si/PS/Air}$ = -5.9x10^{-20}mJ/m^2, $A_{SiO2/PS/Air}$ = 2.2x10^{-20}mJ /m^2, c= 6.3x10^{-76}J/m^6

- A second assumption is to consider forces due to chain deformation. Zhao et al. report that when h is of the order of the radius of gyration (R_G), the spreading for the polymer is more complicated because one has to account for the effects of polymer stretching. As the film thickness decreases to approximately less than R_G, the film must stretch in order for the film to wet the surface. Zhao et al. take in account an additional excess free energy ΔG. Then the effective spreading coefficient S_{eff} is obtained by calculating –dG/dA [de Gennes1985, Zhao1993, Muller-Buschbaum2003] :

$$S_{eff} = S - \frac{A_{Si/PS/Air}}{12\pi h^2} - \frac{\pi^2}{3} k_B T n \left(\frac{R_0^2}{h^2} \right)$$

where k_B is the Boltzmann's constant, T is temperature, h is thickness of the film, A is the area and 'n' is the number of chains/unit area. If S_{eff}>0, the surface is completely wetted while if S_{eff}<0 the dewetting phenomenon takes place.

- The first term is the spreading coefficients, S, with $\gamma_{SL} = \left[\gamma_{SG}^{0.5} - \gamma^{0.5}\right]^2$ for a thin film of polystyrene on silicon treated by HF, the value of S is 9.1mJ/m^2.
- The second term is the Van der Walls term, where '$A_{Si/PS/Air}$' is the total Hamaker constant for the PS/Si(HF) system. This term can be estimated from the Hamaker constant of each material (see Table 4.1.3 and Eq. [4.1.7]) '$A_{Si/PS/Air}$' =–5.9× 10^{-20} J.
- The last term ΔS is the free energy cost for stretching n polymer chains per unit area, each of unperturbed end-to-end distance$R_0 = \sqrt{6}R_g$. For Polystyrene (M_W=136K and Rg=10nm), the number of chain per unit area is estimated to be around 4x10^{-8}xN_A, where N_A is the Avogadro constant.

In Figure 4.2.9, S_{eff} is plotted as a function of h for Si treated with HF. The maximum thickness for which the film will dewet corresponds to a value of S_{eff}=0, and is approximately 5 nm. This is consistent with the data shown in Fig. 4.2.6, where film thicker than 5 nm wet the surface of silicon.

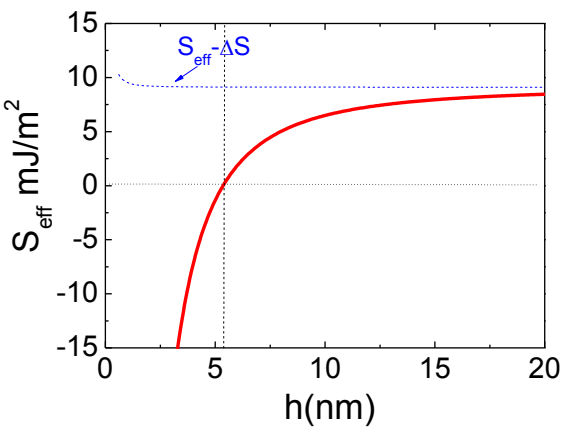

Figure 4.2.9 S_{eff} as a function of film thickness of PS for a silicon treated with HF (red-line). For comparison, (blue dash) correspond to S_{eff}-ΔS on the silicon surface.

4.3. X-ray Characterization at ambient conditions

In the next section, we focus our attention to the results obtained on the morphological characterization of PS islands using the GISAXS technique and on the characterization of PS thin films using XRR at ambient conditions.

4.3.1. Homogeneous Polystyrene Thin Film using XRR

The thickness, electron density and the roughness of a Polystyrene thin film can be monitored by XRR. The measurements were carried out at the ID10B beamline (ESRF) facilities using a monochromatic beam having energy of 22keV.

Samples were prepared following the preparation method described in section 4.2.1 and using a PS/toluene concentration of 1.5 g/L. The corresponding XRR curve is presented in Figure 4.3.1. The data were then fitted using the modeling program REFLEX18 [Gibaud&Vignaud] in which a three layer model was considered. The first layer is a PS region with a high electron density due to the agglomeration of PS chains at the interface with the substrate. A second PS layer having an average electron density was then terminated by a third layer with a low electron density due to dispersion of polystyrene chain tails at the surface. For each layer, the electron density, the thickness and the roughness of the film were the fitting parameters. The optimal parameters obtained are shown in Table 4.3.1.

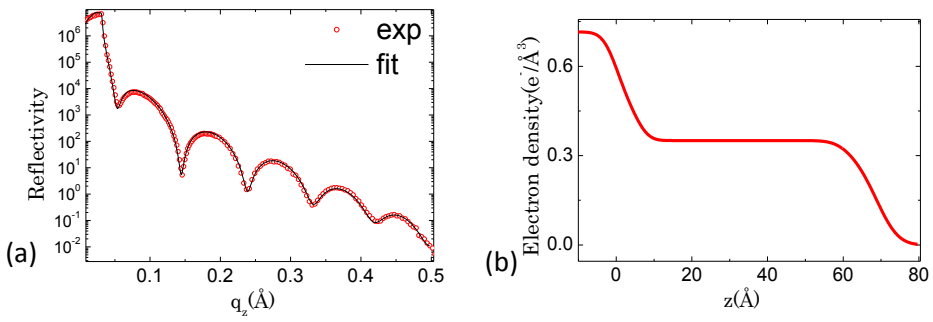

Figure 4.3.1 a) Experimental (circles) and fitted data (line) of Polystyrene thin film b) Electron density profile corresponding to Polystyrene thin film.

Layer	electron density (e^-/A^3)	roughness (Å)	thickness (Å)
Si	0.71	3	-
1st PS layer	0.40	2	5.8
2nd PS layer	0.34	3	56
3rd PS layer	0.23	4	7.5

Table 4.3.1 Parameters obtained from XRR curves of PS film prepared with a concentration of PS/toluene of 1.5g/L.

4.3.2. Polystyrene Islands using GISAXS

GISAXS experiments were performed with synchrotron radiation at the ID10B Beamline (ESRF). A MAXIPIX detector was used to record the 2D GISAXS images with a pixel size of 55µm. To get a high resolution, the beam was focussed at the detector position. The distance between the sample and the detector was 4000 mm. GISAXS patterns were collected at several incident angles (see Figure 4.3.2). At large incident angles, the lateral profile does not overlap with the reflected beam. The GISAXS patterns were saved as EDF file and processed with a matlab program to produce intensity maps in the q_{xy}-q_z plane, where q_{xy} is the scattering vector component parallel to the sample surface and perpendicular to the scattering plane and q_z is the component perpendicular to the sample surface.

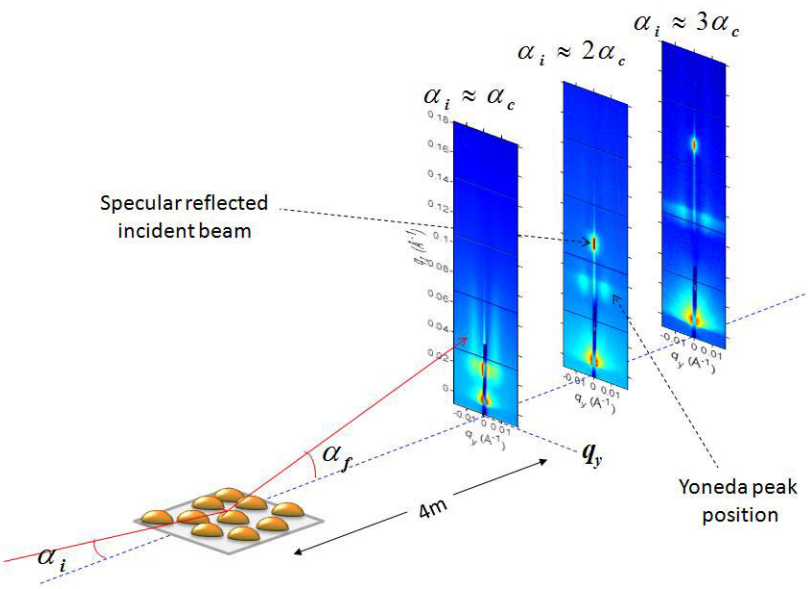

Figure 4.3.2 Setup used for the characterization of the Polystyrene Island performed at ID10 Beamline (ESRF) for several incident angles ($\alpha_i \sim \alpha_C$, $\alpha_i \sim 2\alpha_C$, $\alpha_i \sim 3\alpha_C$) where α_C is the critical angle of silicon substrate. (**α_C (silicon at 22keV)= 0.08 degrees**)

Figure 4.3.2 shows the measured GISAXS pattern at ambient conditions *as* a function of both wave vector transfers q_{xy} and q_z parallel and perpendicular to the surface of the substrate at an incident angle at $\alpha_i \approx \alpha_C$, $\alpha_i \approx 2\alpha_C$ and $\alpha_i \approx 3\alpha_C$. The GISAXS patterns exhibit a specular rod that is partially masked by the beam stop and a very intense elongated spot due to the specularly reflected incident beam which can be seen close to $q_z=4\pi \sin(\alpha_i)/\lambda$.

More interestingly are the 2 off-specular truncation rods located at $q_{xy}=\pm 0.007 A^{-1}$ on each side of the specular rod. The q_{xy} position of such rods is characteristic of the average distance between the pair neighboring islands. The rod extension along q_z is inversely proportional to the islands height. The line shape of the q_z scan (2D image cut at a fixed q_{xy} position) is strongly depending on the morphology of the islands which can be obtained by a correct model and a fit to the data.

It is important to highlight that GISAXS patterns need to be measured at an angle of incidence high enough to avoid a strong signal contamination coming from the foot of the incident reflected beam in the diffuse scattering. The reflected beam is indeed very intense compare to the scattered beam but its intensity decays very fast along q_z. In this case as the distance between the islands is quite large, the diffuse rods are located very close to the specular ridge so that the beam spilling is even more problematic.

Information about the morphology of PS islands can be extracted from line cuts along the q_z and q_{xy} of the GISAXS images (Fig. 4.3.6). We have selected at α_i =0.05° a vertical cut at $I(q_z,q_{xy}=0.0075\ Å^{-1})$ and a horizontal cut at $I(q_{xy},q_z=0.025\ Å^{-1})$ and at α_i =0.18° a vertical cut $I(q_z,q_{xy}=0.0075\ Å^{-1})$ and a horizontal cut $I(q_y,q_z=0.05\ Å^{-1})$.

Hemispherical and cylindrical morphologies were chosen to model the particles shapes. We have also considered the effect of absence (or presence) of a PS residual layer (see Figure 4.3.3). The fitting parameters included in our model were the radius and height of islands, the neighboring distance of islands and thickness and electron density of the residual layer.

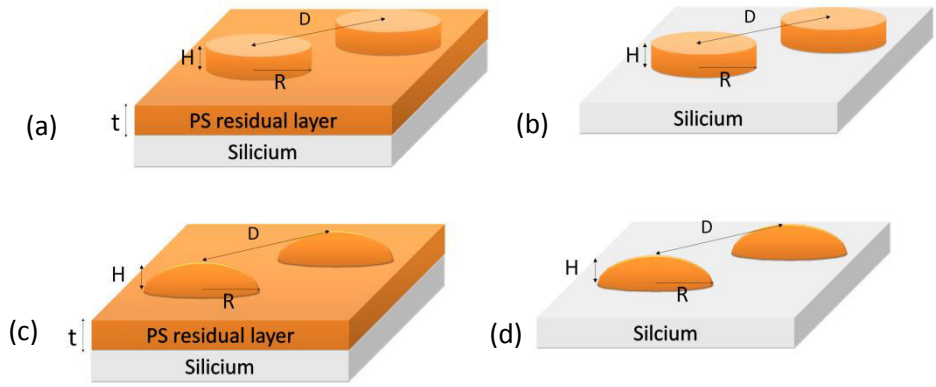

Figure 4.3.3 Schematic representation for different geometries included in our model a) Cylinder shape of island + residual layer between the silicon and island, b) Same as Fig a) without the residual layer. c) Hemispherical shape with and d) same as Fig c) without the residual layer.

The fitting results of $I(q_z)$ are shown in Figure 4.3.4. It can be seen that the best agreement was obtained with cylinders lying on a very thin PS film located between the islands and the substrate. This thin layer was necessary to correctly fit the width of the Yoneda peak.

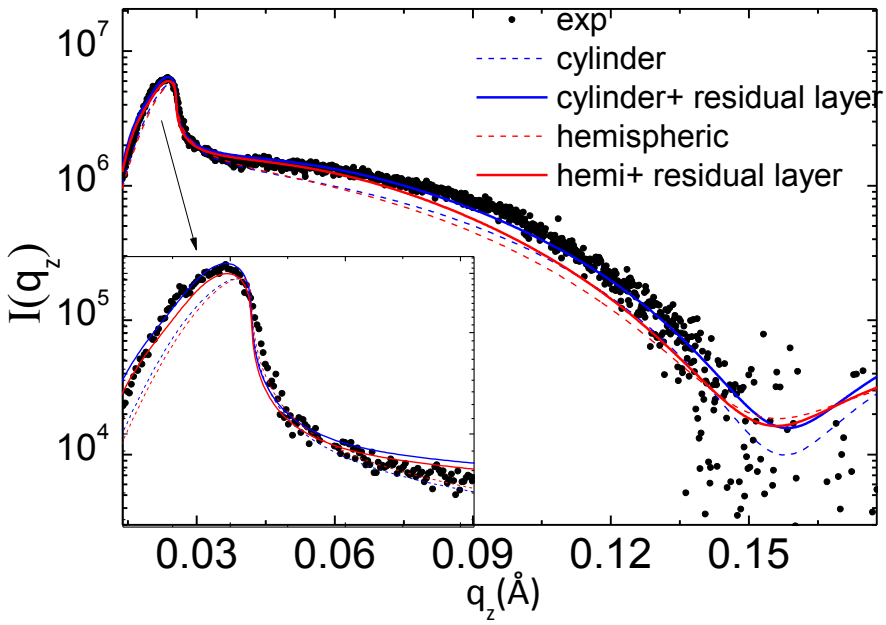

Figure 4.3.4: Observed and calculated scans along q_z direction from GISAXS image (Cut made at q_y=0.07Å^{-1} (α_i=0.05^o). using different models (a cylinder or a hemispheroid shape of the PS island with or without a PS residual layer)

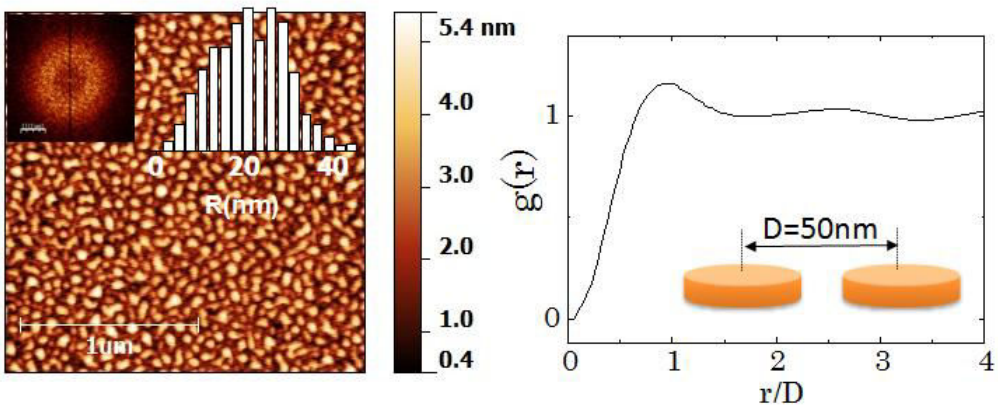

Figure 4.3.5 (a) Topographic AFM image of the film surface showing the pressence of well separated islands of maximum height 5.4nm (b) Pair correlation function extracted from AFM image.

The characteristics of the islands obtained from AFM image (Fig. 4.3.5) were used as an initial guess in the fitting process. In order to correctly reproduce the data, it was compulsory to utilize the DWBA which implies the calculation of four terms in the scattered amplitude described in the section 2.5.5.

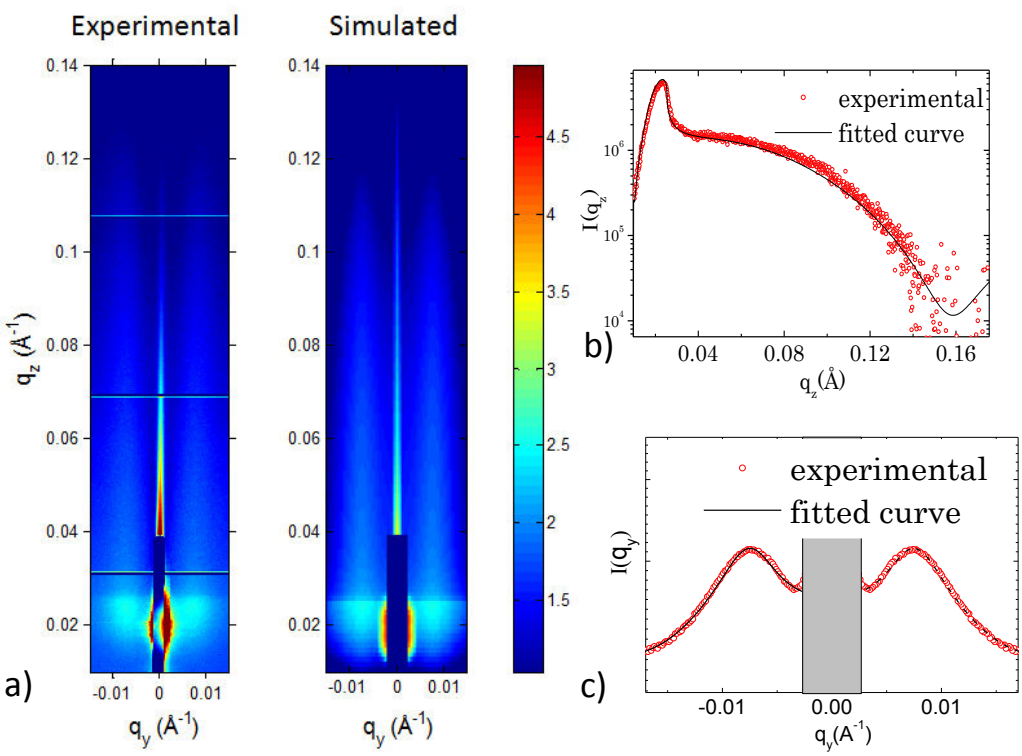

Figure 4.3.6 a) Experimental and Simulated GISAXS patterns of as prepared PS island film (α_i =0.05^o) b) and c) Observed and calculated scans along q_y and q_z direction from GISAXS image (Cut made at q_z=0.025Å^{-1} and q_{xy}=7.5x10^{-3}Å^{-1}.

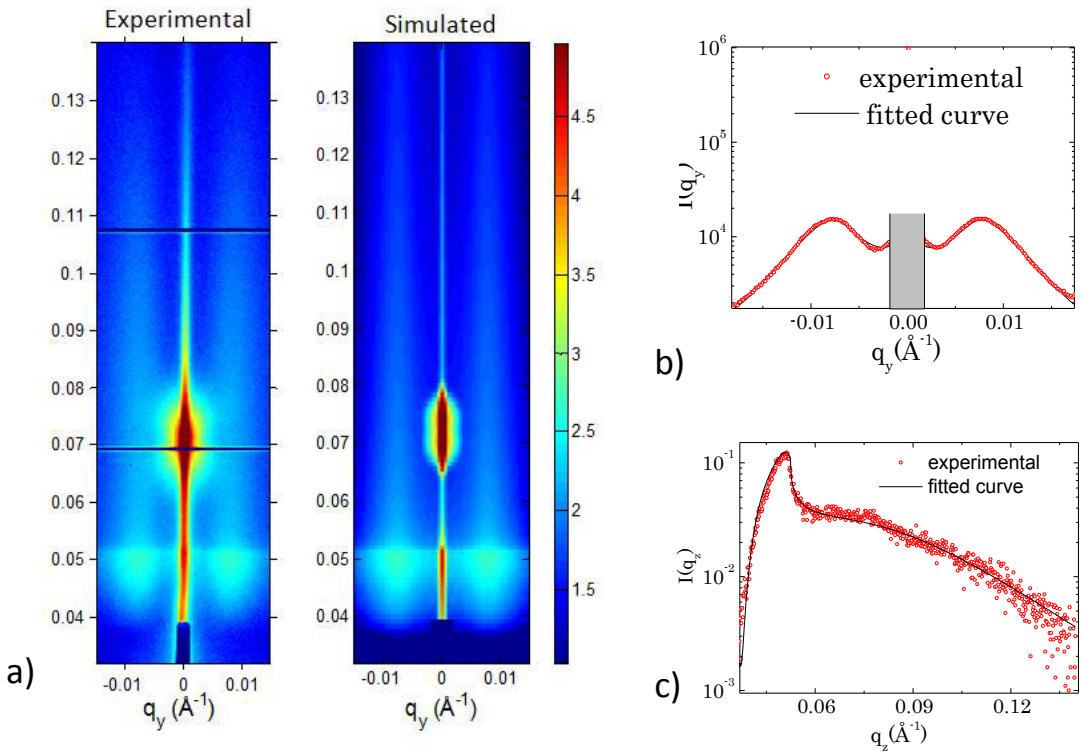

Figure 4.3.7 a) Experimental and Simulated GISAXS patterns of as prepared PS island film (α_i=0.18°) b) and c) Observed and calculated scans along q_y and q_z direction from GISAXS image (Cut made at q_z=0.051Å^{-1} and q_{xy}=7.5x10^{-3}Å^{-1}).

The results of the fits to the observed data are shown in Fig 4.3.6 and 4.3.7 b) and c) for the q_y and q_z scans at α_i =0.05° and α_i =0.18° respectively. This yields an average height of islands of about 4.3±0.1nm, a lateral radius of 19 ± 4 nm, a distance between neighbours of around 60 ± 20nm, and a PS residual layer of 2.2±1nm of thickness. These values are in very good agreement with the ones obtained from the analysis of the AFM image (see Fig. 4.3.8). They were then used to calculate the whole 2D GISAXS pattern shown in Fig.4.3.6 and Fig.4.3.7 a).

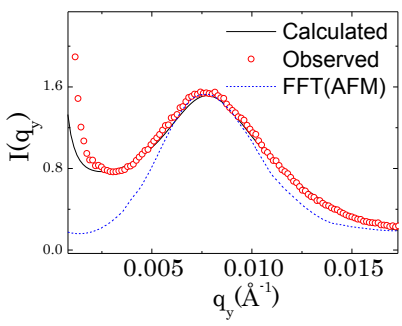

Figure 4.3.8 Fits (thin line) of the experimental cuts (circles) (see Fig 4.3.7c) in the q_y direction compared with the FFT from the AFM image Fig. 4.3.5a).

Residual wetting layer

In order to confirm the existence of the residual wetting layer , the sample was rinsed in toluene for 10 min. In Figure 4.3.9 we oberve the AFM image of the PS islands before and after rinsing the sample with toluene. The toluene rinsing should disolve and remove all the Polystyrene present on the sample. However, a residual layer is always observed which has a thickness of about h ~2 nm (see Figure 4.3.9c). The AFM phase image showed in Figure 4.3.9b and 4.3.9c suggests that this residual layer is covering all the surface of silicon and is present before and after the toluene rinsing.

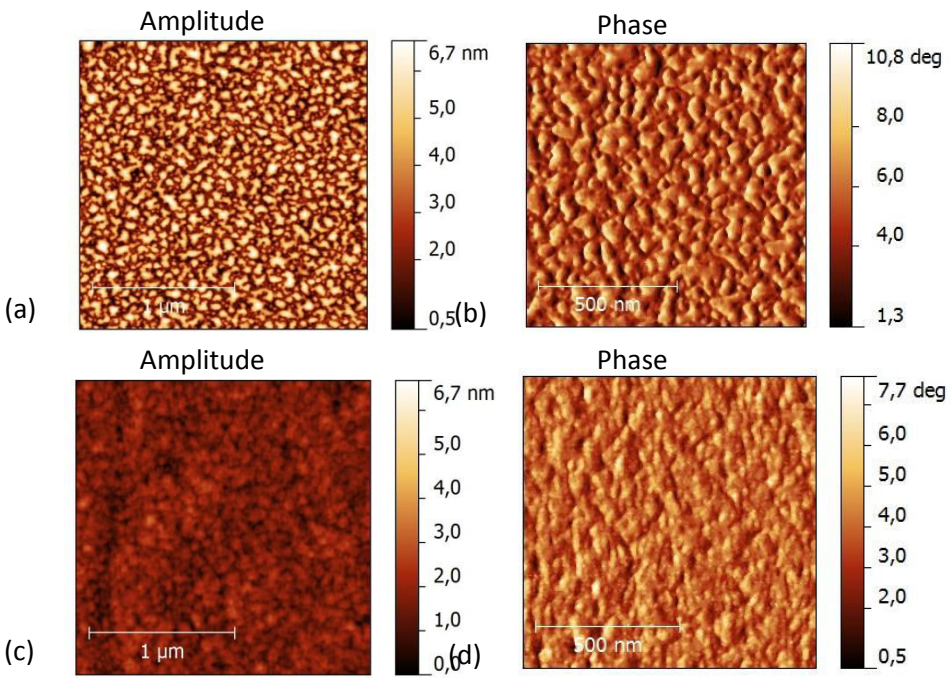

Figure 4.3.9 Polystyrene island using a solution of 0.5g/L a) AFM amplitude b) Phase before rinsing c) AFM amplitude and d) phase after rinsing the sample for 10 min with toluene.

AFM provides clear information about the dewetting process of the Polystyrene on silicon under normal environmental conditions. The next step of this study was to investigate the behavior of these islands when they are exposed to CO_2 with pressure conditions ranging from 0 bar to the pressure corresponding to the supercritical state. These experiments were carried out in a dedicated cell that was mounted on the diffractometer of the ID10 beam line (ESRF). This cell allows to carrying out in-situ GISAXS and XRR measurements as

a function of the CO_2 pressure or temperature. This kind of experiment yields invaluable information that cannot be accessed by AFM studies in such stringent experimental conditions making GISAXS a unique technique to probe the influence of CO_2 pressure on the island morphology and arrangement .

4.4. Exposure of PS thin films and islands to CO_2

In the next section we report the investigation of the behavior of these thin films and islands when they are exposed to CO_2 under pressure ranging from 0 bar to the pressure corresponding to the supercritical state. The main objective of this study was to compare the swelling of ultra thin films and islands of similar thickness and to relate the swelling to the pressure of CO_2 and the possible uptake of CO_2 by PS.

4.4.1. Introduction

The use of carbon dioxide as an inert solvent has emerged recently as an important development in polymer chemistry. It is therefore of great interest to use specific techniques to elucidate the physical behaviour of a range of polymers either exposed to CO_2 or immerged in carbon dioxide solution. In particular in-situ experiments are the most valuable ones since they offer the possibility to fully understand the role of the solvent on the physical properties of the exposed polymers as a function of the fluid temperature and pressure. In the case of CO_2, one of the main reasons to get interest in this solvent is that it has intrinsic environmental advantages: it is nontoxic, non flammable, and can be easily separated and recycled. Examples of the use of CO_2 as a solvent can be found both in polymerisation reactions as well as in polymer processing [Cooper2000]. In all cases, the ability of CO_2 to decrease the glass transition temperature, Tg, of polymers is exploited: during reactions, plasticization enhances the diffusivity of molecules into the polymer matrix [DeSimone1992] and, in polymer processing, and it facilitates impregnation of or extraction from the polymer matrix [Kazarian1997, Lou1995]. To design these processes, information about the dilation of the polymer matrix and the associated amount of CO_2 adsorbed in the polymer are necessary.

Several investigations are reported concerning the effects of sc-CO_2 on the properties of Polystyrene thin films [Li2007a, Meli2004, Oka2008, Koga2002]. These properties are: swollen volume, wetting, viscosity and Tg which are modified when the polystyrene

interacts with CO_2. Pham et al. show the existence of a glass transition pressure "Pg" induced by sc-CO_2. They also show that the referred 'Pg' at which the transition occurs decreases with decreasing film thickness in PMMA and PS thin films [Phan2003]. Meli et al. showed that PS thin films formed on SiO_2/Si are metastable in a CO_2 environment. In addition, they found that the contact angle formed for PS droplets on SiO_2/Si in CO_2 are higher than for PS droplets in air. This result is a clear indication that the wetting is less favourable under CO_2 exposure [Meli2004]. Koga et al. used neutron reflectivity to explore the swellability of polystyrene thin film in scCO_2. They observe a maximum in the swelling percentage as a function of CO_2 pressure in the vicinity of the critical point [Koga2011]. The authors attribute this anomalous swelling to an enhancement in carbon dioxide solubility, produced by an enhancement in the carbon dioxide density fluctuations across the "ridge" and suggested that the swelling isotherms are density dependent far from the ridge conditions and density fluctuations dependent otherwise.

Interactions between polymers and CO_2 molecules has been largely studied in the literature. Kazarian et al. have shown that acid base interactions of the Lewis type exist between CO_2 and the carbonyl group (C=O) in the backbone of polymers such as PMMA [Kazarian1996]. However Polystyrene does not possess this kind of group, hence the sorption and swelling of PS films cannot be attributed to such interactions. On the contrary, the quadrupole moment of CO_2 that interacts with phenyl group of PS is generally considered as the key point [Plonka2013].

The behaviour of ultra thin films of PS isothermally exposed to CO_2 starting from a pressure of 0 bar up to 80 bar is now discussed. XRR measurements were used to monitor the evolution of the swelling on the film. Furthermore, dewetted films of PS were exposed to CO_2 in order to observe the effect on the stability of island on HF-etched silicon and also to compare the swellability with a uniform film of the same thickness. GISAXS technique was used to monitor the evolution of the neighbouring distance, the radius and height of the islands.

4.4.2. Experimental Procedure

Samples were prepared according to the method described in section 4.2.1. Thin films were then placed in a high pressure cell [Mattenet2010] containing CO_2 at T=32°C. XRR and GISAXS experiments were performed at the ID10B beamline of the European

Synchrotron Radiation Facility (ESRF, Grenoble, France) with a 22 keV monochromatic x-ray beam. High energy X-rays are required to minimize the absorption of the beam going through the diamond windows of the cell (1 mm) and 35 mm of CO_2 in the gas or sc-state. Extreme care was taken to correct the effect of beam damage on PS films by translating the film during the course of experiments.

For data analysis, we had to take in account the change of the critical angle of silicon which decreases when the CO_2 pressure increase. This can be observed clearly in the GISAXS and XRR curves, where the critical wave vector transfers of silicon is shifted towards lower values of q when the pressure of CO_2 is increased (see Appendix B). This effect was directly included in the Reflectivity program Reflex18 [Gibaud&Vignaud] by adding a medium of variable electron density at the top of the stacking sequence.

In all measurements made under pressure, the swellability of the film is a key parameter to monitor. Under the assumption of uniaxial volume expansion dictated by a constant surface of the substrate, the swellabillity reads as :

$$\boldsymbol{Swellability}\% = \frac{\boldsymbol{h} - \boldsymbol{h}_{\boldsymbol{initial}}}{\boldsymbol{h}_{\boldsymbol{initial}}} \boldsymbol{x} 100$$

where h is average thickness at a given pressure and $h_{initial}$ is the average thickness at ambient pressure.

4.4.3. Polystyrene Thin film

We first describe the behaviour of an ultra thin film of polystyrene having an initial thickness of 6.8nm at 35°C and atmospheric pressure as a function of CO_2 pressure.

Figure 4.4.1 shows the XRR results during the in-situ monitoring of the swelling of this PS film exposed to sc CO_2. At low pressure, Kiessig fringes typical of a smooth film of finite thickness are observed. The period of the fringes progressively decreases when pressure is raised. This is a clear indication of the swelling of the film. Nevertheless it can be seen that when pressure is raised, the amplitude of Kiessig fringes progressively decreases and the extent in q range where they are visible also diminishes. These two combined effects give a clear indication that two phenomena occurs during pressurisation. First the change

in amplitude is explained by a continuous decay of the electron density contrast between CO_2 and the PS film. This decay comes from the fact that the electron density of CO_2 continuously increases with pressure and steeply raises at the sc-point. This change is so prominent that the electron density of the polymer becomes almost equal to the one of CO_2 in the sc-state.

In addition we interpret the disappearance of the fringes at high q by an increase of the interfacial roughness at high pressure. This is a clear consequence of the uptake of CO_2 molecules in between the polymer chains. This uptake is accompanied by a swelling of the chains. In particular we infer that a disentanglement of the chains at the top surface of the polymer occurs which in turn yields a roughening of the top surface of the film. The change in thickness can be monitored up to a pressure of 70 bars after which the Kiessig fringes disappear.

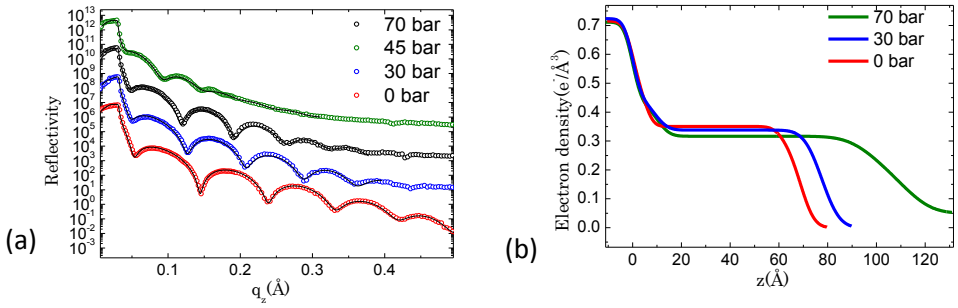

Figure 4.4.1 a) Evolution of in-situ XRR curves during pressurization of CO_2 in the cell. Symbols are experimental in-situ data for different pressure. Solid lines represent the fits to the data. b)electron density profile in the normal direction to the substrate.

From this analysis, one can highlight the following two main changes in the behavior of the film with CO_2 pressure. First, at low pressure, i.e., below P = 40 bar, a small decrease of the electron density of the film is visible. This change is accompanied by a relatively small swelling (Figure 4.4.1). Second, for pressures above 40 bar, the electron density of the film further decreases along with a more important swelling of the film as reported in Figure 4.4.2. This change in the swelling behaviour can be explained in the framework of previous works [Phan2003, Phan2004] that introduced the existence of a glass transition pressure Pg. This quantity could be defined as a pressure at which a PS thin film exhibits a glass transition when pressure is varied at a fixed temperature. This definition is

analogous to the one of the glass transition temperature (Tg) for which temperature is varied at fixed pressure (see Fig 4.4.2a)

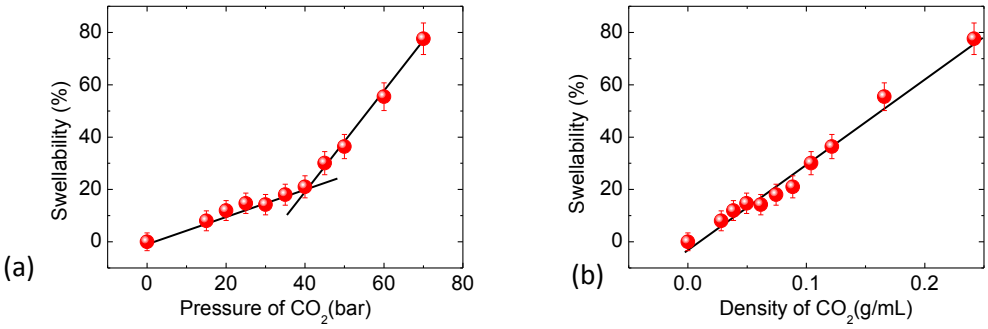

Figure 4.4.2 Swellability of a PS thin film a) as a function of pressure b) as a function of density of CO_2.

However, if the swellability of the film is plotted as a function of CO_2 density (see Fig 4.4.2 b) a linear behaviour is observed that makes unclear the hypothesis of the existence of glass transition pressure (Pg). This result suggests that the swellability is mostly governed by the evolution of the CO_2 density in the cell rather than by the pressure. In line with these results, it is possible to assume that the polymer swellability is directly related to the amount of CO_2 absorbed in the polymer. This statement is valid at a given temperature of 32°C and it is important to check if it remains true at other temperatures.

In order to probe this assumption, we performed isobaric measurements at 42 bar. During this experiment the pressure inside the cell was fixed at 42 bar and data were collected in the range 10°C to 70°C.

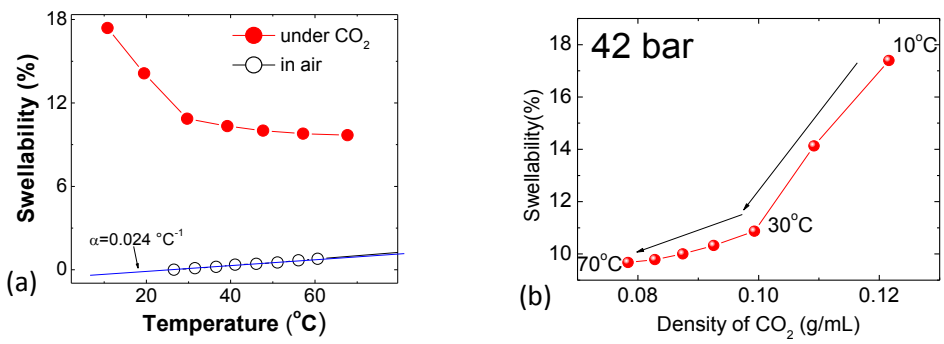

Figure 4.4.3 a) Swellability in air (circles) and under CO_2 (holes) of PS thin film as a function of the temperature. b) Swellability under CO_2 as a function of density of CO_2.

The swellability versus temperature and CO_2 density curves are shown in Figure 4.4.3a and 4.4.3 b. As shown in Fig 4.4.3 a (open circles) the swellabillity of a PS thin film in air

slightly increases when temperature is raised. This behaviour is typically expected when a material is heated. It allows to define the coefficient of thermal expansion (CTE) of the material which for PS in air is found to be α=0.024 °C^{-1}. When PS is heated under CO_2 at a constant pressure P=42bar, the swellability (shown in full red circles) is drastically different. We clearly observe a decrease of the swellability when the temperature is increased. This yields a negative non linear CTE at this pressure. Once again this shows that the thermodynamical parameters (T, P) are not sufficient to explain the behaviour of the swellability.

If we now plot the evolution of the swellability versus the density of CO_2 we clearly observe that the swellability is not linear with the density of CO_2 (see Fig 4.4.3b). In conclusion, these experiments clearly evidence that the behaviour of a thin film of PS exposed to CO_2 under pressure is quite difficult to parameterize. The isothermal swellabillity is linear with the density while the isobar swellabilty is not.

So far these two experiments do not allow any firm conclusion and further experiments are needed to fully understand these observations.

4.4.4. Polystyrene Islands

We now consider the structural stability of PS islands of average thickness 1.72 nm supported by HF-etched Silicon in CO_2 environments at 32°C.

Figure 4.4.4, shows the GISAXS results during the in-situ monitoring of the morphology of islands when they are exposed to CO_2. One of the main changes is the extension of the 2-off specular rods located at q_{xy} = 0.007 Å^{-1} which decreases progressively as the pressure is increased. On the other hand, it is observed that the q_y position of each specular rod is fixed at all pressures. In addition to these two phenomena, a decrease in the contrast due to the increase in the CO_2 electron density is observed. In order to analyze these changes in more detail, we have performed linear cuts in the GISAXS images to extract information about the evolution of the morphological parameters. A vertical cut $I(q_z)$ at q_{xy}=0.0075Å^{-1} from the GISAXS image at α_i=0.05° and a horizontal cut $I(q_y)$ at q_z=0.05 Å^{-1} from the GISAXS image at α_i =0.18° were used to fit the data.

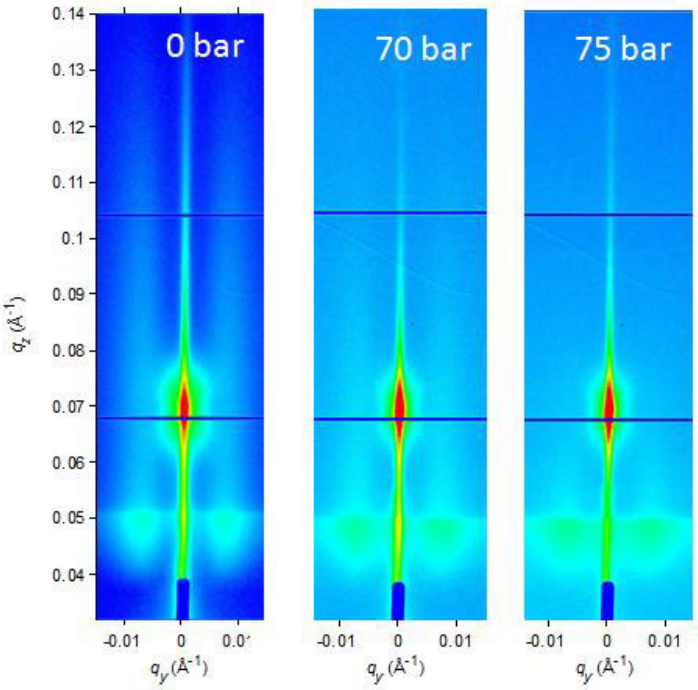

Figure 4.4.4 Experimental GISAXS patterns of PS islands at increasing CO_2 pressures.

At low pressure, polysdisperse islands with a cylindrical shape on a very thin film of PS were first considered in the fitting (see Fig. 4.4.5). Then at higher pressure, since islands are hyper swelling in the z direction while they do not swell laterally, we have considered that the central part of the island could swell more than the outer part and therefore we have assumed a hemispherical shape. Such an assumption was also motivated by the impossibility to properly fit the observed data to a cylindrical shape for the islands.

.

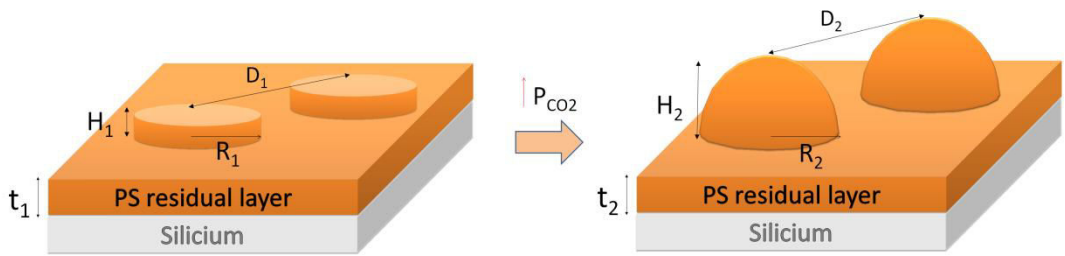

Figure 4.4.5 A cylindrical and hemispherical shape on a PS thin film.

Figure 4.4.6 shows the scattering curves in the q_z direction during the in-situ monitoring of the swelling of the PS islands exposed to CO_2. From this figure, we can clearly see that the location of the first minimum in the q_z-cut progressively decreases when the CO_2 pressure increases. This is the clear signature that the height of the islands increases.

The evolution of thickness versus pressure is shown in Fig. 4.4.6b and the values are reported in Table 4.4.1. From the fit to the data we find that the height changes from 4.3 nm at 0 bar to 12.4 nm at 80 bars showing a swelling of about 188%. Such a swelling is assigned to the sorption of CO_2 inside the polymer matrix. At low pressure the swelling is quite weak which supports the idea that the swelling is a function of the density of CO_2. When the density increases (i.e. close to 40bars) the swelling becomes much more pronounced. The swelling is drastically enhanced by the onset of critical fluctuations of CO_2 density as already reported by Koga et al.[Koga2011] as pressure becomes close to the supercritical pressure. Nevertheless a very high swellability of 188% was never reported in PS. The main reason is that the swelling varies in the opposite way of the thickness so that it is expected that thinner films should swell more than thicker ones. Let us now comment on the model used for fitting the data. During the fitting process we have encountered two major difficulties:

- modeling the width of the Yoneda peak
- describing the abrupt change in the intensity close to the silicon critical wave vector (q_z=0.025Å^{-1}) where a first minimum of the curve was observed.

These two problems were solved by considering the existence of a PS interlayer with a initial thickness of 2.2 nm at 0 bar that was gradually swelling to 4.5 nm at P=80 bar.

Pressure (bar)	R	D	$H_{CYLINDER}$ (nm)	$H_{HEMI-SPHEROID}$ (nm)	PS interlayer thickness 't' (nm)	Maximum Swellability[1] (%)	Φ_{CO2} [2]
1	19±4	60±20	4.3± 0.1	-	2.2±1	0	0
20	20±3	60±20	4.3± 0.1	-	2.2±1	0	0
40	20±4	60±21	4.5± 0.1	-	2.2±1	4.6	0.04
60	20±4	60±20	5.1± 0.1	-	2.6±1	18.6	0.15
70	19±4	60±20		7.4±0.8	3.6±1	72	0.41
75	19±4	60±20		10.5±1.4	3.8±1	144	0.59
80	19±5	60±20		12.4±1.8	4.5±1	188	0.65

[1] Maximum swellability= (H(P)-H (P=1bar))/H(P=1bar))x100%, where H(P) is the height of island at a given pressure.
[2] $\Phi_{CO2} \approx$ (H(P)-(H(P=1 bar)/H(P) where H(P) is the height of island at a given pressure.

Table 4.4.1 Parameters deduced from the GISAXS analysis, H is the height of the island, h_0 is the average thickness if it is consider as a homogeneous film, Φ_{CO2} is the fraction in volume of CO_2 in the PS island.

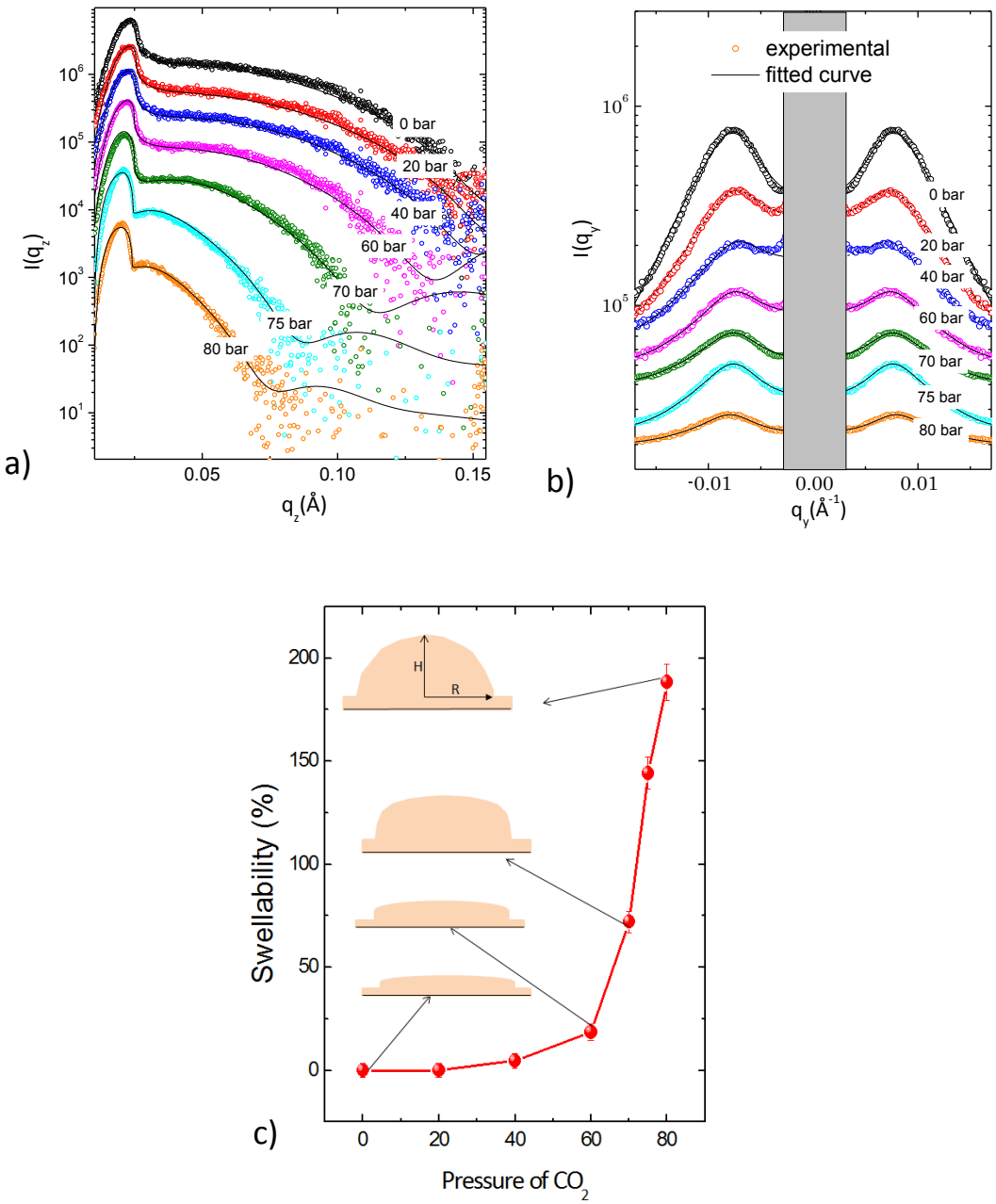

Figure 4.4.5 a) and b) Observed and calculated scans along q_z and q_y direction from GISAXS image during process of pressurization with carbon dioxide. Cut made at q_{XY}=7.5x10^{-3}Å^{-1} (α_i =0.05°) and q_Z=0.05 Å^{-1} (α_i =0.18°). c) Swellability (%) evolution as a function of CO_2 pressure. The best fits are plotted in this picture: for 0, 20, 40, 60 bar a cylindrical shape is used, for 70, 75 and 80 bar a hemispherical shape is used for fitting the data.

It is important to note that all the fitting results reported until 60 bars were obtained under the cylindrical shape approximation for the islands. However at higher pressures, the fits to the data were much better for hemispherical-shaped islands.

As a conclusion, we can state that PS islands exposed to CO_2 under pressure present the following characteristics:

- Neither the distance between neighbouring islands nor the average radius of the islands are affected by the elevation of pressure.

- The swelling of the islands is extremely important in the z direction with a swellability of 188% at a pressure of 80bar.

4.4.5. Spreading or stability of islands with CO_2

We want now to address why islands of PS do not spread when they are exposed to sc-CO_2. For this, we are going to calculate the intermolecular potential to analyze the wetting behavior for films exposed to sc-CO_2. It is important to keep in mind that for thicknesses less than 100 nm, the predominant interaction are the van der Waals forces, that are expressed through the effective intermolecular potential governed by the Hamaker constants. Hence, we calculate in the following section the Hamaker constant of the different materials before discussing the stability of PS on Si substrate in CO_2 environment through the effective intermolecular potential.

4.4.5.1. Calculation of the Hamaker constant of CO_2 and PS'

The Hamaker constant of CO_2 can be calculated using equation 4.1.12 provided the refractive index n and the dielectric constant ε of CO2 are known. In order to get these values, we have used the Clausius-Mossotti related following equations [Obriot1993].

$$\left(\frac{\boldsymbol{n}^2-1}{\boldsymbol{n}^2+2}\right)\frac{1}{\rho}=\boldsymbol{A_R}+\boldsymbol{B_R}\rho+\boldsymbol{C_R}\rho^2, \qquad \left(\frac{\varepsilon-1}{\varepsilon+2}\right)\frac{1}{\rho}=\boldsymbol{A_E}+\boldsymbol{B_E}\rho+\boldsymbol{C_E}\rho^2 \qquad [4.4.1]$$

The refractive index and the dielectric constant of CO_2 at a given pressure are calculated using the virial coefficients A_R,A_E ,B_R ,B_E and C_R,C_E given by Obriot et al. [Obriot1993] (A_R=6.664 cm^3mol^{-1}, B_R=1.9 cm^6mol^{-2}, C_R=-287 cm^3mol^{-3}, A_E=7.356 cm^3mol^{-1}, B_E=55.7

cm^6mol^{-2},C_E=-2694 cm^3mol^{-3}. The density was obtained from the National Institute of Standard and Technology NIST[1]. Using these values and equation 4.1.12, we can derive the Hamaker constant of CO_2 as a function of pressure (see Figure 4.4.6)

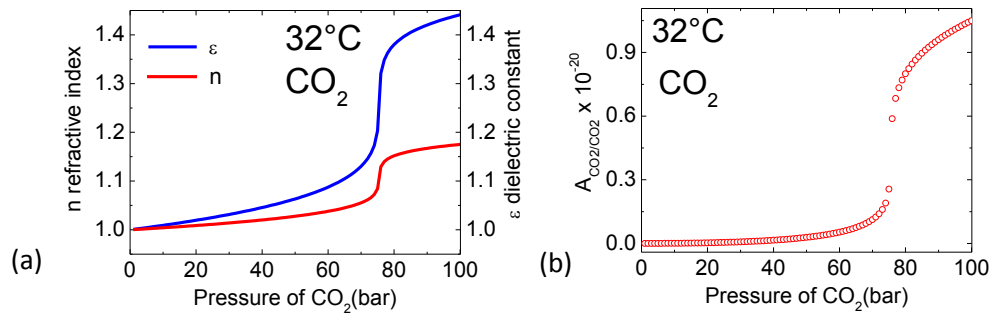

Figure 4.4.6 a) Refractive index, dielectric constant [Dunn1964, Michels1937] and b) Hamaker constant of CO_2 at 32°C as a function of pressure.

In the next step, we have to calculate the Hamaker constant of the CO_2-filled PS denoted , $A_{PS'}$. For the PS -CO_2 mixture, the dielectric constant $\varepsilon_{PS'}$ and the refractive index $n_{PS'}$ are calculated using the Lorentz-Lorentz mixing rule which is defined by

$$\frac{(n_{PS'}-1)^2}{(n_{PS'}+2)^2} = \Phi_{PS}\frac{(n_{PS}-1)^2}{(n_{PS}+2)^2} + \Phi_{CO_2}\frac{(n_{CO_2}-1)^2}{(n_{CO_2}+2)^2} \qquad [4.4.2]$$

$$\frac{(\varepsilon_{PS'}^{1/2}-1)^2}{(\varepsilon_{PS'}^{1/2}+2)^2} = \Phi_{PS}\frac{(\varepsilon_{PS}^{1/2}-1)^2}{(\varepsilon_{PS}^{1/2}+2)^2} + \Phi_{CO_2}\frac{(\varepsilon_{CO_2}^{1/2}-1)^2}{(\varepsilon_{CO_2}^{1/2}+2)^2}$$

where n_{PS}=1.75 and ε_{PS}=3.50 for PS thin film [Ata2012, Li2003], n_{C02} and ε_{CO2} in the visible frecuency are given in figure 4.4.6a. Φ_{PS} and Φ_{CO2} are the volume fraction of PS and CO_2 respectively and can be obtained from the GISAXS swelling measurements as shown in table 4.4.1. For the purposes of our calculation, we assume that the concentration of CO_2 in the islands is uniform. The volume fraction of CO_2 was estimated to be approximately 0, 0.04, 0.15, 0.41, 0.59 and 0.65 at 20, 40, 60, 70, 75 and 80 bar respectively (see Table 4.4.1).

The refractive indexes and the dielectric constant of CO_2/PS mixtures are given in the table 4.4.2. With the dielectric constants $\varepsilon_{PS'}$ and the refractive indexes $n_{PS'}$ at each pressure, we can calculate their respective Hamaker constant $A_{PS'/PS'}$ with equation 4.1.12.

[1] http://webbook.nist.gov/chemistry/

Then using the Hamaker constant of each material and replacing them in equation 4.1.8, we can finally calculate the Hamaker constant of the system Si/PS'/CO_2 and SiO_2/PS'/CO_2 which is given in the table 4.4.2

	0 bar	**20 bar**	**40 bar**	**60 bar**	**70bar**	**75 bar**	**80 bar**
Φ_{CO2}	0	0	0.04	0.15	0.41	0.59	0.65
$n_{PS'}$	1.75	1.75	1.73	1.67	1.54	1.44	1.42
$\varepsilon_{PS'}$	3.51	3.51	3.41	3.18	2.65	2.28	2.21
$A_{PS'-PS'}$ **x10^{-20} J**	10.7	10.7	10.2	9.02	6.32	4.49	4.13
$A_{Si/PS'/CO2}$ **x10^{-20} J**	-5.9	-5.9	-5.74	-5.71	-5.54	-4.74	-3.45
$A_{SiO2/PS'/CO2}$ **x10^{-20} J**	2.2	2.2	1.9	1.2	-0.12	-0.72	-0.61

Table 4.4.2 Calculation of the Hamaker constant of PS-CO_2 mixture. $A_{SI/SI}$= 25.6x10^{-20} J and $A_{SIO2/SIO2}$=6.6 x10^{-20} J.

4.4.5.2. Discussions

From Table 4.4.2, it can be observed that the Hamaker constants for $\mathbf{A_{Si/PS'/CO2}}$ and $\mathbf{A_{SiO2/PS'/CO2}}$ are influenced by the CO_2 volume fraction Φ_{CO2} filled inside the polymer. Hence the shape of the effective intermolecular potential is also modified.

- If we consider that the system is given by Si(HF)/PS'/CO_2, the Hamaker constant given in Table 4.4.2 has a negative sign over all the interval of pressures. This suggests that Polystyrene films on HF treated silicon in a CO_2 environment has a complete wetting behaviour at all the considered pressures. However this is not what is experimentally observed which rules out this hypothesis.

- If we assume the presence of SiO_2 covering the surface due to the quick oxidation of HF treated silicon, the system becomes composed of four materials Si/SiO_2/PS'/CO_2. In section 4.4.2, this consideration gave us a fair explanation for the appearance of islands instead of a film as the most stable structure in air condition. For this reason, we also consider this hypothesis as a reasonable starting point for the study of the stability of PS islands in CO_2 environment.

The effective intermolecular potential of the system Si/SiO_2/PS'/CO_2 is defined as:

$$\Phi_{VDW}(\boldsymbol{h}) = \frac{\boldsymbol{c}}{\boldsymbol{h}^8} - \frac{\boldsymbol{A}_{SiO_2/PS'/CO_2}}{12\pi\boldsymbol{h}^2} + \frac{\boldsymbol{A}_{SiO_2/PS'/CO_2} - \boldsymbol{A}_{Si/PS'/CO_2}}{12\pi(\boldsymbol{h}+\boldsymbol{d})^2} \qquad [4.4.3]$$

Here PS' indicates that in the calculation, carbon dioxide is absorbed within the PS film. $A_{SiO_2/PS'/CO_2}$ and $A_{Si/PS'/CO_2}$ are given in table 4.4.2 at each pressure. From these values we can derive the potential Φ(h) plotted in Figure 4.4.7 for thicknesses up to 7nm.

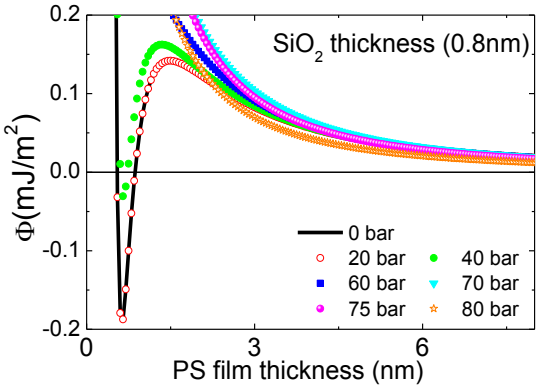

Figure 4.4.7 Reconstructed effective interface potential Φ(h) for polystyrene film on silicon wafer with oxide layer thicknesses of 0.8nm under CO_2 environment using equation 4.4.3. $A_{Si/PS/CO2}$ and $A_{SiO2/PS/Air}$ are given in table 4.4.2 at each pressure. For all pressures, we consider the same strength "c" for the short range repulsive interactions c= 6.3×10^{-76} J/m^6.

The curves of the potential Φ(h) for the $Si/SiO_2/PS'/CO_2$ system at 32°C describe a metastable film at low pressure and stable at high pressure. At low pressure, the curves show a shift to smaller values of "h" as the CO_2 content in the film increased. Hence spinodal dewetting should be achieved in thinner regimes when CO_2 interacts with PS islands. Interestingly there is a threshold pressure (60bar) above which the effective potential smoothly decreases with h. Above this threshold, the effective potential is consistent with a stable film which means that the film should spread. However this behaviour was not experimentally observed as PS islands were not disappearing at high pressure.

- Another explanation of why polystyrene islands do not spread over the silicon surface and swell only in the perpendicular direction can come from the anisotropic dynamic of polymer thin films. Inoue et al. shows that for a film of 20 nm, the thermal expansion is much easier along the normal direction with respect to the substrate than in the parallel direction [Inoue2007]. These studies suggest that the rate of swelling is anisotropic for a 20nm film which in turn should be

even more anisotropic for 5 nm PS islands. This assumption can explain our observations.

- The last hypothesis lies on the fact that very thin films on the order of h <10nm may present strong interaction between the substrate (silicon treated with HF) and the polymers that can dominate over the van der Waals interaction in the analysis of the stability of PS thin films.

Despite the various hypotheses offered none of them seem to explain clearly and satisfactorily the observed behaviour. As a conclusion the reason for which islands are very stable when they are exposed to sc-CO_2 is still controversial and deserves further studies.

In conclusion, we have presented in-situ XRR and GISAXS studies of the swellability as a function of pressure of Polystyrene confined in one (thin film) and two dimensions (islands). The results are similar to those reported by other groups confirming that thin films swell when they are exposed to CO_2. However in the case of PS islands, we observe a much larger swellability than for a homogeneous thin film. This effect can be attributed to the larger free surface in the island compared with that of thin films which allows for a greater absorption of CO_2. In addition, it was shown that PS islands (h<10 nm) supported on HF treated silicon do not spread in supercritical CO_2 environment. PS islands remain at a fixed position and grow only in the perpendicular direction.

Bibliography

[Angell2000] Angell, C.A.; Ngai, K.L.; McKenna, G.B.; McMillan, P.F.; Martin, S.W. J. Appl. Phys. (2000) 88, 3113.

[Ata2009] Ata, S.; Muramatsu, M.; Takeda, J.; Ohdaira, T.; Suzuki, R.; Ito, K.; Kobayashi, Y.; Ougizawa, T. Polymer 50 (2009) 3343–3346.

[Ata2012] Ata, S.; Kuboyama, K.; Ito, K.; Kobayashi, Y.; Ougizawa, T., Polymer 53 (2012) 1028-1033.

[Bergeron2000] Bergeron, V.; Bonn, D.; Martin, J. Y.; Vovelle, L. Nature (2000) 405, 772.

[Bertrand2002] Bertrand, E., J. Petrol. Sci. Eng. (2002)33, 217.

[Bonn2009] Bonn, D.; Eggers, J.; Indekeu, J.; Meunier, J.; Rolley, E., Rev. Mod. Phys. (2009) 81, 739,

[Brochard-Wyart1990] Brochard-Wyart, F. Langmuir (1991), 7, 335-338.

[Cohen1959] Cohen, M.H.; Turnbull, D., J. Chem. Phys. (1959) 31 1164.

[Cooper2000] Cooper, A. J Mater Chem (2000) 10, 207–234.

[de Gennes1985] de Gennes P. G., Reviews of Modern Physics, (1985), Vol. 57, No. 3, Part I.

[DeSimone1992] DeSimone, J.; Guan, Z.; Elsbernd, C. Science (1992) 257, 945–947.

[Donth2001] Donth, E. The Glass Transition: Relaxation Dynamics in Liquids and Disordered Materials, Springer, Berlin, 2001.

[Dublek2004] Dlubek, G.; Kilburn, D.; Bondarenko, V.; Pionteck, J.; Krause-Rehberg, R.; Alam, M. A., Positron Annihilation: A Unique Method for Studying Polmers Macromolecular Symposia 210, Reactive Polymers 2003, Ed. H.-J. Adler, Weinheim, WILEY-VCH, March 2004, p. 11.

[Dunn1964] Dunn, A.F. Canadian Jounal of Physics, (1964) Volume 42.

[Forrest2002] Forrest, J. A., European Physical Journal E: Soft Matter (2002), 8, (2), 261-266.

[Gibaud&Vignaud] G. Vignaud and A. Gibaud, Program REFLEX18, a matlab routine for the simulation of specular x-ray reflectivity data with the matrix technique.

[Graf1990] Gräf, D.; Grundner, M.; Schulz, R.; Mühlhoff, L. Journal of applied physics, 1990, 68(10), 5155-5161.

[Hsu2000] Hsu, D. T.; Shi, F. G.; Zhao, B.; Brongo, M. In Theory for the thickness dependent glass transition temperature of amorphous polymer thin films, Proceedings - Electrochemical Society (2000), 99-7(Low and High Dielectric Constant Materials, and Thin Film Materials for Advanced Packaging Technologies), (2000) pp 53-61 .

[Jacobs1998] Jacobs, K.; Herminghaus, S.; Mecke, K.R. Langmuir (1998) 14, 965.

[Kazarian1996] Kazarian, S. G.; Vincent, M. F.; Bright, F. V.; Liotta, C. L.; Eckert, C. A. , J. Am. Chem. Soc. (1996) 118, 1729-1736.

[Koga2002] Koga, T.; Seo, Y. S.; Zhang, Y.; Shin, K.; Kusano, K.; Nishikawa, K.; Rafailovich, M. H.; Sokolov, J. C.; Chu, B.; Peiffer, D.; Occhiogrosso, R.; Satija, S. K. Phys. Rev. Lett. (2002) 89, 125506.

[Koga2004] Koga, T.; Ji, Y.; Seo, Y. S.; Gordon, C.; Qu, F.; Rafailovich, M. H.; Sokolov, J. C.; Satija, S. K. J. Polym. Sci. B: Polym. Phys. (2004) 42, 3282.

[Koga2003] Koga, T.; Seo, Y. S.; Shin, K.; Zhang, Y.; Rafailovich, M. H.; Sokolov, J. C.; Chu, B.; Satija, S. K. Macromolecules (2003) 36, 5236.

[Koga2005] Koga, T.; Akashige, E.; Reinstein, A.; Bronner, M.; Seo, Y. S.; Shin, K.; Rafailovich, M. H.; Sokolov, J. C.; Chu, B.; Satija, S. K. Physica B (2005), 357, 73.

[Koga 2011] Koga, T.; Gin, P.; Yamaguchi, H.; Endoh, M. K.; Asada, M.; Sendogdular, L.; Kobayashi, M.; Takahara, A.; Akgun, B.; Satija, S. K.; Sumi, T. Polymer (2011) 52, 4331−4336.

[Lee1968] Lee, L.H., J. Appl. Polym. Sci., (1968). 12, 719

[Li2002] Li, F.; Balazs, M.K., 21th Annual Semiconductor Pure Water and Chemicals Conference Proceedings, Santa Clara, CA, March 2002.

[Li2007a] Li, Y.; Park, E. J.; Lim, K. T.; Johnston, K. P.; Green, P. F. Journal of Polymer Science: Part B: Polymer Physics, Vol. 45, (2007) 1313–1324.

[Li2007] Li, Y.; Pham, J. Q.; Johnston, K. P.; Green, P. F. Langmuir (2007) 23, 9785-9793.

[Lou1995] Lou, X.; Janssen, H.G.; Cramers, C. A. J Microcolumn (1995), 7, 303–317.

[Meli2004] Meli, L.; Pham, J. Q.; Johnston, K. P.; Green, P. F., Physical Review E(2004) 69, 051601.

[Michels1937] Michels, A.; Hamers, J., Physica IV, (1937)10.

[Mukherjee2011] Mukherjee, R.; Sharma, A.; Steiner, U., Surface Instability and Pattern Formation in Thin Polymer Films Generating Micro- and Nanopatterns on Polymeric Materials. Edited by A. del Campo and E. Arzt, 2011 WILEY-VCH Verlag GmbH & Co. KGaA, Weinheim.

[Muller-Buschbaum2003] Muller-Buschbaum P., Eur. Phys. J. E (2003)12, 443–448

[Obriot1993] Obriot, J.; Ge, J.; Bose, T.K.; St-Arnaud, J.M., Fluid Phase Equilib. (1993) 86 315–350.

[Oka2008] Oka, T.; Ito, K.; He, C.; Dutriez, C.; Yokoyama, H.; Kobayashi, Y., J. Phys. Chem. B (2008) 112, 12191–12194.

[Phan2003] Pham, J. Q.; Sirard, S.M.; Johnston, K. P.; Green. P. F., Physical Review Letters, (2003) 91, 17, 175503-1.

[Phan2004] Pham, J. Q; Johnston, K. P.; Green, P. F., J. Phys. Chem. B (2004), 108, 3457.

[Plonka2013] Plonka, A. M.; Banerjee, D.; Woerner, W. R.; Zhang, Z.; Nijem, N.; Chabal, Y. J.; Li, J.; Parise, J. B., Angew. Chem. Int. Ed. (2013), 52, 1692 –1695.

[Seeman2000] Seemann, R.; Herminghaus, S.; Jacobs, K., Phys. Rev. Lett. (2001), 86, 5534.

[Seeman2001] Seemann, R.; Jacobs, K.; Blossey, R. J. Phys.: Condens. Matter, (2001), 13, 4915–4923.

[Shahidzadeh2003] Shahidzadeh, N.; Bertrand, E.; Dauplait, J.P.; Borgotti, J. C.; D. Bonn, (2003) Transp. Porous Media 52, 213.

[Struik1977] Struik, L.C.E., Polymer Engineering and Science, (1977) Vol 17, No. 3.

[Tabelin2004] Tabeling, P., Microfluidics (2004); EDP Sciences: Paris.

[Tsui2003] Tsui, O.K.C.; Wang, Y.J.; Zhao, H.; Du, B.,Eur. Phys. J. E (2003) 12, 417–425.

[Wu1982] Wu, S., Polymer Interface and Adhesion, Marcel Dekker, New York, NY, 1982, p. 87.

[Zhao1993] Zhao, W.; Rafailovich, M. H.; Sokolov, J.; Fetters, L. J.; Plano, R.; Sanyal, M. K.; Sinha, S. K.; Sauer , B., Phys. Rev. Lett. (1993), 70, 1453.

CHAPTER 5

5. Analysis of Silica Mesoporous thin film

The aim of this chapter is to describe the study of mesoporous silica thin films by x-ray scattering. We first focus in section 5.1 and 5.2 on the preparation of these silica films using two types of surfactants to template and to structure the silica backbone. One of them is the well-know cethyl trimetyl ammonium bromide (CTAB) while the second one is a fluorinated one the so-called FSN that we will present later on. For the preparation of CTAB/silica films, we briefly recall the procedure already reported by [Besson2003] and [Dourdain2006]. On the other hand, for FSN/silica films, several experiments were performed with the aim of optimizing the methodology to obtain an ordered structure. For the characterization of these films, we have mainly used X-ray scattering techniques such as XRR and GISAXS.

In section 5.3, we show that GISAXS patterns of thin films with ordered internal 3D mesoscale structures can be quantitatively modeled, using the Distorted Wave Born Approximation (DWBA) and related approximations. We go beyond what has previously been achieved in this field by addressing how the anisotropy of the scattering objects can be assessed from a complete fit to the data contained in the GISAXS patterns.

Finally, It is very important to understand that once a silica thin film has been templated by a surfactant and is highly organized, the removal of the surfactant is a critical issue. This is addressed in section 5.4 in which we report in-situ x-ray measurements. For CTAB templated thin films, the surfactant was removed by simple annealing while for FSN, we used an alternative method to extract the surfactant, based on the use of supercritical carbon dioxide. The different stages of the surfactant removal were studied with in-situ by x-ray scattering techniques.

Materials presented in this chapter are published in the paper 'Using Three-Dimensional 3D Grazing-Incidence Small-Angle X-ray scattering (GISAXS) Analysis to probe pore deformation in Mesoporous Silica Film' E. A. Chavez Panduro, Håvard Granlund, Michael Sztucki, Oleg Konovalov, Dag W. Breiby , and Alain Gibaud, ACS App. Mater. Interfaces, (2014), v. 6, pp. 2686−2691

5.1. Preparation of mesoporous thin films

The preparation of mesoporous silica thin films on silicon substrate is based on sol-gel chemistry combined to the use of the Evaporartion Induced Sel-Assembly (EISA) concept pioneered by J. Brinker. The principle is to use ampliphilic molecules known as surfactants that are diluted an acidic aqueous solution containing ethanol at a concentration below their Critical Micelle Concentration (CMC) . This solution is then mixed with another one that contains the inorganic precursor. The final solution is dip-coated on a silicon substrate at a given speed and at a controlled Relative Humidity (RH). During the withdrawal of the silicon substrate from the solution a liquid film forms on the substrate. Due to the fast evaporation of ethanol, the surfactant concentration becomes bigger than the CMC so that it self-assembles into an hybrid organic/inorganic organised mesostructure (see Fig. 5.1.1).

In this section, an overview is performed of the principles and mechanism for each step in the preparation of the mesotructured film, i.e. the reactions which take place to form the inorganic matrix, the different surfactants used and the EISA mechanism.

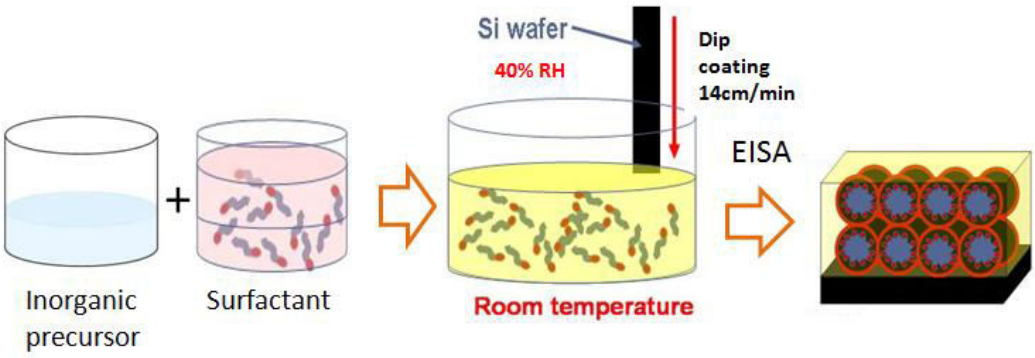

Figure 5.1.1 Steps for the preparation of a mesorporous thin film.

5.1.1. Inorganic matrix: Sol-gel process

The inorganic matrix formed by the precursor was prepared using the sol-gel method. This method was discovered by Elbelmen [Ebelmen1846] and it is based on the hydrolysis and condensation of the inorganic precursor [Brinker1999, Hench1999].

In this study, we use the tetraethyl ortholsilicate (TEOS) or silicon tetraethoxide as a precursor. The formula of this silicon alkoxide is given by $Si(C_2H_5O)_4$ or $Si(OR)_4$ where the alkyl group R is C_2H_5.

During the hydrolysis the liquid precursor, $Si(OR)_4$ is replaced via the nucleophilic attack of the oxygen atom of a water molecule under release of alcohol and the formation of a the silanol groups (Si-OH):

$$Si(C_2H_5O)_4 + H_2O \rightarrow (C_2H_5O)_3Si(OH) + C_2H_5OH$$

Then, the hydrated silica tetrahedral interacts in a condensation reaction during which a water molecule is released thus forming a Si-O-Si bond.

$$(C_2H_5O)_3Si(OH) + (HO)Si(C_2H_5O)_3 \rightarrow (C_2H_5O)_3SiOSi(C_2H_5O)_3 + H_2O$$

Linkage of additional Si-OH tetrahedral occurs during the polycondensation reaction and eventually results in a silica gel network. The gel is mainly formed of silica colloidal particles that are not fully condensed together with water molecules which are trapped inside the network. The H_2O and alcohol expelled from the reaction remains in the pores of the network.

With time the colloidal particles and condensed silica species link together to become a three-dimensional network. The physical characteristics of this gel network depend greatly upon the size of particle and extent of cross-linking prior to gelation [Hench1990].

The existence of residual Si-OH groups allows further condensation reaction and causes contraction of the gel. This leads to a contraction of the lattice and a release of solvent. This phenomenon is called "syneresis". The gel is called xerogel when after a period of aging is dried at low temperature (25-100°C). When the xerogel is then densified by heat treatments, glasses or ceramics can be formed [Brinker1990].

Finally, it is important to remark that the rates of hydrolysis-condensation reactions can be controlled by adjusting some of the following reaction conditions:

- precursor type,
- solvent type and pH,
- Concentrations of the various species present in solution.

A precise adjustment of these variables is a key to tuning the size, shape and surface chemistry of the inorganic polymers therefore allowing a precise control the properties of the final material [Brinker1990, Pierre1998].

5.1.2. Surfactants

The surfactants are amphiphilic polymers that form micelles at a specific concentration known as the CMC. These micelles form supramolecular structures that can be cemented by inorganic molecules. In the preparation of mesoporous materials it is necessary to use these micelles, which can serve both as a model pattern as well as a support in the formation of an inorganic matrix.

Depending on the type of surfactant, its concentration and temperature as well as other variables such as the surfactant/water weight percentage and especially the surfactant/Si molar ratio, the mesoporous material can adopt different structures as 3D hexagonal, cubic, lamellar, etc.

5.1.2.1. Hydrogenated surfactant (CTAB) :

Surfactant such as CTAB has been widely used for the formation and structuring of mesoporous materials. CTAB is an ionic surfactant consisting of an alkyle hydrophobic long chain and of a hydrophilic cationic head. Its chemical formula is expressed as $(CH_3(CH_2)_{15}\ N^+(CH_3)_3\ Br$ with a molar mass of 364.4g/mol

Figure 5.1.2 Schematic representation of the Cetyltrimethylammonium bromide(CTAB) surfactant

The average radius for the spherical and cylindrical micelles formed by the molecules of CTAB is about 2.1 nm. The phase diagram of the mesostructured silica films was studied by Sophie Besson [Besson2003]. It was shown in the study that three different crystallographic structures can be obtained by varying the molar ratio CTAB/Si and the silica condensation time. These three structures are:

- A 3D hexagonal ($P6_3/mmc$) structure formed by dense packing of spherical micelles.
- A 3D cubic (Pm3n) structure, composed of ellipsoidad and spherical micelles.
- A 2D hexagonal (p6m) structure composed of cylindrical micelles. (see Fig. 5.1.3)

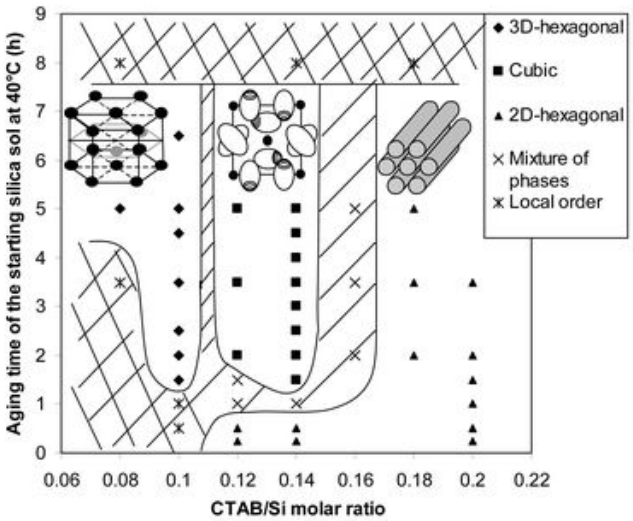

Figure 5.1.3 Phase diagram deduced from GISAXS experiments for mesoporous silica thin film. The domain of existence of the three micellar phases is showed as a function of the CTAB/Si molar ratio and aging time of the initial silica sol at 40°C [Besson2003].

5.1.2.2. Fluorinated surfactant (FSN)

The FSN-100 is a fluorinated surfactant whose terminal chains contain not only C-H groups but also C-F groups. The approximate chemical formula for FSN is expressed as $C_8F_{17}C_2H_4(OCH_2CH_2)_9OH$ also labeled as $R_8^F(EO)_9$ with an approximate molar mass of 870g/mol. This surfactant has been provided by the Group of Marie Joe and J.L. Blin of the University of Nancy.

The fluorine atom is larger than the hydrogen atom (Van der Waals radius, R=1.74 Å vs R=1.20 Å). With this values, the resulted average volumes of CF_2 and CF_3 groups are estimated respectively about 38 and 92 $Å^3$, while the average volumes of CH_2 and CH_3 groups are of the about 27 and 54 $Å^3$ respectively. Consequently, the fluorinated chain is more rigid and bulkier than the hydrogenated chain and also adopts a helical conformation. The lengths of hydrophobic (C-F) and hydrophilic (C-H) part of the FSN are 1.5 and 1.6 nm respectively. Thus, the diameter of the micelles rod can be estimated 6.2nm [Blin2004].

The phase diagram of the binary system FSN/water presented in the Fig. 5.1.4a has been reported by the J. L. Blin group [Blin2004]. This diagram shows two micellar phases Hexagonal and Lamellar. In contrast to the case of CTAB surfactant, the cubic phase was not observed. The hexagonal symmetry is observed for a FSN/water weight concentration between 50 % -75 % at a temperature of 20°C.

The preparation of powder mesoporous materials for FSN/TMOS[2] systems has been reported in the work of [Blin2004, Blin2005, Zimmy2009]. The molar ratio of FSN/TMOS, for which the hexagonal 2D structure is found, is within the range of 0.119 to 0.175 (see Fig. 5.1.4b).

However, at the present time no reports on the formation of silica mesoporous films using FSN as a surfactant were found in the literature. With no precedent, we had to performed several experiments based on a trial and error procedure in which we have varied some parameters to obtain the formation and structuring of a hybrid mesophase formed by the FSN and TEOS.

[2] TMOS : Tetramethyl orthosilicate

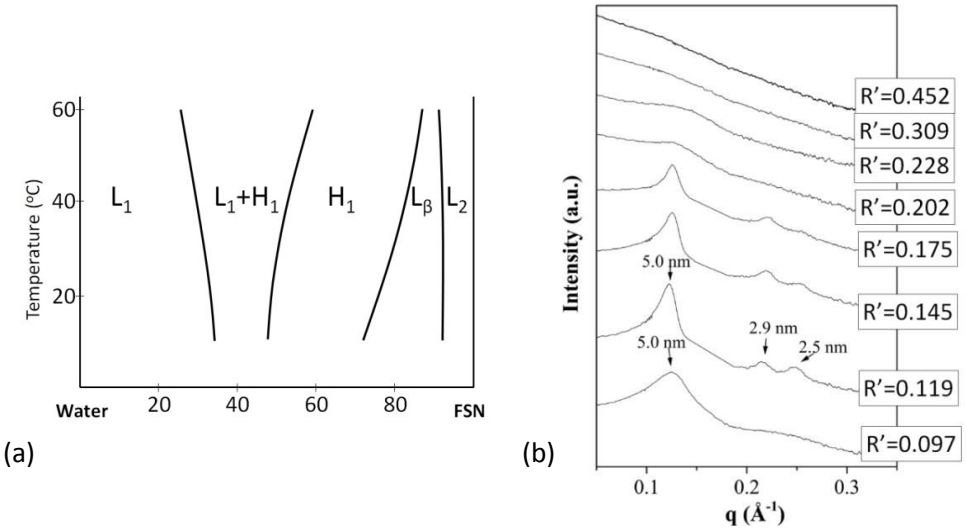

Figure 5.1.4 a) Phase diagram of the binary system FSN/water. b) Mesoporous materials SAXS patterns synthesed with different surfactant/Si molar ratio (R').

It is worth noting that the substitution of hydrogenated atoms by fluorines ones enhances the chemical and thermal stability of the surfactant. i.e. a C-F bond energy of 552kJmol^{-1} instead of 338kJmol^{-1} for the C-H bond [Kissa1994]. The presence of fluorine atoms also strongly affects the properties of the surfactants and particularly its hydrophobicity.

The specific solvent-molecular interactions between low dielectric fluids, such as CO_2, and fluorocarbon surfactants can be exploited also for pore expansion of mesostructured silica because the '**CO_2-philic'** fluorinated tail is readily penetrated by CO_2 at high pressure [Ghosh2008]. The interaction can be expected to be further enhanced when partly fluorinated surfactants are used, such as those described here, because local dipole created by the CF_2 to CH_2 transition induces CO_2 quadruple –surfactant interaction.

5.1.3. EISA mechanism

In the preparation of mesostructured films it is necessary that the reactions between the inorganic matrix (sol-gel) and the formed micelles are properly achieved. In order to favour this interaction a mechanism known as EISA (Evaporation-Induced Self-Assembly) has been widely used since it was established in 1997 by Brinker [Brinker1997, Brinker1999].

This mechanism consists in preparing a very diluted solution containing the precursor, the surfactant in a volatile solvent in which the surfactant concentration is lower than the CMC. Then, when the solution is deposited on the substrate via dip-coating or spin-

coating, a very thin silica-surfactant layer will form on the substrate. The drying process begins as soon as the substrate is withdrawn from the solution. As the film dries, the evaporation of solvent concentrates the surfactant, silica and other non-volatile species.

The progressive drying increases the surfactant concentration and this drives the self-assembly of silica-surfactant micelles, which further organize themselves into an organized silica-surfactant mesostructure [Brinker1999, Grosso2004]. The Figure 5.1.5c shows schematically the formation of these materials.

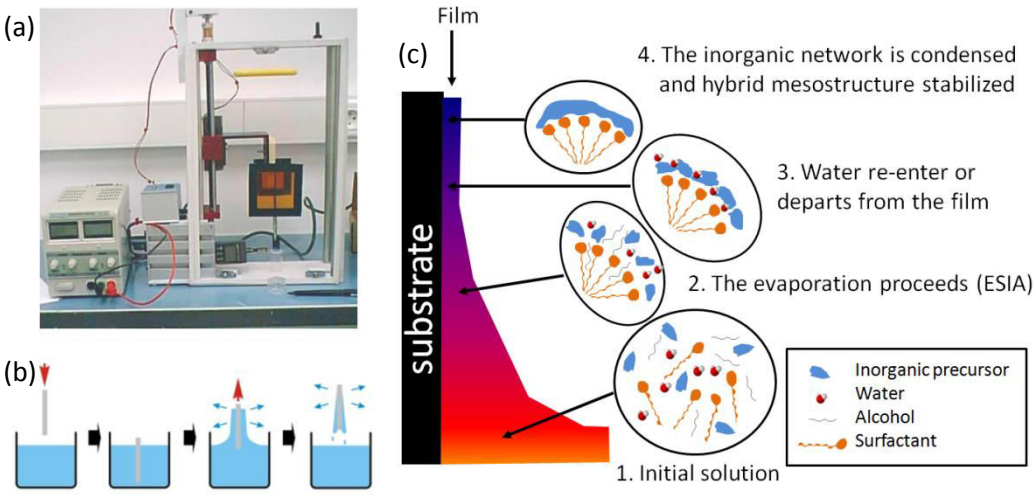

Figure 5.1.5 a) Dip-coater designed by A. Gibaud and built by G. Ripault, b) Stages of the dip coating process b) Schematic diagram of mesoestructure thin film by **dip coating**. Step1: Initial solution, where surfactant and silica are mixed homogenously. Step2: Evaporation proceeds and micelles start to form. Step 3: Evaporation is complete. The film equilibrates with its environment and the final structure depends on the humidity. Step4: Further inorganic condensation and stabilisation

5.2. Preparation and Characterization of mesoporous thin films

This section is focused on the description of the methodology used to prepare these films as well as on their characterization . For the preparation of the CTAB/silica film we briefly summarize the procedure already reported by [Besson2003] and [Dourdain2006]. For the preparation of FSN/silica film, several experiments were performed with the aim of optimizing the methodology to obtain an ordered structure. For the characterization process of these films, we have used mainly X-ray scattering techniques such as XRR and GISAXS.

5.2.1. **Using CTAB as a surfactant:**

Film Preparation

The preparation of silica thin films with a 3D hexagonal structure using CTAB as a surfactant requires a molar ratio **R'(surfactant/Si) =** 0.1 [Besson2003], and a CTAB/water weight percent of **33% .**

The process begins with the preparation of a ***stock solution*** containing *5.2g of tetraethoxysilane (TEOS), 3.45g of ethanol and 0.55g of* H_2O *(pH = 2.57) that is mixed and stirred at room temperature for 1h. Then, a second solution (**micellar solution**) containing 0.911g of CTAB, 20g of EtOH and 1.8g of* H_2O *(pH = 1.26) is prepared. Finally the stock solution iss added to this solution*

After 4 days of stirring at 400rpm, the thin films are dip-coated at a constant withdrawal velocity of 14cm/min on a silicon wafer cleaned in an ultrasonic bath using ethanol and dried. The final solution has a molar composition of 1 TEOS: 20.4 C_2H_5OH : 5.2 H_2O : 4.10^{-3} HCl : 0.10 CTAB . The composition of the solution is adjusted so as to make films about 120nm thick.

In the present study, all films were prepared at a relative humidity about 40% and a temperature of 25°C. The optimization of the parameters such as time of aging, thickness, relative humidity, etc, were studied by Sandrine Dourdain [Dourdain2006] in a previous work of LPEC Group at the university of Le Mans.

Film Characterization

A mesoporous silica thin film with the 3D hexagonal structure was then characterized by x-ray techniques.

We first performed x-ray reflectivity measurements to obtain the thickness and the roughness of each layer of the film. The main objective is to define the electron density profile (EDP) of the film. The observed data are analyzed with a program written in Matlab by Alain Gibaud and G. Vignaud [Gibaud&Vignaud]. The model used for the data fitting is composed by a buffer of silica, a repetition of N-bilayer of CTAB and silica and a cap-layer of silica (see Fig. 5.2.1).

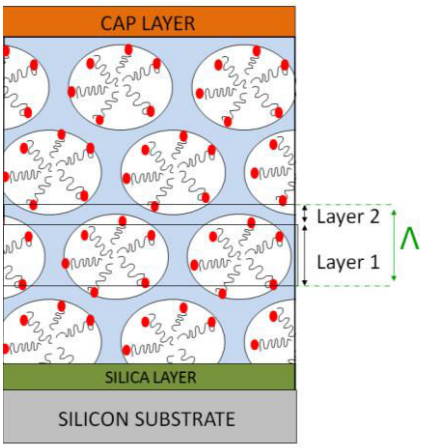

Figure 5.2.1 Schematic representation of the CTAB/silica mesoporous film composed of a periodic repetition of a bi-layer (LAYER 1+LAYER2) that is supported by a silicon substrate. For this model the interface substrate-film and film-air are considered as buffer and cap-layer respectively. For clarity, the figure shows only 3 bi-layers of the N bi-layers in the film.

In Fig. 5.2.2., we show the XRR curve of the as prepared film. On the measured q_z-range, this curve exhibits 2 Bragg peaks and a series of Kiessig fringes that are the signature of a quasi perfect organization of the film having smooth interfaces. The Bragg peaks evidence the existence of a period Λ inside the film which is due to the alternated repetition of two effective layers made of silica walls (LAYER 2) and silica walls plus the surfactant (LAYER 1). Note that when the surfactant is removed from this layer, layer 1 is composed of pores + silica walls. The separation Δq between the two Bragg peaks immediately gives the period of repetition Λ of these layers. At room temperature this value is Λ= 3.97nm. Counting the number of fringes between two Bragg peaks reveals that 25 periods are observable in this film which in turn shows that the total thickness of the film is close to 27Λ. The inset of this figure shows a zoom around the critical angle of total reflection. Two q_c are visible: the first one corresponds to the average electron density of the film whereas the second one is that of the silicon substrate (~ 0.0317 $Å^{-1}$). We have already reported how such an XRR curve can be calculated by the matrix technique with as a result the determination of the electron density profile of the film. All the parameters adjusted by a fit to the experimental data are reported in Table 5.2.1.

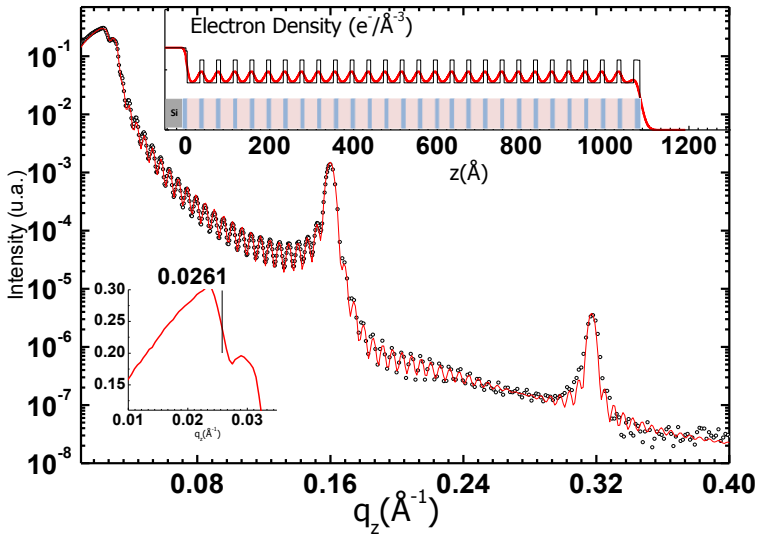

Figure 5.2.2 a) Observed and Calculated XRR curves of the as prepared film, the electron density profile is shown in the top inset while a zoom of the critical q_c region is shown in the bottom inset. This XRR measurement was performed at IMMM (Université du Maine) with 8KeV.

	Substrate	Buffer Substrate-Film	Layer 1 silica wall +surfactants	Layer 2 silica wall	Caplayer Film-Air
q_c(Å^{-1})	0.032	0.031	0.024	0.032	0.025
density (e-/ Å^3)	0.73	0.688	0.419	0.732	0.444
roughness (nm)	0	0.27	1.10	0.68	0.82
thickness (nm)	-	0.93	3.01	0.96	1.5

Table 5.2.1 Parameters used to simulate the XRR curve

GISAXS measurements were performed to determine the 3D structure of the films. The GISAXS images were simulated using the so-called *SimDiffraction* software [Breiby2008].

In Figure 5.2.3 we show the GISAXS pattern of the as prepared film together with a simulation of this pattern according to the *SimDiffraction* program. This pattern is fully consistent with a structure having the $P6_3mmc$ symmetry, colloquially referred to as "hexagonal close packed" structure. The pattern can be indexed according to the given hexagonal space group with lattice parameters *a* = 5.56 nm and *c* = 6.97 nm, oriented with the *c* axis parallel to the substrate normal. This shows that the initial structure is a distorted hexagonal compact structure since the ratio c/a strongly differs from 1.73 due the shrinkage of the structure along the c axis. In order to correctly simulate the Bragg spots intensities it was necessary to consider ellipsoidal shaped micelles with the ratio of

the long axis over short axis of the ellipsoid of about 0.8. The ellipsoid was found to be oriented along the x,y axis of the hexagonal structure (see Fig. 5.2.4). The simulated pattern is shown in figure 5.2.3b. These values are in perfect agreement with those reported by [Besson2000], who first unravelled this structure. A more detailed analysis of this sample was reported in the section 5.3.

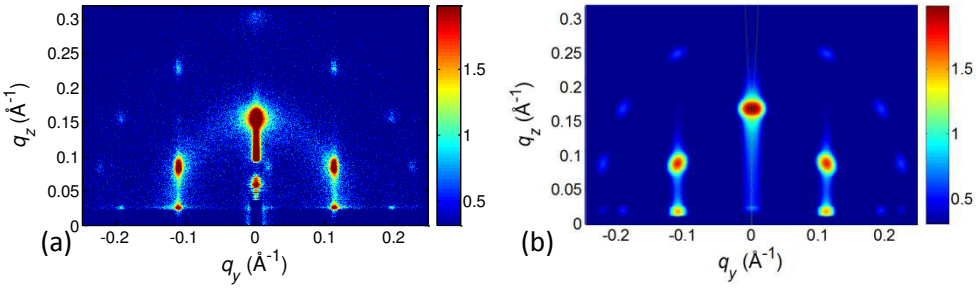

Figure 5.2.3 (a) Observed and (b) simulated GISAXS pattern of the as prepared film. This GiSAXS measurement were performed at IMMM (Université du Maine) with 8KeV, the incidence angle was 0.20°.

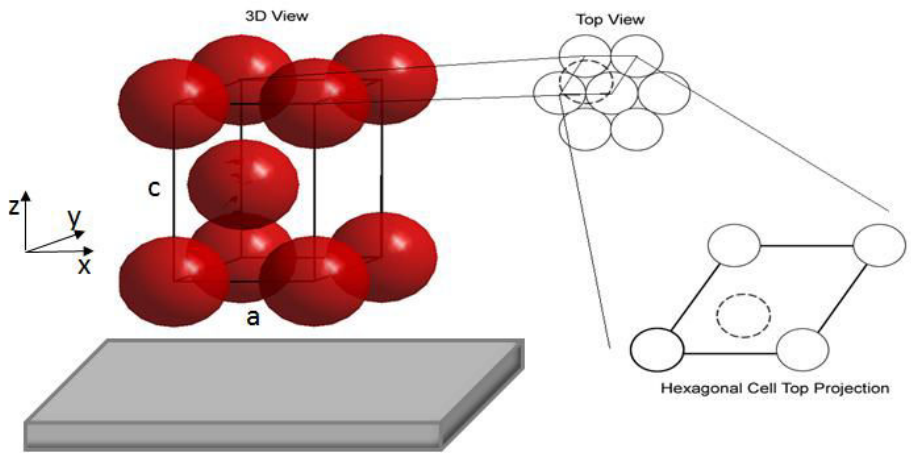

Figure 5.2.4 Schematic representation of pore structure obtained in silica mesoporous thin film using a CTAB/Si molar ratio of 0.1. The space group of the structure obtained is $P6_3mmc$.

5.2.2. **Using FSN as a surfactant :**

Film Preparation

Silica thin films were also designed using FSN as a surfactant. Different parameters were varied in order to obtain a highly organized hybrid mesostructure formed between FSN and TEOS.

In order to form well-structured 2D or 3D hexagonal thin films, we prepare (FSN/TEOS) solutions following the same method adopted for CTAB silica films using ethanol as the solvent and HCl as the acid. The FSN /H_2O weight percentage used for these solutions was of 65%, this weight percent is located in the center of the hexagonal zone in the binary pattern FSN /H_2O represented in Figure 5.2.5a.

For the stock solution, the preparation is similar to the CTAB case. *"5.2g of tetraethoxysilane (TEOS), 3.45g of ethanol and 0.55g of H_2O (pH = 2.57) were mixed and stirred at room temperature for 1h."*

For the micellar solution, a mass quantity m_{FSN} (g) of FSN was dissolved in 20g of ethanol and m_{H20} (g) of acid water (0.055 M with a pH = 1.26 using HCl). *Then the stock solution was added to this solution.* The mass m_{FSN} (g) of FSN and m_{H20} (g) of water were calculated using molar ratio and weight percent formula defined by:

$$\text{Mole ratio} = \frac{n_{FSN}}{n_{Si}} \quad , \quad \%weight_{FSN/\mathrm{H2O}} = \left(\frac{m_{FSN}}{m_{FSN} + m_{\mathrm{H2O}}} \cdot 100\% \right)$$

n_{FSN}/n_{Si}	m_{FSN} (g)	m_{H2O} (g)
0.1	2.175	1.13
0.13	2.92	1.5

For the formation of mesostructured films, several different molar ratios and aging times of the final solution were tested in order to achieve the same structure showed by K. Zimmy [Zimmy2009], who reported an hexagonal phase (for the mesoporous silica powder) using a mole ratio between 0.11 until 0.17.

In this study, we tested two molar ratio (R'=0.1 and R'=0.13) and 4 different aging time (t= 3 h, 1 day, 2 days and 3 days). After three hours of aging, the lamellar phase is observed in both cases R'=0.1 and 0.13, (see Fig. 5.2.5). For the sample with R'=0.1, after 1 day of the solution aging, we could observe reflexions corresponding to a 2D hexagonal phase. However, the intensity of the Bragg reflections decreases after 2 days and for longer time of aging they vanish completely. In the case of R'=0.13, the solution became a gel after 2 days of aging because of the condensation reaction rate was faster than the hydrolysis rate. For this solution and at shorter times no structured phase could be observed. All the

films were obtained by dip coating at a constant withdrawal velocity of 14cm/min and a relative humidity (HR) of 50%.

R'=0.1

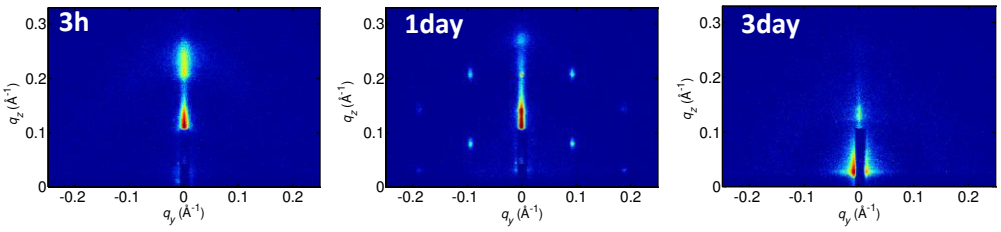

R'=0.13

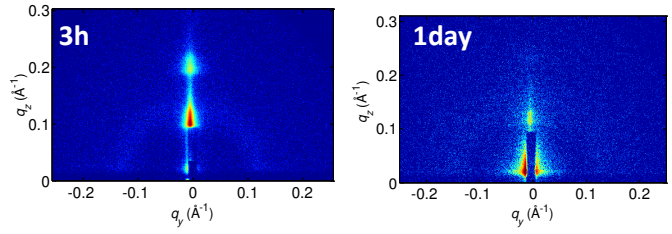

Figure 5.2.5 GISAXS image of silica thin film prepared with two molar ratio R'=0.1 and 0.13 and with several different aging times. GISAXS measurement were performed at IMMM (Université du Maine) with 8 KeV with an incidence angle was 0.20^{o}.

Structural analysis

Figure 5.2.6 shows the GISAXS pattern of a thin film prepared from a solution containing a molar ratio of 1TEOS; 20EtOH; 3.6H_2O; 2.5.10^{3}HCl; 0.1FSN which was deposited on silicon substrate after 1 day of aging the solution. The indexing of the GISAXS pattern indicates that the system belongs to 2D rectangular structure, i.e., the cylinder micelles would be stacked according to rectangular array aligned parallel to the substrate (see Fig.5.2.7).

The d-spacing (d_{hkl}) was calculated for each Miller index from the GISAXS image. These obtained values were used to calculate the unit cell parameters b and c corresponding to the structure formed by the cylindrical micelles through this formula,

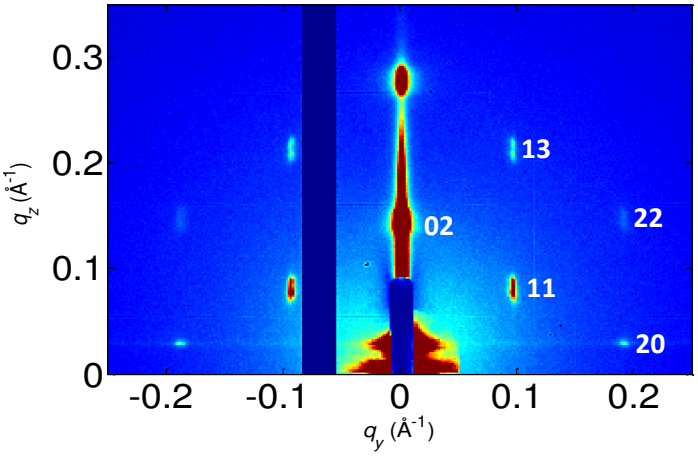

Figure 5.2.6 GISAXS data for the mesoporous thin film prepared from silica using micelles of FSN as a template. The measurement was performed at ID10 Beamline (ESRF) with 22KeV. The incidence angle was 0.06^{o}.

$$d_{hkl} = \frac{1}{\sqrt{\left(\frac{k^2}{b^2} + \frac{l^2}{c^2}\right)}} = \frac{2\pi}{q}$$

Where q is the wave vector defined as $q=q_y^2+q_z^2$

From the calculation the following unit cell parameter b=6.4nm and c=9.1nm are obtained. The ratio between the lattice parameters c/b is estimated to be 1.4, which is less than the expected ratio for a perfect 2D hexagonal symmetry (1.73). This leads us to conclude that the structure belongs to a rectangular symmetry (c2mm) as show in Fig. 5.2.7.

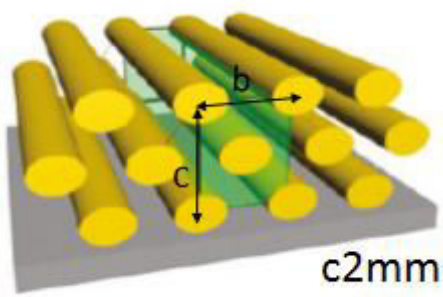

Figure 5.2.7 Schematic representation of pore structure obtained in silica mesoporous thin film using a FSN/Si molar ratio of 0.1.

The reflectivity curve plotted in Fig. 5.2.8 corresponds to a molar ratio R'=0.1 and an aging time of 1 day. For this sample the Kiessig oscillations are not observed due to the non-uniformity of the film. However the Bragg peaks are well defined, indicating that the micelles are well organized.

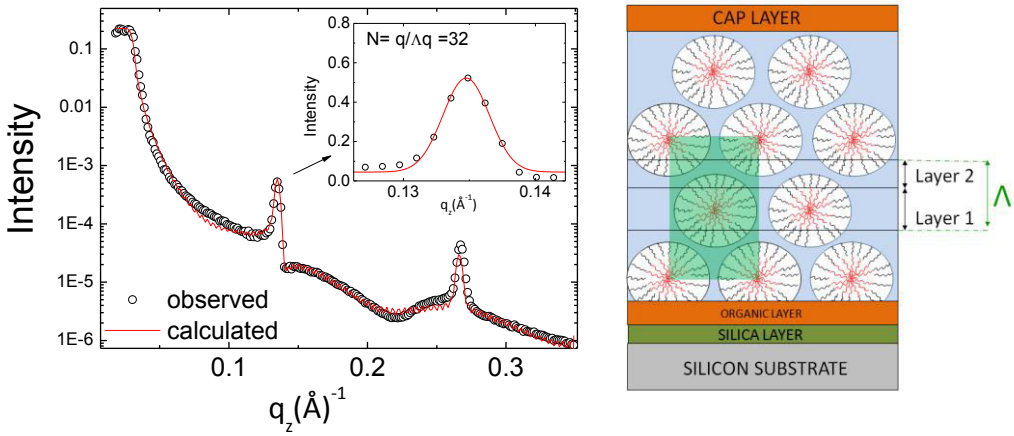

Figure 5.2.8 a) Observed and Calculated XRR curves of the as prepared film. b) Schematic representation of the FSN/silica mesoporous film, it consists of a periodic repetition of a bi-layer (LAYER 1+LAYER 2). The films are supported by a silicon substrate. This XRR measurement was performed at ID10 Beamline (ESRF) with 22KeV.

	Substrate	Buffer native SiO_2	Buffer (organic layer)	Layer 1 FSN	Layer 2 SiO_2walls	Cap-layer
$q_c(Å^{-1})$	0.032	0.0279	0.018	0.029	0.0285	0.015
density (e-/ $Å^3$)	0.73	0.553	0.23	0.63	0.577	0.170
Roughness(nm)	0.3	0.8	0.7	0.1	0.1	0.8
thickness (nm)	-	4.5	0.67	3.24	1.5	4.87

Table 5.2.2 Parameters used to simulate the XRR curve.

The XRR data were analyzed according to the model schematized in Fig. 5.2.8 b. The curve fitting allows us to obtain the characteristic parameters of each layer present in the film that are shown in table 5.2.2. The film is thus composed of a native SiO_2 buffer layer 4.5 nm thick, of an organic layer about 0.7 nm thick at the substrate/film interface, followed by 32 repeating bilayers of SiO_2 and FSN being 4.7nm thick for each bi-layer and finally capped by a SiO_2 layer about 4.8nm thick at the film/air interface. Thus, the total thickness of the deposited film is 160.4nm.

Within the bilayers, the silica layers (LAYER 2) are ~1.5 nm thick and have an electron density of 0.57 $e^-/Å^3$ (q_c = 0.0285 $Å^{-1}$). This density is less than that solid silica (0.66 $e^-/Å^3$) and it suggests that the silica walls in the as-prepared films are porous. The electron density of the fluorinated layer (LAYER 1) of 0.63 $e^-/Å^3$ (0.0296 $Å^{-1}$) . The thickness of the fluorinated layer is 3.2nm corresponding to the diameter of the hydrophobic part of the cylindric micelle formed by the fluorinated surfactant. In fact, the length of the hydrophobic part is 1.5nm [Blin2004]. Thus, it can be concluded that the fluorinated part of the FSN is elongated in the hybrid mesophase. These results were obtained under the assumption that the hydrophilic part of the FSN is integratd into the silcia walls [LAYER 2] as shown in the FIgure 5.2.8 b.

On the other hand, the layer of 4.5nm thickness that was observed in the subtrate/film interface could be atributed to the presence of formed silica due to the favorable interacion between Si/silica compared to Si/FSN.

5.3. Using GISAXS analysis to probe pore deformation in mesoporous silica films

In this section, we show that GISAXS patterns of thin films with ordered internal 3D mesoscale structures can be quantitatively modeled, using the Distorted Wave Born Approximation (DWBA) and related approximations. The extreme sensitivity of this technique was used to probe the anisotropy of pores in a mesoporous silica thin film having the $P6_3mmc$ symmetry. Taking advantage of the nearly zero intensity of allowed Bragg reflections, we prove that the casual extinction or existence of some reflections is related to the anisotropy of the form factor of the pores. We thus evidence that pores are spheroidal shape rather than spherical with a radius of 2.3nm in the equatorial plane and 1.85 nm in the normal direction thus probing a change of only 0.45nm.

5.3.1. Introduction

Mesoscale structures and phenomena are currently amongst the most intensely studied fields in physics, chemistry and nanotechnology [Kresge1992, Sanchez2008, Saxena2004, TrongOn2001, Zukalova2005]. Being intermediate between the atomic/molecular and macroscopic/continuum length scales, they often require multiscale theories and approaches to be measured and understood. Measuring material samples and devices

with mesoscale structures is done using both local probes (STM, AFM) and scattering methods like X-ray powder diffraction and transmission electron microscopy (TEM) [Zhao1998]. Structural analysis of mesoscale materials processed to thin films is increasingly carried out by the two surface-sensitive techniques of X-ray reflectivity (XRR) and GISAXS [Dourdain2005,Gibaud2006], which have the advantage over TEM of not necessitating sample sectioning that potentially alters the internal structures. In addition, they are excellently suited for *in situ* studies, as the highly penetrating nature of X-ray beams facilitates the use of bulky sample environments [Breivy2013]. XRR provides quantitative information about the electron density profile in the direction normal to the surface of the films, by modeling of specular reflectivity data [Dourdain2005, 2008, Gibaud2003, 2006, Besson2003]. GISAXS, which is essentially SAXS applied to surfaces in reflection geometry [Besson2000, Doshi2003, Smarsly2005, Grosso2004, Altamura2012, Buljan2012, Pietra2012] , cf. Fig. 5.3.1, is complementary to XRR, providing information both in the directions parallel and perpendicular to the thin-film surface, from the diffuse scattering signal. As the incidence and exit angles involved are small, the usually negligible effects of refraction and multiple scattering ought to be included for a faithful quantitative modeling of the scattering data. This is difficult, and in many cases, GISAXS users report only qualitative structural information. A much studied simplified case is that of oriented nanoparticles [Renaud2003, Breiby2009] more or less randomly dispersed on a 2D surface, for which the computer programs isGISAXS [Lazzari2002] or FitGISAXS [Babonneau2010] are highly adequate. A few researchers [Doshi2003, Smarsly2005, Grosso2004, Altamura2012, Smilgies2012, Senesi2013, Lee2005, Busch2006, Stein2007] have tried to extract more quantitative information also from 3D structures in thin films, however with limited general success because it is quite challenging to analyze the intensity of Bragg reflections in GISAXS patterns of materials with highly organized porous structures. It seems fair to state that whereas GISAXS is a relatively easy technique to apply experimentally, the rather complicated data analysis has impeded GISAXS from becoming a truly widespread technique.

In this work, we show that GISAXS patterns of thin films with ordered internal 3D mesoscale structures can be quantitatively modeled, using the Distorted Wave Born Approximation (DWBA) and related approximations. We go beyond what has previously been achieved in this field by addressing how the anisotropy of the scattering objects can be assessed from a complete fit of the data contained in the GISAXS patterns.

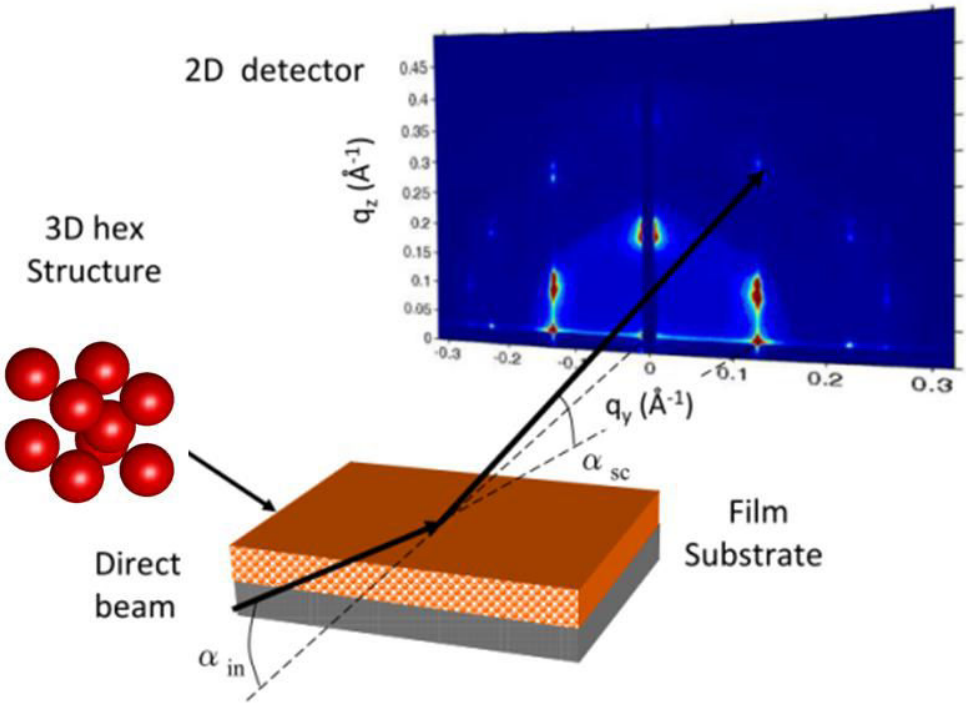

Figure 5.3.1 Principle of GISAXS. The incident monochromatic beam is impinging on the surface of the film at a fixed angle of incidence α_{in} and the beam scattered by the scattering objects contained in the film is collected at angles α_{sc} on a 2D detector having the specular direction masked to avoid saturation of the detector.

5.3.2. Results and Discusions

The outlined formalism has been applied to a CTAB-templated mesoporous silica thin-film produced by evaporation-induced self-assembly [Doshi2003]. A selected experimental pattern obtained with an incidence angle of 0.13°, chosen slightly above the critical angle of the film to exhibit the full interplay between the DWBA scattering terms, is shown in Figure 5.3.2. The space group of the porous structure in this film is $P6_3/mmc$, colloquially referred to as "hexagonal close packed", and there are two micelles per unit cell located at positions (1/3,2/3,1/4) and (2/3,1/3,3/4). The pattern can be indexed according to the given hexagonal space group with lattice parameters a = 5.56 nm and c = 6.97 nm, oriented with the c axis parallel to the substrate normal. The film is composed of crystalline regions which assume random orientations about the surface normal, effectively constituting an ideal "2D powder", as evidenced by the symmetry, both position and intensity, observed in the experimental patterns. All features seen in the

scattering patterns are accounted for by the presented formalism, where in particular the doubling of peaks along the q_z direction can be explained by the application of the DWBA formalism, see previous section.

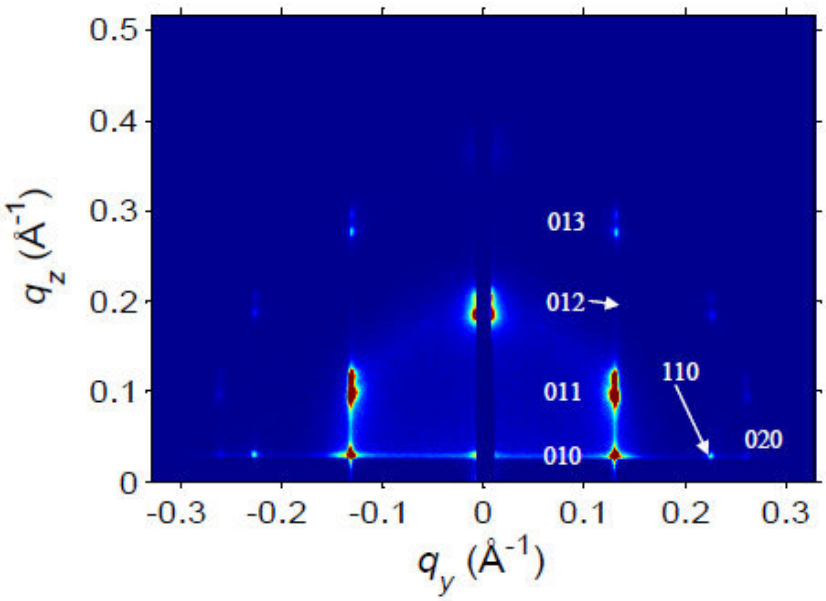

Figure 5.3.2 Experimental GISAXS pattern measured on a mesoporous film in which the CTAB surfactant was removed, showing the presence of Bragg reflections characteristic of the $P6_3/mmc$ structure. White arrows are indicating two specific reflections which are located essentially at the wave vector transfer with the same modulus. While the 012 reflection is absent, the 110 reflection is clearly observed although both of them are allowed by the space group.

Most importantly, the 012 reflection allowed by the space group and shown by an arrow in Figure 5.3.3b does not exist, while the 110 reflection that is located at a similar wave vector transfer q from the origin is clearly seen. This rather puzzling observation can be explained by assuming that the pores are not spherical but rather ellipsoidal in shape, as we shall explain in detail. If a minimum of the form factor function coincides with the location of a Bragg peak, this peak, even if predicted by the space group symmetry, will vanish, see Figure 2.5.8. The precision with which one can address the extinction of a Bragg reflection is related to the fact that the micelles being formed by surfactants are highly monodisperse so that their form factors exhibit sharp minima, as discussed by Tate and Hillhouse [Tate2007]. Gratifyingly, we are able to conclusively confirm the slight out-of-plane compression of the pores previously reported by ellipsometric measurements [Boissiere2005], relying solely on the GISAXS signal, which opens the path for future *in situ* studies of the creation and evolution of the porous networks.

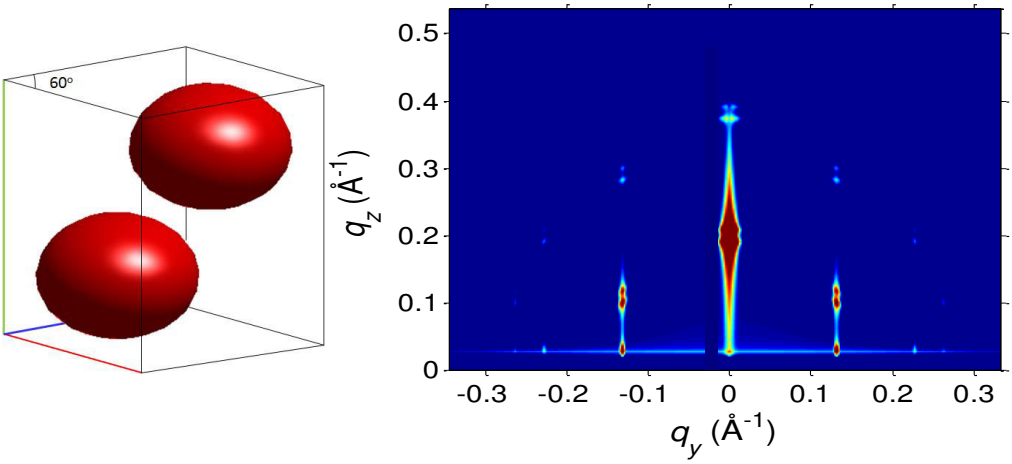

Figure 5.3.3 a) Hexagonal unit cell with slightly compressed, i.e. spheroidal, pores used to carry out the simulation *R*=2.3 nm and *H*=1.85 nm. b) Simulated GISAXS pattern corresponding to the spheroidal pores shown

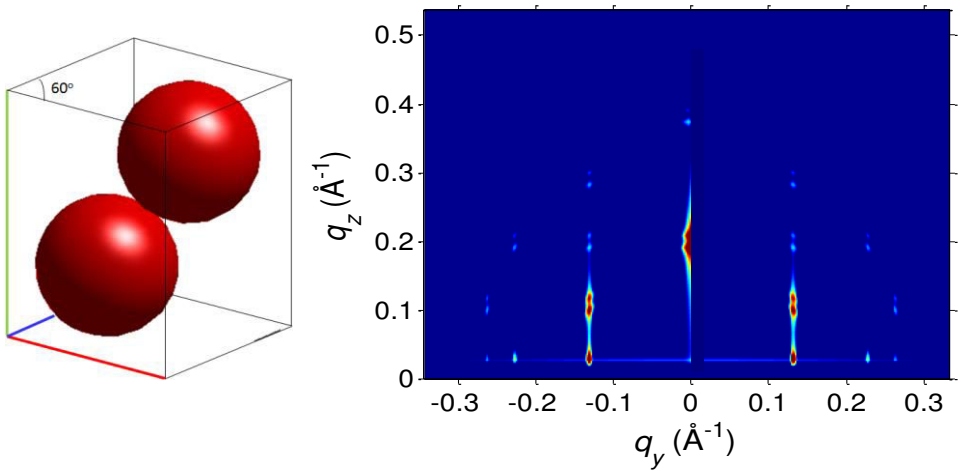

Figure 5.3.4 a) Hexagonal unit cell with spherical pores *R*=2.3 nm. b) Simulated GISAXS pattern corresponding to the spherical pores.

The two simulated images differ only by a slight change in the shape of the micelle; Figure 5.3.3b is calculated with a spheroidal object (see Figure 5.3.3a) in which *H* = 1.85 nm and *R* = 2.3 nm (see Figure 2.5.4 for more details); Figure 5.3.4b is calculated with a spherical micelle with *R* = 2.3 nm (see Figure 5.3.4a). These two objects are quite similar in shape, but nevertheless the scattering patterns are qualitatively different upon closer investigation. As shown, it is possible to see minute differences in the intensities of the 102 and 110 Bragg reflections, as expected for a change in the anisotropy of the form factor of the pores. Comparing the calculated patterns to the experimental one (shown in Figure 5.3.1), it is clear that the best agreement corresponds to the simulation of Figure

5.3.3a. This shows unambiguously that a distortion as small as H/R = 0.8 of the sphere, corresponding to a change in radius of 0.45 nm, is measurable. The excellent quantitative agreement is further highlighted by refining extracted lines of intensity along the q_z and q_y directions as shown in Figure 5.3.5, clearly demonstrating the feasibility of quantitative analysis of GISAXS patterns from 3D mesoscale structures. For an even better description of the intensity, we have included in these simulations two additional contributions of diffuse scattering. One of them arises from a minor fraction of the film volume having a disordered "worm like" structure. It is located on a ring of constant q and appears at the outer tail of the 010 reflection. The second one is due to scattering by the beam defining slits having a very narrow aperture (20 µm). This streak gives rise to scattering located along the Yoneda line in the q_{xy} scan of Figure 5.3.5 going from -0.2 to 0.2 $Å^{-1}$. We can extract from this calculation all the parameters reported in Table 5.3.1. Hence the simulation provides not only the space group and the lattice parameters but also the anisotropy of the pores and the size of the domains which scatter coherently in the plane of the film. Thus, by looking at the intensity of symmetry-allowed Bragg reflections, we can probe the anisotropic shape of the pores. Specifically, we take advantage of the observation that some reflections that are allowed by the space group vanish, while others located at the same wave vector transfer remain observable. It is remarkable that measuring zero intensity at given locations is a key to determine the anisotropic shape of the scattering objects.

parameter	value
lattice parameter a c	 5.56 nm 6.97 nm
Pore radius in the plane of the substrate, R	2.3 nm
Pore radius perpendicular to the substrate, H	1.85 nm
In-plane correlation length, ξ	1500 nm
Critical angle of the film, α_{cfilm}	0.108^{o}
Absorption of the film	$0.2x10^{-7}$
Roughness of the surface, σ	0.3 nm
Number of pore layers, Nz	13

Table 5.3.1: Refined parameters used in the fit to the data of the q_{xy} et q_z scans shown in Figure 5.3.5 (Lattice parameters a and c, pore radius in the plane of the substrate, pore height H perpendicular to the substrate, in plane correlation length, critical angle of the film, absorption of the film, roughness of the surface, number of pore layers).

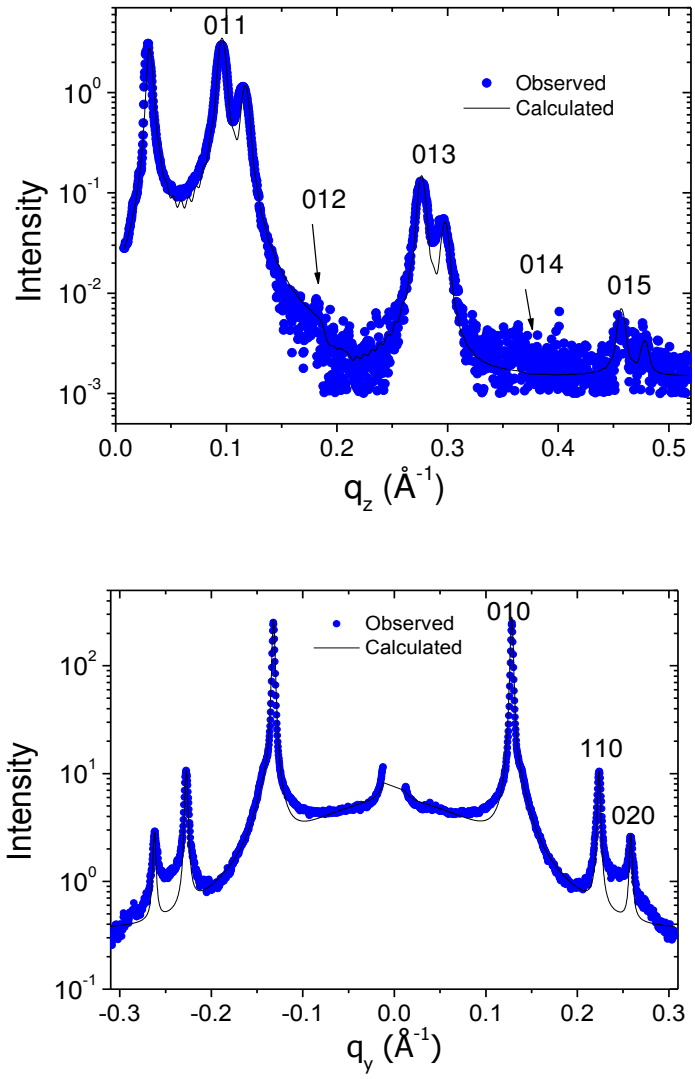

Figure 5.3.5: Fitted scans along the q_z (cut along q_y=0.132Å^{-1}) and q_{xy} (cut along q_z=0.116Å^{-1}) directions according to the formalism presented in the text. In this case, the scan along the q_y direction was calculated by adding a central background and a peaked background at q_{xy} = 0.135 Å^{-1} to account for the existence of a shoulder on the right side of the first Bragg peak. This shoulder is consistent with the existence of a fine diffuse halo seen in the GISAXS pattern which might come from the presence of "wormlike" domains in the film. The GISAXS pattern was measured at an incidence angle of 0.13°.

This specific example of a $P6_3/mmc$ mesoporous silica structure was chosen to illustrate the capabilities of our approach to simulate GISAXS patterns. We have outlined a general and versatile method based on the use of the DWBA and related approximations, with analytical expressions for calculating the GISAXS patterns of any mesoscopically ordered

periodic structure in thin films. This approach yields excellent quantitative fits to the experimental intensities of the Bragg reflections measured in the GISAXS patterns. In this respect, the present analysis provides unprecedented access to the anisotropy of scattering objects, such as pores. Our approach can be generalized to extract quantitative information from GISAXS patterns of any 3D ordered structure including not only micelles and block copolymer liquid-crystalline phases, but also core/shell nanoparticle superstructures, ordered nanocomposites, and any crystalline mesoporous materials deposited on a substrate, thus further substantiating the claim of GISAXS as the method of choice for studying nano- and mesoscale thin-film assemblies.

5.4. Surfactant extraction analysis

The use of mesoporouss silica as the oxide has been extremely studied for practical applications in optical devices, water or CO_2 sensors or for studying the capillary condensation of fluids or the impregnation by metallic nanoparticles. For that, it is necessary to remove the surfactant from the as prepared film to liberate its porosity.

The mesoporosity revealed after extraction of the surfactant is dictated by the size of the surfactant molecules. Most of the studies reported so far, show the influence of such treatments before and after the removal of the surfactant. It is thus surprising that very little is known about the evolution of such materials during the removal of the surfactant.

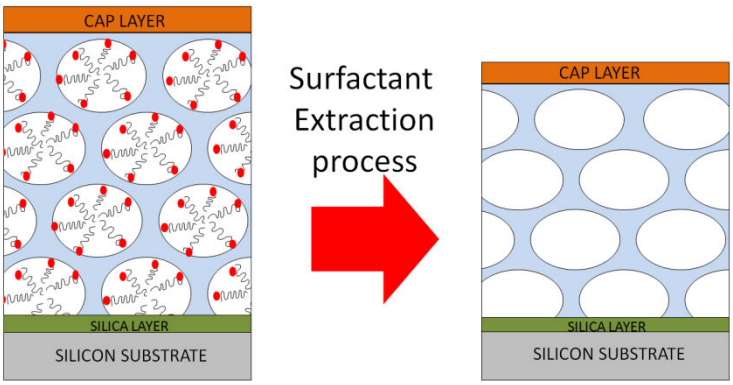

Figure 5.4.1 Schematic representation of mesoporous silica thin film before and after the removal of the surfactant.

5.4.1. Mesoporous silica template by CTAB having a 3D structure

For mesoporous **thin film templated by CTAB surfactant having a 3D structure**, the extraction of surfactant can be achieved by the annealing of the film above a given temperature at which the organic surfactant decomposes.

The in situ analysis of the mesostructured film during this annealing process was carried out using GISAXS, XRR and Raman techniques. The XXR and GISAXS measurements described here were performed at the IMMM facilities at 8KeV and at the ID10 Beamline (ESRF) at 22KeV respectively.

GISAXS experiments were made to evidence the structure evolution of the film both in and out of plane and to observe the pore shape evolution during the annealing process. On the other hand, XRR was carried out to analyze in a very precise way how the film was evolving in the direction normal to the surface. In particular it was thus possible to monitor the evolution of the electron density profile of the film as a function of temperature. By this method on can get invaluable information on the interplay between heat treatment and structural evolution of the film.

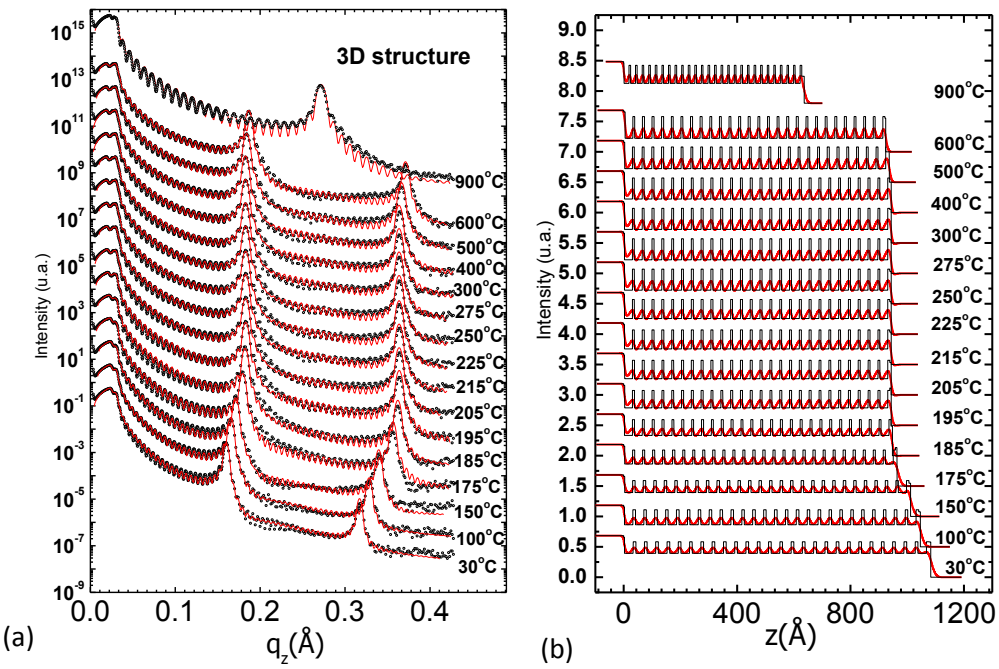

Figure 5.4.2 a) Observed (black dots) and calculated (red solid line) X-ray reflectivity curve of as prepared film during the annealing up 900°C. b) Electron density profile calculated from the fit.

From XRR curves (Figure 5.4.2), it can be seen that the film structure is strongly affected by the elevation of temperature. At temperatures below 185°C, the film thickness and the periodic unit length shrink quite significantly as shown by the shift of the Bragg peaks position towards higher q_z values and by the decrease of q_z spacing between the Kiessig fringes while the q_c of the film remains constant as the intensity of the Bragg peaks. This is the evidence that the water molecules contained in the silica gel tend to evaporate producing the contraction of the silica matrix. The surfactant is not affected by this treatment since the q_c of film remains unchanged as is the contrast of electron density between the two layers. When the temperature is raised above 180°C, both the position of the critical q_c of the film and the intensity of the Bragg peaks are affected. This shows that T=180°C is the onset of the removal of the surfactant. When the surfactant is removed from the film, the contrast of electron density increases between the two layers and so does the intensity of the Bragg peaks. In addition the electron density of LAYER 1 (i.e. silica walls + surfactant) decreases significantly and so does the critical q_c of the film.

The full removal of the surfactant was obtained at a temperature of 250°C (time scale between each measurements was 4h 20 min). Above this temperature the system is quite stable up to 500°C. Above 500°C both the film thickness and the periodic unit length shrink further however the periodic organization of the film along normal, one dimensional crystal, remains. We were able to follow its behaviour up to 900°C. At this temperature, GISAXS measurements were performed on the sample confirming that the 3D structure still remains.

Structural evolution~~s~~ of the film was also monitored by GISAXS. This technique is particularly useful to correlate the distortion of the micelle aspect ratio (H/R) (Fig. 5.4.5) with the evolution of the electron density (Fig. 5.4.4) of the mesoporous film obtained by XRR.

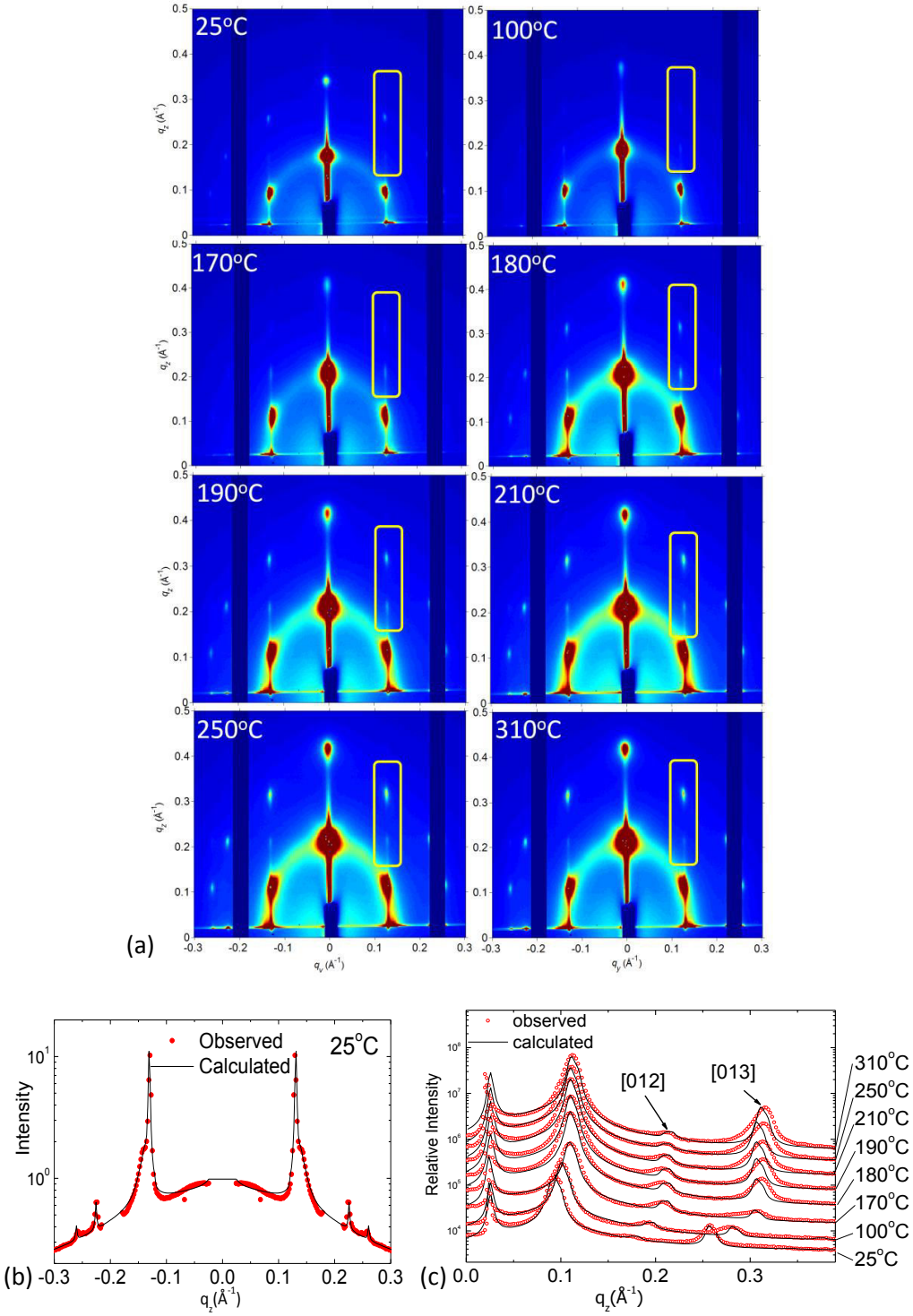

Figure 5.4.3 a) GISAXS pattern corresponding to the mesoporous thin film during the annealing up to 310°C. b) and c) Fitted scans along q_{xy} (cut at q_z=0.116Å^{-1}) and q_z (cut at q_y=0.132Å^{-1}) directions. The GISAXS patterns were measured at an incidence angle of 0.13°.

From the GISAXS pattern, the change in the pore anisotropy during the annealing process of the film can be understood by looking at the change in the intensity of the Bragg peaks (012) and (013) (see Fig. 5.4.3a). In order to calculate the anisotropy a homemade

program was used that take in account the four scattering terms as well as others approximations to quantify the distortion of the scattering objects (see section 5.3 for more details). From the q_y direction, we could extract the pore radius in the plane of the substrate which was found to be R= 22Å. We observe that this radius remains constant during the process. On the other hand, in the q_z direction a clear shift of Bragg peaks is observed due to the shrinkage of the matrix without affecting the distortion of the micelle aspect ratio before 180°C. After this temperature, the electron density (Fig. 5.4.4b) and the micelle distortion (Fig. 5.4.5b) decrease simultaneously until a temperature of 250 °C is reached. This can be interpreted as the evidence of the micelle disappearance.

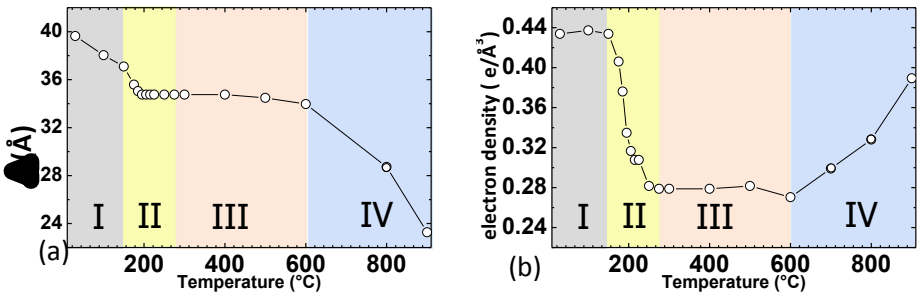

Figure 5.4.4 Evolution of a) the thickness 'Λ' (Layer 1+ layer 2) and b) the electron density of the mesoporous film as a function of the temperature. The Parameters were obtained from a **fit to the XRR data.**

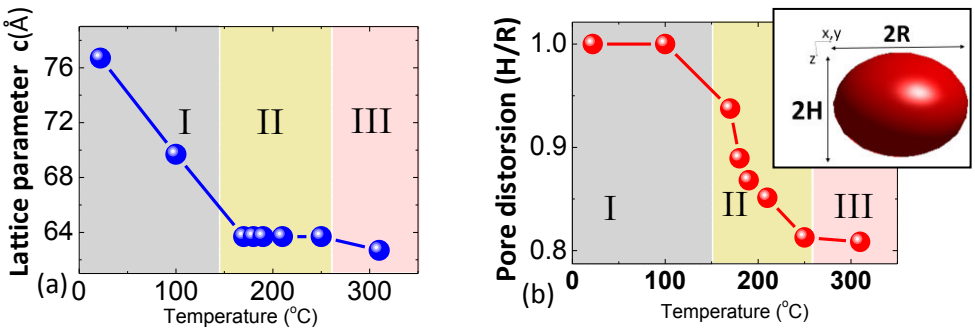

Figure 5.4.5 Evolution of a) the **lattice parameter 'c'** and b) **pore distortion H/R** as a function of temperature. Parameters are obtained after **fitting GISAXS data.**

The CTAB extraction has been verified through a quasi in-situ analysis using the Raman spectroscopy technique. For this analysis a small furnace specially adapted to carry out in-situ measurements was used at the IMMM facilities. During the measurements we observe a progressive increase of the background (luminescence) as function of temperature (see Fig. 5.4.6b) that make difficult the in-situ observation of the evolution of vibration peaks. This luminescence has been attributed to the CTAB degradation during

the annealing process. The time gap between two successive measurement was 60 minutes. At 215°C several measurements were performed in a 2 hours period. During this time an increase in the luminescence was still observed, this indicate that the kinetics of dissolution of the CTAB is slow.

At this temperature, we observe a collapse of the peak at 2850 cm^{-1} corresponding to the stretching vibrations of CH_2 group. However, the CH_3 vibrations corresponding to the headgroup seem to be stable. This results suggest that, CH_2 groups are the first to be degraded.

At 300°C (see Fig. 5.4.6a), the luminescence decreases. The signal between 2800 and 3100 cm^{-1} shows that there are still CTAB molecules but in very small quantities. According to [Kusak 2009] these remaining molecules belong to the groups a CH_3(1), CH_2(2) y CH_3(17) (see Fig. 5.4.6c). This result suggests that the remaining molecules are those that form bonds with the walls of the silica matrix.

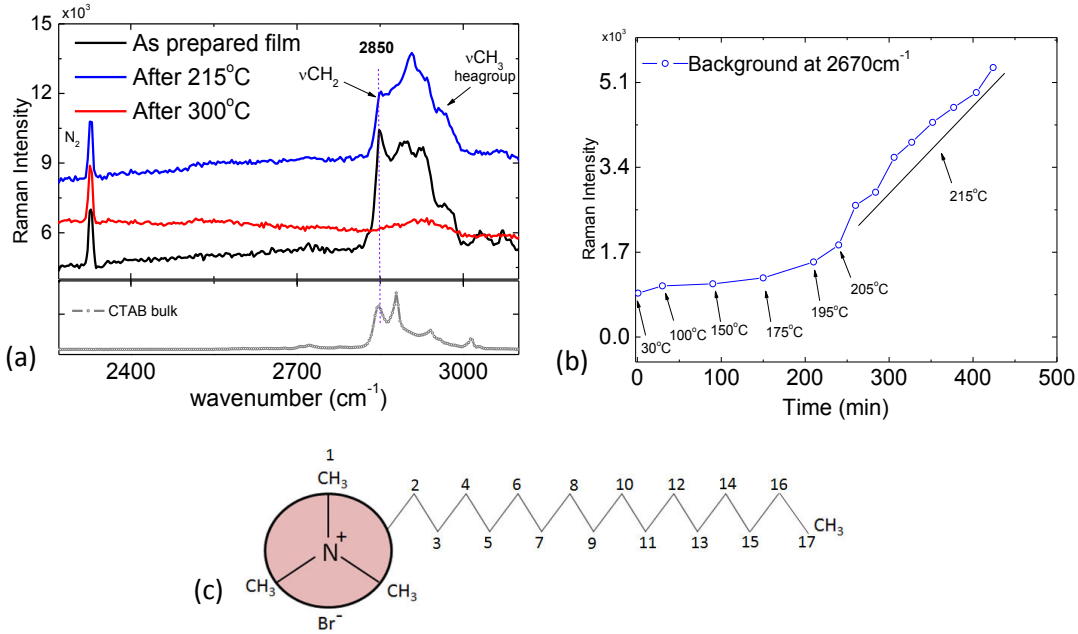

Figure 5.4.6 a) Raman spectra of mesoporous thin film templated from CTAB surfactant before and after a heat treatment b) Background at 2670cm^{-1} as a function of the temperature c) Representation of the CTAB surfactant numbered.

In summary, we can conclude that we identified 4 regimes of temperature during the heat treatment. The first regime is observed between 20°C and 180°C during which the film essentially shrinks without any change in its average electron density. A second regime

which occurs between 180°C and 250°C corresponds to **distortion of the pore shape due** to the removal of the surfactant. Above 300°C the surfactant has been removed, but a small quantity of organic fragments may still remain. This situation is followed by a regime which extends from 300°C to 500°C where the film remains remarkably stable. Above 500°C we reach phase 4 of the heat treatment where we observe that the film shrinks and gets denser without losing the 3D structure.

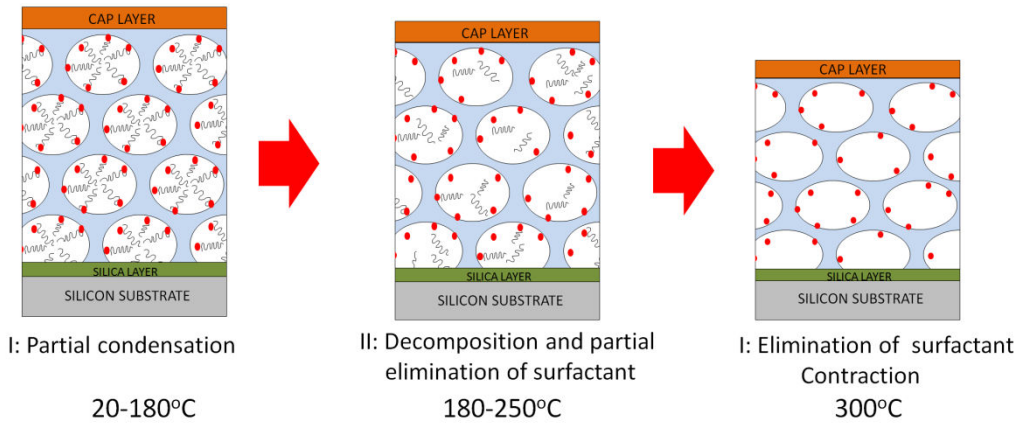

Figure 5.4.7.: Schematic representation of mesoporous silica thin film during the removal of the surfactant.

5.4.2. **Mesoporous silica templated by CTAB having a 2D structure**

Similar to carried out in the Section 5.4.1. an in-situ XRR study was performed during the annealing treatment of mesoporous silica with a 2D hexagonal structure. The experiments described in this section have been performed at the IMMM facilities at 8keV.

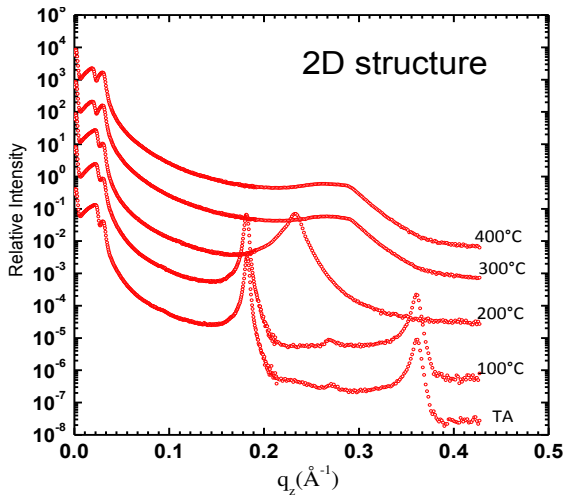

Figure 5.4.8 Observed X-ray reflectivity of silica mesoporous having a 2D structure during the annealing process up to 400°C.

In Figure 5.4.8, we show the curves of XRR as a function of the annealing temperature 'T'. From these figures is possible to observe that at temperature below 100°C the film is not affected by this treatment since the Bragg peak position and intensity remain unchanged. This behaviour can be explained by the procedure of the sample preparation which was done at 80°C.

On the other hand, at T = 200°C, it can be seen that the reflectivity curves shows a shift in the Bragg peak position to higher values of q as well as the peak broadening. These two effects reflect a loss of the 2D structure with the film contraction. The destructuring of the films due to the surfactant extraction suggests that the silica matrix is not adequately condensed and therefore is not stiff enough to withstand the formed mesoestructure.

An alternative method of surfactant extraction without affecting the 2D structure would be presented in the following section.

5.5. Fluorinated surfactant (FSN) removal from mesoporous film using Sc-CO_2

Conventionally, the surfactant removal has been carried out by high temperature calcinations. Although the surfactant could be effectively burnt off, such thermal treatment may have negative effects on the mesoporous structure. At very high temperature treatment, partial collapse of the structure may occur and up to a conventional 400 °C, a small quantity of organic fragments may still remain [Keene1999, Kusak2009].

An alternative challenging procedure for the surfactant removal with less destructive effects is sc-CO_2 extraction [Kawi1998, Huang2013]. Sc-CO_2 has several features making them suitable solvents for the extraction. Most notably they can solubilise non volatile components at near ambient temperatures and can be completely separated from the solute via a pressure reduction. The efficiency of the sc-CO_2 extraction depends in particular on the type of the surfactant. Surfactants having low cohesive energy density and high free volume (e.g. siloxanes, surfactants with methyl groups and tail branching, oxygen containing molecules, e.g. carbonyls, ethers, and fluorocarbon groups) have favourable interactions with CO_2 and are termed 'CO_2-philic' [Beckman2004, Eastoe2006, Dickson2005, Lee2001].

In the previous section 5.2.2, we reported the preparation of 2D rectangular silica thin films template with $C_8F_{17}C_2H_4(OCH_2CH_2)_9OH$ (FSN). In this section, we present the study of the extraction of the template using supercritical carbon dioxide, based on the fact that these surfactants have CO_2-philic nature. Here the surfactant extraction was carried out at 100 bar and 32°C.

5.5.1. Experimental part

The mesoporous silica thin film was prepared using a FSN/silica with the molar ratio of 0.1 and aging time of 1 day. The obtained crystalline structure was 2D **rectangular cell** in the plane perpendicular to the axes of the closely packed cylindrical micelles while the axes are parallel to the substrate plane. The space group of this structure is c2mm (see more details in the section 5.2.2).

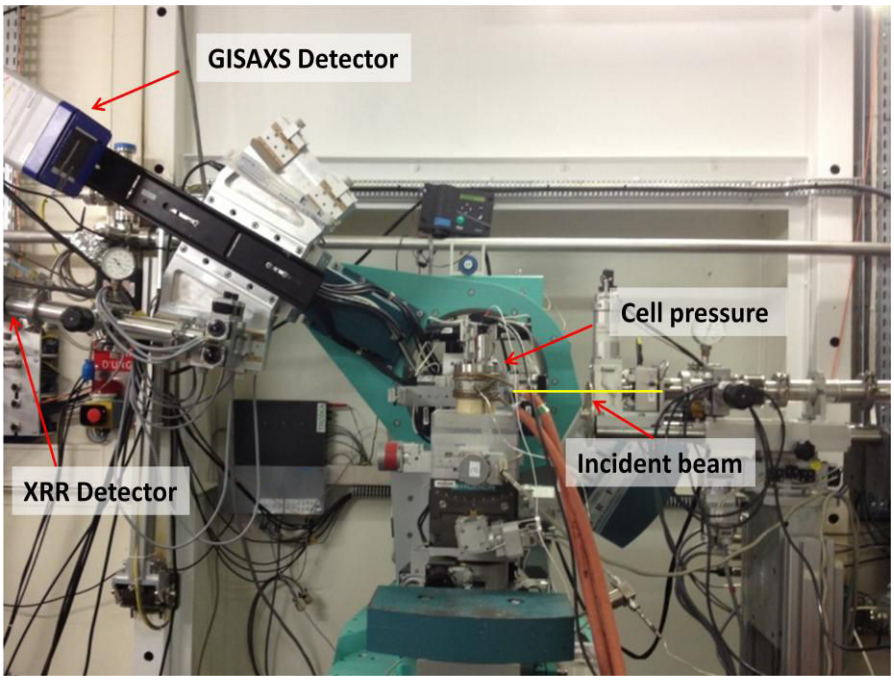

Figure 5.5.1 Experimental setup used in the XRR and GISAXS measurement at ID10 Beamline of the ESRF.

The film was placed inside a high pressure cell that was thermo regulated up to 0.1°C. Pressure was automatically adjusted with a precision better than 0.1 bar via specially designed mechano-electronic control device. Specifications about the pressure cell and

the control device are given in bibliography [Mattenet2010]. All measurements made on these films were carried out at a constant temperature of 32°C.

XRR experiments were performed at the ID10B beamline of the European Synchrotron Radiation Facility (ESRF, Grenoble, France) with the monochromatic X-rays beam of 22 keV energy. The high energy X-rays are required to minimise the absorption of the beam going through the diamond windows of the cell (1 mm) and 35 mm of CO_2 in gas and particularly liquid or sc- state. The time scale between each measurement was 30 min. The depressurisation process usually took 1h.

5.5.2. Results and Discussion

The experimental results obtained during the pressurisation up to 100 bars are presented in Fig. 5.5.2. The experiment was carried out on a fresh film which was not yet stabilized. First, it is noted that XRR curves are not very affected by the elevation of pressure. At the pressure below 50 bars, a small increase of the thickness Λ(LAYER 1+ LAYER 2) is observed which is manifested by the shift of the Bragg peak position towards lower q_z values. This result suggests that CO_2 penetrates into the micelle causing a slight expansion of the structure.

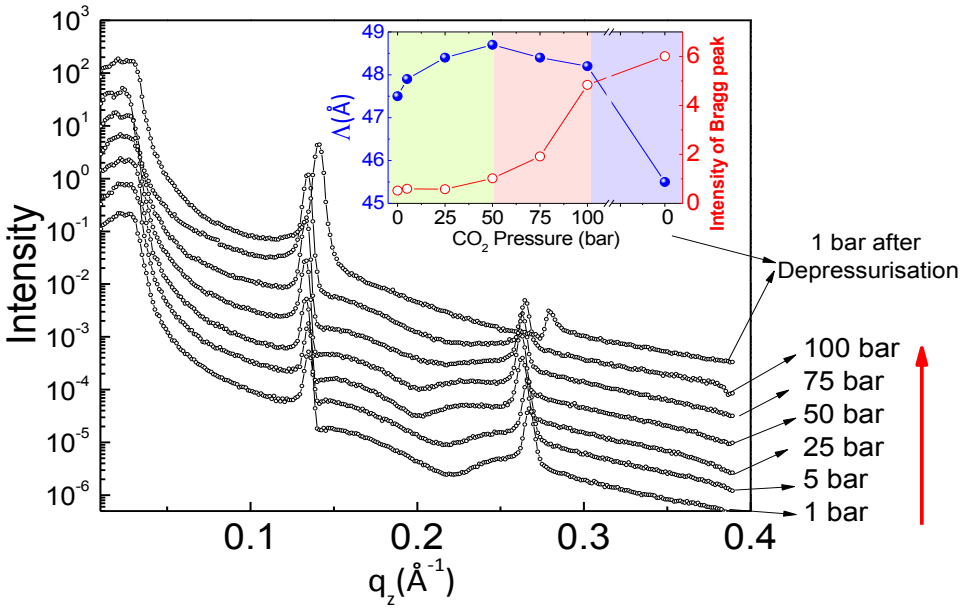

Figure 5.5.2 The evolution of in-situ XRR curves during pressurization of CO_2 in the cell. Curves are translated vertically for clarity. In the top inset, in blue line, the evolutions of the thickness of (LAYER1+LAYER2) are shown. In the same picture, in red line, we show the evolution of the intensity of Bragg peak.

However, when the pressure is raised above 50 bars, we observe a contraction of the silica matrix concomitant to an increase of the intensity of the Bragg peaks. According to the scattering theory, the intensity is directly proportional to the electron density contrast $I \sim (\rho_{wall}^{e-} - \rho_{pore}^{e-})^2$. Therefore an increase in the intensity of Bragg peak as a function of CO_2 pressure can be associated with the progressive removal of the surfactant via its dissolution (see Fig. 5.5.3).

The full removal of the surfactant was obtained after the depressurisation. We observed that the final contraction of the thickness 'Λ' of (LAYER1 +LAYER 2) in the whole process has been only 0.2nm which is 3 times less as compared with the annealing process applied to mesoporous silica templated by CTAB.

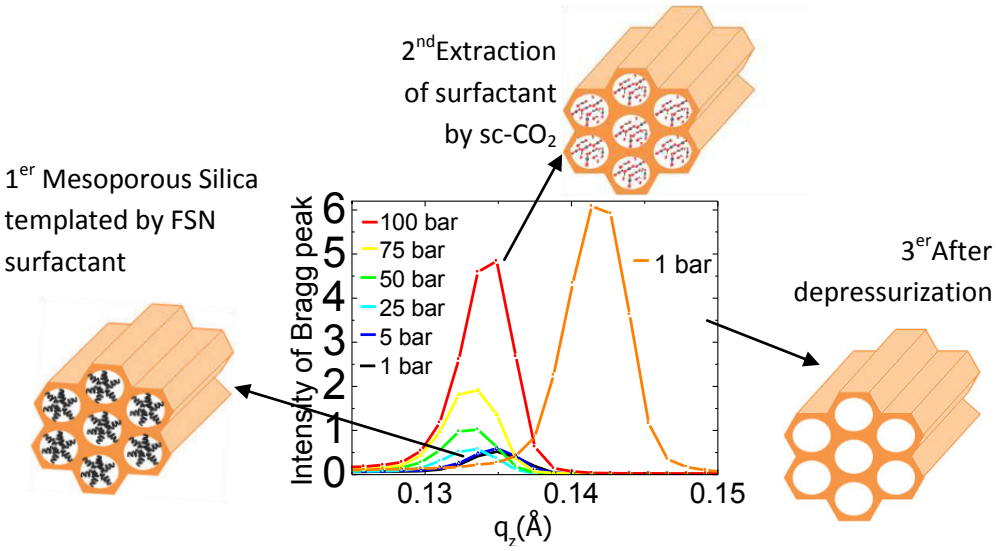

Figure 5.5.3 The surfactant dissolution was monitored by the evolution of Bragg peak

The structural features of mesoporous thin films before and after the CO_2– treatment were studied by GISAXS measurements (see Figure 5.5.4). The GISAXS patterns show characteristic Bragg peaks of the 2D hexagonal structure for FSN mesoporous thin film (see section 5.2.2). These Bragg peaks can be indexed as reflections on the 11, 13, 20, 22, 02 planes. The GISAXS image show that ordered mesoporous structures are preserved after the CO_2 treatment. The weaker reflections corresponding to planes 13, 22, 20 are hardly observed in the sample after the CO_2-treatment. The disappearing of these

reflections can be assigned to the aspect ratio ~~a~~ distortion of the pores due to the shrinkage of the sample due to the surfactant removal by sc-CO_2.

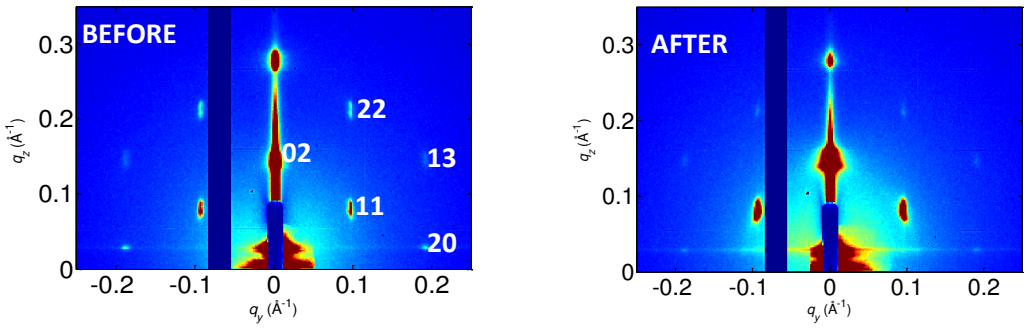

Figure 5.5.4 GISAXS image of FSN mesoporous thin film before and after the removal of the surfactant. This GiSAXS measurement was performed at ID10 Beamline (ESRF) with 22KeV. The incidence angle was 0.06^{o}.

In conclusion, supercritical carbon dioxide extraction is effective extracting the fluorinated template from the pores of as-prepared mesoporous thin film. The structure of the mesopore is preserved after the sc-CO_2 treatment with a thickness contraction of the (LAYER1+LAYER2) of 0.2nm.

Bibliography

[Altamura2012] Altamura, D.; Holý, V.; Siliqi, D.; Chaitanya Lekshmi, I.; §, Nobile, C.; Maruccio, G.; Davide Cozzoli, P.; Fan, L.; Gozzo, F.; Giannini, C., Cryst. Growth Des. (2012).12, 5505−5512.

[Babonneau2010] Babonneau, D. J., FitGISAXS: software package for modelling and analysis of GISAXS data using IGOR Pro. J. Appl. Cryst. (2010) 43, 929−936.

[Beckman2004] Beckman, E.J. Chem. Commun. (2004) 1885.

[Besson2000] Besson, S.; Gacoin, T.; Jacquiod, C. ; Ricolleau, C.; Babonneau, D,; Boilot, J. P., J. Mater. Chem. (2000) 10, 1331–1336.

[Besson2003] Besson, S.; Gacoin, T.; Ricolleau, C.; Jacquiod, C. ; Boilot, J. P., J. Mater. Chem. (2003) 13,404.

[Blin2004] Blin, J.L.; Lesieur, P; Stébé, M.J., Langmuir (2004) 20, 491-498.

[Blin2005] Blin, J.L.; Lesieur, P; Stébé, M.J., Microporous and Mesoporous Mater. (2005) 87, 67-76.

[Boissiere2005] Boissière, C.; Grosso, D.; Lepoutre, S.; Nicole, L.; Bruneau, A.B.; Sanchez, C., Langmuir (2005) 21 12362.

[Breiby2008] Breiby, D. W.; Bunk, O.; Andreasen, J.; Lemke, H.; Nielsen, M. M. J. Appl. Cryst. (2008), 41, 262–271.

[Breiby2009] Breiby, D. W.; Chin, P.; Andreasen, J.; Grimsrud, K. A.; Di, Z.; Janssen Rene, A.J., Langmuir (2009) 25, 10970-10974.

[Brinker1990] Brinker, C. J.; Hurd, A. J.; Frye, G. C.; Ward, K. J.; Ashley C. S., Journal of Non-Crystalline Solids (1990) v.121, no.1-3, p.294-302.

[Brinker1997] Lu, Y.; Cangull, R.; Drewlen, C. A.; Anderson, M. T.; Brinker, C. J.; Gong, W.; Guo, Y.; Soyez, H.; Dunn, B.; Huang M. H.; Zing, J.I., Nature (1997) 389-364.

[Brinker1999] Brinker, C. J.; Lu, Y.; Sellinger, A.; Fan, H., Advanced Materials (1999) 11, 7, p.579.

[Busch2006] Busch, P.; Rauscher, M.; Smilgies, D.; Posselt, D.; Papadakis, C. J. Appl. Crystallogr. (2006) 39, 433-442.

[Dickson2005] Dickson, J. L.; Smith, P. G.; Dhanuka, V. V.; Srinivasan, V.; Stone, M. T.; Rossky,P. J.; Behles, J. A.; Keiper, J. S.; Xu, B.; Johnson, C.; DeSimone, J. M.; Johnston, K.P., Ind. Eng. Chem. Res. (2005) 44, 1370.

[Doshi2003] Doshi, D.A.; Gibaud, A. ; Goletto, V.; Ocko, B.; Brinker, J.J, Am. Chem. Soc. (2003), 125, 11646.

[Dourdain2005] Dourdain S.; Gibaud, A., Appl. Phys. Lett., (2005) 87, 223105.

[Dourdain2006] Dourdain, S., Caracterisation structurale, poreuse et mécanique de films minces de silice mésoporeuse, PhD thesis, Université du Maine, 2006.

[Dourdain2008] Dourdain, S.; Britton, D. T.; Reichert, H.; Gibaud, A., Appl. Phys. Lett. (2008) 93, 183108.

[Eastoe2006] Eastoe, J.; Gold, S.; Steytler, D. C. Langmuir (2006) 22, 9832.

[Ebelmen1846] Ebelmen, J. J., Ann. Chem. Phys. (1846) 57.

[Ghosh2008] Ghosh, K.; Bashadi, S.; Lehmler, H. J.; Rankin, S. E.; Knutson, B. L. Microporous Mesoporous Mater. (2008) 113, 106-113.

[Gibaud2003] Gibaud, A.; Baptiste, A.; Doshi, D. A.; Brinker, C. J.; Yang, L.; Ocko, B., Europhys. Lett. (2003)63, 833–839.

[Gibaud2006] Gibaud, A.; Dourdain, S.; Vignaud G., Appl. Surf. Sci., (2006) 253, 1, 3.

[Gibaud&Vignaud] Vignaud, G.; Gibaud, A. Program REFLEX18, a matlab routine for the simulation of specular x-ray reflectivity data with the matrix technique.

[Grosso2004] Grosso, D.; Cagnol, F.; Soler-Illia, G.J. de A. A.; Crepaldi, E. L.; Amenitsch, H.; Brunet-Bruneau, A.; Bourgeois, A.; Sanchez, C., Adv. Funct. Mater. (2004)14, 309-322.

[Förster2005] Förster, S.; Timmann, A.; Konrad, M.; Schellbach, C.; Meyer, A.; Funari, S.S.; Mulvaney, P.; Knott, R., J. Phys. Chem. B, (2005) 109, 1347-1360.

[Hench1990] Hench, L. L.; West, J. K., Chem. Rev. (1990) 90. 33-72 93.

[Huang2013] Huang, Z.; Li, J.; Li, H.; Miao, H.; Kawi, S.; Goh, A.H., Separation and Purification Technology (2013) 118 120–126.

[Kawi1998] Kawi S.; Lai, M. W., Chem. Commun. (1998) 1407-1408.

[Keene1999] Keene, M.T.J.; Gougeon, R.D.M.; Denoyel, R.; Harris, R.K.; Rouquerol, J.; Llewellyn, P.L.; J. Mater. Chem. (1999) 9 2843–2849.

[Kissa1994] Kissa, E., Fluorinated Surfactants Synthesis properties Applications; Ed.; Surfactant Science Series 50; Dekker: New York, 1994.

[Kresge1992] Kresge, T.; Leonowicz, M.E.; Roth, W.J.; Vartuli, J.C.; Beck, J.S.; Nature(1992) 359, 710.

[Kusak2009] Goworek, J.; Kierys, A.; Gac, W.; Borówka, A.; Kusak, R., Journal of Thermal Analysis and Calorimetry (2009) Vol. 96 2, 375–382.

[Lazzari2002] Lazzari, R., J Appl Cryst (2002)35, 406-421.

[Lee2001] Lee, C. T.; Johnston, K. P. Dai, H. J.; Cochran, H. D.; Melnichenko, Y. B.;Wignall, G. D. J. Phys. Chem. B (2001) 105, 3540.

[Lee2005] Lee B.; Park I.; Yoon J.; Park S.; Kim J.; Kim K.; Chang T.; Ree M. Macromolecules (2005) 38, 4311-4323.

[Mattenet2010] Mattenet, M.; Lhost, K.; Konovalov, O.; Fall, S.; Pattier, B., An X-Ray ThermoPressure Cell For Carbon Dioxide AIP Conf. Proc., (2010)1234, 111.

[Pierre1998] Pierre, A. C., "Introduction to Sol Gel Processing", 1era edición, Kluwer Publishers, 1998.

[Pietra2012] Pietra, F.; Rabouw, F. T.; Evers, W. H.; Byelov, D. V.; Petukhov, A. V.; Donegá, C. M.; Vanmaekelbergh, D., Nano Letters (2012) 12, 5515–5523.

[Sanchez2008] Sanchez, C.; Boissière, C. ; Grosso, D. ; Laberty, C. ; Nicole, L., Chem. Mater. (2008) 20, 682–737.

[Smarsly2005] Smarsly, B.; Gibaud, A.; Ruland. W.; Sturmayr, D.; Brinker, C.J., Langmuir (2005) 21, 3858-3866.

[Saxena2004] Saxena, R.; Rodriguez, O.; Cho, W.; Gill, W.N.; Plawsky, J.L.; Baklanov, M.R.; Mogilkinov, K.P., J. Non Crist. Sol. (2004) 349, 189.

[Senesi2013] Senesi, A.; Eichelsdoerfer, D.; Macfarlane, R.; Jones, M.; Auyeung, E.; Lee, B.; Mirkin, C., Angew. Chem. Int. Ed. (2013) 52, 6624 –6628.

[Smilgies2012] Smilgies, D.; Heitsch, A.; Korgel, B. J. Phys. Chem. B (2012) 116, 6017−6026.

[Stein2007] Stein, G.; Kramer, E.; Li, X.; Wang, J. Macromolecules (2007) 40, 2453-2460.

[Tate2007] Tate, M. P.; Hillhouse, H. W. J. Phys. Chem. C. (2007) 111, 7645−7654.

[TrongOn2001] Trong On, D.; Desplantier Giscard, D.; Danumah, C.; Kaliaguine S., Applied Catalysis A : General (2001) 222, 299-357.

[Zhao1998] Zhao, D.; Feng, J.; Huo, Q.; Melosh, N.; Fredrickson, G. H.; Chmelka, B. F.; Stucky, G.D., Science (1998) 279, 548-552.

[Zimmy2009] Zimny, K.; Blin, J.L.; Stébé, M.J., J. Phys. Chem.C (2009) 113, 11285-11293.

[Zukalova2005] Zukalova, M.; Zukal, A.; Kavan, L.; Nazeeruddin, M.K.; Liska, P.; Grätzel,M. Nano Letters (2005) 5, 9, 1789.

GENERAL CONCLUSIONS AND PERSPECTIVES

This thesis work has been focused on exploring, by using x-ray techniques available at synchrotron facilities, the structure of materials exposed to supercritical CO_2 under different pressures. The originality of this work consists in following the evolution of morphology or the structure of materials during their exposure to this fluid.

The Chapter 3 is concerned to the study of the porosity of $CaCO_3$ microparticles of vaterite made by a conventional chemical route and by supercritical CO_2. It it is shown that this microspheres exhibit hierarchical porosity made of macropores and mesopores. The quantitative determination of the pore size and of the pore smoothness was achieved by implementing the Guinier Porod model recently proposed by Hammouda for two types of pores. The radii of gyration of the two components and their fractal dimension were obtained. It was found that macropores have fractal dimension close to 4 indicating smooth surfaces whereas mesopores located inside the microspheres have smaller fractal dimension which highlights a rough surface. In both cases radii of gyration are of the order of 280 nm for the macropores and about 20 times smaller for the mesopores. The porosity and the surface area was furthermore determined following the approach of for powders by calculating a Porod invariant based on the effective thickness of the pulverulent pellet. The specific surface and the mesoporosity are quite close to the results extracted from N_2 adsorption-desorption analysis. This analysis was recently complemented by CDI experiments at the ID10A beam line of the ESRF. Using the data acquired from these experiments we were able to reconstruct a 3D image of the complete shape of these particles and to evidence their inner geometry by 3D tomography. These types of particles are of great interest for their use as a host matrix for proteins. Thus for future research, it would become fruitful to carry out a similar 3D image analysis on this particles after protein encapsulations in order to know the location of these proteins in the host matrix.

Chapter 4 is devoted to the study of ultra thin films of polystyrene under pressurized CO_2 conditions. In a first stage, the analysis of AFM images revealed that PS films of 4nm dewet the surface of HF treated silicon. This was quite surprising as this fact contradicts theorical expectations. In a second part an in-situ XRR and GISAXS study was conducted on the swellability as a function of pressure of Polystyrene materials either confined in one (thin film) and two dimensions (islands). Our results were similar to those reported by other groups concluding that thin films swell when they are exposed to CO_2. However in the case of PS islands, we observe a much larger swellability than for a homogeneous thin film. This effect can be attributed to the larger free surface in the island compared with that of thin films which allows for a greater absorption of CO_2. In addition, it was shown that PS islands (h<10 nm) supported on HF treated silicon do not spread in supercritical CO_2 environment. PS islands remain at a fixed position and grow only in the perpendicular direction. For future research, it would interesting to study the stability of PS thin film deposited on native Silicon under CO_2 pressure in order to go further on the analysis of the stability of thin film of Polystyrene. Additionally, the behaviour of such films exposed to other pressurized gas would be quite instructive.

In Chapter 5, we focused on the analysis of mesoporous silica thin films. These thin films have been successfully prepared using CTAB and FSN as a surfactant. The CTAB-surfactant was successfully removed by calcination, a detailed study using XRR and GISAXS identified various regimes of temperature during the heat treatment. The regime which occurs between 180°C and 250°C corresponds to the removal of the surfactant accompanied with a distortion of the pore shape. Above 300°C the surfactant was removed, but it was found that a small quantity of organic fragments may still remain. After this treatment the structure doesn't shrink up to 600°C. For FSN, an alternative method of surfactant extraction without affecting the 2D structure have been presented where we show that supercritical carbon dioxide extraction is effective to extract the fluorinated template from the pores of as-prepared mesoporous thin film. The structure of the mesopore is preserved after the sc-CO_2 treatment. Finally, we have outlined a general and versatile method based on the use of the DWBA and related approximations, with analytical expressions for calculating the GISAXS patterns of any mesoscopically ordered periodic structure in thin films. This approach yields excellent quantitative fits to the experimental

intensities of the Bragg reflections measured in the GISAXS patterns. In this respect, the present analysis provides unprecedented access to the anisotropy of scattering objects, such as pores. Our approach can be generalized to extract quantitative information from GISAXS patterns of any 3D ordered structure including not only micelles and block copolymer liquid-crystalline phases, but also core/shell nanoparticle superstructures, ordered nanocomposites, and any crystalline mesoporous materials deposited on a substrate, thus further substantiating the claim of GISAXS as the method of choice for studying nano- and mesoscale thin-film assemblies.

APPENDICES

APPENDIX A

A. CO_2 Pressure cell

A pressure cell (see Fig.A.1) was built with the aim of studying systems such as surfaces, polymer and mesoporous films in an environment with CO_2 at gas, liquid and supercritical states. This device is available at the ID10 (ESRF) facilities and offers the possibility to perform studies with X-ray Reflectivity, Grazing Incidence Small Angle, Grazing Incidence Diffraction.

The pressure inside the cell can be varied from 0 to 100 bars with a precision of 0.05 bar using a system designed at the ESRF. The temperature inside the cell can be set in the range from 5°C to 70 °C with a precision of 0.05°C. The inner volume of the cell is 100cm^3. The maximum sample size is 30 x 25 x 1mm^3. More details can be found in [Mattenet 2010]

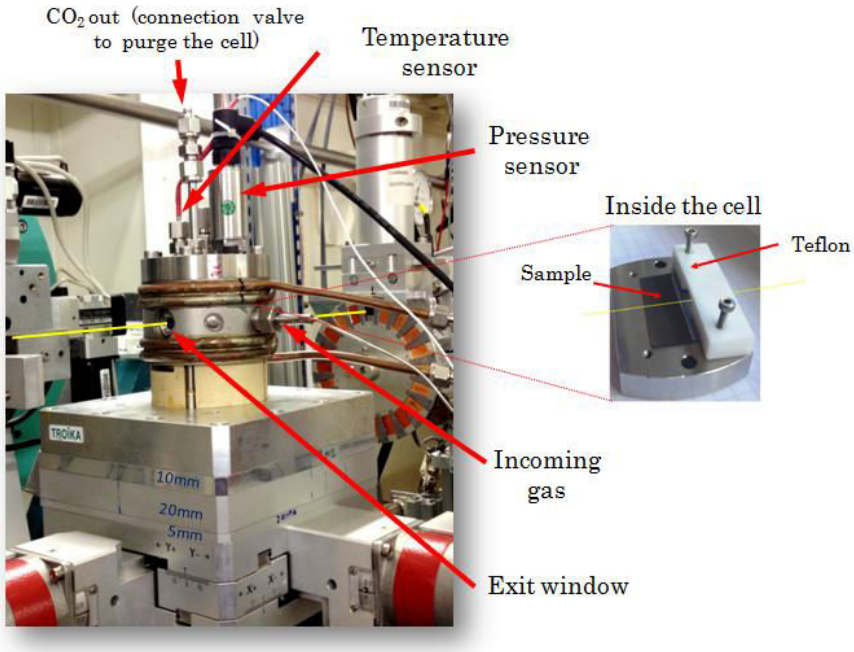

Figure A.1 Picture of cell mounted on the ID10B difractometer. The pressure and temperature sensor are fixed on the cover. The X-rays pass through the diamond window with an 89.7 % transmission at 22Kev.

The X-ray beam enters and exits the cell trough an aperture with a diameter of 2mm. Two diamond windows of 0.5mm thickness glued on the apertures provide both the high transmission for the incident and scattered X-ray beam and the mechanical resistance to high pressures. The breaking pressure of the windows is 650 bars. This diamonds, were CVD-single crystals provided by *Element Six* Company. For the operation of the pressurization CO_2 system. It is necessary first increase the pressure in the tank (see Fig.A.2B) e.g. 200 bar. This pressure is achieved by compressing the gas coming from a CO_2 bottle (see A.2A) using the *ROB* (see Fig.A.2C). Then the pressure cell is filled with CO_2 at any pressure. The pressure in the cell is controlled by the *Eurotherm* regulator (see Fig.A.2F) which measures the pressure inside the cell. The temperature control is performed using pipes welded around the cell that are connected to a thermostat bath (chiller with silicon oil) (see Fig.A.2E). The temperature range of this device is from -40°C to 140°C while the present temperature limitation of the pressure cell is from -10°C to 70°C due to the pressure sensor.

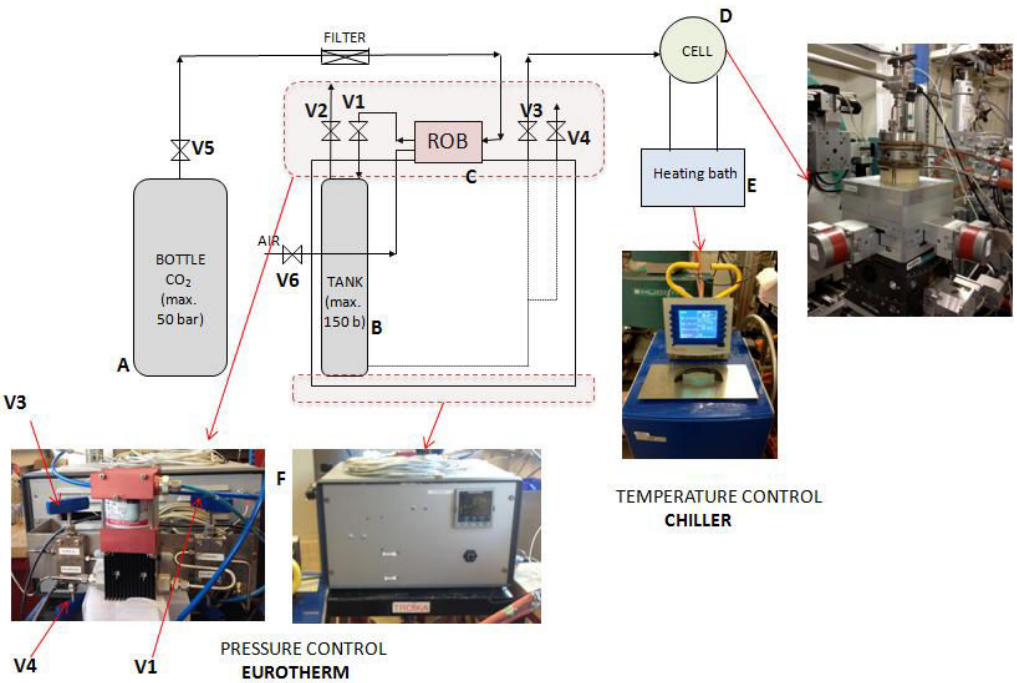

Figure A.2 Scheme of the pressure system

A	CO2 gas bottle	**V1**	Tank CO_2 inlet
B	Tank of compressed CO_2	**V2**	Tank CO_2 outlet
C	CO_2 compressor	**V3**	Cell CO_2 inlet
D	Pressure Cell	**V4**	Cell CO_2 outlet
E	Heating bath	**V5**	CO_2 manometer and pressure regulator
F	Pressure control system	**V6**	Air pressure regulator

Table A.1 General Description of each component

Bibliography

[Mattenet2010] Mattenet, M.; Lhost, K.; Konovalov, O.; Fall, S.; Pattier, B., An X-Ray ThermoPressure Cell For Carbon Dioxide AIP Conf. Proc., (2010)1234, 111.

APPENDIX B

B. Influence of CO_2 pressure on the data analysis

When XRR and GISAXS experiments are conducted under pressure it is important to notice that the medium through which the beam is impinging on the sample has an index of refraction which varies continuously with pressure. The index of refraction of a gas can be obtained by application of the elastically bounded electron model. Such model yields

$$\mathrm{n} = 1 - \delta - \mathrm{i}\beta \qquad [B.1]$$

where the difference to unity is given in the real part by $\delta = \boldsymbol{r}_e \lambda^2 \rho_e / 2\pi$. When working with a gas under pressure, any change in pressure will produce a change in density (ρ_e) so the index of refraction for x-rays of a gas under pressure is therefore changing with pressure. This is quite obvious given the fact that the pressure is just a macroscopic consequence of the number of molecules embedded in a container.

The fact that the electron density of the pressurized gas on top of the substrate increases with pressure has a clear impact on the critical edge of the silicon reflectivity. This statement can be understood from the Snell Descartes law. This law can be seen as a conservation law in which the conserved quantity is simply the component of the k wave vector parallel to the surface of the sample and this, whatever the encountered interface.

The conservation of this quantity is established by writing the continuity of the electric field and of its first derivative in the z direction normal to surface so that one can state that

$$\boldsymbol{k}_j \cos(\theta_j) = \boldsymbol{C} \qquad [B.2]$$

where k_j is the wave vector modulus in medium j , the grazing angle θ_j is the angle between the x-ray beam and the interface j-1,j and C is a constant [Gibaud2009]. Assuming that the pressurized gas is labelled medium 1, and the substrate medium 2, it follows that $\boldsymbol{k}_1 \cos(\theta_1) = \boldsymbol{k}_2 \cos(\theta_2)$. In any medium j, the modulus of the wave vector is related to the wave vector, k_0, in air as $\boldsymbol{k}_j = \boldsymbol{k}_0 \boldsymbol{n}_j$.

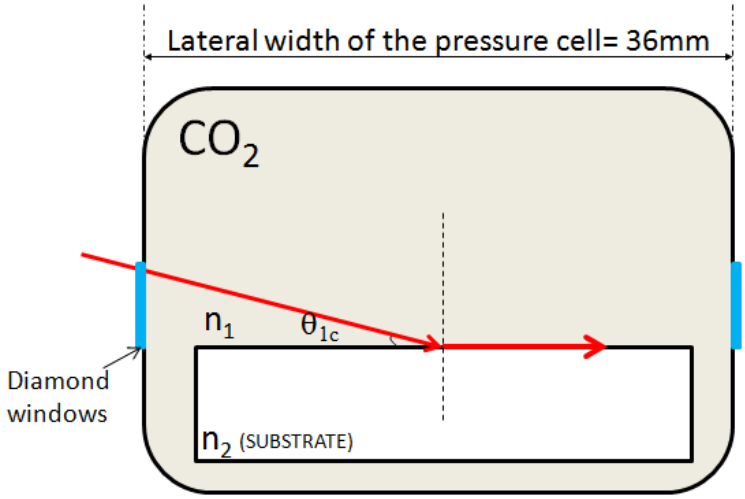

Figure B.1 Scheme of the total reflection at the critical angle of substrate.

Finally Snell law in the case of total reflection can be expressed as

$$\boldsymbol{n}_1 \cos(\theta_{1c}) = \boldsymbol{n}_2 \qquad [B.3]$$

where θ_{1c} is the critical angle in the medium 1 and $\cos(\theta_{1c})$ may be replaced by the corresponding Taylor's series,

$$\theta_{1c} = \sqrt{2(\delta_2 - \delta_1)} \qquad [B.4]$$

This last expression shows unambiguously that the critical angle of the substrate itself is affected by the presence of the pressurized gas in contact with it. A simulation of this effect can be achieved by using the density of the pressurized gas. In the case of carbon dioxide, information about the density of CO_2 at a given pressure can be obtained from the NIST data base[3]. The last expression can be transformed into a critical wave vector transfer $q_c(P)$ as follow:

$$\boldsymbol{q}_c(\boldsymbol{P}) = \frac{4\pi}{\lambda} \sin(\sqrt{2(\delta_2 - \delta_1(\boldsymbol{P}))}) \qquad [B.5]$$

It is remarkable to notice that the pressure in the cell of the gas above the substrate affects not only the critical angle of the layer in contact with the gas but

[3] http://webbook.nist.gov/chemistry/.

also all the other buried layers via the conservation of the component of the k wave vector parallel to the surface.

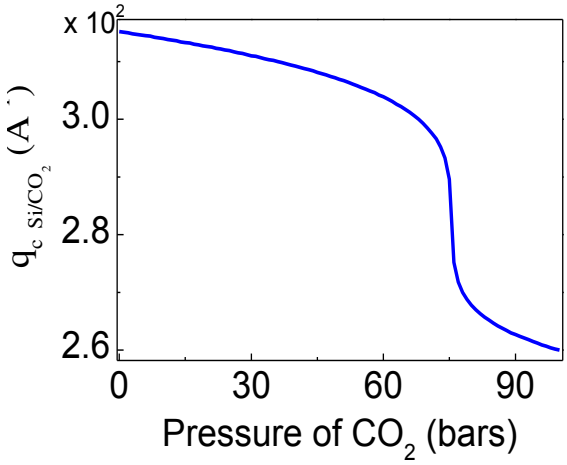

Figure B.2 Change of the critical wave vector of silicon in presence of pressurized CO_2. Data obtained from NIST at 32 °C.

Additionally the shift of the critical wave vector transfer with pressure is accompanied by a loss of the reflected intensity. This effect is mainly related to the fact that the incident and reflected beams are attenuated in the cell by the increasing pressure of the gas. This effect can also be understood by calculating the transmission coefficient of the cell under pressure.

$$T_{CO2} = e^{-u_a x} \qquad [B.6]$$

This coefficient is given by the Beer-Lambert law and depends on both the pathway 'x' in the cell (see fig. B.1) and the absorption coefficient μ_a.[4] However to have a true and complete idea for the total transmission T_F in the cell we have to add to our calculations the intensity lost due to the attenuation by the diamond windows. Thus the total transmission becomes:

$$T_F = (2xT_D)T_{CO2} \qquad [B.7]$$

[4] The Lawrence Berkeley Laboratory (LBL) database [http://henke.lbl.gov/optical_constants/] provides full access to this value at any energy and for any gases provided that the density of the gas is known at the given pressure.

where T_D is given by exp(u_Dt), t=0.5 mm is the thickness of the diamond windows and u_D= 1.08e-4 μm^{-1} is the attenuation coefficient of the diamond .

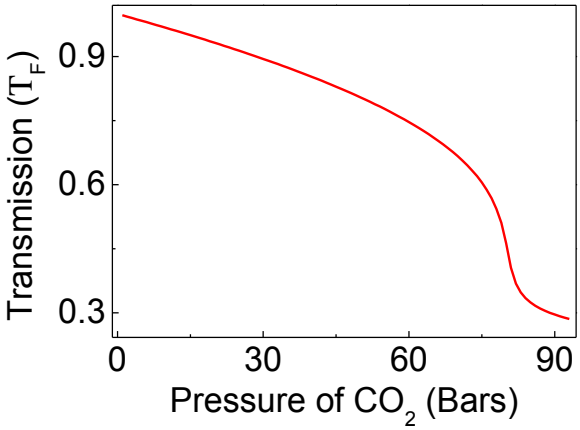

Figure B.3 Total transmission T_F thought the cell as a function CO_2 pressure. This value was calculated taking in account the attenuation of the intensity by the diamond windows. Data obtained from NIST at 32 °C and 22 keV.

Bibliography

[Gibaud2009] Gibaud, A. Specular Reflectivity from Smooth and Rough Surfaces, X Ray and Neutron Reflectivity: Principle and Applications, Edited by Daillant, J. and Gibaud, A. (Springer, Paris 2009), pp 133-182.